An Examination of Sonocrystallization Kinetics of L-Glutamic Acid

By

Siyi Jiang

Submitted in accordance with the requirements for the degree of

Doctor of Philosophy

University of Leeds

Institute of Particle Science and Engineering

School of Process, Environmental and Materials Engineering

April 2012

Dedicated to my beloved parents, *Guangze Jiang* and *Najia Shi*

And

My brother, *Shang Jiang*

"*To make you proud*"

Acknowledgements

Abstract

The power ultrasound effects, the sonocrystallization kinetics and mechanism are investigated for cooling crystallization of l-glutamic acid (LGA) from aqueous solution.

Sonocrystallization experiments involving slow and crash cooling have been undertaken for the metastable zone width and induction time measurement. LGA nucleation kinetics was extracted using Nývlt's method. The results revealed that application of ultrasound can effectively narrow the metastable zone width, significantly reducing the induction time, and accelerate the nucleation rate. The calculated critical nucleus size and interfacial tension suggested that ultrasound reduces the nucleation energy barrier to allow crystallization to occur readily. These effects became more obvious with the increase of ultrasound power.

The pressure upon the collapsing cavitation bubble was calculated along with the nucleation rate under the collapsing pressure. In order to identify the mechanism, an approach was developed in the literature for calculating the ultrasound-induced nuclei number which was employed to establish the inter-relationship between the cavitation number and nucleation event. Whilst the theoretical calculation did not fully match the experimental measurement, the total induced nuclei number was found to be proportional to the cavitation issue; therefore, it still provides a potentially credible mechanism for illustrating the sonocrystallization process.

Studies on seeded crystal growth in the ultrasound field indicated that the effect of ultrasound irradiation on LGA growth depends on the supersaturation. The ultrasound increased the growth rate at low supersaturation, while it appeared to have no effect at high supersaturation. The corresponding growth mechanism is believed to be the 2-D nucleation growth. A population balance model was applied for the seeded growth process to predict the dynamic evolution of the particle size distributions that are validated by experimental measurements.

The influence of operating conditions on LGA polymorphism was also studied. Investigation of the ultrasound effect on polymorphism suggested that ultrasound favours the precipitation of the stable β-form by improving the surface nucleation of the β-form and hence increasing the transformation rate. The analysis of the LGA crystals produced proved that the variation of ultrasonic power and insonation interval can be utilized to manipulate the particle size distribution and crystal morphology.

Notation

Symbols	Definition	Units
a	Activity of the solute	-
A, A'	Pre-exponential factor	-
a_d	Detected limit of instrument	-
a_e	Equilibrium activity between liquid and solid phase	-
a_f, b_f, k_v	Shape factor of crystals	-
A_n, A_{for}	Surface area	m^2
b	Cooling rate	$°Cmin^{-1}$
B	Total cavitation bubbles number in the reactor	-
b'	Cavitation bubble formation rate	m^3s^{-1}
C	Solution concentration	gL^{-1}
$C*$	Equilibrium concentration	gL^{-1}
C_0	Nucleation site on the surface	m^{-3}
C_{inital}	Initial concentration	gL^{-1}
C_L	Sound velocity in the liquid	ms^{-1}
C_{max}	Maximum allowable supersaturation	g
D	System-relative nucleation parameter	-
d	Growth dimension	-
D_{ab}	Diffusion coefficient	m^2s^{-1}
d_m	Molecular diameter	m
f	Frequency of sound wave	Hz
$f*$	Collision factor	s^{-1}
$G*$	Free energy at critical nucleus radius	J
G_c, G	Growth rate	ms^{-1}
G_{final}	Final Gibbs free energy	J
G_{gibbs}	Overall excess free energy	J

Symbols	Definition	Units
G_{inital}	Initial Gibbs free energy	J
G_S	Surface excess free energy	J
G_V	Volume excess free energy	J
He_{ad}	Adsorption constant	-
I	Intensity	W/m^2
J	Nucleation rate	$m^{-3}s^{-1}$
J	Average nucleation rate	mol^{-1}
J_{het}	Heterogeneous nucleation rate	$m^{-3}s^{-1}$
J_{hom}	Homogeneous nucleation rate	$m^{-3}s^{-1}$
K	The Polytropic index	-
k_B	The Boltzmann constant	J/K
k_g	Growth rate constant	-
k_m	Nucleation rate constant	-
k_{SN}, k_{SG}	System-relative nucleation parameter	-
L	Particle characteristic size	m
M	Molecular weight	$gmol^{-1}$
m	Apparent nucleation order	-
n	Number	-
n'	Apparent growth order	-
$n*$	Molecule number in critical nucleus	-
N_A	Avogadro's number	mol^{-1}
N_b	Nuclei number generated by a single bubble	-
N_m	Nuclei number	-
P	Pressure in the cavitation bubble	atm
P_0	Ambient pressure	atm
P_A	Ultrasound pressure amplitude	atm
P_a	Acoustic field pressure	atm

Symbols	Definition	Units
P_g	Gas pressure	atm
P_m	Liquid pressure	atm
P_{max}	Maximum pressure	atm
P_{output}	Ultrasound output power	W
P_v	Vapour pressure	atm
R	Cavitation bubble radius	m
R	Acceleration of the cavitation wall	m
R	Cavity wall velocity	ms^{-1}
R_0	Initial cavitation bubble radius	ms^{-2}
r_c	Critical nucleus size	m
R_e	Equilibrium bubble radius	m
R_m	Maximum cavitation bubble radius	m
S	Supersaturation ratio	-
T	Temperature	°C, K
t	Time	s
T_0	Ambient temperature	°C, K
t_{ind}	Induction time	s
$t_{insonation}$	Insonation interval	s
T_{int}	Initial temperature	°C, K
T_{max}	Maximum undercooling	°C, K
$t_{shockwave}$	Shock wave lifetime	s
v_c	Molecular volume of solid	m^3
$V_{cavitation}$	Cavitation volume	m^3
$V_{effective}$	Effective caviation volume	m^3
v_s	Partial molecular volume	m^3
W^*	Nucleation work	$Jmol^{-1}$
z	Zeldovich factor	-

Greek letters	Definition	Units
μ	Chemical potential	J
γ	Interfacial tension	Jm^{-2}
$\gamma_{effective}$	Effective interfacial tension	Jm^{-2}
θ	Angle	°
ε	Correlation factor	-
σ	Relative supersaturation ratio	-
λ	Wavenumber	-
η	Liquid viscosity	sm^{-2}
τ	Collapse duration of cavitation bubble	s
ρ_c	Solid density	gm^{-3}
ρ_L	Liquid density	gm^{-3}
υ	Growth index	-
ψ	Active pre-factor for heterogeneous nucleation	-
Φ	Total surface energy	J

Abbreviation	Definition
LGA	L-glutamic acid
MSZW	Metastable zone width
FBRM	Focused Beam Reflectance Measurement
ATR-FTIR	Attenuated Total Reflectance-Fourier Transform Infrared
PXRD	Powder X-Ray Diffraction
PLS	Partial Least Square

Content

Chapter 6 Studies of Power Ultrasound Effects on the Crystal Growth Kinetics of L-Glutamic Acid

Chapter 7 Studies of Power Ultrasound Effects on the Crystal Growth Kinetics of L-Glutamic Acid

Figure List

Table List

Chapter 1

Introduction

Summary: A brief introduction to the research work background together with the project overview is given in this chapter. This is followed by presentation of the thesis structure and chapter description.

1.1 Research Background

Crystallization is one of the oldest, but most important techniques in the chemical and pharmaceutical industries where the products or intermediates are solids and permitting separation and purification of substances from the mother liquid phase. Compared with other separation processes for solid material, crystallization is advantageous as it is relatively low in energy consumption and mild operation condition requested. In addition, it is an economical method and a convenient operation for either large scale production with continuous operation or small scale production with batch operation. Approximately 70% of the compounds are solids in the chemical industry and over 90% of pharmaceutical products have their active ingredient in crystalline form (Giulietti et al., 2001). Such significant proportion of materials produced in crystalline form makes the crystallization process undoubtedly stand out from other industrial separation processes.

However, crystallization is a very complex process involving variable parameters, multi-phases equilibrium, polymorphism transformation, uncertain nucleation and growth kinetics. This makes the prediction, design and control of crystallization processes very challenging. In order to achieve satisfactory crystallization product quality, great efforts are being made on crystallization process development:

➢ Systematic investigation of various relevant process parameters aiming at improving operational performance, such as the cooling profile, stirring, seeding, activities etc. (Kim et al., 2003, Kougoulos et al., 2005, Mackellar et al., 1994, Widenski et al., 2009).

➢ The application of state of the art process analytical techniques on process monitoring and control like ATR-FTIR, FBRM, NIR, XRD, Acoustic attenuation technique and Image analysis etc. (Ma, 2010, Dharmayat et al., 2006, Scholl et al., 2007, Hammond et al., 2007).

➢ Towards strategy on final product polymorphism manipulation and particle size distribution control (Kitamura, 2009, Kurotani and Hirasawa, 2008, Kougoulos et al., 2005).

➢ Implication of the external field on crystallization: magnetic field, ultrasound field, electric field etc. (Nanev and Penkova, 2001, Dalas and Koutsoukos, 1989, Kurotani et al., 2009, Revalor et al., 2011).

➢ Computer simulation (Ma and Wang, 2012, Kalbasenka et al., 2011, Hammond et

al., 2005).

Ultrasound used as an external factor in crystallization offers significant potential to promote and modify the crystallization process and crystallization products. This technology is called sonocrystallization and has been rapidly developed over the last 20 years. A large amount of researchers have revealed that ultrasound affected the nucleation and growth by initiating primary nucleation, narrowing metastable zone width, shortening induction time and accelerating nucleation and growth rate (Dalas, 2001, Luque de Castro and Priego-Capote, 2007, Wohlgemuth et al., 2010, Guo et al., 2006a, Lyczko et al., 2002). Ultrasonic irradiation has also been proven to improve the product in terms of the crystal morphology, particle size distribution and agglomeration (Narducci et al., 2011, Li et al., 2003). Furthermore, ultrasound was expected to be a useful method in isolating selective and desired polymorphic form during crystallization (Gracin and Åke, 2004, Gracin et al., 2005, Louhi-Kultanen et al., 2006, Kurotani and Hirasawa, 2010) and offered an alternative strategy for crystallization process control to eliminate the requirement of seeding (Narducci and Jones, 2012, McCausland.L. J, 2001, Ruecroft et al., 2005).

With regard to the exploit effects described above, cavitation is commonly recognized as the essential causation of ultrasonic actions in crystallization. Several theories and relative research work has been proposed to illustrate the sonocrystallization mechanism, such as the hot-spot theory, the surface chemical theory and segregation model. But the mechanism of sonocrystallization is up to now, not well understood and none of the theory can be used to fully explain the sonocrystallization behaviour because of the lack of correlation between crystallization events and ultrasound irradiation. Moreover, the ultrasound effects on crystallization are diverse and differ from the material substance and ultrasonic condition (Amara et al., 2004, Miyasaka et al., 2006a, Miyasaka et al., 2006b, Chow et al., 2003).

Therefore, although the idea of sonocrystallization is not new, the additional experimental data and further investigation on ultrasound and crystallization event correlation are still needed.

1.2 Research Aims and Objectives

This project concerns the robust power ultrasound assistant l-glutamic acid (LGA) cooling crystallization process which aims to elucidate the ultrasound effect on many aspects of LGA crystallization behaviour and the development of the sonocrystallization mechanism. The specific objectives of the research work are:

➢ Determination of the influence of ultrasound irradiation on nucleation, and elucidating the ultrasound power effective factor.

➢ To develop the ultrasonic nucleation mechanism and establish the cavitation number and nucleation event correlation.

➢ To examine the crystal growth from bulk solution in ultrasonic field and the corresponding growth mechanism.

➢ Numerical simulation of ultrasound assisted crystallization.

➢ To investigate the effect of ultrasound irradiation on the behaviour of polymorphs and the possibility of applying ultrasound in the LGA polymorphs manipulation.

➢ To study the serviceability of ultrasound irradiation on final particle size distribution and crystal habit control.

1.3 Structure of the Thesis

Following this introduction, an extensive description of important fundamental crystallization theory is given in Chapter 2. From the nucleation kinetic evaluation, the discussion moves to the crystal growth mechanism. The polymorphism phenomenon and process analytical techniques are also introduced and reviewed.

In Chapter 3, the background theory of power ultrasound is presented. Particularly the focus is on the review of previous work on sonocrystallization investigation, including the ultrasonic effects on many aspects of crystallization and possible proposed mechanisms of ultrasound action.

Chapter 4 describes the experimental work including the material examined and details of analytical techniques utilized in this project.

The basic ultrasound assisted crystallization behaviour of LGA is investigated in

Chapter 5, including the metastable zone width, the induction time measurement and solubility and supersolubility curves determination. From the measuring data, nucleation parameters and kinetics were determined. The observation of LGA polymorphs isolated in an ultrasound field with process related conditions is carried out.

An attempt to develop the ultrasonic nucleation kinetics by correlating the cavitation collapsing pressure and nucleation rate is presented in Chapter 6. The developed induction time equation is implemented to calculate the ultrasound-induced nuclei number which allows the comparison of the theoretically estimated results from an ultrasound point of view.

Chapter 7 is dedicated to the study of LGA growth from different supersaturation level bulk solutions with ultrasound irradiation based on the seeding process. The possible growth mechanism under irradiation of power ultrasound is discussed followed by the investigation of ultrasound effects on particle size distribution and crystal habit.

From the seeding growth, a population balance model considering of only the crystal growth is proposed in Chapter 8, allowing for the validation of growth kinetics obtained in Chapter 7.

Eventually, the main observation results are concluded, along with the suggestions for the direction of future work.

A list of references is included at the end of the thesis.

1.4 Closing Remarks

The introduction of the investigation background and project motivations and objectives are described in this chapter. The delivery framework and thesis structure are also given.

Chapter 2

Fundamental Theory of Crystallization

Summary: In this chapter, the fundamental theory of crystallization including nucleation, growth process and the crystal polymorphism are given. The associated experimental process analytical techniques are also discussed.

2.1 Introduction

Crystallization is the formation process of solid crystals from gaseous phase, liquid or liquid melt state and in the chemical industry, the most frequent process used is the crystallization from liquid. The industrial scale liquid crystallization method including the cooling crystallization, distillation crystallization, salting-out crystallization and reaction crystallization which are assorted depend upon the way that supersaturation was created. A general crystallization process can be depicted in the following schematic steps:
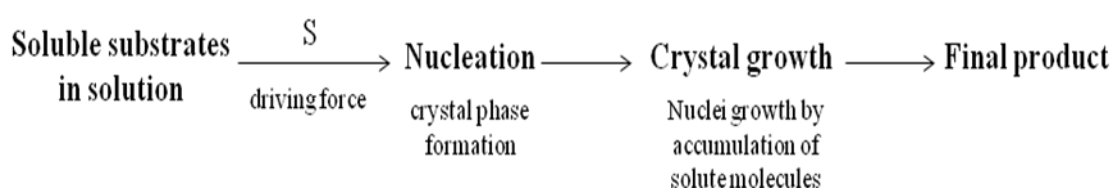
Figure 2.1: The general scheme of crystallization process from solution

In this chapter, the fundamentals of the crystallization process, including supersaturation driving force, nucleation and crystal growth, as well as the polymorphism behaviour of crystals，are given. The crystallization process analysis and characterization techniques associated with the current work are also presented.

2.2 Solubility and Supersaturation

Crystallization depends on the equilibrium relationship of the solute and solvent, when a solution is still under saturated condition, the solid in the solution can still dissolve until it reaches the saturation point where the solid and liquid state are thermodynamic equilibrium. This point can be represented by solubility which is the maximum amount of solute dissolved in a solvent at equilibrium. Therefore, solubility represents the ability of a substance to dissolve in solvent and is normally expressed as a function of temperature. However, spontaneous crystallization will not occur in this circumstance because crystallization required the addition of a driving force to overcome the energy barrier. The typical solubility and supersolubility diagram shown in Figure 2.2 developed by Miers and Isaac (Miers and Isaac, 1906, Miers and Isaac, 1907) in the early 1900's has explained well the supersaturation and spontaneous crystallization correlation and an important crystallization control parameter

7

metastable zone width.
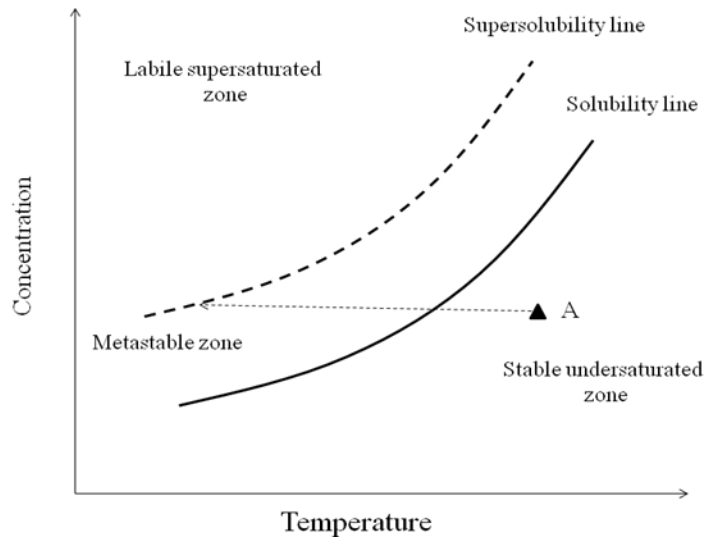
Figure 2.2: The typical solubility and supersolubility diagram

The solubility and supersolubility lines where spontaneous crystallization can occur divide the diagram into three regions:

➢ the stable undersaturated zone, where the solution is still under saturated conditions and no crystallization occurs;

➢ the metastable zone, as the name implies, is metastable and spontaneous nucleation is not possible but growth may occur;

➢ the unstable supersaturated zone, where spontaneous and rapid nucleation can be experienced.

Considering the solution at point A, in this project for instance, to achieve nucleation conditions, temperature must be cooled down across the solubility line and further into the labile zone. The most common expressions of the supersaturation level are the supersaturation ratio, S, and the concentration driving force, $\triangle C$, as shown in Equation (2.1) and (2.2), respectively (Mullin, 1993).

$$S = \frac{C}{C*} \qquad (2.1)$$

$$\Delta C = C - C* \qquad (2.2)$$

where C is the solution concentration at the specific temperature and $C*$ is the equilibrium concentration at the same temperature. Therefore, it is important to control the width of the metastable zone within a precise scope in order to control the supersaturation-dependent crystallization. It is worth noting that the nucleation will

not occur immediately, even in the labile zone, owing to the reason mentioned previously, that the nucleation is a new phase formation process and energy accumulation is needed to overcome the energy barrier of nucleation. The delay duration of nucleation is so-called induction time which corresponds to the time from the saturated state to the first nucleus being formed in the supersaturated solution. The value of induction time greatly depends on the supersaturation level, the higher the supersaturation ratio, the shorter the induction time.

2.3 Nucleation

Nucleation is the first step of crystallization when the solid phase is transformed from the liquid phase. Figure 2.3 reveals the classification of nucleation according to how the nucleation takes place: whether or not the solid interface exists:
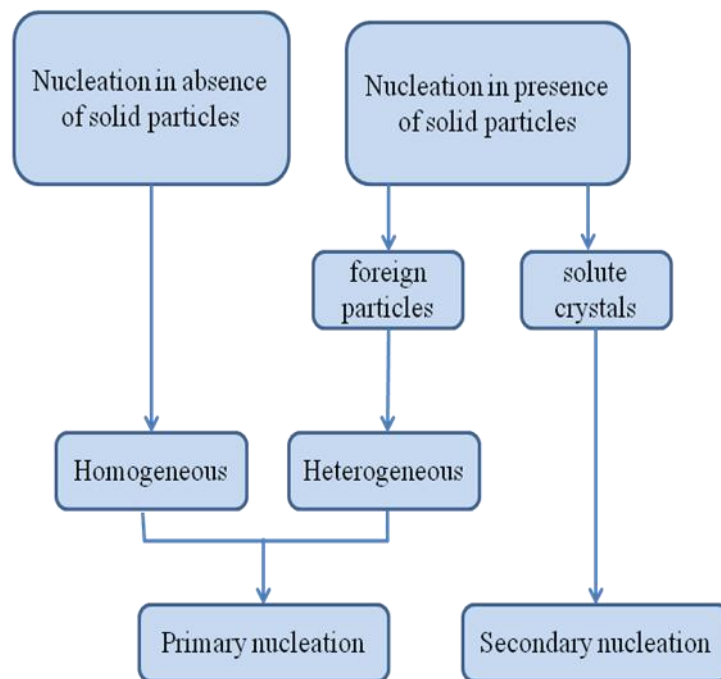
Figure 2.3: The schematic presentation of nucleation classification modified from Chow et al. (Chow et al., 2003, Luque de Castro and Priego-Capote, 2007)

2.3.1 Primary Nucleation

2.3.1.1 Homogeneous Nucleation

Homogeneous nucleation normally occurs in a random manner, as shown in Figure 2.4(a). The small solute molecules randomly join together to form a cluster, the cluster can grow to a larger size crystal only when it is larger than a critical size or a minimum stable nucleus size r_c, otherwise it can also reversibly dissolve back to the solvent. According to the classical nucleation theory root in Gibbs free energy, the free energy $\triangle G^*$ at critical cluster size reaches its maximum value which is the system energy barrier for nucleation (Figure 2.4(b)).
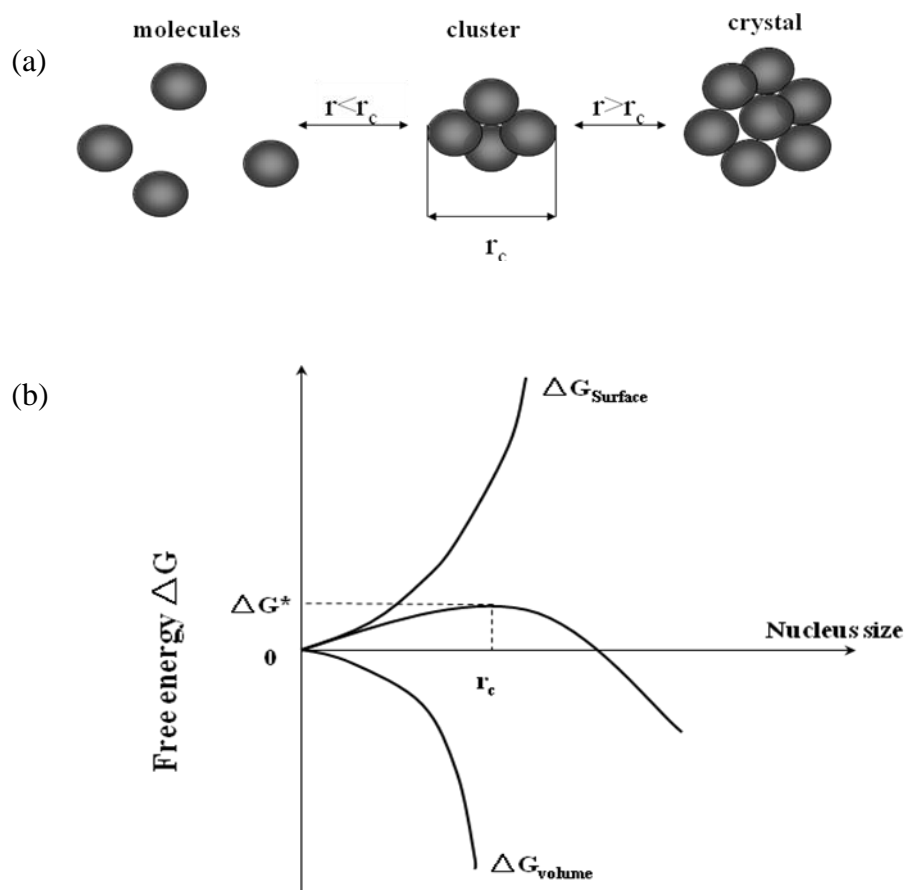
Figure 2.4: The nucleation process (Mullin, 1993). (a) the transition of nucleation; (b) the Gibbs free energy change at critical nucleus size

If a concept of the work $W(n)$ is adopted to describe the work to form a cluster of n molecules, it can be presented as (Kashchiev, 2000):

$$W(n) = \Delta G_{gibbs} = G_{final} - G_{initial} = -n\Delta\mu + \Phi(n) \tag{2.3}$$

where G_{final} and $G_{initial}$ are the final Gibbs free energy after cluster formation and the initial Gibbs free energy before the cluster formation, respectively. The value of $n=1,2,3,\ldots$ is the number of molecules in the cluster, $\Delta\mu$ is the chemical potential for nucleation normally expressed by supersaturation S and temperature T:

$$\Delta\mu = k_B T \ln S \tag{2.4}$$

where k_B is the Boltzmann constant and the total surface energy of the cluster formed $\Phi(n)$ can be approximated as:

$$\Phi(n) = \gamma A_n = a\gamma n^{2/3} \tag{2.5}$$

γ refers to the interfacial tension between solid and liquid phase, A_n is the total surface area of cluster and a is the shape factor.

Therefore, the nucleation work W^* which is the energy barrier to nucleate at the critical nucleus size, can be expressed by n^* molecules in critical cluster:

$$W^* = W(n^*) = \Delta G^* = -n^*\Delta\mu + \Phi(n^*) \tag{2.6}$$

For homogeneous nucleation, assume a spherical crystal,

$$n^* = \frac{8a^3\gamma^3}{27\Delta\mu} \tag{2.7}$$

Combining the Equations (2.4), (2.5), (2.6) and (2.7) and taking into account that $a^3 = 32\pi v_c^2$, the nucleation work W^* is found to be:

$$W^* = \frac{16\pi v_c^2\gamma^3}{3k_B^2 T^2 (\ln S)^2} \tag{2.8}$$

The nucleation rate J, defined as the number of nuclei formed per unit time per unit volume, is generally expressed by:

$$J_{hom} = A \exp(-W^*/k_B T) \tag{2.9}$$

which is applicably used in any kind of nucleation and in which the pre-exponential factor A is defined by:

$$A = zf^* C_0 \tag{2.10}$$

Typically, the value of z lies in the range 0.01 to 1, the concrete kinetic f^* in s^{-1}:$1<f^*<10^{12}$ and the nucleation volume on the old phase C_0 in m^{-3} is between 10^{15} and 10^{19}. Thus, Equation (2.9) becomes:

$$J_{hom} = A \exp\left(\frac{16\pi v_c^2\gamma^3}{3k_B^3 T^3 (\ln S)^2}\right) \tag{2.11}$$

The above equation indicates that the crystallization temperature, the interfacial tension and the solution supersaturation are three main variables govern the homogeneous nucleation rate.

2.3.1.2 Heterogeneous Nucleation

Homogeneous nucleation in practical crystallization processes is actually highly unlieable due to the fact that avoiding impurity during the process is impossible. As stated previously, heterogeneous nucleation involves foreign solid interface which acts as heteronuclei that reduces the free energy to a certain extent. Its effect on heterogeneous nucleation exhibits in terms of interfacial tension (Volmer, 1939, Mullin, 1993). In view of a crystallization solution, as shown in Figure 2.5, the presence of foreign particles results in a contact angle between the solid crystalline phase θ and the foreign solid surface, which corresponds to a smaller interfacial tension $\gamma_{effective}$ in comparison to the interfacial tension involved in homogeneous nucleation:

$$\gamma_{effective} = \Psi^{1/3}(\theta)\gamma \tag{2.12}$$

where $\psi(\theta)$ is the activity factor $0 \leq \psi(\theta) \leq 1$ reflecting the extent of wetting between the liquid-solid phase expressed as:

$$\Psi(\theta) = \frac{1}{4}(2 + \cos\theta)(1 - \cos\theta)^2 \tag{2.13}$$

Thus, in complete non-wetting where $\theta=180°$, $\gamma_{effective}=\gamma$ and nucleation is homogeneous; in circumstances of wetting angle $\theta<180°$, $\gamma_{effective}<\gamma$ and deducing the heterogeneous nucleation.
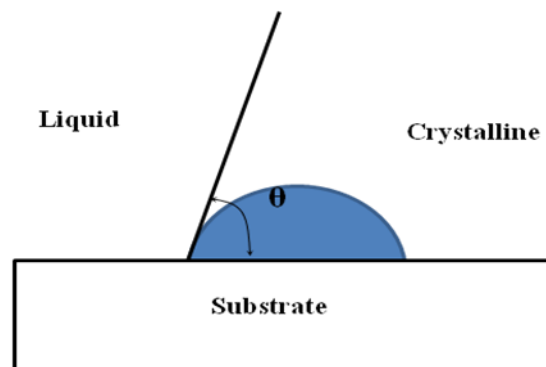
Figure 2.5: Illustration of foreign solid particle in crystallization system

To evaluate the heterogeneous nucleation rate from Equation (2.11), the interfacial tension term γ is simply replaced by $\gamma_{effective}$:

$$J_{het} = A \exp(\frac{16\pi v_c^2 \gamma_{effective}^3}{3k_B^3 T^3 (\ln S)^2})$$

(2.14)

Considering the different energy barriers involved in homogeneous and heterogeneous nucleation, it can be speculated that homogeneous nucleation dominates at relatively high supersaturation, while heterogeneous nucleation dominates at low supersaturation. Recent theoretical nucleation studies on consideration of the pressure effect were given by Kashchiev (Kashchiev and van Rosmalen, 1995) and performed in this work for sonocrystallization nucleation kinetic development.

2.3.2 Secondary Nucleation

For low supersaturated solutions, primary nucleation is not favoured, but secondary nucleation, which is catalyzed by the presence of solute crystals and associated with lower activation energy, is preferred. There are two possibilities that secondary nucleation occurs, either from the added seed crystals or from the existing crystals in the supersaturated solution. Some of the mechanisms are advanced to describe the secondary nucleation, such as initial breeding, needle breeding, contact nucleation, fluid shear nucleation.

The initial breeding nucleation, also known as dust breeding, is defined by Stricklan-Constable (Strickland-Constable, 1972) as the formation of crystals resulting from the microcrystals that have been swept away from the surface of seed crystals. Treated as the nuclei for growth, the size of the fragments must be over the critical nucleus size and if the immersed solution is supersaturated, the microcrystalline will grow and plays no role in operation as it is supersaturation independent (Girolami and Rousseau, 1986). In the needle breeding mechanism, the nucleation is initialized when the needle fragments desquamate from the growing crystals in high supersaturation solution and act as nuclei. The contact nucleation mechanism occurs due to the collision or fluid shear force when crystals contact with the crystals or impact with the vessel wall or agitator. In this case, the number of crystals created depends on both the supersaturation and the fluid motion (Thompson, 2001).

2.3.3 Nucleation Kinetics Evaluation: Nývlt's Method

Since primary nucleation in the actual crystallization process is believed to be heterogeneous rather than the homogeneous, the only justifiable empirical correlation for direct primary nucleation evaluation for real industrial systems is Nývlt's method (Nývlt, 1968):

$$J = k_m \Delta C_{\max}{}^m \qquad (2.15)$$

The nucleation rate J, the generated nuclei mass per unit mass of solution, is written in terms of the nucleation constant k_m and the apparent order of nucleation m with the maximum allowable supersaturation $\triangle C_{max}$ expressed as:

$$\Delta C_{\max} = (\frac{dC^*}{dT}) \Delta T_{\max} \qquad (2.16)$$

where C^* is the equilibrium concentration at temperature T and $\triangle T_{max}$ is the maximum undercooling which is the difference between the saturation temperature and crystallization temperature (the metastable zone width). Assuming that the nucleation is driven by cooling, the nucleation rate can also be determined from the cooling rate b, the temperature change per unit time $b = -\frac{dT}{dt}$:

$$J = \varepsilon \frac{dC^*}{dT} \cdot b \qquad (2.17)$$

where ε is the correlation factor for equilibrium concentration change with temperature. Combining Equations (2.15), (2.16) and (2.17) yields:

$$k_m [(\frac{dC^*}{dT}) \Delta T_{\max}]^m = \varepsilon \frac{dC^*}{dT} \cdot b \qquad (2.18)$$

Taking logarithms of both sides of Equation (2.18) leads to:

$$\log b = (m-1)\log \frac{dC^*}{dT} - \log \varepsilon + \log k_m + m \log \Delta T_{\max} \qquad (2.19)$$

which is also known as 'Nývlt's Equation' and has widespread use for primary nucleation kinetics determination by measuring the metastable zone width with different cooling rates. This method was performed in basic experimental part of this work for sonocrystallization kinetics evaluation presented in Chapter 5.

According to the classical relation of Equations (2.11) and (2.14), two important nucleation parameters, interfacial tension and critical nucleus size, can be determined from primary nucleation rate. However, direct measurement of nucleation rate is difficult and the most convenient method is to measure and calculate from the

induction time which is inversely proportional to the nucleation rate (Mullin, 1993):

$$t_{ind} \propto J^{-1} \tag{2.20}$$

Based on the homogeneous nucleation model, logarithmic induction time and nucleation gives:

$$\log t_{ind} \propto \frac{1}{T^3 \log^2 S} \tag{2.21}$$

Therefore, plotting $\log t_{ind}$ versus $T^3 \log^2 S$ will result in a straight line with a slope of A' which allows for evaluation of interfacial tension γ and hence the critical nucleus size r_c:

$$r_c = \frac{2\gamma v_c}{k_B T \ln S} \tag{2.22}$$

It is worth noting that Nývlt's method proposed here is established upon some of the assumptions and simplification (Mullin and Jančić, 1979, Liang, 2002): 1) the calculated nucleation rate equal to the rate of supersaturation at the moment nuclei are detected; 2) the measured induction time corresponds to the first nuclei generated from the supersaturated solution and does not account for the partial growth time; 3) the spherical nuclei are isolated. Nevertheless, this is still the preferred and the most capable method for nucleation process investigation. In Chapter 6, the time allowed for nuclei to grow to a detectable size will be taken into account in nucleation rate evaluation for a more accurate assessment on sonocrystallization.

2.4 Crystal Growth

After formation of nuclei, the crystals will grow by ordered deposition of the solute molecules diffused from the solution and cause the increase in crystal size. The growth process comprises a series of separated steps, as illustrated in Figure 2.6(a): (1) the transportation of solute molecules to the surface boundary layer; (2) diffusion of molecules through the boundary to the crystal surface following Fick's Law based on the concentration gradient; (3) adsorption on the crystal surface; (4) surface diffusion to the energetically favorable sites; (5) attachment to a step or edge; (6) diffusion along the step or edge; (7) incorporation into kink site. Like the nucleation process, crystal growth is a dynamic process with attachment and detachment occurring simultaneously, even at the equilibrium state, as is shown in step (4*) desorption from

the crystal. The free energy barrier to be overcome for associated growth steps are shown in Figure 2.6(b). Larger free energy is usually required for steps like the crystal adsorption, the step or edge attachment and the kink site incorporation.

Regarding the above steps of crystal growth which occur in series, the slow process is the growth rate-determined factor and the crystal growth can be either diffusion control when steps (1) and (2) are slowest or surface integration control when steps (3)-(7) are slowest.
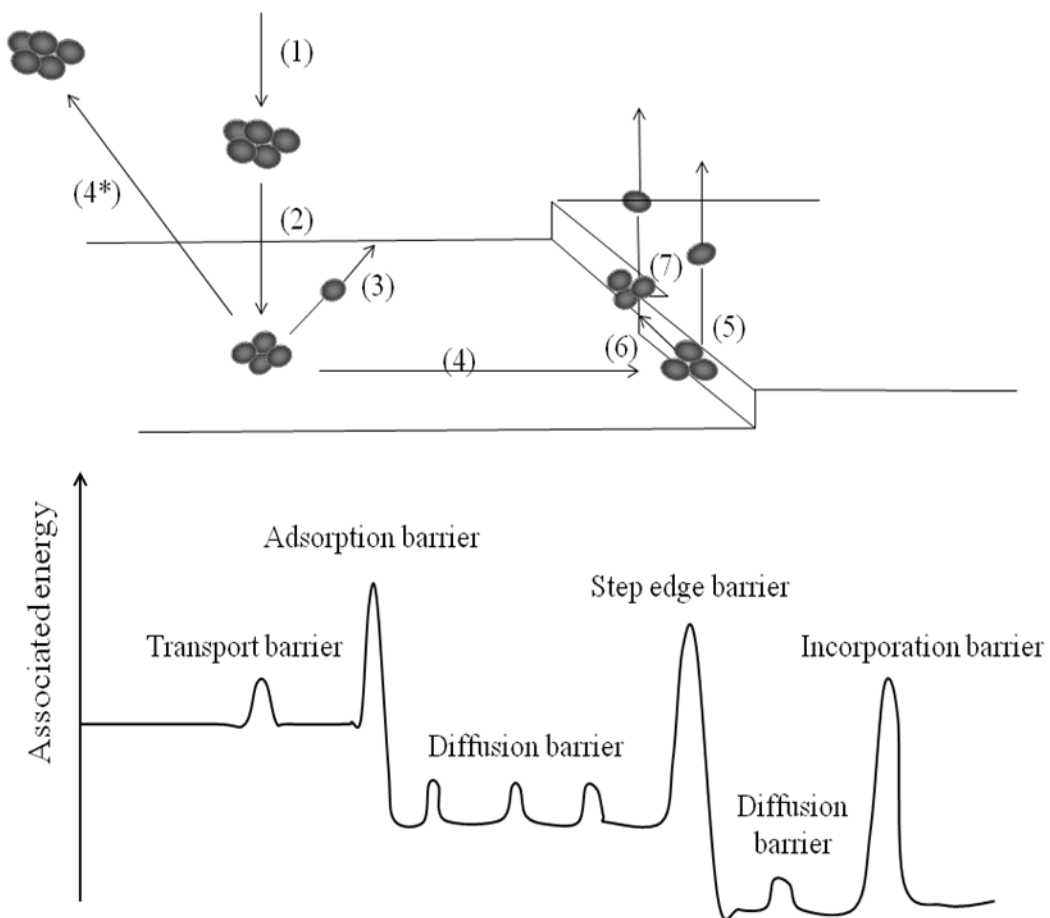
Figure 2.6 (a) Schematic representation of steps involved in crystal growth; (b) The energy landscape for processes depicted in physical landscape (a). Figure modified from (Cubillas and Anderson, 2010, Yoreo and G, 2003)

During the growth, the growth rate at each crystal face can be different and makes the growth become the key issue in determining the habit of the final crystal product. Generally, the most rapidly growing faces are those smaller and less well developed faces on which the interaction bond is relative secure (Yoreo and G, 2003). The face

growth of the crystal not only depends on the mass transform from the bulk solution, but also the crystal surface structure of the growing interface. Three basic types of surface structure result in the main growth models: normal growth, 2-D nucleation growth and screw dislocation growth.

2.4.1 Normal Growth

The so-called normal growth is also known as continuous growth in which the growing surface is molecularly rough and preserves this structure through the process, and due to the roughness of the surface, every molecular site on the crystal surface can be regarded as the growth site at which building units from the solution can be incorporated, as seen in Figure 2.7 (Kashchiev, 2000).
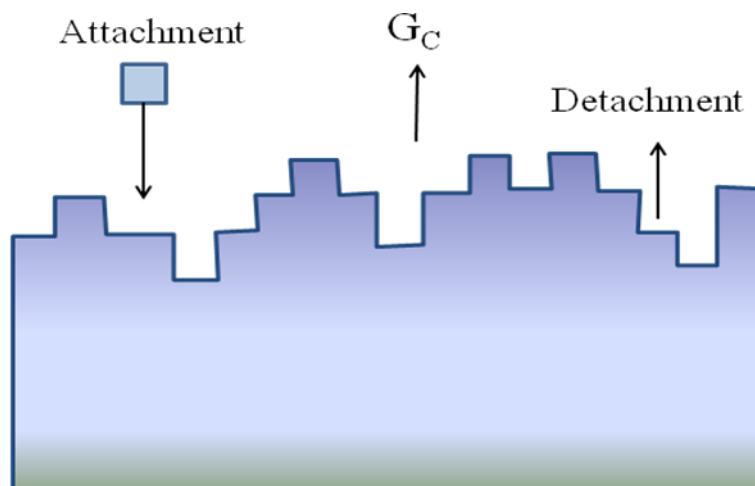
Figure 2.7: The molecular rough crystal surface advanced by normal growth

Therefore, the continuous growth normally associates with the available low energy integration site and leads to the corresponding crystal growth rate depending linearly on supersaturation in a range of small supersaturations ($S<0.2kT$) (Nauman, 1972, Randolpha and Larson, 1971, Kashchiev, 2000):

$$G_C = k_g S \tag{2.23}$$

where k_g is a kinetic factor characteristic for continuous growth and the growth is diffusion-controlled.

2.4.2 2-D Nucleation Growth

Unlike growth from a rough face, the crystals are growing on a molecularly smooth face in a 2-D nucleation growth mechanism. Kossel (Kossel, 1934) proposed a model of crystal surface made of monatomic height layers to depict the possible adsorption sites for growth unit incorporation. As is depicted in Figure 2.8, there are some kinks, steps, growth units and vacancy on the surface which provide different numbers of available interaction sites for incorporation. Clearly, the kink has three sites and is the most energetically favorable and offers the most stable configuration for attachment of growth units. These kinks will move along the step and eventually finish the face growth. A new growing step could be then generated by 2-D nucleation on the surface of the crystal. Similarly, a three-dimensional crystal surface of K, S, and F faces introduced by Hartman and Perdock (Hartman and Perdock, 1955) also delivers the same bonding energy concept for growth unit adsorption. The flat F face requires the surface nucleation of 2-D nuclei or screw dislocations to ensure the available steps and kinks.
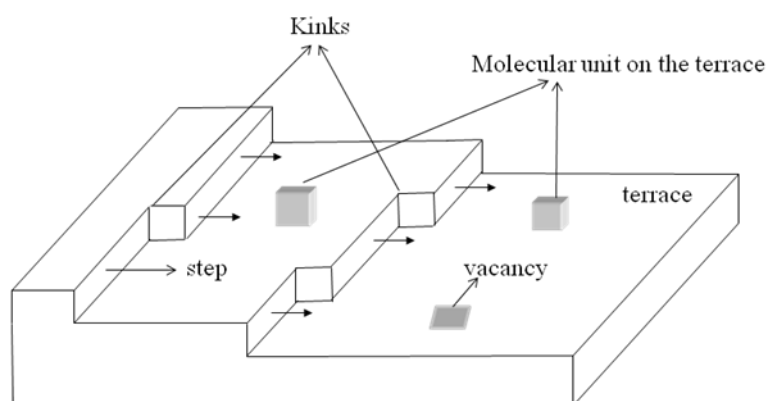
Figure 2.8: The schematic representation of the Kossel model of crystal surface

In the 2-D nucleation growth mechanism, Volmer (Volmer, 1939) suggested that a monolayer island nucleus is formed on the existing layer and becomes the continuous source of new steps and kinks to grow and spread across the surface. This is why the 2-D nucleation growth has another name of the birth and spread growth. In addition, the spread 2-D nucleus can be further distinguished to mononuclear monolayer growth, polynuclear monolayer growth and polynuclear multilayer growth (Kashchiev, 2000). The 2-D nucleation growth is only expected to occur at relatively high supersaturation solutions due to the high energy barrier discouraging surface

nucleation, the expression of its nucleation rate is:

$$G_C = k_{SN} S^{5/6} \exp(-\frac{D}{S})$$

(2.24)

where the k_{SN} and D are the system-relative nucleation parameters.

2.4.3 Screw Dislocation Growth

For crystals grown at the low supersaturation level, Frank (Franck, 1949) postulated that screw dislocations emerge on the surface resulting in the presence of spiral steps at which incorporation of growth units take place. As is shown in Figure 2.9, the emergent step extends over the surface when its length is over $2r_{2D}*$ and creates the next growth step. Based on this, the growing surface in this growth mechanism is between the extremes of completely rough (the continuous growth) and smooth (the 2-D nucleation growth). The screw dislocation theory was later developed by Burton, Cabrera and Frank (Burton et al., 1951), giving rise to what is known as the BCF relationship to express the correlation of the growth rate and supersaturation:

$$G_C = k_{SG} \sigma^2 \tanh(\frac{D}{\sigma})$$

(2.25)

where the k_{SG} and D are complex temperature-dependent constants and $\sigma = S\text{-}1$. It is worth noting that each crystal has its own growth rate depending on the specific dislocation structure in the spiral growth model (Davey and Garside, 2000).
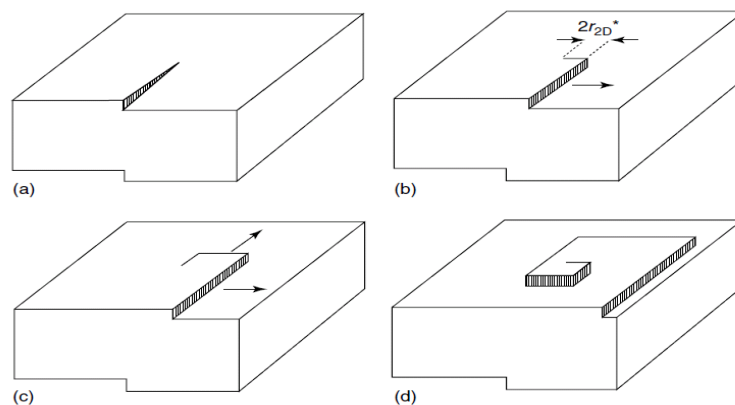
Figure 2.9: Development of growth spiral initiated by screw dislocation (Cubillas and Anderson, 2010). $r_{2D}*$: the critical nucleus size in 2-D nucleation growth

2.5 Polymorphism

The word 'polymorphism' comes from the Greek of 'many forms', and just as it suggests, polymorphs are those crystals having the same chemical composition but different internal crystal structures in the lattice, either due to the different molecules arrangements or the different molecular conformation with varied torsion angles. Polymorphism occurs frequently in solid state compounds, especially in pharmaceutical substances and over one third of the organic compounds exhibits polymorphism (Gracin and Åke, 2004). The crystal polymorphism control is of tremendous importance in the pharmaceutical industry because the polymorphism affects the physical and thermal properties of compounds such as the melting point, solubility, morphology, compressibility and hence the industrial handling processes and the bioavailability.

There are two types of polymorphism system known as monotropic polymorphism and enantiotropic polymorphism. In terms of solubility, as seen in Figure 2.10, the metastable polymorphic form is β-form, with higher solubility than the stable α-form at the full temperature range for the monotropic polymorphism system and the transition of polymorphic forms is irreversible. For the enantiotropic polymorphism system on the other hand, there is a crossing point on their solubility curves, under this critical temperature, β-form is the stable form with smaller solubility but it becomes the metastable polymorphic form when the temperature is above the critical temperature point. Based on this, it came be deduced that the transition of polymorphic forms in enantiotropic system is reversible.
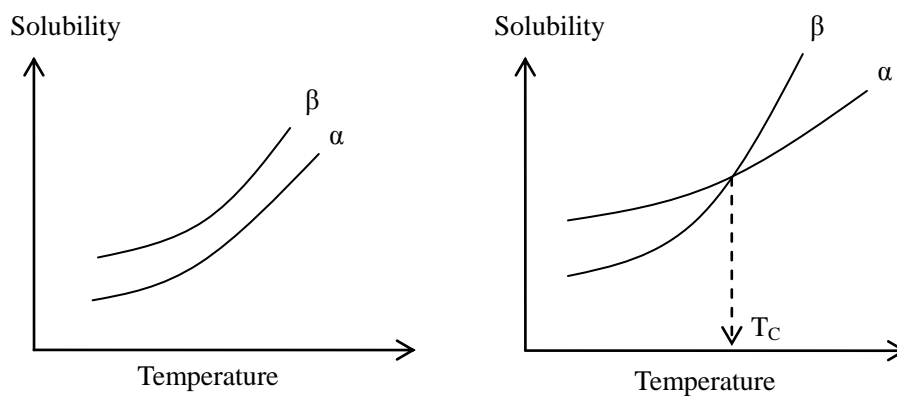
Figure 2.10: Solubility curves of monotropic polymorphs (left) and enantiotropic polymorphs (right)

From the energy point of view, seen in Figure 2.11, the metastable β-form, with lower free energy barrier, will be crystallized first. Consequently, the transformation behaviour of polymorphs either occurred in solid state or via the solution-mediated path, following the well known 'Ostwald's rule of stages' which states that rather than the direct formation of the stable state, the metastable polymorph is formed first then transforms into the stable form during the crystallization process (Mullin, 1993).
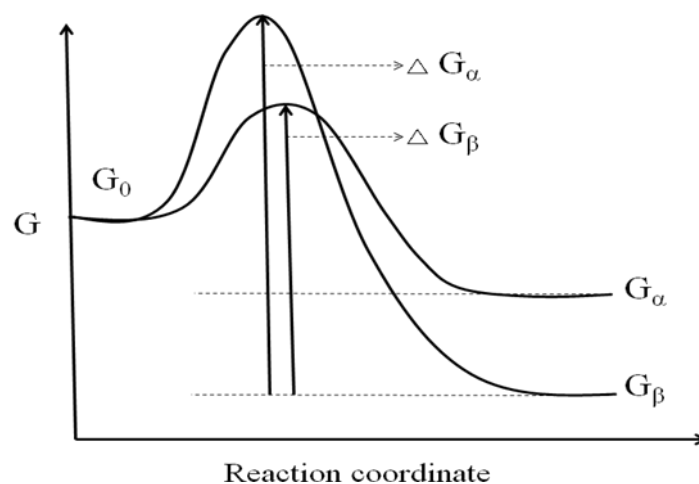
Figure 2.11: Free energy barrier associated with crystallization of polymorphs adapted from (Bernstein, 2002)

The control strategy of polymorphism in the crystallization process can be illustrated by Figure 2.12. In virtue of the solubility differences of polymorphs, desired polymorphic form, can be obtained by careful control of temperature and solubility. During the crystallization process, the controlling factors can be some basic, but important, operating parameters such as the temperature, the supersaturation and mixing condition. The cooling rate is another primary control factor that simultaneously affects and changes the temperature and solution supersaturation hence determines the formation of polymorphs. To produce processing favour polymorphic form, seeding is possibly the most effective method in the crystallization process. The other external factors such as external substances of solvent, or additives and the pH value control, are also the influential factors for polymorphism control. The ultrasound field, as studied in this project, is considered to be a potential and challenging control task for polymorphism crystallization.
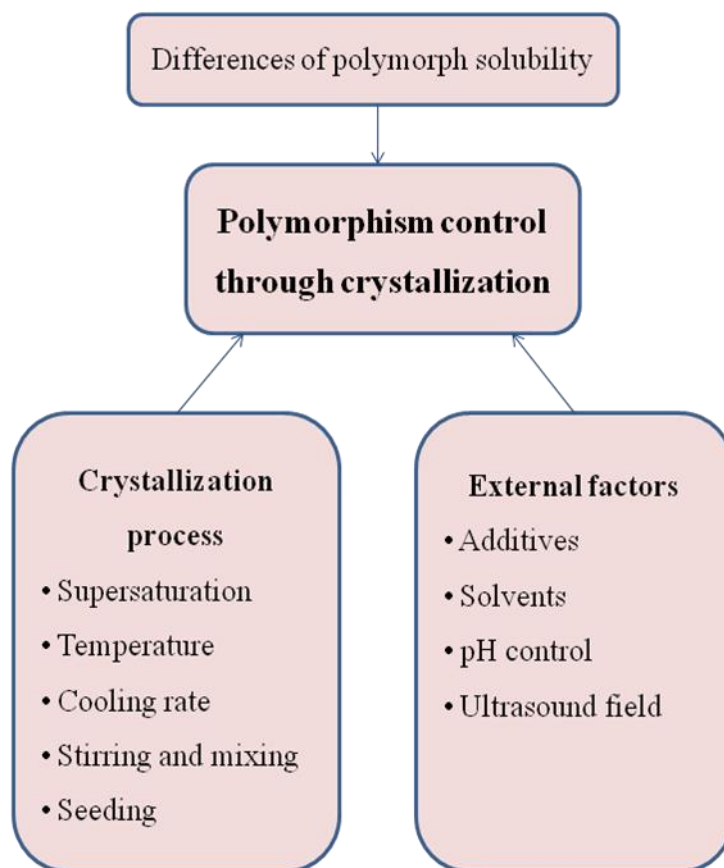
Figure 2.12: Polymorphism control strategy in the crystallization process modified from (Kitamura, 2009)

About the polymorphs of l-glutamic acid (LGA), it is known that LGA is a typical dimorphic amino acid with the kinetics favour metastable α-form in prismatic shape and the thermodynamic stable β-form in needle-like habit. LGA transformation was systematically studied by Kitamura (Kitamura, 2003, Kitamura, 1989, Kitamura and Funahara, 1994, Kitamura and Ishizu, 2000, Kitamura and Nakamura, 2001, Kitamura, 2009). He pointed out that the polymorphic transformation of LGA was solution-mediated and can be affected by crystallization temperature and additives. Above a temperature of 45°C, only the needle-like β-form was isolated and when crystallization was lower than 25°C, the crystals produced were α-form predominant. With an increase of additive L-Phe concentration, the nucleation and transformation of β-form crystals were hindered. Other studies (Sakata, 1961, Liang et al., 2003, Mougin et al., 2002) examined the cooling rate effect on l-glutamic acid polymorphs formation and found that β-form was generated by using a slow cooling rate while the α-form can be obtained with rapid cooling. On the other hand, Ni et al. proposed that with fast cooling rate and crash cooling, they still failed to produce α-form l-glutamic

acid even above 45°C (Ni et al., 2004).

According to Ostwald's step rule, theoretically, the stable form is preferentially generated at low supersaturation because of the supersaturation ratio difference between the competitive polymorphs. On the other hand, high supersaturation leads to the precipitation of less stable polymorphic form as the interfacial energy difference becomes relatively dominated (Kitamura, 2009). In practical research, the intensive effect of solution supersaturation was observed for the determination of l-glutamic acid polymorphs: a high concentration condition was favoured by β-form and low to medium concentration was preferred by α-form (Ni et al., 2004). Whereas Kitamura demonstrated that the precipitation of LGA polymorphs was supersaturation independent (Kitamura, 2003). Molecular modelling study of energetic stability of LGA given by Hammond (Hammond et al., 2005) revealed that the metastable α-form was the energetically stable form at small nucleation-cluster size and, hence, should be anticipated at the high supersaturation where the cluster size was expected to be small.

Since the β-form crystal was known to grow on the surface of the preformed α-form crystal (Kitamura and Funahara, 1994, Garti and Zour, 1997), arguments as to whether the agitation factor enhances the polymorphic transformation were opposed: works proposed by Ferrari (Ferrari and Davey, 2004) and Roelands (Roelands et al., 2007) insisted that intensified mixing would result in the enlarged surface area on the metastable α-crystal for the β-form nucleation. Cashell et al. suggested that agitation was adequate to destroy the crystallographic facet of α-form crystal where the β-form nucleated (Cashell et al., 2003).

As stated above, various aspects of operating condition of crystallization are of importance and can potentially influence and determine the dynamic behaviour of l-glutamic acid polymorphism but the current experimental outcome from different researchers still under dispute. Therefore, additional experimental data of these effective factors is necessary. Furthermore, so far no literature has been reported to investigate the external ultrasound irradiation effect on l-glutamic acid crystallization and polymorphism. The corresponding studies will be given in this project and described in Chapters 5 and 6.

2.6 Crystallization Process Analysis and Characterization Techniques

A vast array of process analytical techniques exist, characterization, measurement and analysis of every aspect of chemicals during the crystallization process (on-line/off-line) to control the process, monitor the condition and ensure the final product quality:

➢ Thermal techniques: Differential Scanning Calorimetry (DSC) and Thermo Gravimetric Analysis (TGA);

➢ Spectroscopic techniques: UV-Visible Spectroscopy, Attenuated Total Reflectance-Fourier Transform Infrared instrument (ATR-FTIR), Near Infrared Analysis (NIR), Roman Spectroscopy;

➢ Optical and diffraction techniques: X-ray Diffraction (XRD), Focus Beam Reflectance Measurement (FBRM), MasterSizer, UltraSizer;

➢ Chromatography techniques: Gas Chromatography (GC), High Pressure Liquid Chromatography (HPLC);

➢ Image technique: Optical microscope, Morphologi 3, PharmaVision System, High Speed Camera.

The general introduction and principle description of the techniques of XRD, ATR-FTIR and FBRM which were utilized in this study are presented here and the corresponding instruments are detailed in Chapter 4.

2.6.1 X-Ray Diffraction

The x-ray diffraction method is an indispensable analytical tool and a non-destructive technique for solid state material structure study in pharmaceutical science and engineering. The diffraction phenomenon occurs due to the interference of a scattering incident beam passing through the atomic plane. Bragg's Law has been proposed and developed to explain how the x-ray reveals the lattice structure of the crystal. Considering the parallel rays X and Y are incident with an angle of θ and scatter from the successive and inerratic lattice plane, as shown in Figure 2.13, the difference of two rays' path length $AB+BC$ can be expressed with the incident angle θ and the spacing between planes d :

$$AB + BC = 2d \sin \theta \tag{2.26}$$

The constructive interference occur only when

$$n\lambda = 2d \sin \theta \hspace{6cm} (2.27)$$

where n is an integer number and λ is the radiation wavelength of the order of 10^{-10}m.
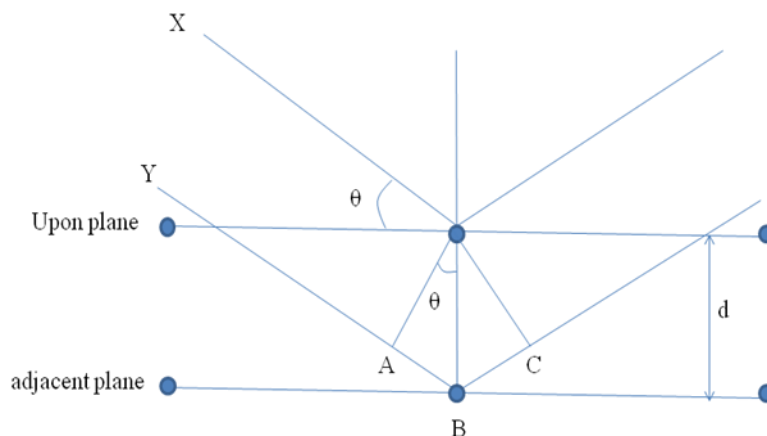
Figure 2.13: Derivation of Bragg's Law

Thus, the constructive and destructive interference waves from different lattice planes result in the intensity peaks at certain angles and provide fingerprinting diffraction patterns for specific crystal structure. The output data of x-ray diffraction is the intensity as a function of angle (2θ), and with the combination of characteristic radiation wavelength, peak position, width and intensity, the crystal structural properties and chemical information such as the compound identification(Wu et al., 2009), crystallographic orientation (Nunes et al., 2001), particle size and strain analysis (Wang et al., 2011) can be characterized and determined.

In this project, the x-ray diffraction technique was employed in the application of crystal polymorph identification. It has been reported to use on-line for polymorphic form monitoring and identification (Hammond et al., 2004, Davis et al., 2003) and it can also be coupled with on-line video microscopy to observe the phase transformation of pharmaceutical substance (Dharmayat et al., 2006).

2.6.2 Attenuated Total Reflectance-Fourier Transform Infrared Technology (ATR-FTIR)

Infrared Spectroscopy permitting quantitative and qualitative analysis in the process is based upon the principle that electrometric infrared radiation, whose wavenumber ranges from 4000 to 400cm^{-1}, can be absorbed and interact with the dipole atom when its dipole moment of the bond changes due to the vibration. Since each bond has a particular resonance frequency at which the infrared radiation is absorbed, the analysis of the infrared spectrum yields the information of bond strength and system mass change under investigation, as shown in Figure 2.14, and therefore can be applied for identification of functional groups. Moreover, different polymorphic forms give rise to slight differences in the vibrational structure, which makes infrared spectroscopy also capable for structure or polymorph identification by fingerprinting.
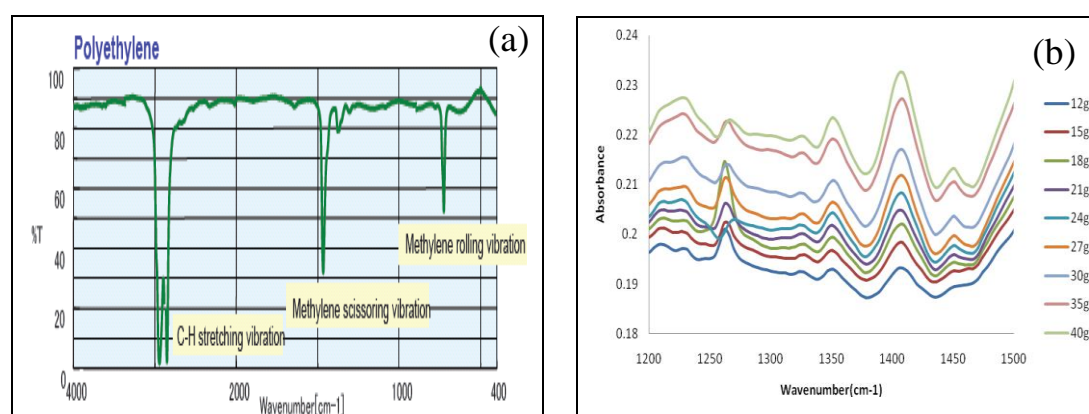
Figure 2.14: Examples of infrared spectrum analysis: (a) Polyethylene infrared spectrum for stretching vibration (Jasco, 2008); (b) Infrared spectrum of different concentration l-glutamic acid in aqueous solution at 50°C (Ma, 2010)

Fourier Transform Infrared is one of the infrared spectrometers that simultaneously collects all the frequency interferogram and the resultant interferogram transforms to single beam spectrum by mathematically extracting the individual frequency via fast Fourier transform. The Fourier Transform Infrared attaching with attenuated total reflectance sampling probe, known as ATR-FTIR, is also a non-destructive tool for surface information collection. There is no need to prepare the sample which allows direct real-time measurement of aqueous solution and solid samples that are difficult to measure using the thin film method or the insoluble, infusible and gel substances (Jasco, 2008). Figures 2.15 illustrates the ATR probe prism in the aqueous solution,

although the infrared beam penetrates into the medium through the reflection surface with a penetration depth of a few microns, it is totally reflected inside the zinc selenide crystal and collect by the detector.

For its application to crystallization, ATR-FTIR was proved to be a promising technique for sufficiently accurate and precise determination of the solubility, supersaturation and the metastable zone limit (Dunuwila et al., 1994, Dunuwila and Berglund, 1997). Latterly, Lewiner and Klein presented a calibration procedure study to measure the supersaturation during the cooling solution crystallization process (Lewiner et al., 2001b). As an extension of former work, Lewiner and Fevotte adopted ATR-FTIR to monitor the organic crystallization process aiming at improving seeding conditions and the final particle size distribution (Lewiner et al., 2001a). Other research work used the measured solution concentration as a feedback variable to maintain the supersaturation during crystallization and successfully utilized ATR-FTIR for crystallization process monitoring and control(Khan, 2008, Ma, 2010).
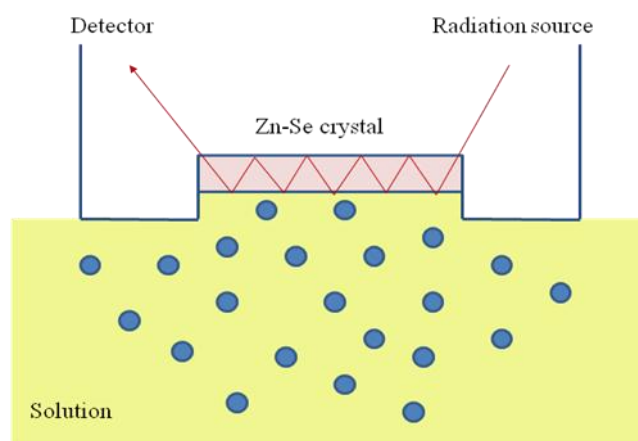
Figure 2.15: The attenuated total reflectance probe in solid-liquid slurry

2.6.3 Focused Beam Reflectance Measurement Technology (FBRM)

Focused Beam Reflectance Measurement (FBRM) is a probed-based real-time particle number and dimension analysis technique based on the principle of backward light scattering. Figure 2.16 illustrates the operating schematic of a FBRM probe, the laser light travels down to the probe and focuses through a set of optics to a light spot, the optics are rotates at fixed high velocity and the focused beam then scans in a circular path outside the sapphire window. Since laser beam is much faster than the particle movement in the solution, the particle that passes the window and interacts

with the scan path can be treated as essentially fixed during the measurement and giving a backscattering light to the detector. Hence, the velocity of laser multiplies the measured time giving a distance known as 'Chord length' which is the straight line between two random points on the particle edge.
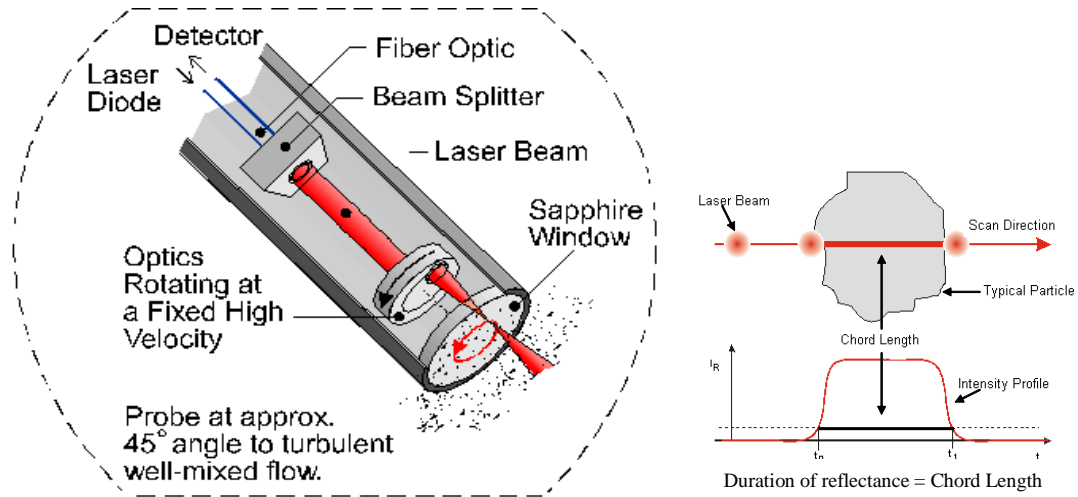
Figure 2.16: The cut-away schematic of the Focused Beam Reflectance Measurement probe (Haley, 2009)

The Focus Beam Reflectance method provides the chord length information of particles ranging from 0.25μm to 1000μm. Other on-line measurement techniques, such as ATR-FTIR and PVI, has been used together with FBRM in crystallization process to monitor the solid phase (Tadayyon and Rohani, 1998, Sparks and Dobbs, 1993, Barrett and Glennon, 1999, Lindenberg et al., 2008) and crystal habit progression(Kougoulos et al., 2005, Monnier et al., 1997), and determined the crystallization kinetics and onset of particle formation(Scholl et al., 2007). In this work, FBRM was applied to verify that no nucleation occurred during seeded growth measurement.

2.7 Closing Remarks

This chapter started with the concept of supersaturation and its importance through the crystallization process followed by the introduction of the principles behind the nucleation and the crystal growth of crystallization. The polymorphism and brief review of L-glutamic acid polymorph synthesis in crystallization, together with the additional crystallization process analytical techniques were also discussed. This chapter provides a fundamental knowledge of crystallization and process background for sonocrystallization investigation.

Chapter 3

Fundamentals of Power Ultrasound Science and Engineering and Its Usage in Crystallization

Summary: The fundamental acoustic theory including the basic concept of power ultrasound and cavitation phenomenon, the precipitation, growth and collapse of cavitation bubbles, and the accompanying acoustic effects is introduced. It is followed by a comprehensive literature review of power ultrasound application in crystallization.

3.1 Introduction

Since the first commercial application on the depth estimation in the early 1900's, ultrasound has been recognized as being a distinctive technique used in medical diagnosis field and by the chemical industry. Power ultrasound, as a member of the ultrasound family, has attracted more and more attention from scientist in recent years due to its great potential in broad variety of processes in the chemical industry, such as the crystallization process. In this chapter, some fundamental knowledge of acoustic theory is given for a better understanding and insight of power ultrasound and its physical and chemical effects through the processes.

3.2 Acoustic Theory

3.2.1 Power Ultrasound

Sound can travel through the medium via a vibration motion, as a wave with a specific frequency. When the frequency is low, the sound is audible at about 16 Hz, but it becomes more difficult to sense by the human body when the wave frequency exceeds the human hearing threshold at 20 kHz. Therefore, the inaudible sound of frequency above 20 kHz is defined as ultrasound. A classification of sound based on frequency and its usage is shown in Figure 3.1. Power ultrasound refers to the frequency range between 20 kHz and 100 kHz and is broadly utilized by the chemical and allied industries such as in plastic welding, cleaning, cutting and processing (Mason, 1999). The ultrasound frequency range extended to 2 MHz is currently in specific use for chemical synthesis (sonochemistry) and the field of therapeutic medicine. High frequency ultrasound from 5MHz to 10MHz is low in power or energy which is extremely useful in diagnostic analysis, for example for infant images. The project study focuses on the power ultrasound used as an external effective factor to affect the crystallization process and the relative detailed literature review is described in Chapter 3, Section 3.3.
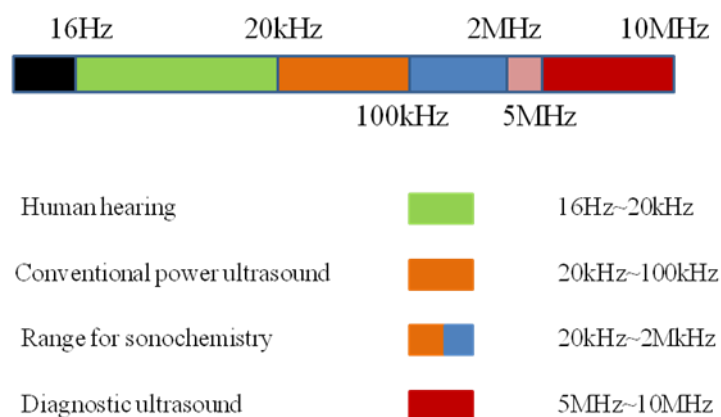
Figure 3.1: Classification of sound frequency

3.2.2 Cavitation

Like other sound waves, ultrasound is transmitted by alternately stretching and compressing the medium molecular structure and applying negative and positive pressure to the liquid medium during which liquid molecule oscillation is generated as a result. Under the conditions of high negative pressure which is sufficiently great to destroy the attraction and pull the liquid molecules apart, the liquid is broken down to create cavitation bubbles at the rarefaction cycle, as can be seen in Figure 3.2 (Timothy J.Mason and Peters, 2002). It is worth noting that if the ultrasound frequency is of the order of megahertz, the corresponding rarefaction cycles become too short to generate cavitation bubbles. Theoretically, the negative pressure required to produce cavitation in pure water is as high as 10000 atm (Manson, 1991). The pressure allows cavitation propagation in water but it is considerably much lower in practice due to the presence of dissolved air bubbles or tiny suspended particles which reduce the tensile strength of water and act as the cavitation nuclei (Timothy J.Mason and Peters, 2002).

After the 'heterogeneous' nucleation in the rarefaction cycle, cavitation bubbles are compressed, the gas pressure inside the bubble is higher than the outside pressure, hence diffusing out of the bubble. The bubble is shrinking in the compression cycle as a result while expanding again in the rarefaction cycle. It is known that diffusion flux is proportional to the bubble surface area. Since the surface area in the rarefaction cycle is larger than that in the compression cycle, the gas diffusion into the bubble is greater than the diffusion out and the cavitation bubbles are recognized to eventually grow and collapse, see Figure 3.2.
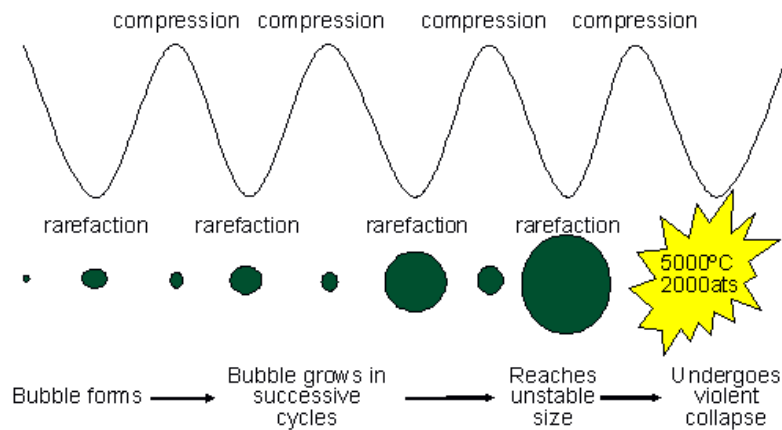
Figure 3.2: The propagation, growth and collapse of cavitation bubble (Mason, 1999)

Table 3.1:The main differences between stable and transient cavitation (Chow-McGarva, 2004)

Stable cavitation	Transient caviation
Oscillates (often non-linear) around some equilibrium size	Oscillates to many times more its equilibrium radius before imploding
Oscillates for many cycles	Oscillates for only a few cycles
Relatively permanent	Relatively short lived
Sufficient time for mass diffusion of gases in and out of the bubble	Insufficient time for mass diffusion of gases
Gentle collapse	Violent collapse
No shock wave, no hot-spot, little fluid flow	Shock wave, hot-spot and high fluid flow
No sonoluminescence	Sonoluminescence

Two distinct types of cavitation were introduced by Flynn (Flynn, 1964) to describe the extremes of bubble behaviour: stable cavitation and transient cavitation. The stable cavitation bubbles are usually produced at low intensities, pulsating, about some equilibrium size over relatively lifetime of many cycles before they reach the maximum size. The transient cavitation bubbles absorb energy from the ultrasound waves and grow to a maximum size, at least twice of its initial size, within a few cycles then collapse violently. A summary of the main differences between the stable and transient cavitation is listed in Table 3.1.

Figure 3.3 shows the radius-time plot for different initial size bubbles in a 10 kHz ultrasound field. For those larger bubbles with a slower response, the time is not long enough to allow bubbles to grow as much as in a single cycle and bubbles consequently take many cycles to reach the maximum size. On the other hand, the smaller bubble size the more rapid in the timescale over which it responds. The small

bubbles are able to grow to a very large size and store much more energy which releases violently in collapse. It can be seen that in a particular ultrasound field, large equilibrium radius bubbles are more likely to undergo stable cavitation, whilst the smaller bubbles undergo transient, and there exists a threshold radius for a bubble denotes the transient cavitation and stable cavitation transition (Leighton, 1997).
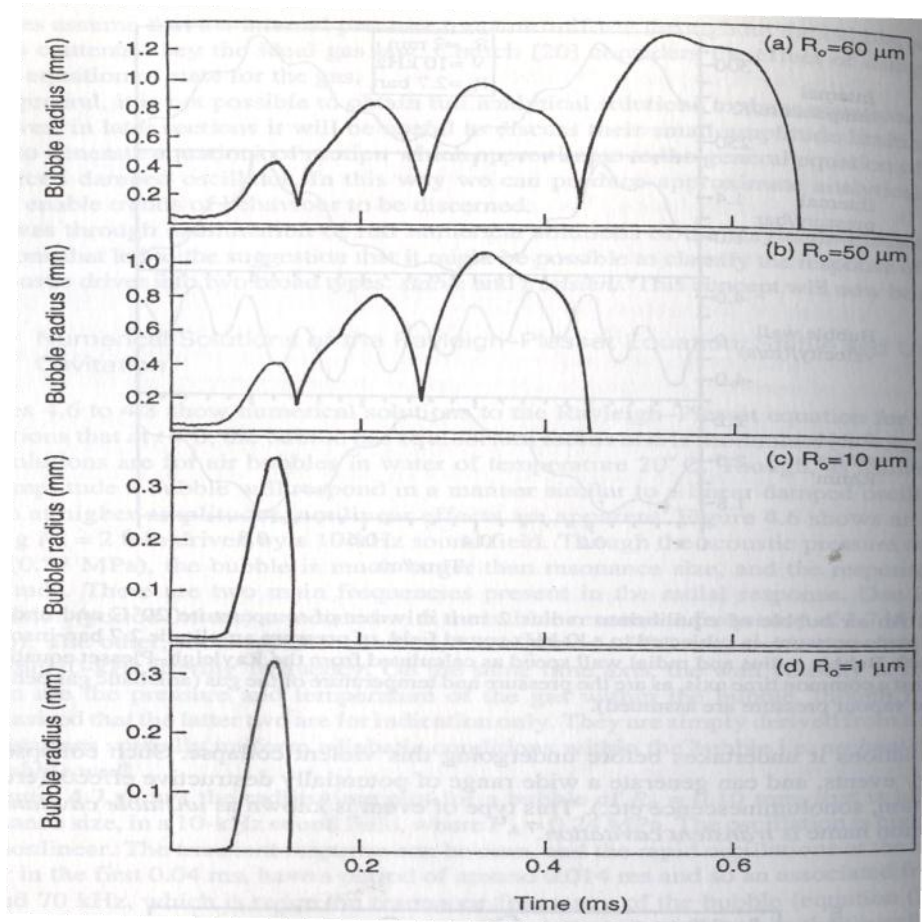
Figure 3.3: The radius/time predictions for four bubbles of progressively smaller size in a 10-kHz sound field (PA=2.4 bar). Equilibrium bubble radii are (a) 60 μm, (b) 50μm, (c) 10μm and (d) 1μm (Leighton, 1997)

The transient cavitation used to be regarded as the original cause of spectacular effects in sonochemistry; nowadays, the stable cavitation is also believed to make a significant contribution to the overall sonochemical effect (Timothy J.Mason and Peters, 2002). Therefore, although the fundamental concept of the transient cavitation and stable cavitation is different, the cavitation effect is the overall effect with no concern for distinction between the two cavitation types in sonochemistry.

3.2.3 Cavitation Bubble Collapse

When a cavitation bubble is overgrown, it no longer absorbs sound energy as the elastic energy has exceeded the state that it can sustain and experience collapse. The Rayleigh-Plesset equation which depicted the bubble radius-time curve over the collapsed phase was introduced by Noltingk and Neppiras (Noltingk and Neppiras, 1951) to describe the motion of a spherical bubble in an applied acoustic field in an incompressible liquid:

$$R\ddot{R} + (\frac{3}{2})\dot{R}^2 = \frac{1}{\rho}\left[(P_0 + \frac{2\gamma}{R_e} - P_v)\left(\frac{R_e}{R}\right)^{3K} - \frac{2\gamma}{R} - 4\eta\frac{\dot{R}}{R} - P_0 + P_a)\right] \tag{3.1}$$

where $\dot{R} = \dfrac{dR}{dt}$ is the cavity bubble wall velocity, $\ddot{R} = \dfrac{d^2R}{dt^2}$ is the acceleration of the cavity wall, R is the cavitation bubble radius, R_e is the equilibrium bubble radius under ambient pressure, P_0 is the ambient pressure, P_v is the vapour pressure of liquid, γ is the liquid surface tension, K is the polytropic index of the gas, η is the liquid viscosity, P_A is the amplitude of the ultrasound driving pressure relating to the ultrasonic system power and P_a is the applied acoustic pressure which varies with time.

Consider an empty cavitation bubble collapsing completely from its maximum size R_m, by neglecting the effect of surface tension and vapour pressure in the liquid which is likely to be present in the bubble, the collapsing time τ can be estimated by (Timothy J.Mason, 2002):

$$\tau \approx 0.915R_m(\rho/P_m)^{1/2} \tag{3.2}$$

where ρ is the density of the liquid and P_m is the pressure of the liquid. For the vapour filled transient bubble collapse, the above correlation is modified by Khoroshev (Khoroshev, 1963):

$$\tau = 0.915R_m(\rho/P_m)^{1/2}(1+P_v/P_m) \tag{3.3}$$

In presence of the acoustic field, P_m is the sum of P_h and P_a while in absence of acoustic field, P_m is equal to the hydrostatic pressure P_h.

Theoretically considered by Noltingk and Neppiras (Noltingk and Neppiras, 1951) and Flynn (Flynn, 1964), later separately by Neppiras (Neppiras, 1980), the maximum temperature T_{max} and pressure P_{max} of an adiabatic transient cavitation bubble collapse

at the moment of collapse can be calculated by (Timothy J.Mason, 2002):

$$T_{max} = T_0 \left\{ \frac{P_m (K-1)}{P} \right\} \tag{3.4}$$

$$P_{max} = P \left\{ \frac{P_m (K-1)}{P} \right\}^{K/(K-1)} \tag{3.5}$$

where T_0 is the ambient temperature, P is the pressure in the bubble at its maximum size and usually assumed to be equal to the vapour pressure P_v. This high temperature and pressure energy will release during the violent collapse of transient cavitation and affect the surrounding environment.

3.2.4 Effects Caused by Acoustic Cavitation

The generation, growth and collapse of cavitation bubbles lead to a series of physical, chemical and biological effects on the surrounding solution. To expound those effects accompanied by cavitation, some competing theories were proposed from different aspects. Lepoint et al. (Lepoint-Mullie et al., 1996) suggested that the plasma-based high-energy sparks triggered off under high pressure during the collapse was the root of single-bubble sonoluminescence. The electrical theory emphasizes the strong electrical field which developed during the asymmetric collapse was proposed by Margulis (Margulis, 1996).

The most popular theory is the Hot-spot theory which focuses on the high concentrated energy release from the collapsing bubble createing a drastic local condition of extremely high temperature and pressure. This is also believed to be the most acceptable theory for sonocrystallization mechanism interpretation and mechanical concern of this research project. A temperature of around 5000K for gas phase of hot spot was experimentally estimated by Suslick using sonoluminescence as a spectroscopic probe, he   pointed out that the liquid shell temperature surrounding the collapsing cavity was about 1900K within a period of 100ns, and hence deduced that cooling rates of process were more than 10^{10} K/s and thepressure inside the bubble was calculated to be up to 1700 atm (Suslick, 1989). Similarly, the internal temperature and pressure associated with bubble collapse were proved to be up to 2900°C and 4140 atm (Apfel, 1997). The strong pressure is first generated in the liquid shell surrounding the transient bubble and then released as a form of shock wave attributed to the abruptly halted bubble wall by the compressed bubble contents

and travels from the collapsing centre. The schematic representation of the development is shown in Figure 3.4.
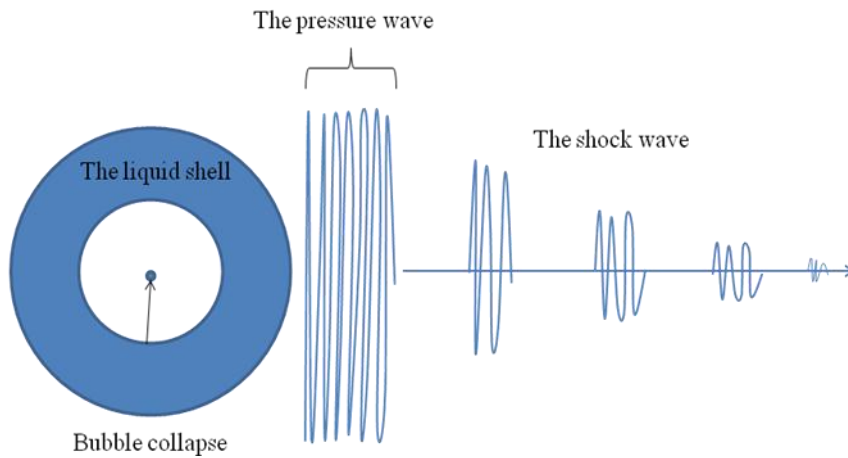
Figure 3.4: The schematic representation of the development of shock wave

As noted by Lauterborn and Ohl (Ohl et al., 1999, Lauterborn et al., 1999), the shock wave can be experimentally observed by using high-speed photography, as is shown in Figure 3.5. The photographs were taken at approximately 45ns interframe time with the dark spot being the collapsing bubble. The propagated shock wave can be observed at the end of bubble collapse and expanding as a ring into the surrounding liquid with a velocity of sound which is about 1500 m/s in water. However, the shock wave does not retain the strength very far but attenuates due to the absorption, only a few radial distances from the collapsing bubble and causes localized damage such as the fragmentation of nearby bubbles. It was experimentally measured that the shock wave pressure can be up to 5.5kbar (Holzfuss et al., 1998) or even higher (Pecha R and Gompf B, 2000).
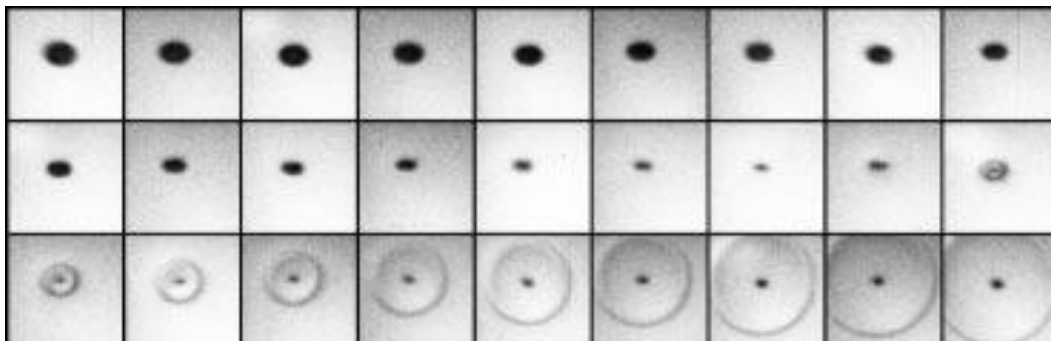
Figure 3.5: A spherically symmetric shock wave emitted by a collapsing single bubble into the surrounding liquid (Ohl et al., 1999)
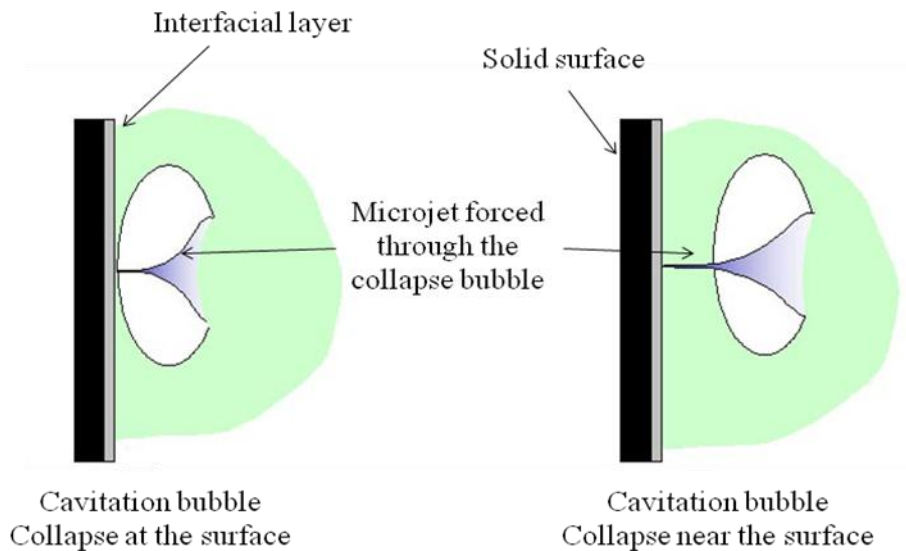
Figure 3.6: Cavitation bubble collapse at, or near a solid surface (Timothy J.Mason, 2002)

In case the bubble collapse is not symmetrical, i.e. at or near to a large solid surface, the liquid will expel into the bubble attributing to the solid surface resistance and results in a liquid microjet being formed, targeted at the surface, as shown in Figure 3.6. The velocity of the microjet can be of the order of 100 m/s which is high enough to eject the particles from the surface efficiently (Timothy J.Mason, 2002). This is also the mechanism of ultrasonic cleaning.

3.2.5 Generation of Power Ultrasound

There are two basic paths to perform acoustic energy to liquid loads for the acceleration or modification of the chemical engineering process: low intensity bath system and high intensity probe system. The schematic classic laboratory scale ultrasound systems are shown in Figure3.7.
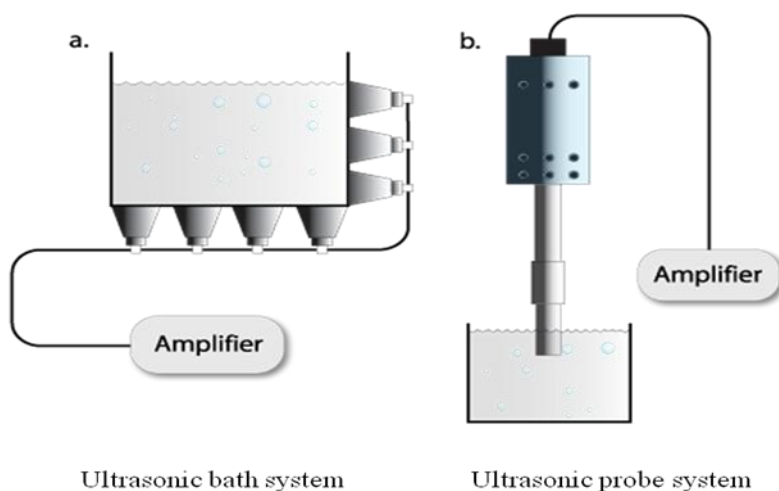
Figure 3.7: The basic ultrasonic operating system (a) ultrasound bath system and (b) ultrasound probe system (Perkins, 2009)

The ultrasonic cleaning bath is the most widely available for the laboratory and the cheapest source of ultrasound irradiation with the most commercial frequency of 40 kHz. It is easily established for sonochemical reactions but the ultrasonic bath normally dissipates a relatively low intensity of ultrasound power (< 5 W/cm^2) and its temperature and adjustable power control are usually poor. Generally, sonochemical reactions are required to be performed in a vessel immersed in the sonicated liquid in the ultrasonic bath so the vessel design is necessary, a flat-bottomed vessel is normally preferred. The bath itself being used as the reactor is possible, but corrosive and volatile reagents are hence not allowed. Another disadvantage of the ultrasonic bath is that they usually have no vapour-tight lids which limits their application in reactions require inert atmosphere or reflux condenser (Mason, 1999).

The ultrasonic probe system on the other hand, is very easy to fit and utilize with different glassware and vessels and the intensity of the ultrasound irradiation can be up to several hundreds of W/cm^2 or even greater in large scale manufacture, this offers considerable advantage to achieve a better sonochemistry effect. Most of the modern ultrasonic probe units have the pulse facility enabling adjustable power control and monitoring during the processes (Mason, 1999). Some of them even provide alternative frequency for intense cavitation field and optimum performance. However, the probe system usually has the problem of probe tip erosion, an unstable ultrasound field and poor bubble distribution which make the characterization of the bubble system very difficult.

Other power ultrasound systems including the acoustic bubble trap and an optically

induced cavitation system are also available for ultrasonic cavitation generation (Chow-McGarva, 2004). In this project, a probe sonicator with a frequency of 20 kHz was applied to influence the crystallization process.

3.3 Literature Review of Sonocrystallization

Power ultrasound has been studied with various crystallization systems including adipic acid (Wohlgemuth et al., 2010, Narducci et al., 2011), amino acids (Narducci et al., 2011, Hottot et al., 2008), polymers (Cao et al., 2002), fat (Ueno et al., 2003, Higaki Kaoru, 2001), inorganic compounds (Amara et al., 2004, Dalas, 2001) and some poorly soluble pharmaceutical substances (Dalvi and Dave, 2010) and have proven to be a considerably powerful and efficient technology in crystallization promotion and crystallization product enhancement. In this section, a literature review of the research into power ultrasound effects on various aspects of crystallization is given in detail.

3.3.1 Observed Effects of Power Ultrasound on Nucleation

Power ultrasound can be utilized to influence every aspect and different steps of the crystallization process, nevertheless, its effect is especially significant on nucleation processes. The metastable zone width and induction time are two of the most fundamental parameters to describe how difficult the crystallization can occur and characterize the nucleation process. The effect of ultrasound on cooling-based primary nucleation was investigated by Lyczko et al. (Lyczko et al., 2002), results suggested that ultrasound had a significant effect on reducing the induction time, especially at low supersaturations, and the main mechanism is a heterogeneous primary nucleation. Their results also verified that the metastable zone width can be reduced by application of ultrasound and ultrasound decreased the apparent order of nucleation rate and increased the solid formation rate. They considered the action of ultrasound was due to the presence of shock waves in the solution, by which the molecular collision and aggregation were enhanced. A similar study based on the anti-solvent crystallization process indicated the ultrasound effect on reducing the metastable zone and induction time (Guo et al., 2005). The apparent order of nucleation was small

while the nucleation constant increased tremendously suggesting the acceleration of the diffusion was the reason for shortening the induction time. Other studies on ultrasound effects on nucleation (Li et al., 2006, Guo et al., 2006b, Kordylla et al., 2008, Luque de Castro and Priego-Capote, 2007) also agree with the statement that ultrasound exhibits a positive effect on nucleation by inducing primary nucleation in the solution and allowing nucleation to occur at much lower supersaturation levels, see Table 3.2.

Although the positive ultrasound effect on nucleation was reported often, there are still exceptions. Miyasaka et al. (Miyasaka et al., 2006b) revealed that there was an energy threshold above which ultrasonic irradiation increased the crystal number and promoted nucleation, at the region where a low level of ultrasonic energy applied, power ultrasound inhibited the primary nucleation by decreasing the average number of crystals. The extensive investigation (Miyasaka et al., 2006a) successfully established the relationship between the necessary critical energy to form a stable nucleus ($\triangle G_{crit}$) and the ultrasonic energy at which the ultrasound exhibits an improved effect (E_{crit}): E_{crit} decreased with decrease of $\triangle G_{crit}$. The research also found that ultrasonic irradiation inhibited and activated the primary nucleation at various degrees of supersaturation. Moreover, sonocrystallization studies on amino acids again pointed out that the induction time increased with increasing ultrasonic irradiation energy up to a certain degree then decreased, indicating the earlier energy threshold theory (Kurotani et al., 2009).

Table 3.2: Ultrasonic crystallization of mono- and disaccharides from aqueous solutions (Ruecroft et al., 2005)

Solute	Quantity dissolved in 10 mL water (g)	Temp(°C) at which solid appeared	
		Without ultrasound	With ultrasound
D-xylose	25.0	36	43
D-sucrose	18.0	<40	47
D-lactose	5.5	41	43
D-maltose	13.0	<20	40
D-glucose	100.0	<30	75
D-cellubiose	2.0	<20	42

Large-scale ultrasonic processing technologies have also been developed in different ways: either with probes in a flow cell or immersed in a large volume delivering high

local intensities (Dennehy, 2003), or, opposing parallel transducers arranged around a duct, through which the process solution or suspension flows (Vaxelaire, 1995). However, compared with the probe system that directly contact with the processing solution where the ultrasonic energy cannot particularly well focused other than the tip area, the parallel transducers offered a greater extent. A typical developed scaling up flow cell is shown in Figure 3.8. The flow cell employed direct bonding of 40 transducers manufactured from stainless steel with a hard chrome internal surface for additional corrosion residence time (Perkins, 2000). The low output of individual transducer and improved bonding method allowed large number of transducers to give uniform and noncoherent acoustic pattern above the cavitational threshold throughout the working volume. It also offered additional advantage of avoiding the phenomenon of acoustic decoupling.

Figure 3.8 20L flow cell fabricated in hard chrome-plated stainless steel with multi-transducers for use in the alumina industry shown with acoustic shield removed for clarity (Ruecroft et al., 2005)

3.3.2 Ultrasonic Crystal Growth

Different from the dramatic ultrasonic effects on nucleation, ultrasound effects on crystal growth seems much smaller. The theoretical study of ultrasonic crystal growth rate suggested that the effect of ultrasound on growth rate depended on the magnitude of the supersaturation driving force: At low S with growth velocities of around 10^{-10} m/s, ultrasonic irradiation doubled the growth rate; at high S with faster growth of

10^{-7} m/s, ultrasound appeared to have no effect. Under the condition of low supersaturation levels, the quantity of available growth units in the vicinity of the crystal surface is small and bulk-phase mass transfer is the rate limiting in supplying growth units to the crystal surface, and the application of ultrasonic irradiation will enhance the growth rate(Ruecroft et al., 2005, Arakelyan, 1987).The growth of sugar crystal was found to be faster with ultrasound irradiation than with mechanical agitation (Kortnev and Martynovskaya, 1974). According to work reported by Devarakonda et al. (Devarakonda et al., 2003), ultrasonic energy was found to increase the overall mass rate of crystal growth due to the enhancement of secondary nucleation. The influence of power ultrasound on potash alum growth rate was investigated by Delmas et al. (Amara et al., 2004) and found that the mass growth rate was faster under ultrasound but the experiments could not determine which step of the growth was improved by ultrasound. The volumetric crystal growth rate based on the seeded sonocrystallization of calcite was enhanced by 46% through the ultrasound treatment because the disruption and erosion of seeded crystals accompanied by the ultrasonic irradiation led to the increase of surface area available for crystal growth (Boels et al., 2010a). Boels et al. (Boels et al., 2010b) also studied the effect of ultrasound on calcite growth in presence of the inhibitors. They found that the inhibiting effect of the inhibitor on crystal growth was seriously mitigated and the recovery of the growth rate following inhibition was strongly improved under the influence of ultrasound. The possible explanation was the chemical effect of ultrasound causing the degradation of the inhibitor.

However, contradictory results given by Dalas (Dalas, 2001) suggested that a retardation effect on the water formed scale deposition, which resulted in the reduction of the crystal growth rate by 62%-76%, was observed on calcium carbonate growth investigation in presence of the ultrasonic field. The ultrasonic radiation did not affect the mechanism, the nature, the morphology or the size of calcium carbonate, only the crystal growth rate via the dehydration and surface diffusion of growth molecules. Similarly, ultrasound introduced to the precipitation of nanoparticle revealed that the mechanical influence produced by cavitation like commination, emulsification and stir could effectively prevent the crystal growth and aggregation. But when the ultrasonic time was too long, shock wave with high pressure, micro-emission fluid and 'Brown phenomenon' of nanoparticle itself could result in the aggregation of nanoparticles (Tang and Shi, 2008).

3.3.3 Ultrasound Effects on Polymorphism and Particle Size Distribution

Power ultrasound has been extensively investigated to polymorphic systems for selective and designed polymorphic form generation. P-aminobenzoic acid is an enantiotropic polymorph with the transition temperature at approximately 25°C above which the β-form is metastable polymorph and impossible to produce in absence of ultrasound. Interestingly, pure β-form can be obtained above the transition temperature by application of controlled ultrasound, if the providing supersaturation is not too high (Gracin et al., 2005, Gracin and Åke, 2004). There was a sonication intensity threshold near to the critical supersaturation threshold above which pure β-form could not be produced. Since the α-form is based on the centro symmetric carboxylic acid dimers, the ultrasound disturbed structure and reduced the dimerization in the solution; this was believed to be the possible hypothesis that precise ultrasonic irradiation results in the selective favour polymorph. For l-glutamic acid, the concentration of metastable α-form was increased with only 30s of sonication at high supersaturation; but ultrasound was not applicable for polymorphism control at low supersaturation (Hatakka et al., 2010). Furthermore, it has been specified that more unstable δ-form was obtained, independent of nucleation temperature, during freeze-drying of mannitol from an aqueous solution in presence of ultrasound (Hottot et al., 2008).

On the other hand, Kurotani et al. (Kurotani and Hirasawa, 2010) based on their work about using precise amounts of ultrasonic energy in polymorph control, suggested that large ultrasonic energy irradiation conditions associated with rapid transformation can assist in the isolation of the stable polymorphic form. Conversely, without ultrasonic irradiation or with small ultrasonic energy input, one may expect to generate the kinetically favoured metastable polymorphic form. According to Ueno et al. (Ueno et al., 2003) the ultrasound was reported to favour formation of the stable polymorphic form. More literature discussing ultrasonic irradiation on polymorphism control during the crystallization process can be found elsewhere (Louhi-Kultanen et al., 2006, Price et al., 2011, Kougoulos et al., 2010, Higaki Kaoru, 2001, Cao et al., 2002).

Reliable evidence has shown that power ultrasound is potentially applicable in manipulating the 'tailoring' of crystal size and particle size distribution and efficiently preventing agglomeration during crystallization. To control the particle size

distribution through ultrasonic irradiation, two of the extreme cases are worth noting: firstly, a short burst of ultrasound to a low supersaturation solution to induce nucleation and allow growth to large crystals; and secondly, a longer burst or continuous insonation to the high supersaturation solution where prolific nucleation occurs to achieve smaller crystals (Ruecroft et al., 2005), as was shown in Figure 3.9. Commonly, the reason is that secondary nucleation results from the ultrasonic mechanical influence or the loosely bound agglomerates in the solution. With different ultrasonic energy intensity, crystal size was found to be decreased with the increase of ultrasound power and the longer residence time attempted to produce smaller size and more uniform particles, see Figure 3.10 (Narducci et al., 2011). Consistent ultrasonic effect on particle size distribution can be found in more reported work (Luque de Castro and Priego-Capote, 2007, Li et al., 2003, Kim et al., 2002, Amara et al., 2004).

| a | b | c |
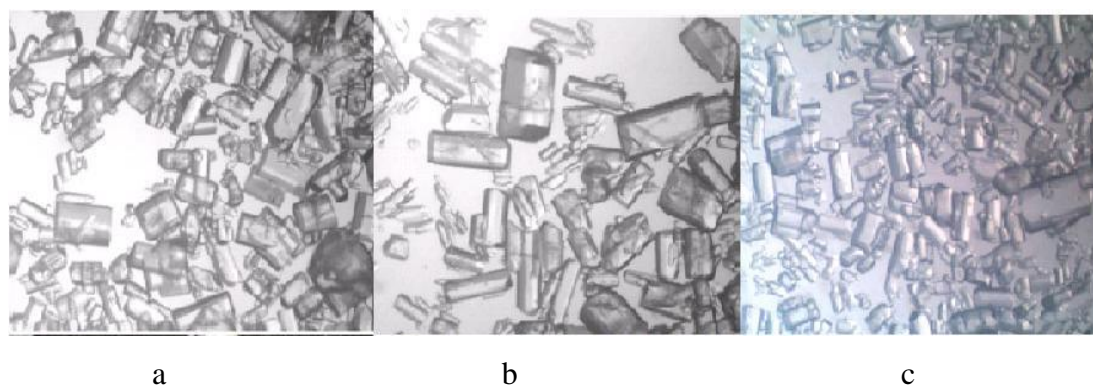
Figure 3.9: Final product of L-Arg at S=1.58: (a) without ultrasound (b) ultrasonic energy 4.3J (c) ultrasonic energy 43J (Kurotani et al., 2009)
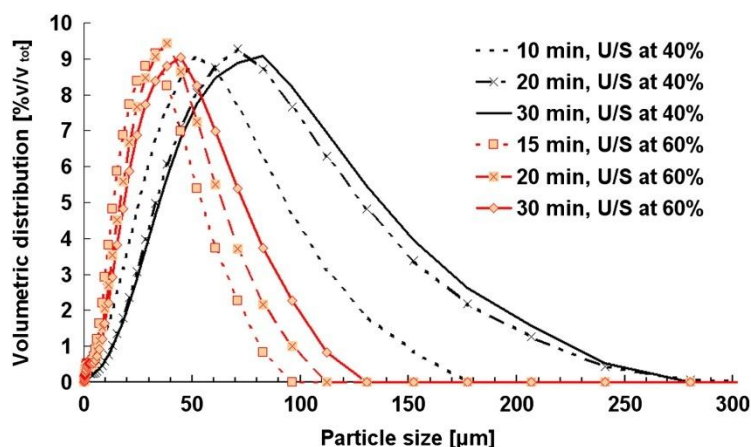
Figure 3.10: Effect of power amplitude and residence time on the crystal size distribution (Narducci et al., 2011)

Considering the ultrasound action effect on crystal morphology, some of the authors (Dalas, 2001, Nishida, 2004) hold the perspective that in both the presence and absence of ultrasound, irradiation results in the same shape crystal, whereas some reported that crystal morphology can be modified by ultrasound. It was demonstrated that potash alum crystals exhibited an octahedral shape in silent conditions, but if the crystals were born and grown in an external ultrasonic field, a decahedron shape was observed due to the erosion (Amara et al., 2004). For those needle-like, difficult to handle crystals, Kim et al. (Kim et al., 2003) used ultrasound to reduce the particle length and subsequent temperature cycling helped grow the shorter needle-like segments into thicker rods. The crystal habit of aluminum hydroxide (Enomoto et al., 1992) and iron hydroxide (Enomoto et al., 1992) appeared to be affected by ultrasound.

In addition to controlling the crystal habit, thanks to the cavitation relevant improved mixing and local thermodynamics, the amount of agglomerates was visibly reduced with the application of ultrasound (Guo et al., 2005, Li et al., 2006, Wohlgemuth et al., 2010, Narducci et al., 2011).

3.3.4 Ultrasonic Variables Influence on Sonocrystallization

Sonochemical effects of ultrasound vibration can be distinguishable, or even contradictory, if the ultrasonic variables such as the ultrasound frequency, intensity and horn size as well as the external experimental conditions are different. Table 3.3 lists some of the discussion and findings from the literature about those variables

effect on sonocrystallization.

Table 3.3: Literatures of ultrasound-related variables effects on sonocrystallization

Variables	Authors	Findings
Frequency	Li et al.(Li et al., 2003)	· low frequency ultrasound (15, 20, 25 and 30kHz) have the same effect on nucleation and growth · no obvious differences in the shape, the mean size and size distribution of resulting products
	Ichitsubo et al. (Ichitsubo et al., 2004)	· high frequency ultrasound (0.3~1.5MHz) results in the stochastic resonance phenomena by which crystallization was considered to be accelerated
Ultrasonic power	Li-yun et al. (Li-yun et al., 2005)	· no crystal form above 300w · below the threshold, particle size decreased with the increase of ultrasonic power
	Li et al. (Li et al., 2003)	· high ultrasonic power (1000w) results in thicker and shorter crystals while low ultrasonic power (100w) results in longer and thinner crystals · the mean size of the produced crystals under treatment of various ultrasonic powers are found to be the same
Horn tip size	Nishida (Nishida, 2004)	· the crystal precipitation rate was observed to be proportional to the horn tip area
	Luque de Castro and Priego-Capote (Luque de Castro and Priego-Capote, 2007)	· the horn tip diameter determined the intensity of ultrasound hence impact the crystallization matter formed
Horn immersion depth	Nishida (Nishida, 2004)	· there is optimum range of depth for accelerating crystal precipitation
Sonication volume	Amara et al. (Amara et al., 2004)	· large reactor associated with lower vibration and cavitation and resulted in fewer nuclei and larger crystals · increased sonication volume reduced the crystal collision and abrasion
	Manson and Peters (Timothy J.Mason and Peters, 2002)	· For given input power the sonochemical effect would diminished with the enlarge of volume

3.3.5 Proposed Mechanisms of Sonocrystallization

It is not difficult to conclude from previous discussion that the ultrasound effects on crystallization are quite diverse, but all the researchers agree with the statement that cavitation is the original causation of sonochemistry. Although the link and correlation between the cavitation issue and crystallization behaviour are still unclear and not yet fully understood, a wide variety of mechanisms have been proposed to explain and describe the ultrasonic effects on the crystallization process.

Amount the mechanisms, the 'hot-spot' theory is the broadly acceptable and most reasonable one in sonocrystallization investigation. As is detailed in the previous section, 3.2, ultrasound waves passing through the medium solution will result in the

generation of cavitation bubbles which are associated with extremely high local temperature and pressure, this has been proven to be over 5000K and 2000 atm, during its collapse. The extreme excitation of such large energy release, together with the concomitant shock wave, is believed to be the intense trigger for crystallization. Interestingly, counter-intuitive effects state that local temperature increase may remove the crystallization driving force since the supersaturation in the immediate vicinity will be reduced or eliminated. On the other hand, the shock wave and collapsing turbulence may contribute to the nucleation in the environment (Ruecroft et al., 2005). Other postulates suggest that: 1) subsequent rapid local cooling rates, calculated at $10^7 \sim 10^{10}$ K/s, play a significant role in increasing supersaturation; 2) the reduced crystallization temperature results from localized pressure increasing; and 3) the cavitation events allow the excitation energy barriers associated with nucleation to be surmounted, in which case it should be possible to correlate the number of cavitations and nucleation events in a quantitative way (Luque de Castro and Priego-Capote, 2007). Experimental work carried out in crystal-free supercooled liquid (Frawley and Childs, 1968, Hunt and Jackson, 1966) suggested that the negative and the positive pressure, which can result in the cooling and melting point change during the collapse, were the possible mechanism of sonocrystallization. Virone et al. (Virone et al., 2006) designed a novel reactor where the ultrasound pressure was well-defined and attempted to establish the relationship between cavitation number and nucleation event based on the assumption that the nucleation rate was a function of the collapsing pressure of cavitation bubbles.

According to the diffusion theory, the pressure gradient is capable of segregating the mixing species by pushing the densest toward low pressure regions and the lightest to the high pressure zone (Bird et al., 1960). This pressure diffusion idea was put forward by Louisnard and Grossier et al. who proposed a molecular segregation model based on the pressure gradient to illustrate the mechanism of sonocrystallization. Following the model representation shown in Figure 3.11, the relevant studies (Grossier et al., 2007, Dodds et al., 2007) concluded that the clusters segregated near a cavitation bubble wall including: 1) the solute molecules and small clusters in the solution would remain unsegregated, like C_1; 2) the medium clusters such as C_m and C_n near the collapsing bubble wall would be over-concentrated, favouring the attachment of the cluster and solute molecules (C_n and C_1) and direct aggregation of the clusters (C_m and C_n); and 3) the larger clusters would by driven

away far from the bubble wall. Eventually, the cavitation effect would efficiently finish the segregation and accelerate the overall nucleation kinetics hence promoting crystallization.
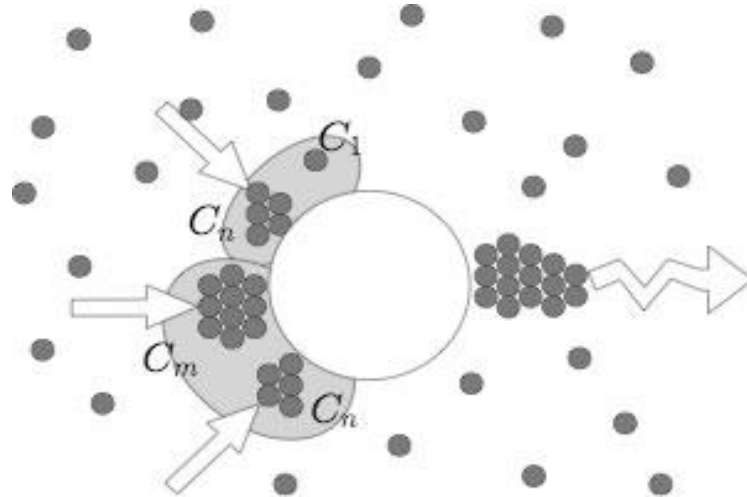
Figure 3.11: The cluster growth in the presence of cavitation bubbles: the solute molecule C1, the existing cluster Cm and Cn (Dodds et al., 2007)

Ultrasonically induced heterogeneous primary nucleation or secondary nucleation is another hypothetical mechanism of ultrasound action. Lyczko et al. (Lyczko et al., 2002) proposed that ultrasound changes the activation energy to act on either the surface energy or the contact angle and suggested a heterogeneous nucleation mechanism. Kordylla et al. (Kordylla et al., 2009) developed the kinetic approach by introducing the heterogeneous primary nucleation and secondary nucleation to the mechanism to simulate the ultrasound-induced nucleation during cooling crystallization. In addition, the photographic study of ultrasound effect on ice crystallization given by Swallowe et al. (Swallowe et al., 1989) indicated that the oscillating, acoustically induced, cavitation bubbles disrupted the crystal to fragment to form more crystal nuclei which grow as they drift away from the interaction regions. Similar investigation of ice crystallization confirmed that sonication resulted in the production of small new ice crystals from growing ice dendrite and primary and secondary nucleation were both possible (Chow et al., 2003). It is also assumed that cavitation bubbles themselves acted as nucleation centre and the ultrasonic induced nucleation can be treated as a heterogeneous nucleation (Wohlgemuth et al., 2010).
The localized turbulence of the solid-liquid boundary caused by the microstream and shock wave is considered to be another possible sonocrystallization mechanism since

it results in the acceleration of mass transfer through the film by increasing the intrinsic mass transfer coefficient (Hagenson and Doraiswamy, 1998). Assuming a homogeneous nucleation mechanism, Guo et al. (Guo et al., 2006a) investigated the effect of ultrasound in reactive crystallization and found that the diffusion coefficient was increased in presence of ultrasound, implying the main reason for ultrasound action was the acceleration of diffusion. Based upon the concept that ultrasound increased the rate of diffusion of solute $(-\frac{dC_A}{dt})$, Thompson and Doraiswamy (Thompson, 2001) proposed a model where the intrinsic mass transfer coefficient k_{sl} and the interfacial area a would simultaneously benefit the mass transfer within a sonicated solid-liquid system with saturated driving force of (C_A*-C_A). The representation of several events is shown in Figure 3.12. Other mechanisms from energy and gas cloud point of view to explain the ultrasonic effects can be found in (Qiu.Tai Q, 1993, Nanev and Penkova, 2001).

$$-\frac{dC_A}{dt} = k_{sl}\ a\ \left(C_A^* - C_A\right)$$

| Increased by microstreaming (localized turbulence in the solid-liquid film) (Hagenson and Doraiswamy, 1998; Elder, 1959) | Increased by interparticle collisions leading to particle degradation or by erosion of the particle surface due to microjets (Neppiras, 1980; Suslick *et al.*, 1987) | 1. Increased solubility in SCF at cavitation site, leading to supersaturation of bulk solvent at ambient conditions (Thompson and Dorasiwamy, 1999)
 2. Possible Ostwald ripening of particle fragments <1.0 μm |

Figure 3.12: Ultrasound enhancement of the diffusion rate (Thompson, 2001)

3.4 Closing Remarks

In this chapter, the fundamentals of power ultrasound including the introduction, formation, growth and collapse of cavitation, as well as the cavitation associated effects, are given. A comprehensive review of the application of power ultrasound in crystallization is demonstrated from various aspects, followed by the illustration of proposed mechanisms in sonocrystallization.

Chapter 4

Materials and Process Analytical Techniques

Summary: This chapter provides the introduction to the material and description of the principle of process analytical techniques that were performed in the experimental work.

4.1 Introduction

In this research work, a series of experiments were carried out to assess the influence of power ultrasound on various aspects of l-glutamic acid crystallization. Therefore, a collection of process analytical techniques (ATR-FTIR, FBRM, powder x-ray diffraction, etc.) and the crystallization experimental apparatus (crystallizer, Julabo and ultrasonic system, etc.) together with the chemical materials used in this project are described.

4.2 Materials

4.2.1 L-Glutamic Acid

L-glutamic acid is an amino acid which consists of two carboxylic groups and an amino group. Since it is an important component in many chemical reactions and organism protein metabolism processes, it is widely used in the pharmaceutical, chemical and food industries. L-glutamic acid is also known as the first industrially prepared amino acid due to the flavor-enhancing property of its monosodium salt which is used extensively as a food additive. Some of its physical properties are listed in Table 4.1.

Table 4.1: Physical properties of L-glutamic acid (AminoScience, 2009)

Molecular Formula	$C_5H_9NO_4$
Crystal Structure	Orthorhobic
Molecular Weight (g/mol)	147.13
Density (kg/m^3)	1538
Melting Point (°C)	247

Like most of the other pharmaceutical compounds, LGA appears in more than one polymorphic form and belongs to the monotropical polymorphism system. The known polymorphs of LGA are the metastable α-form and the stable β-form, of which the α-form is prismatic crystal habit while the β-form is needle-like crystal as shown in Figure 4.1. Generally, the metastable α-form is preferred due to its advantage of crystal habit for industrial process handling, sedimentation and filtration, for instance. Two of the polymorphic forms have different solubility in aqueous solution and hence undergo transformation of the metastable α-form to the stable β-form in accordance

with Ostwald's law of stages. Figure 4.2 presents the solubility of the l-glutamic acid polymorphs as a function of temperature, as expected, the metastable α-form has higher solubility than the β-form in all temperature ranges. But above 45°C, the solubility of the α-form is difficult to measure due to the precipitation of the β-form (Kitamura, 1989).

(a)   (b)
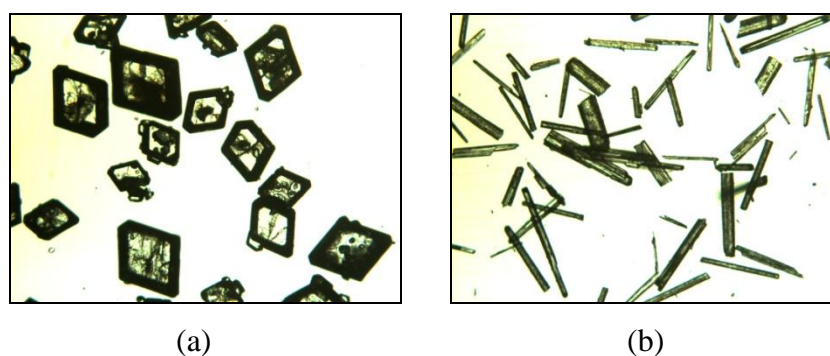
Figure 4.1: L-glutamic acid crystals of polymorphs: (a) α-form, (b) β-form
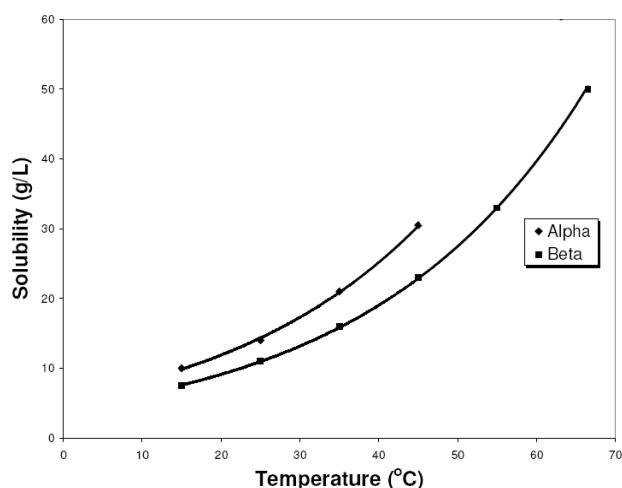
Figure 4.2: Solubility profile of the α-form and β-form of l-glutamic acid (Kitamura, 1989, Ma, 2010).

The polymorphic transformation of l-glutamic acid was found to be solution-mediated (Kitamura, 1989) with the stable β-form nucleated and grown on the surface of the metastable α-form (Ferrari and Davey, 2004, Cashell et al., 2003, Scholl et al., 2006). Even these previous studies claimed that the dry α-form l-glutamic acid was indefinitely stable since it separated from the solution and there was no solid state route for α-form to β-form transformation, current work suggested that the irreversible polymorphic transformation of α-form to β-form can take place in the solid state at high temperature ≥ 140°C (Wu et al., 2009). During crystallization, each polymorph grows competitively and according to Kitamura, the growth of both of the l-glutamic

acid polymorphs are mainly controlled by the surface reaction process, the mechanism of α-form and β-form growth are both the 2D nucleation model rather than the screw and dislocation (Kitamura and Ishizu, 2000).

The LGA used in this work was purchased from the Sigma-Aldrich Company Ltd of 99% purity. For seeded growth experiments, the needle-like β-form was purchased from Van Waters and Rogers (VWR) International Ltd (VWR-website). However, the α-form l-glutamic acid is not commercially available and was recrystallized from the l-glutamic acid in 20L reactor with a fast cooling rate of 0.5°C/min, filtrated, washed in methanol and dried at 60°C.

4.2.2 Solvent

The solvent used in all the experiments carried out in this work is laboratory distilled water which was free of all gasses and minerals. The solvent used for crystal washing after crystallization was methanol purchased from Fisher Scientific Ltd.

4.3 Process Analytical Techniques and Instrumentation

4.3.1 Crystallizers

In this project, a 100mL, 500mL and 1L crystallizer was utilized for kinetic and mechanism development induction time measurement, basic experimental study of the metastable zone width and the induction time, and ultrasound effect crystal growth evaluation, respectively. The control software system and details of various size crystallizers are listed in Table 4.2.

Table 4.2: Description of crystallization reactors and corresponding control programs

Crystallizer	Description	Control software
100 mL	Double-jacketed glass automated crystallization reactor from Hazard Evaluation Laboratory Ltd (HEL) with HEL external heaters power supply	HEL WinISO process control software version 2.2.17.4 E354
500 mL	Double-jacketed glass Autolab crystallization reactor from HEL	HEL WinISO process control software version 2.2.30.3 E227
1L	Double-jacketed glass crystallization reactor from HEL	In-house built and developed control program using Labview

4.3.2 Julabo Circulator

The temperature in the crystallizer during all the crystallization experiments is controlled by the oil bath Julabo circulator connecting with the data interface board. The Julabo refrigerated and heating circulators used in this project allowed the external heating and cooling task, temperature setting and high capacity of heating and cooling capacities to guarantee the temperature and process control within a short time request in the experiments. The Julabo circulator models and the technical specification for different investigation sections are shown in Table 4.3.

Table 4.3: The Julabo model and technical specification for various crystallizer control

	Julabo model for different experimental crystallizer control		
	F32-HE for 100mL	FP50-HP for 500mL	FP50-HE for 1L
Working range	-35°C to 200°C	-50°C to 200°C	-50°C to 200°C
Heater capacity	2000w	2000w	1000w
Cooling capacity	450w at 20°C	900w at 20°C	900w at 20°C
Filling volume	8 litres	8 litres	8 litres
Online communication	available	available	available

4.3.3 Thermometer and Turbidity Probe

The platinum resistance thermometer (PT100) was utilized in this work for solution temperature measurement over a wide temperature range of -250°C to 800°C and a high accuracy of $\pm$ 0.3°C (Khan, 2008). The on-set of crystallization and dissolution were detected by fibre optic turbidity probe which was built in-house by the University of Leeds Workshop. The turbidity value was calibrated from 100 to 0 corresponding to the voltage signal from 0 to 1 volt that was produced due to the light transmittance. The sudden change in the solution turbidity value reflects the occurrence or the disappearance of nuclei. The thermometer and turbidity probe were connected with the interface board and conducted using HEL WinISO process software.

4.3.4 Power Ultrasonic Instrument

The acoustic probe system employed in the crystallization studies was the P100/2-20 processor system with a fixed 20 kHz frequency and adjustable ultrasonic power provided by Prosonix Ltd. (Oxford, UK). As mentioned in Chapter 3 the advantage of the probe ultrasonic system in the laboratory scale was the sufficiently high power to crystallization and the ability to conveniently control energy input to the process. It consisted of a transducer element, an interchangeable step detectable horn with tip diameter of 9mm, and an ultrasonic generator, seen Figure 4.3.
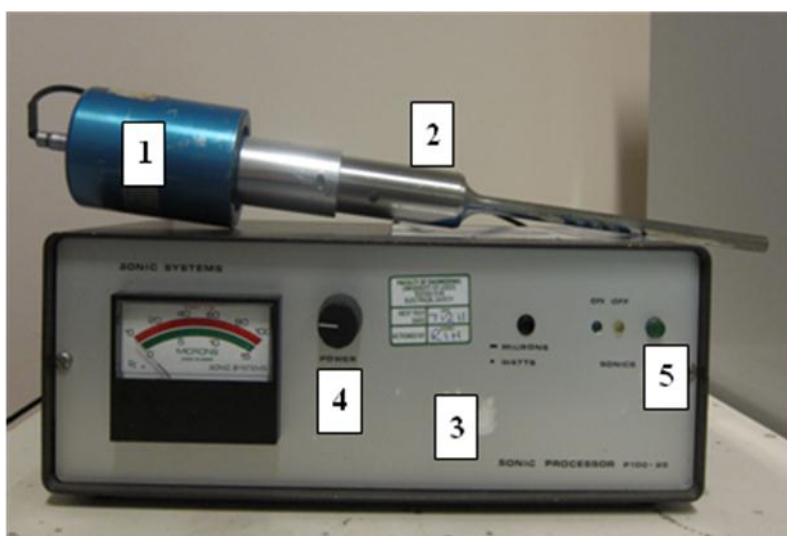
Figure 4.3: Construction of the ultrasonic probe system: 1. the transducer element; 2. the step detectable horn; 3. the generator; 4. the power control; 5. the pulse facility

The piezoelectric ceramic transducer is used for the ultrasonic system and this type of transducer is also the most general driven model in laboratory. The generator is the source of electrical frequency that supplied the transducer and it is recommended to turn on the system in the mixture to avoid the extra power required to drive the system and influence the overall resonance (Timothy J.Mason and Peters, 2002). The switch of the pulse facility on the generator allows the instant on and off control of ultrasound irradiation. The power control facility provides simple adjustment of the input power to the transducer from 0 to 100w. Generally, it is not necessary to set the maximum input power for the greatest and the most effective sonochemical effect. In this work, the maximum power of ultrasound is 35w.

4.3.5 Powder X-ray Diffraction

In this work, the P'Analytical X'Pert MPD (Netherlands) x-ray diffractometer, as shown in Figure 4.4, was utilized to identify the LGA polymorphs by determining the characteristic Bragg peak position and comparing this with the reference patterns of each polymorph. The x-ray source of the unit is the monochromatic Cu-Kα radiation produced from a graphite monochromator. The crystal sample was ground into the sample platform with a flat analysis surface and the x-ray detector revolved around the sample employing an 2 theta scan angle range of 15°~40° with a step size of 0.033° to record the intensity as a function of angle. The analysis was performed highly automatically and data is collected digitally. The resultant XRD patterns were then analyzed using associated X'Pert Highscore Plus software with ICDD Powder Diffraction File database for polymorph identification.
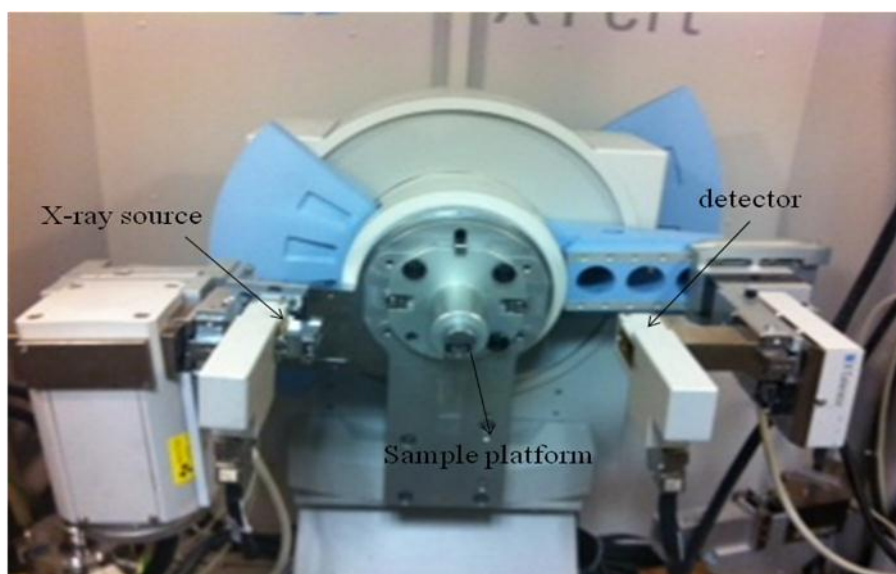
Figure 4.4: The representative photograph of the power x-ray diffractometer

4.3.6 ATR-FTIR

The Attenuated Total Reflectance-Fourier Transform Infrared technique (ATR-FTIR) ReactIR^{TM}4000 spectrometer, purchased from Mettler Toledo Co. Ltd, was employed in the crystal growth investigation for solution concentration measurement. Instrument construction consists of the spectrometer, the measurement probe and the operating PC is shown in Figure 4.5.

Figure 4.5: The ATR-FTIR instrument ReactIR spectroscopy: 1.MTC-detector; 2.insertion probe; 3. detector module; 4. PC

Before the experiment, liquid nitrogen is required for detector cooling and dry air is used to purge the insertion probe to prevent the optics from becoming fogged and remove water and carbon dioxide peaks from the background spectrum (Ma, 2010). The probe tip needs to be completely clean and exposed to the air for background spectrum collection. The instrument specification of mid infrared wavenumber is $4800\sim450cm^{-1}$ and was set to be $1950\sim650cm^{-1}$ which covered the infrared absorption band of l-glutamic acid within the measurement. Spectrum was recorded every 30 seconds and presented in a 3D graph in the spectrum acquisition software iC-IR interface, as is illustrated in Figure 4.6. The spectrum data was then interpreted to the solution concentration via MATLAB programming based on the calibration model built and developed by previous researcher, Chaoyang Ma, in his PhD research at the University of Leeds.

Figure 4.6: The iC-IR spectrum acquisition interface

4.3.7 FBRM

In crystal growth measurement experiments, the S400 Focused Beam Reflectance Measurement instrument (FBRM) manufactured by Lasentec ® (Laser Sensor Technology Corporation) was implemented to monitor the chord length distribution of the particle to make sure no significant nucleation occurred during growth measurement. As shown in Figure 4.7, the instrument has three main components: a PC allowing data acquisition and analysis, a field unit providing laser light energy to the probe and analyzing the signal back from the probe, and a probe mounting directly into the solution for measurement. The chord length distribution and number counts were recorded every 10 seconds and data was analyzed using Lasentec FBRM Data Review 6.0 software.
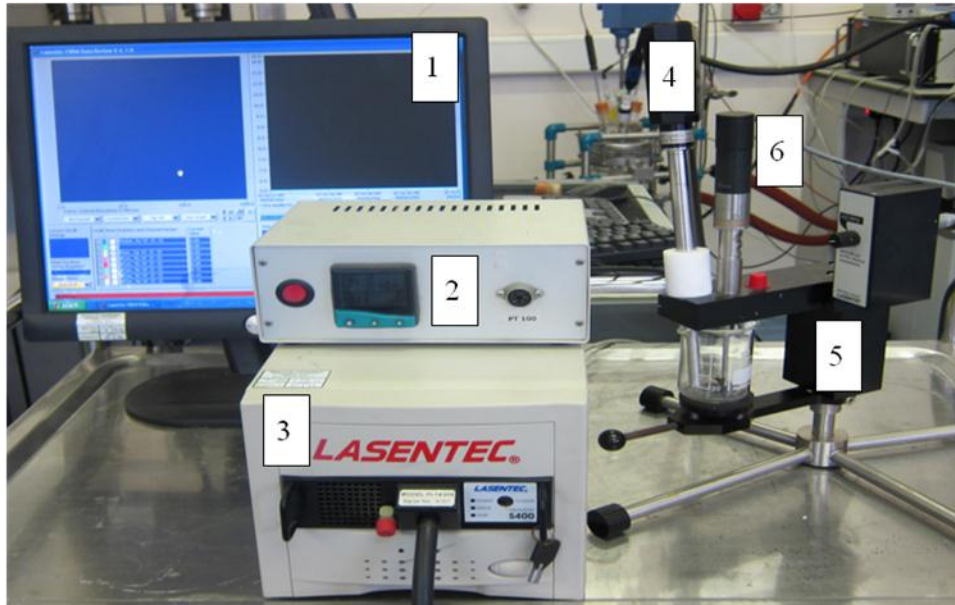
Figure 4.7: The FBRM analysis system: 1. PC monitor; 2. external heater supplier; 3.the field unit; 4. the measurement probe; 5. the reactor stand holder; 6. stirrer

4.3.8 Morphologi G3

To study the growth of l-glutamic acid in this work, Morphologi G3 from Malvern Instruments was employed for off-line particle size measurement. Morphologi G3 is a powerful static image analysis tool for particle size and shape characterization from 0.5μm to 3000μm. Figure 4.8(a) shows the Morphologi G3 particle characterization system with the sample dispersion unit and control PC. The particle sample is placed in a holder sealed using metal foil, air pressure is needed to break the foil and disperse the powder sample through the enclosed chamber on the glass plate below the unit. The automated microscope optics unit with various magnification lenses is then moving and scanning the dispersion area depending upon the advanced standard operating procedure (SOP) setting to capture the individual particle image. The meaningful data analysis software Morphologi provides different parameters, such as CE diameter, HS circularity, elongation, etc., to describe the particle size and shape. It also offers the scattergram to compare and cluster different populations of particles, and individual particle image examination, as shown in Figure 4.8(b).
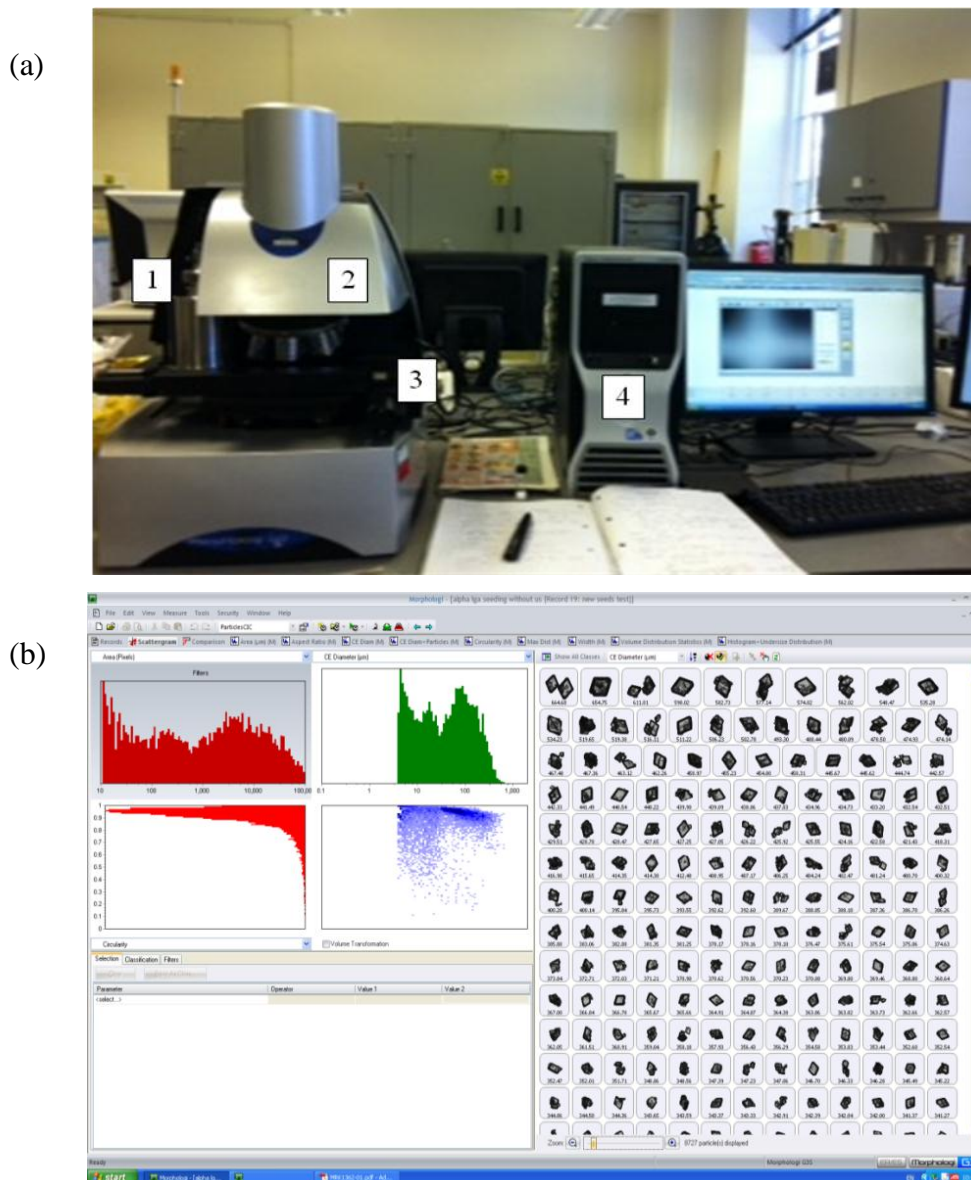
Figure 4.8 (a) the Morphologi G3 instrument: 1.sample dispersion unit; 2.automated optics; 3. sample plate; 4. control PC; (b) Morphologi G3 analysis interface

A constant 9 mm^3 sample volume was dispersed with 0.8 bar pressure on 6μm carrier foil and due to the particle size, a 2.5× objective was performed in the measurement. The resultant number-weighted circle equivalent size distribution (CE Diameter) which defines the diameter of a circle with the equivalent area as the particle under investigation was adopted for particle size characterization. The output data is a number fraction as a function of CE diameter smoothed over 13 points, which means 13 data points are to be averaged during plotting in order to remove spikes from the data graph

4.3.9 Microscopy

The standard Olympus B×51 microscope purchased from Olympus UK Ltd. was connected to the PC and used for image examination of the crystal produced. Measurement performed 5× objective (Mplan 5×/0.10, Japan) and analyzed using QCapture Pro 6.0 software.

4.4 Closing Remarks

This chapter presented the details of materials and various process analytical techniques utilized in this project. The individual experimental procedure is given in the corresponding experimental chapters.

Chapter 5

Investigation of L-Glutamic Acid Primary Nucleation: Effect of Power Ultrasound

Summary: The experimental activities of l-glutamic acid metastable zone width and induction time measurement for power ultrasound are presented together with the nucleation behaviour investigation. A polymorphism study of l-glutamic acid crystallized from various experimental conditions is also given.

5.1 Introduction

As mentioned previously, power ultrasound utilized in crystallization process brings considerable benefits: inducing primary nucleation, manipulating final particle size and size distribution, preventing agglomeration (Lyczko et al., 2002, Kim et al., 2003, Li et al., 2003, Amara et al., 2004), and all these ultrasonic effects mainly act in the nucleation stage. Although sonocrystallization studies were carried out for various substances, the nucleation due to the ultrasound irradiation differs with ultrasonic conditions, chemical substance and the preparation of the saturated solution. Furthermore, former research (Miyasaka et al., 2006b, Miyasaka et al., 2006a) has demonstrated that primary nucleation cannot always be induced by applying ultrasound, they pointed out that ultrasound irradiation can either enhance or inhibit the primary nucleation in different regions. Therefore, it is necessary to gain the knowledge of the nucleation kinetic and mechanism in ultrasound field for later development study. The first aim of the work carried out in this chapter was to measure the phenomenal parameters metastable zone width (MSZW) and induction time under different ultrasound power conditions and then analyzed the relative nucleation kinetics through the homogeneous nucleation theory. This enabled the determination of LGA solubility, supersolubility and relevant nucleation energy functions of the interfacial tension and the critical nucleus radius in different experimental conditions for further sonocrystallization investigation.

Different polymorphs exhibit as different chemical and physical properties which can significantly affect the pharmaceutical performance, quality and efficiency of the final product. The ability to modify the polymorphism with judicious application of ultrasound is another interesting and challenging task in industrial crystallization. Therefore, the second aim of this chapter is to establish the polymorphism profile based on the di-polymorphic compound LGA. To this end, the cooling rate, crystallization temperature and ultrasound power effect on l-glutamic acid polymorphism synthesis were investigated by using powder x-ray diffraction (PXRD).

5.2 Experimental Set-up and Procedures

5.2.1 Experimental Set-up

Metastable zone width and induction time measurement during nucleation were carried out in a 500mL jacketed glass reactor using oil circulation bath Julabo with working range from -50°C to 200°C to control the temperature. The apparatus set-up consisted of a four blades glass stirrer which as operated at 150 r.p.m speed, a Pt100 thermometer and a fibre optic turbidity probe was connected to an automated data logging and regulation program, interfaced with WinIso software. The turbidity was equipped for the crystallization and dissolution onset temperature determination. The immersed ultrasound probe in experiment was positioned on the other side of the turbidity probe to avoid the bubble effect on turbidity measurement and the horn tip position is at the middle of reactor height. The crystallization system set-up is shown in Figure 5.1.
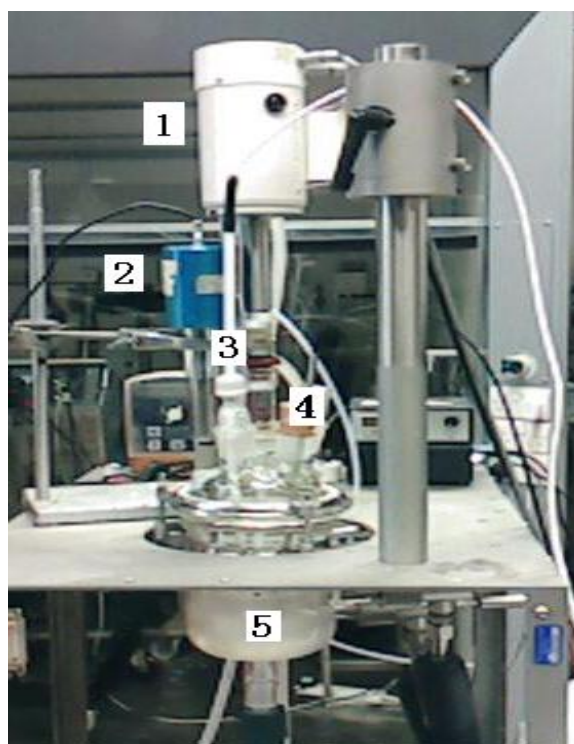
Figure 5.1: Experimental crystallization system set-up: 1. stirrer; 2. step ultrasound probe; 3. thermometer; 4. turbidity probe; 5. Crystallizer

5.2.2 Experimental Procedures

5.2.2.1 Metastable Zone Width Measurement

LGA solids of 15g, 17.5g, 20g, and 22.5g were dissolved in 500 mL distilled water at room temperature to create 30g/L, 35g/L, 40g/L and 45g/L concentration solutions. The solution was initially heated up to 80°C and kept for 60 mins before a linear cooling to the bottom temperature of 10°C using slow cooling rates ranging from 0.1-0.5°C/min. The onset temperature of crystallization (T_{cryst}) and dissolution (T_{diss}) were determined from the changes in turbidity reading. The MSZW was defined as the temperature difference between the dissolution and crystallization temperature measured at different cooling rates.

The MZSW measurements were carried out in a silent, 15W and 25W ultrasound field. Ultrasound was added from the beginning to the end of the whole experimental time. All the experiments were repeated three times and the average onset temperature considered.

5.2.2.2 Induction Time Measurement

The same saturated solutions (30g/L, 35g/L, 40g/L and 45g/L) were heated up and maintained at 80°C for 60 mins before rapidly cooling to different bottom temperatures within the MSZW. The bottom temperatures were maintained under isothermal conditions until crystallization was observed according to the turbidity record. Similarly, the induction time measurement was conducted under silent conditions, in a 15W and 25W ultrasound field. Ultrasound was applied at the moment the bottom temperature was reached. All the measurements were repeated three times and the average induction time was used.

5.2.2.3 Polymorphic Form Identification

To investigate the cooling rate effect on the LGA polymorphism, different concentrations of solution (30g/L, 35g/L, 40g/L and 45g/L) were heated and kept at 80°C for 60 mins to ensure the complete dissolution of solute. The solution was then cooled using different cooling rates (0.1°C/min, 0.25°C/min and 0.5°C/min). After crystallization was completed, the LGA crystals produced were filtrated and washed with methanol, and dried immediately at 60°C for 12 hours. The

polymorphic form of LGA produced was identified by PXRD analysis.

To study the influence of crystallization temperature on LGA polymorphism, solutions with different concentrations were prepared by dissolving known amounts of solids in 500 mL distilled water and heating to 80°C. The isothermal stage was incorporated at 80°C for 1 hour to ensure complete dissolution of LGA. The solution was crash cooled to different bottom temperatures of 50°C, 40°C, 30°C, 25°C and 20°C at which they had the same supersaturation ratio of 1.3. The isothermal method was required at the bottom temperatures until the crystallization was completed. The crystals generated were again filtrated, washed with methanol, and dried at 60°C for 12 hours before analysis using PXRD.

Following the same procedures described above, different powers of ultrasound (15w, 25w and 35w) were applied to assess the effect on LGA polymorph determination.

5.3 Results and Discussions

5.3.1 Metastable Zone Width Determination

The MSZW, induction time, material solubility and supersolubility determination were carried out in various experimental conditions. The corresponding nucleation kinetics and energetic function were then calculated and compared.

5.3.1.1 Nucleation in Silent Conditions

In order to determine the maximum possible undercooling of four different concentration LGA solutions at the equilibrium condition of 0 °C, the cooling rates utilized onset temperature determination are 0.1°C/min, 0.25°C/min and 0.5°C/min. Figure 5.2 presents the reactor temperature and turbidity plot for 45g/L LGA solution crystallized and dissolved at cooling rate of 0.1°C/min. Turbidity value were acutely decreased at 57.2°C and proliferated at 75.5°C which defined the crystallization and dissolution temperature of 57.2°C and 75.5°C, respectively. The same concentrated LGA crystallization and dissolution exemplary plot at 0.25°C/min and 0.5°C/min are shown in Figure 5.3 and Figure 5.4.
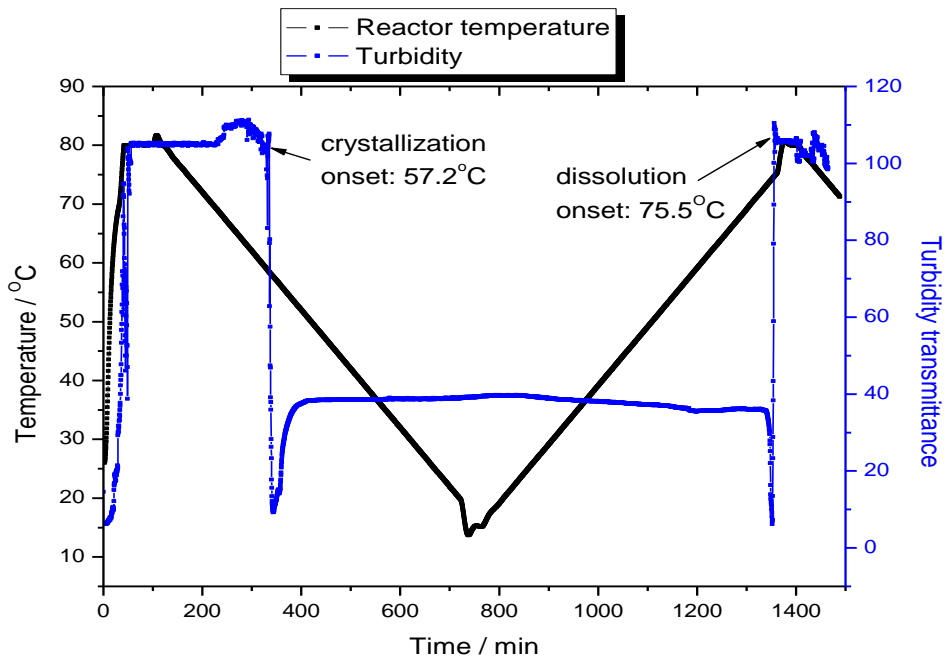
Figure 5.2: Temperature and turbidity plot of 45g/L L-glutamic acid aqueous solution with 0.1°C/min cooling rate in silent conditions
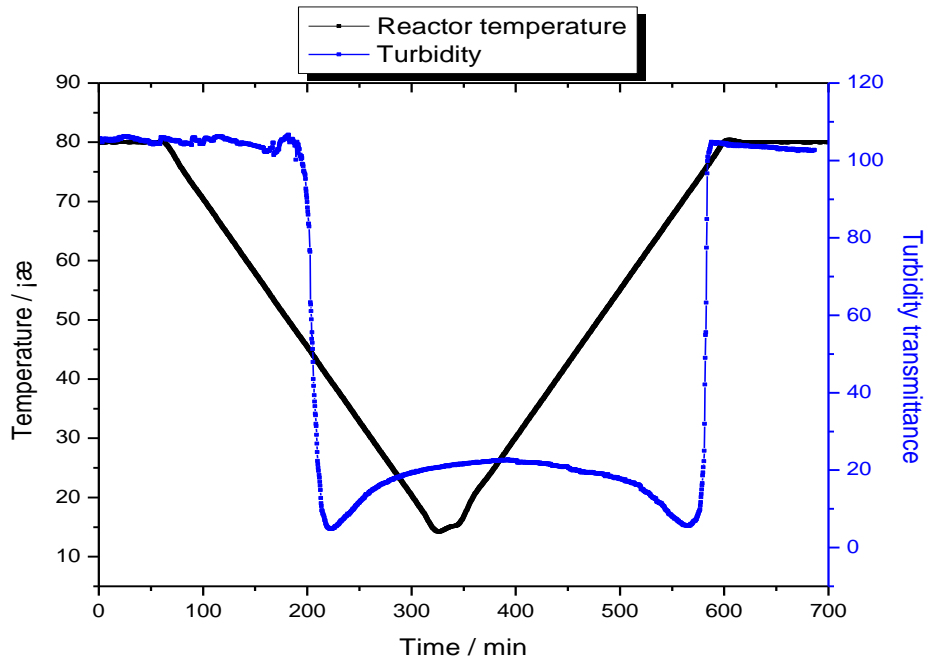
Figure 5.3: Temperature and turbidity plot of 45g/L L-glutamic acid aqueous solution with 0.25°C/min cooling rate in silent conditions
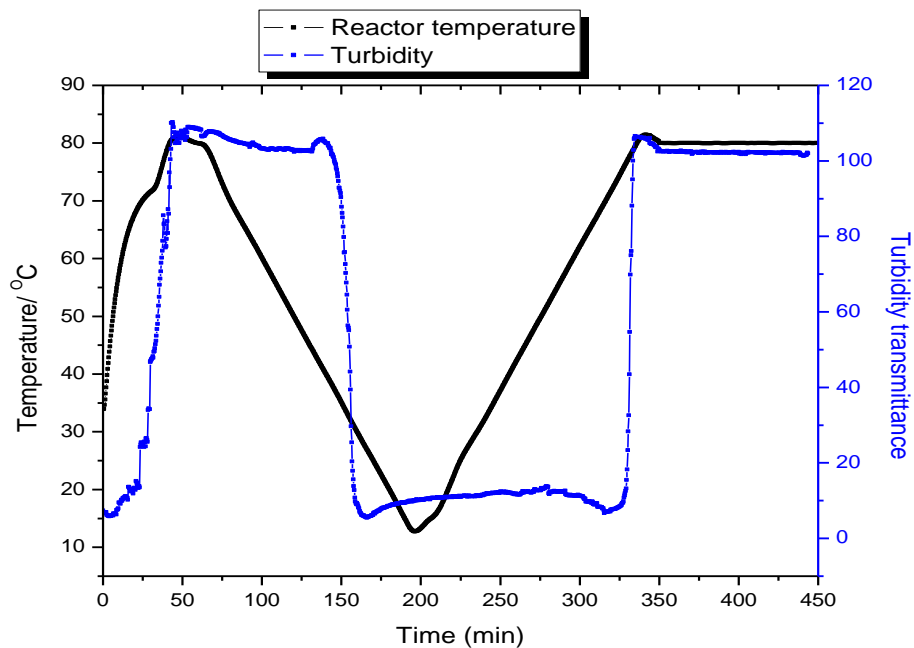
Figure 5.4: Temperature and turbidity plot of 45g/L L-glutamic acid aqueous solution with 0.5°C/min cooling rate in silent conditions

The measured crystallization and dissolution temperatures, as well as the equilibrium metastable value are listed in Table 5.1.The variation in the onset temperatures of crystallization and dissolution are shown in Figure 5.5 for the four solution concentrations considered. The equilibrium metastable value was determined by plotting the cooling rate versus the temperature and extrapolating back the dissolution and crystallization temperature trend line to 0°C/min cooling rate. It can be seen that the MSZW was found to be wider as the cooling rate increased for the four solution concentrations examined, indicating that the crystallization was kinetically limited rather than thermodynamically controlled. This is consistent with the nucleation theory which suggests that the greater supersaturation generation provided for steady-state distribution of nuclei cluster and stable nuclei formation, the longer relaxation time is needed (Mullin, 1993). It can be seen in Figure 5.5 that the nucleation temperature was lower with the faster cooling rate. The MSZW were found to be 11.4°C, 10.8°C, 16.7°C and 17.8°C for four solution concentrations of 45g/L, 40g/L, 35g/L and 30g/L, respectively. The MSZW is a characteristic property of the crystallization system which describes the amount of necessary under-cooling to achieve nucleation. The increased MSZW for decreased concentration indicated that nucleation is easier to occur at higher concentration.

Table 5.1: The determined crystallization and dissolution temperature for four LGA solution concentrations in silence condition

C g/L	Cooling rate °C/min	Tcryst °C	Tdiss °C	Tcryst Arithmetic mean	Standard Deviation σ	Tcryst Arithmetic mean	Standard Deviation σ	MSZW °C
30	0.1	31.8, 31.2, 31.5	51.7, 53.0, 51.3	31.5	0.3000	52	0.889	20.5
	0.25	28.7, 28.6, 32.8	53.4, 53.9, 54.6	30.0	2.396	54.0	0.603	24.0
	0.5	29.4, 29.8, 28.3	58.7, 60.2, 58.8	29.2	0.777	59.9	0.839	30.7
35	0.1	42.0, 43.6, 41.3	59.8. 61.1, 62.4	42.0	1.179	61.2	1.300	19.2
	0.25	35.6, 36.8, 36.5	63.5, 62.5, 63.1	36.3	0.625	63.0	0.503	26.7
	0.5	33.0, 31.8, 32.1	64.3, 64.9, 65.8	32.3	0.625	65.0	0.755	32.7
40	0.1	51.9, 52.6, 54.4	68.3, 69.0, 66.8	53.0	1.289	68.1	1.124	15.1
	0.25	43.5, 45.8, 43.3	70.1, 70, 67.5	44.2	1.389	69.2	1.473	25
	0.5	39.2, 37.4, 38.6	73.0, 74.5, 75.1	38.4	0.917	74.2	1.082	35.8
45	0.1	57.2, 58.3, 58.5	74.0, 72.5, 75.5	58	0.700	74	1.500	16
	0.25	49.0, 51.2, 52.2	76.1, 76.8, 79.2	50.8	1.637	77.4	1.626	26.6
	0.5	41.9, 41.0, 42.1	80.5, 79.2, 78.2	41	0.586	79.3	1.153	38.3
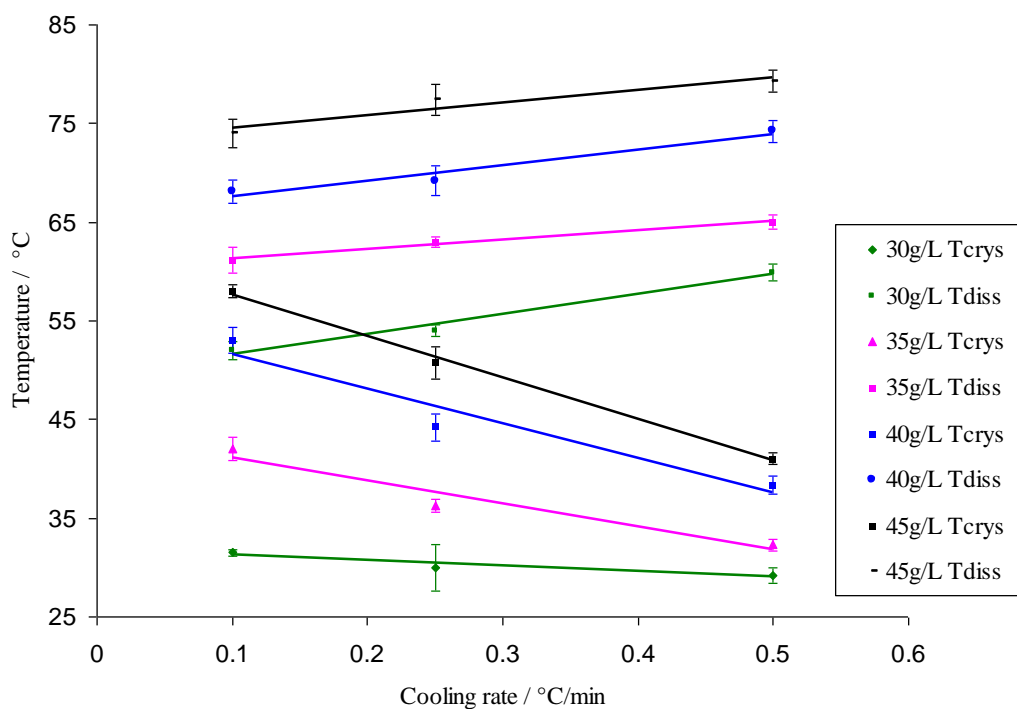
Figure 5.5: Averaged crystallization and dissolution temperatures for four LGA solution concentrations in silent conditions

5.3.1.2 Nucleation in 15W Power Ultrasound Field

The same experimental procedures were adopted and 15W of ultrasound field was applied during the process. Table 5.2 lists the crystallization and dissolution temperatures for the four LGA solution concentrations with different cooling rates. The MSZW under 15W power ultrasound assistance were determined from the cooling rate and temperature plot in Figure 5.6.

Utilizing 15W power ultrasound irradiation during crystallization and dissolution processes, the temperature of dissolution was at values of 73 °C, 65.5°C, 59°C and 50.2°C for 45g/L, 40g/L, 35g/L and 30g/L solution, respectively. This result reveals that ultrasound does not have obvious effect on dissolution because dissolution temperatures did not show much distinctness compared with the 73.3°C, 66°C, 60.2°C and 49.6°C in silent conditions. However, the MSZW for the above four concentrations were found to be 9.9°C, 8.7°C, 13.4°C and 13.9°C which were narrowed by 1.5-3.9°C. It can be therefore concluded that under the 15W ultrasound irradiation, nucleation can occur at a lower supersaturation level.

Table 5.2: The determined crystallization and dissolution temperature for four LGA solution concentrations in 15W ultrasound field

C g/L	Cooling rate °C/min	Tcryst °C	Tdiss °C	Tcryst Arithmetic mean	Standard Deviation σ	Tcryst Arithmetic mean	Standard Deviation σ	MSZW °C
30	0.1	36.5, 37.0, 37.9	54.1, 52.4, 51.1	37.2	0.709	52.5	1.504	15.3
	0.25	31.8, 31.5, 32.8	55.9, 55.0, 58.2	32.0	0.681	56.4	1.650	24.4
	0.5	34.0, 32.6, 34.8	64.1, 62.8, 60.6	33.8	1.114	62.5	1.770	28.7
35	0.1	45.8, 46.2, 44.0	58.7, 60.1, 61.3	45.3	1.172	60.0	1.301	14.7
	0.25	42.4, 41.3, 40.6	61.9, 63.1, 61.3	41.4	0.907	62.1	0.917	20.7
	0.5	40.5, 40.2, 40.3,	63.8, 64.7, 65.2	40.3	0.153	64.6	0.709	24.3
40	0.1	53.9, 55.1, 54.3	67.0, 65.4, 63.9	54.1	0.611	66.1	1.550	12.0
	0.25	52.7, 52.9, 53.4	68.5, 69.2, 68.1	53.0	0.361	68.6	0.557	15.6
	0.5	46.2, 46.7, 46.3	71.2, 69.9, 69.5	46.4	0.265	70.2	0.889	23.8
45	0.1	62.4, 62.8, 62.9	74.1, 73.8, 72.9	62.7	0.265	73.6	0.625	10.9
	0.25	62.9, 61.7, 62.3	76.4, 76.2, 77.1	62.3	0.600	76.6	0.473	14.3
	0.5	61.5, 61.6, 60.5	77.9, 78.0, 78.7	61.2	0.608	78.2	0.436	17.0
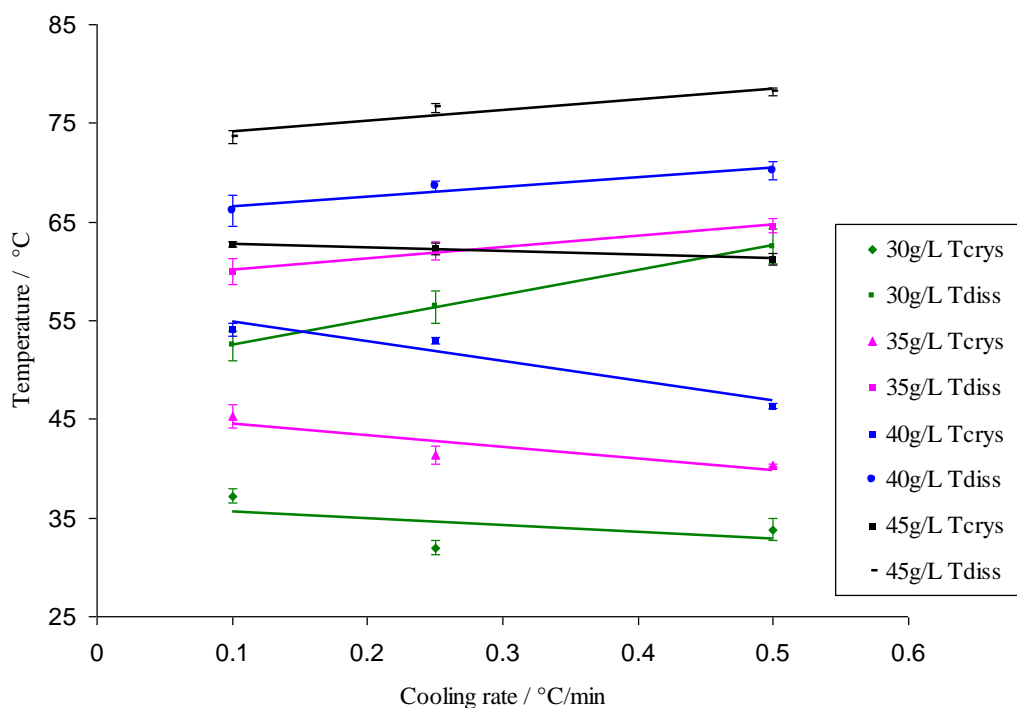
Figure 5.6: Averaged crystallization and dissolution temperatures for four LGA solution concentrations in 15W ultrasound field

5.3.1.3 Nucleation in 25W Power Ultrasound Field

Since the 15W ultrasound narrowed the MSZW, an increased ultrasound power of 25W was extensively used to study the ultrasound power effect on nucleation. Table 5.3 summarizes the crystallization and dissolution temperatures for various concentration solutions. Figure 5.7 demonstrates the average temperature for crystallization and dissolution plot versus the cooling rate. The MSZW is determined from the extrapolated cooling rate at equilibrium 0 °C.

The MSZW in 25W ultrasound experimental condition at 0°C were found to be 8.5°C, 8.9°C, 10.3°C and 12.0°C for 45g/L, 40g/L, 35g/L and 30g/L solution respectively. As expected, these results were also consistent with the nucleation theory that the higher the concentration solution, the smaller the MSZW. In addition, the MSZW in applied 25W ultrasound field for all the concentrations were smaller than the one obtained in former two experimental conditions, which associated with a smaller under-cooling to achieve bulk nucleation.

Table 5.3: The determined crystallization and dissolution temperature for four LGA solution concentrations in 25W ultrasound field

C g/L	Cooling rate °C/min	Tcryst °C	Tdiss °C	Tcryst Arithmetic mean	Standard Deviation σ	Tcryst Arithmetic mean	Standard Deviation σ	MSZW °C
30	0.1	41.0, 40.2, 38.6	52.6, 52.9, 52.9	39.9	1.222	52.8	0.173	12.9
	0.25	40.1, 39.5 40.9	58.1, 56.8, 57.0	40.2	0.702	57.3	0.700	17.1
	0.5	38.5, 38.2, 37.4	62.9, 61.4, 63.2	38.0	0.569	62.5	0.964	24.5
35	0.1	50.2, 49.5, 48.8	59.8, 60.3, 61.3	49.5	0.700	60.5	0.764	11.0
	0.25	48.5, 50.5, 48.6	64.5, 65.3, 63.1	49.2	1.127	64.3	1.114	15.1
	0.5	47.8, 49.0, 48.1	64.1, 65.8, 66.0	48.3	0.625	65.3	1.044	17.0
40	0.1	55.4, 55.7, 56.5	64.3, 66.1, 65.3	55.9	0.569	65.2	0.902	9.3
	0.25	55.5, 54.2, 57.4	68.8, 69.7, 69.8	55.7	1.609	69.4	0.551	13.7
	0.5	51.2, 52.8, 53.4	66.6, 67.7, 68.2	52.5	1.137	67.5	0.819	15.0
45	0.1	65.3, 64.5, 62.6	74.9, 75.2, 75.0	64.1	1.387	75.0	0.153	10.9
	0.25	63.1, 63.8, 63.9	75.4, 76.8, 75.8	63.3	0.436	76.0	0.721	12.4
	0.5	59.0, 61.4, 59.2	77.5, 79.3, 79.2	60.2	1.332	78.7	1.012	18.5
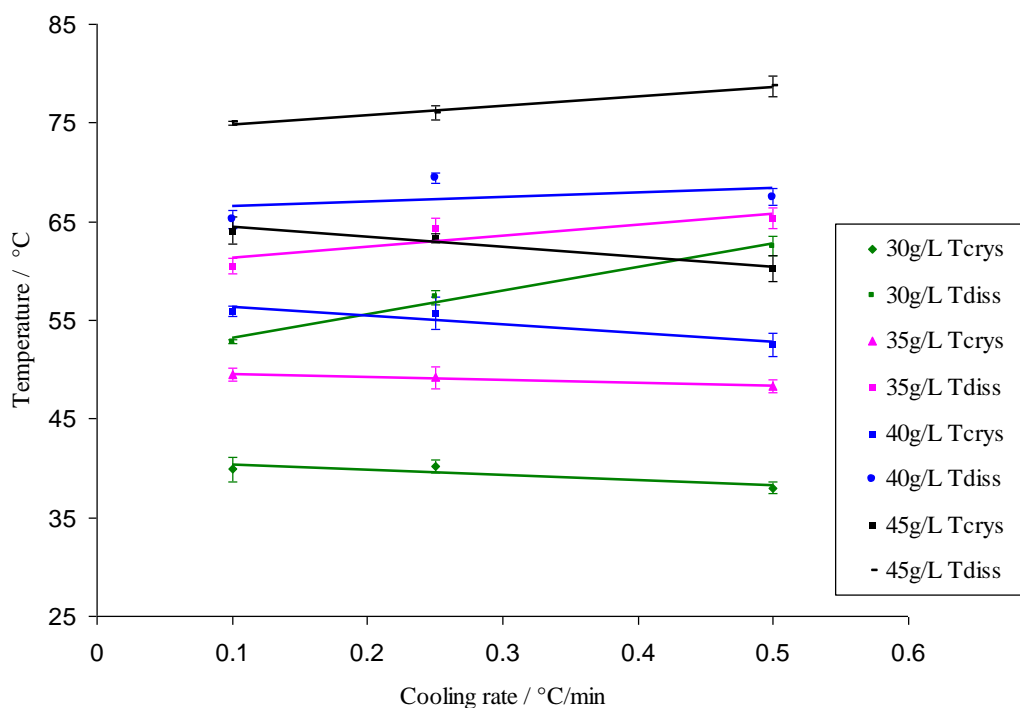
Figure 5.7: Averaged crystallization and dissolution temperatures for four LGA solution concentrations in 25W ultrasound field

73

Figure 5.8 depicts the variation of the solubility and supersolubility curves of LGA aqueous solution under different experimental conditions. It can be seen that the presence of ultrasound did not change the dissolution temperature of LGA as the solubility of the three experimental conditions were kept at the same level. Whereas, the fairly narrow MSZW of 15W and 25W ultrasound irradiation system suggests that the ultrasound-assisted crystallization system required a lower supersaturation and less driving force for nucleation to occur. It also implies that power ultrasound allows enhanced nucleation over a narrower temperature range and results in relatively reduced control of the crystallization system. Therefore, the advantage of ultrasound is that it can induce primary nucleation to the process where spontaneous nucleation cannot occur. The ultrasonic technology employed in crystallization can effectively prevent the impurities being imported since the seeding in conventional industrial crystallization operations can be simply replaced.
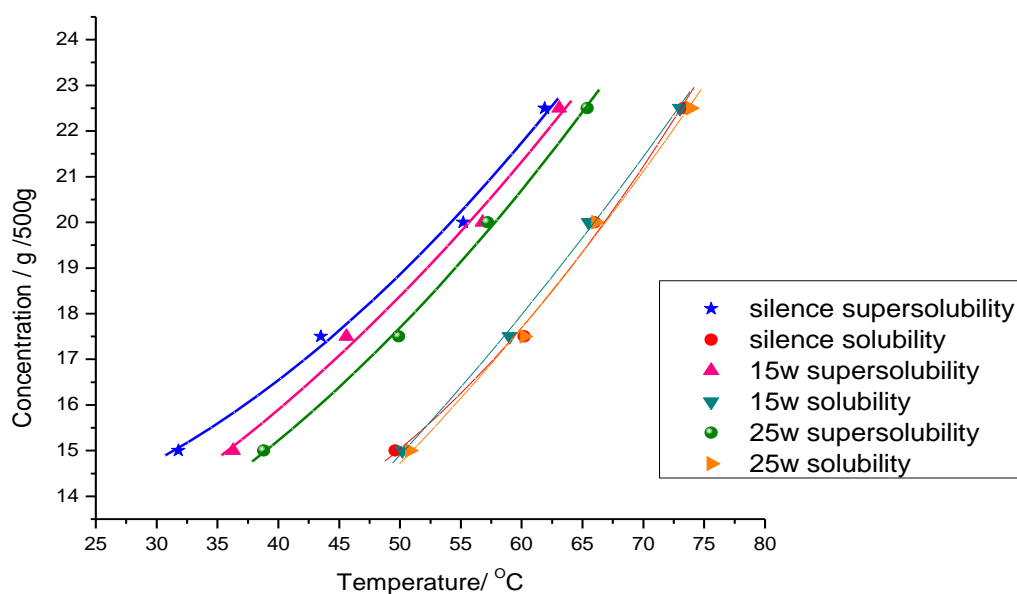
Figure 5.8: Solubility and supersolubility curve of LGA aqueous solution in silent condition, 15W ultrasound field and 25W ultrasound field

5.3.1.4 Calculation of Nucleation Order and Nucleation Rate

Based on Nyvlt's analysis of the data, explained in detail in Chapter 2, the nucleation order, m and the nucleation constant, k_m can be determined by plotting the log (cooling rate, b) against the log (MSZW) for each concentration.

Figure 5.9 shows the plot of log (b) versus log (MSZW) along with the equations for the line of best fit under silent conditions for four solution concentrations. The resulting linear regression line was used to determine the order of nucleation, from the slope, and the nucleation constant, from the intercept according to Equation (2.19). The logarithmic data obtained under 15W and 25W ultrasound irradiation are shown in Figures 5.10 and 5.11. The R^2 of the best fit is the determination coefficient that describes how well the data collected fits to represent the accuracy of the nucleation order and constant. The closer the value is to 1, the better the fit and the more reproducible the system is.
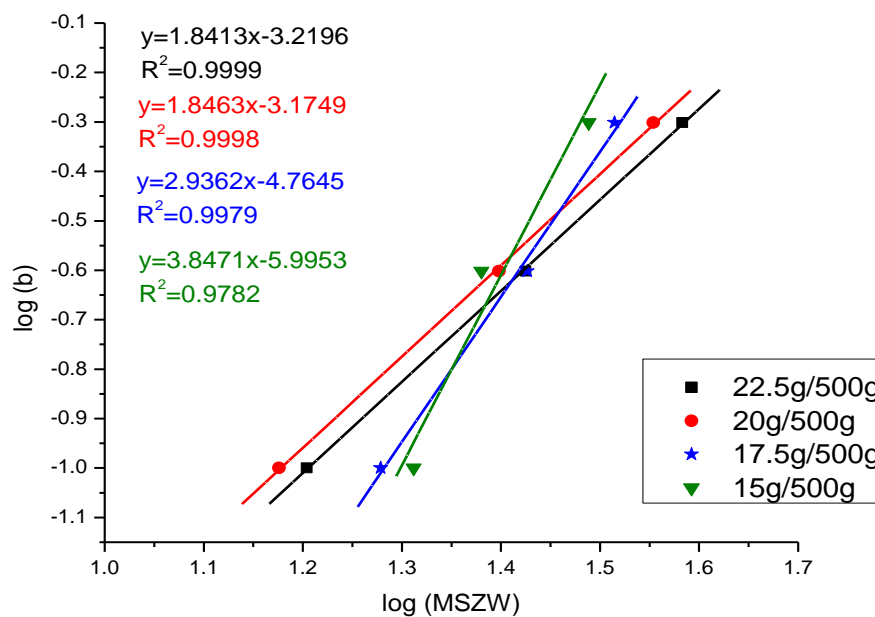
Figure 5.9: Plot of log (b) versus log (MSZW) for four solution concentrations produced under silent condition
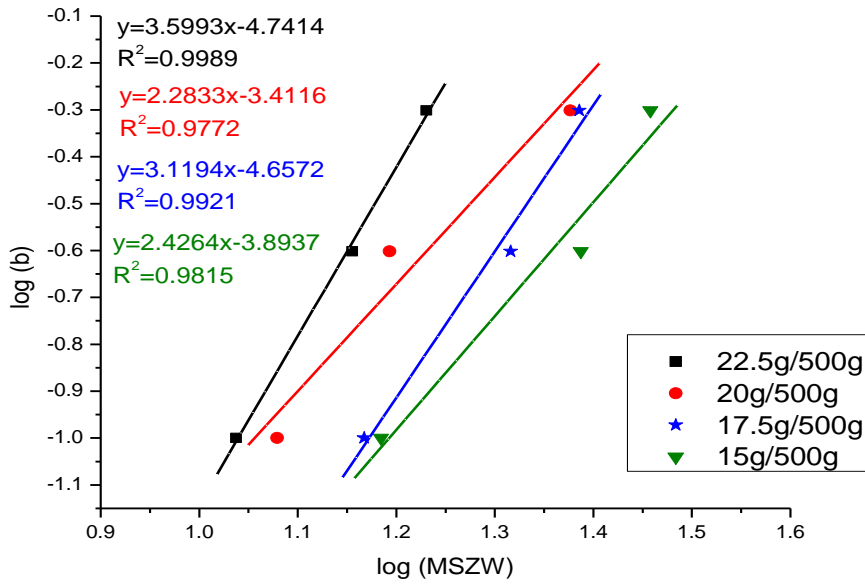
Figure 5.10: Plot of log (b) versus log (MSZW) for four solution concentrations produced under 15W ultrasound irradiation
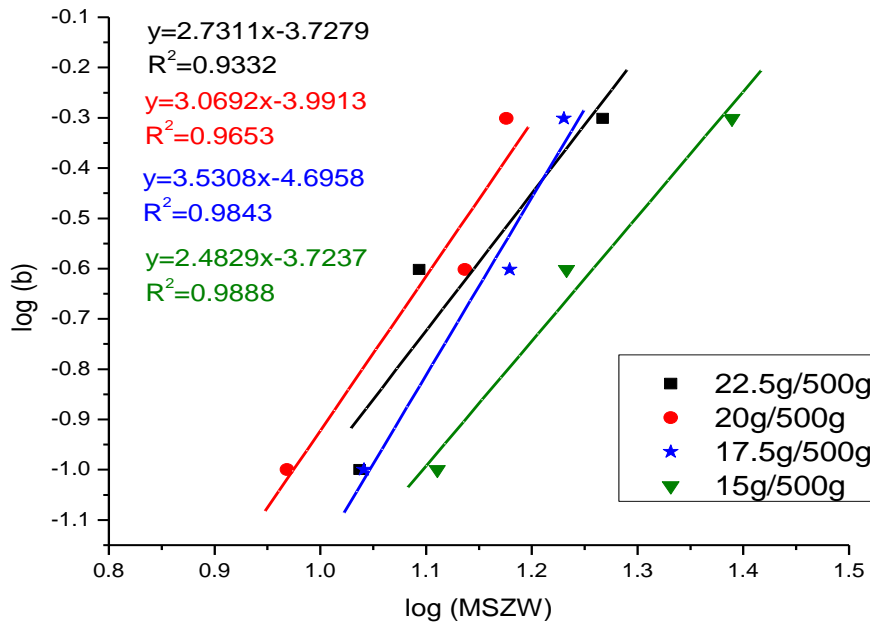
Figure 5.11: Plot of log (b) versus log (MSZW) for four solution concentrations produced under 25W ultrasound irradiation

From Figure 5.9, the nucleation order, m for 45g/L, 40g/L, 35g/L and 30g/L LGA solution in silent environment are 1.8413, 1.8463, 2.9362 and 3.8470, while the calculated nucleation constants, k_m are 1.24×10^{-3}, 2.59×10^{-4}, 1.68×10^{-4} and 8.06×10^{-4}, respectively. According to the nucleation rate expression of Equation (2.15), the

nucleation rate of above concentration solutions in silence are found to be 1.43×10^{-2}/m^{3}s, 2.76×10^{-3}/m^{3}s, 1.13×10^{-2}/m^{3}s and 1.21×10^{-2}/m^{3}s, respectively.

The calculated nucleation order, nucleation constant and nucleation rate of different concentration solutions under silent condition, 15W and 25W power ultrasound irradiation are listed in Table 5.4.

Table 5.4: The summary of calculated nucleation order, nucleation constant and nucleation rate under silent condition, 15W and 25W ultrasound irradiation

Experimental condition	Solution Concentration C/ g/L	Nucleation order m	Nucleation constant k_m	Maximum allowable supersaturation ΔC_{max} / °C	Nucleation Rate J /m^{3}s^{-1}
in silence	45	1.8413	1.24E-3	3.78	1.43E-2
	40	1.8463	2.59E-4	3.60	2.76E-3
	35	2.9362	1.68E-4	4.18	1.13E-2
	30	3.8470	8.06E-5	3.67	1.21E-2
15W ultrasound	45	3.5993	1.37E-3	3.34	2.15E-2
	40	2.2833	2.86E-4	3.14	1.69E-2
	35	3.1194	2.44E-4	3.51	1.22E-2
	30	2.4264	7.54E-4	3.43	1.50E-2
25W ultrasound	45	2.7311	1.53E-3	3.24	3.79E-2
	40	3.0692	9.03E-4	2.77	2.06E-2
	35	3.5308	3.56E-4	3.24	2.25E-2
	30	2.4829	1.26E-3	2.89	1.76E-2

The nucleation order is a fundamental physical parameter of a crystallization system that describes the dependence of the MSZW on the cooling rate under given process conditions. However, this is just an apparent order because it associates with the unknown crystal growth and is therefore not the true nucleation order. It can be seen from the calculated results that the value of the apparent nucleation order is relatively small, which suggests that the nucleation rate is greater than the supersaturation generation and the MSZW is cooling rate independent. In other words, the MSZW is controlled by the kinetics of nucleation. For all the examined concentrations, the apparent nucleation order and the nucleation constant both increased when ultrasound irradiation was applied and hence resulted in the greater nucleation rate. The result is consistent with the previous study of ultrasound effects on nucleation (Guo et al., 2006b) and suggests a diffusion controlled mechanism. Furthermore, Nývlt's work

pointed out that the nucleation order depended on neither the presence/absence of the solid phase, nor on the temperature. Its value reflected the molecular weight of crystallizing substance and is approximately inversely proportional to the number of particles required to form a critical nucleus (Nývlt, 1968). Therefore, the higher value of nucleation orders in the ultrasound field was suggestive of a smaller energy barrier for nucleation.

5.3.2 Induction Time Studies

Rapid cool studies were conducted at the same solution concentrations to examine the induction time and hence evaluate the interfacial tension and critical nucleus size for identical systems.

5.3.2.1 Induction Time Measurement

Once the MSZW was determined, three bottom temperatures within the metastable zone were selected for the crash cool study. The bottom temperatures that were set for induction time measurement for different concentrations of solution were:

➢ 30g/L: 41°C, 43°C, 45°C
➢ 35g/L: 43°C, 45°C, 47°C
➢ 40g/L: 50°C, 52°C, 54°C
➢ 45g/L: 58°C, 60°C, 62°C

Figures 5.12 to 5.14 display the typical induction time measurement data for different operating systems of 30g/L LGA solution at bottom temperatures of 41°C, 43°C and 45°C. It can be seen that the turbidity readings at the early stage of the experiments were increased indicating the initial dissolution of chemicals during the pre-heating stage. The readings then remained constant for a considerable duration and eventually reduced dramatically, which implied the appearance of crystals. Induction time is counting from the moment when the bottom temperature is reached and stays stable until the first detectable crystals appear.
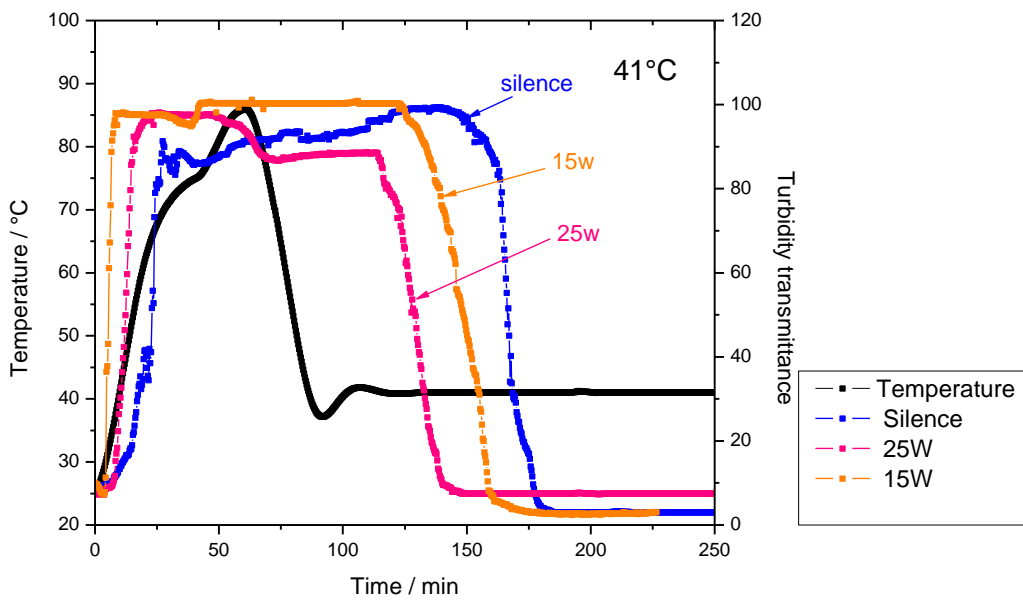
Figure 5.12: Induction time measurements for 30g/L l-glutamic acid solution at a bottom temperature of 41°C
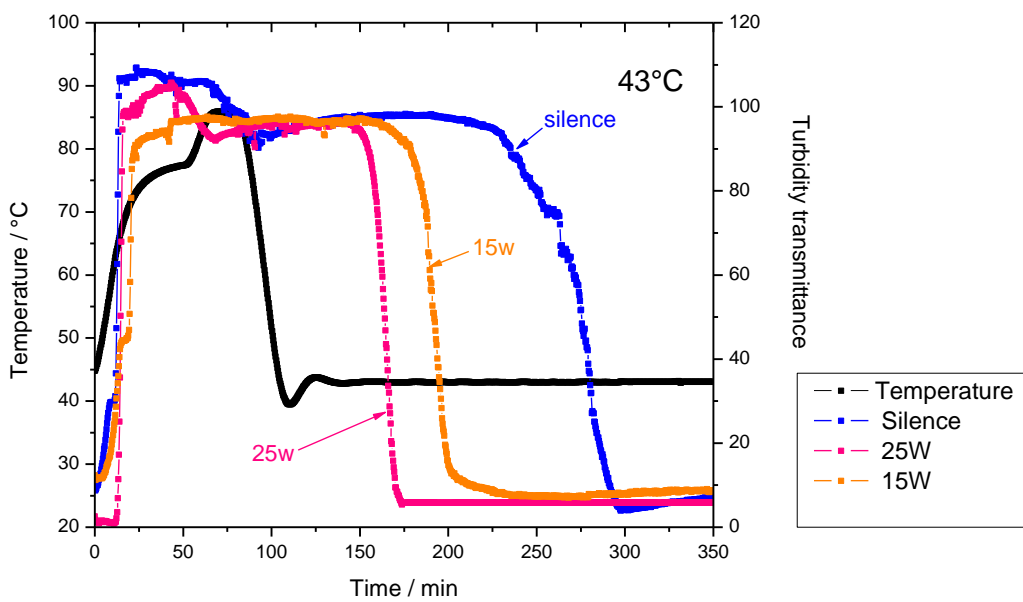
Figure 5.13: Induction time measurements for 30g/L l-glutamic acid solution at a bottom temperature of 43°C
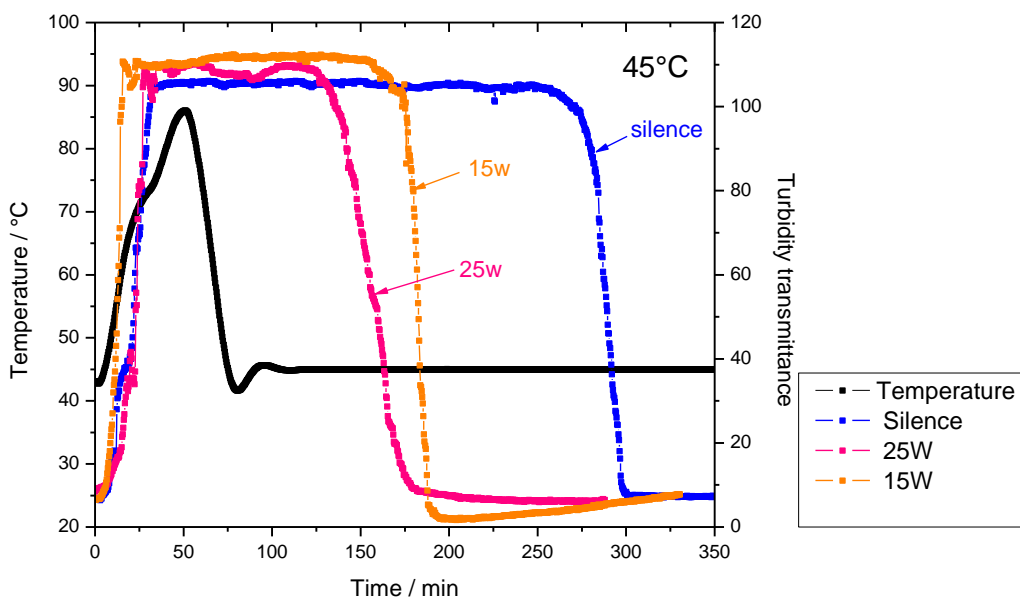
Figure 5.14: Induction time measurements for 30g/L l-glutamic acid solution at a bottom temperature of 45°C

Thus, according to the variation of turbidity readings during the cooling process shown in Figure 5.12, the induction times of 30g/L LGA solution in the absence and the presence of 15W and 25W ultrasound were found to be approximately 56 mins, 20 mins and 8 mins at 41°C, respectively. All the induction times obtained at different bottom temperatures are listed in Table 5.5. Under the same experimental conditions, the higher bottom temperature associated with the lower supersaturation and smaller concentration driving force, as expected, led to the overall longer induction time. It can be seen clearly from the curve that the nucleation induction time was significantly shorten at all the bottom temperatures where ultrasound irradiation was present, and the induction time was reduced with increasing the ultrasound power. This result also agrees with the reported effect of power ultrasound on nucleation kinetics (Luque de Castro and Priego-Capote, 2007, Guo et al., 2006b).

Table 5.5: The summary of recorded induction time

C g/L	Bottom Temperature °C	Induction time min			Averaged induction time min					
		silent	15w	25w	silent	STDEV	15w	STDEV	25w	STDEV
30	41	53, 56, 57	17, 20, 18	7, 8, 8	55	2.082	18	1.527	8	0.577
	43	86, 89, 94	45, 48, 43	24, 23, 26	90	4.041	45	2.517	24	1.528
	45	194, 198, 207	72, 67, 68	29, 31, 30	200	6.658	69	2.646	30	1.000
35	43	23, 19, 17	11, 12, 13	9, 8, 9	20	3.055	12	1.000	9	0.577
	45	26, 22, 26	18, 15, 13	13, 13, 11	25	2.039	15	2.517	12	1.155
	47	46, 48, 42	24, 23, 26	15, 17, 17	45	3.055	24	1.528	16	1.155
40	50	14, 11, 13	7, 7, 8	5, 4, 6	13	1.528	7	0.577	5	1.000
	52	29, 30, 33	12, 14, 15	10, 9, 9	31	2.817	14	1.578	9	0.577
	54	34, 38, 37	19, 21, 18	11, 12, 14	36	2.817	19	1.578	12	1.528
45	58	16, 17, 20	12, 11, 10	8, 9, 7	18	2.082	11	1.000	8	1.000
	60	36, 39, 39	15, 12, 16	11, 10, 10	38	1.732	14	2.082	10	0.577
	62	73, 69, 75	36, 35, 39	18, 19, 22	72	3.055	37	2.082	20	2.082

5.3.2.2 Evaluation of Interfacial Tension and Critical Nucleus Radius

Based on the assumption that the crash cool crystallization performed the homogenous nucleation, the interfacial tension can be calculated according to Equations (2.11) and (2.21) which describes the inversely proportional relationship of induction time and homogenous nucleation rate. By plotting log (t_{ind}) at different bottom temperatures against $1/T^3(\log S)^2$, a straight line will result with a slope of A' that written as:

$$A' = \frac{16\gamma^3 v_c{}^2}{3k_B{}^3} \tag{5.1}$$

where k is the Boltzmann constant of value of 1.3805×10^{-23} J/K and v_c is the molecular volume of the LGA crystal, which can be calculated from its molecular weight and solid density by:

$$v_c = \frac{M}{\rho_c \times N_A} \tag{5.2}$$

with the density ρ of 1560 kg/m³, the molecular weight of 147.13 g/mol and Avogadro's number of 6.02×10^{23}, the LGA molar volume was found to be 1.56×10^{-28} m³. The interfacial tension γ can be determined from the given gradient.
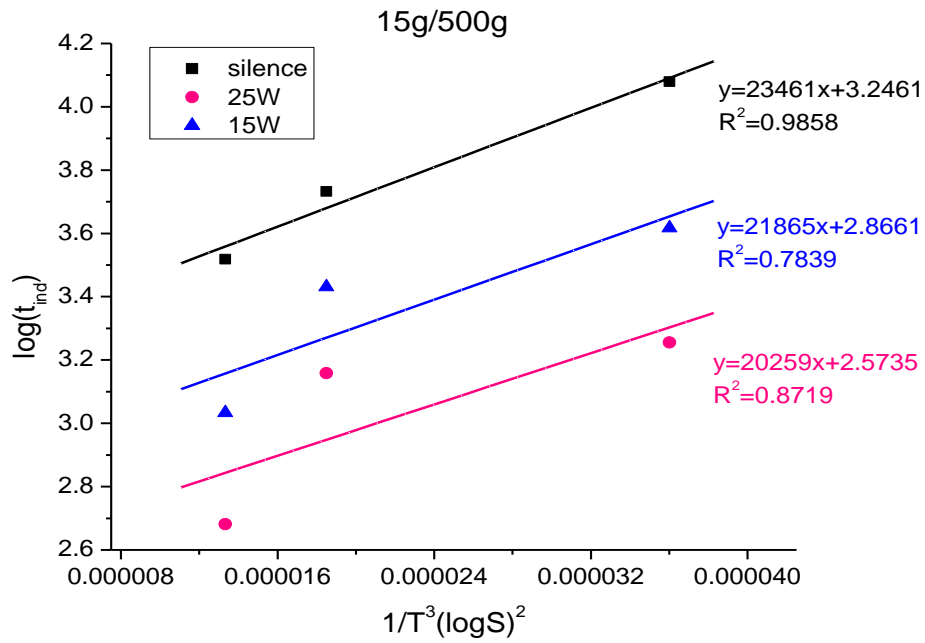
Figure 5.15: Plot of log(tind) against 1/ T3(logS)2 of 30g/L LGA solution in silent, 15W ultrasound and 25W ultrasound conditions
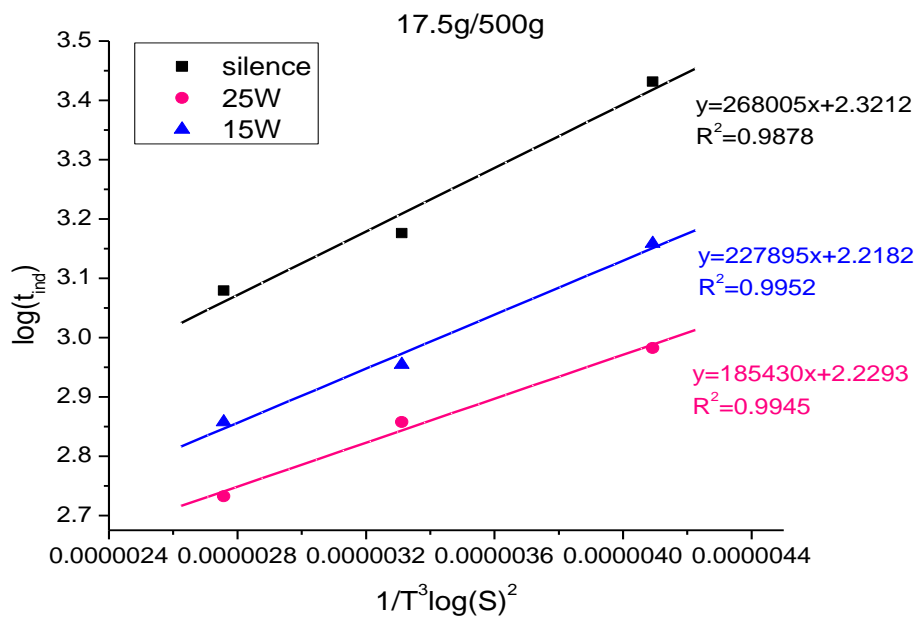
Figure 5.16: Plot of log(tind) against 1/ T3(logS)2 of 35g/L LGA solution in silent, 15W ultrasound and 25W ultrasound conditions

82
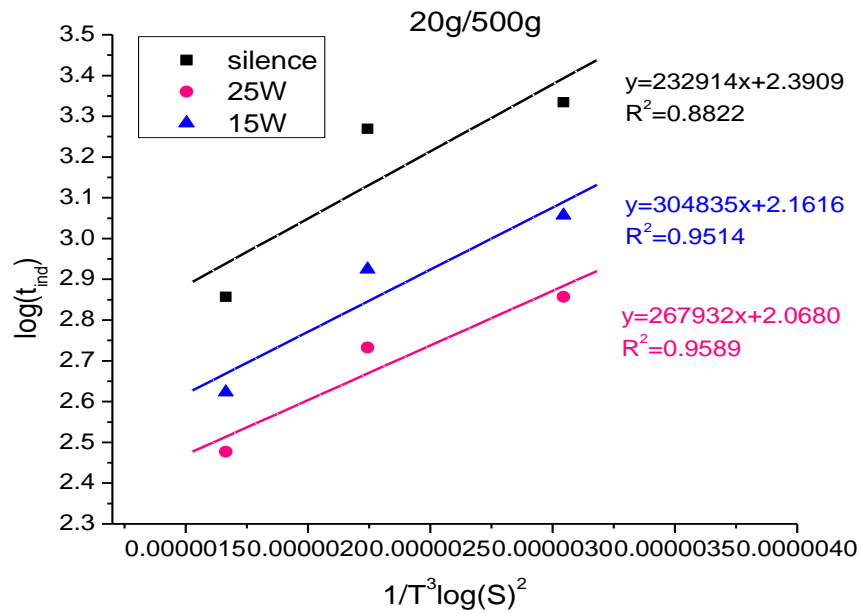
Figure 5.17: Plot of log(tind) against 1/ T3(logS)2 of 40g/L LGA solution in silent, 15W ultrasound and 25W ultrasound conditions
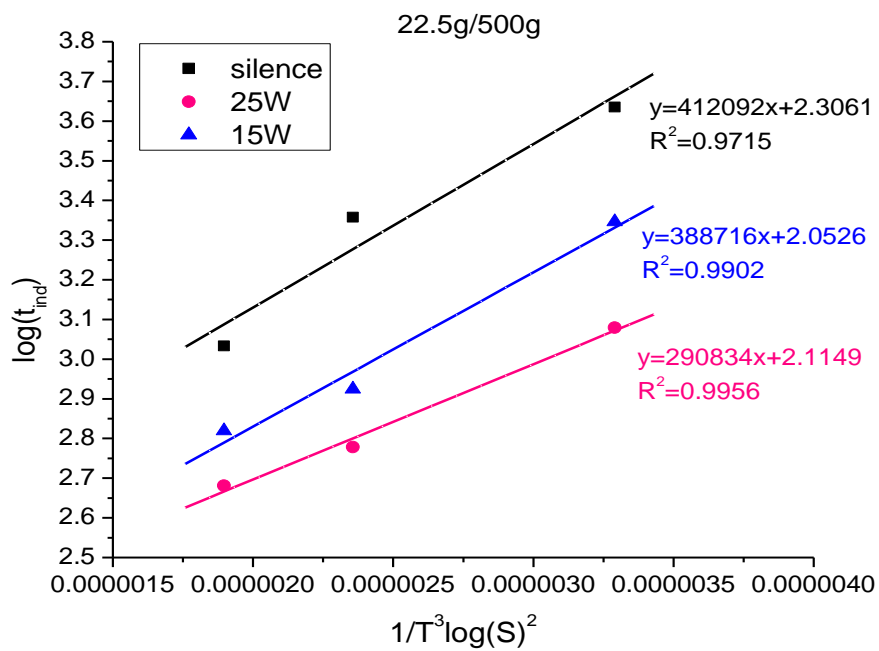
Figure 5.18: Plot of log(tind) against 1/ T3(logS)2 of 45g/L LGA solution in silent, 15W ultrasound and 25W ultrasound conditions

Figure 5.15 shows the plots of log (t_{ind}) versus 1/ $T^3(\log S)^2$ of 30g/L LGA solution in various experimental conditions, where the interfacial tension was determined to be 1.79×10^{-3} J/m^2, 1.74×10^{-3} J/m^2 and 1.70×10^{-3} J/m^2 from the slope of the regression lines used to fit data points for experimental conditions without ultrasound, with 15W and 25W ultrasound irradiation, respectively. The plots of log (t_{ind}) versus 1/ $T^3(\log S)^2$ for other concentrations were displayed in Figures 5.16 to 5.18.

The interfacial tension values determined were then used to calculate the critical nucleus radius, r_c, through the application of Equation (2.22), which assumes that the spherical shape particles are produced. The supersaturation of 30g/L LGA aqueous solution at 41°C, 43°C and 45°C are obtained from previous solubility and supersolubility curves, and hence the critical nucleus radius were calculated to be 11.37Å, 13.43Å and 17.99Å.
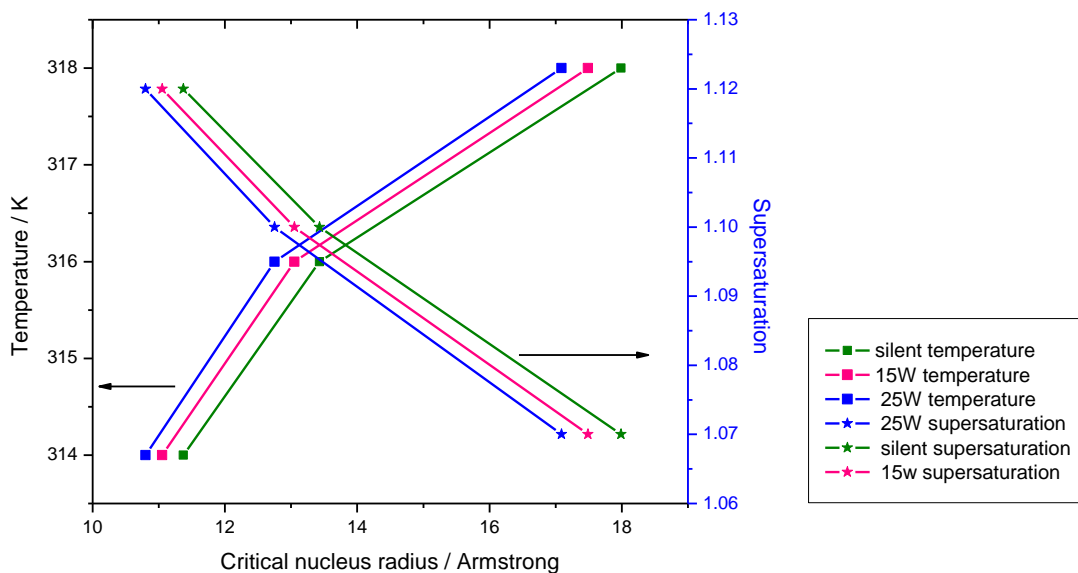
Figure 5.19: The effect of temperature and supersaturations on the critical nucleus radius of 30g/L LGA solution

Figure 5.19 depicts the effect of temperature and supersaturation levels on the size of the critical nucleus for different operating conditions of 30g/L solution. The dependence of the critical nucleus radius on supersaturation and temperature suggests that the size of the critical nucleus decreases for decreasing crystallization temperatures and increasing the supersaturation, which authenticates the classical nucleation theory. At the same temperature and supersaturation level, the size of critical nucleus also decreases as the higher ultrasound power is applied.

The subsequent number of molecules that exist in the critical nucleus, $N*$, can be determined by:

$$N* = \frac{4\pi(r_c)^3}{3v_c}$$ (5.3)

The summary of the measured induction time, the calculated interfacial tension, critical nucleus radius and the number of molecules in the critical nucleus are listed in Table 5.6.

It can be concluded that ultrasound irradiation significantly reduced the induction time, and the ultrasound effect was increased with increasing the ultrasound power. It is worth noting that this ultrasound effect was particularly evident at low supersaturation levels. Taking 30g/L solution at supersaturation of 1.07 for instance, the induction time was 200 mins in the absence of ultrasound while it reduced to only 30 mins in the presence of 25w ultrasound. The interfacial tension and the critical nucleus size are the important characterized parameters to describe the system energy. The calculation results revealed that the interfacial tension and the critical nucleus size are decreased when power ultrasound is present. Additionally, the higher the irradiation power, the smaller the interfacial tension and the critical nucleus size. This can be explained by the postulate that power ultrasound irradiation sufficiently reduces the energy barrier to allow nucleation to occur readily.

Possible reasons for the power ultrasound effect on nucleation are: 1) cavitation phenomenon results in extreme excitation which can greatly improve the nucleation rate or induce the primary nucleation; 2) the presence of cavitation bubbles reduces the solid-liquid surface energy and makes nucleation occur more easily; 3) cavitation bubbles themselves could be acting as nuclei for crystal growth. Based on the idea that the concentrated energy released due to the transient bubble collapse was the cause of power ultrasound effect on crystallization behaviour, an attempt to correlate the cavitation and nucleation was presented in Chapter 6.

Table 5.6: The summary of induction time, interfacial tension, critical nucleus radius and number of molecules in critical nucleus of L-glutamic acid in silence, 15W ultrasound and 25W ultrasound conditions

C	Bottom Temp	S	Induction time t_{ind} / min			Interfacial tension γ / J/m^3			Critical nucleus radius r_c / Å			Number of molecules in critical nucleus N^*		
g/L	T / °C		silence	15w	25w	silence	15w	25w	silence	15w	25w	silence	15w	25w
	41	1.12	55	18	8				11.4	11.1	10.8	39	36	34
30	43	1.10	90	45	24	1.79E-3	1.74E-3	1.70E-3	13.4	13.1	12.8	65	60	56
	45	1.07	200	69	30				18.0	17.5	17.1	156	144	134
	43	1.28	20	12	9				11.6	11.0	10.3	42	36	29
35	45	1.25	25	15	12	4.02E-3	3.81E-3	3.56E-3	12.8	12.2	11.4	56	49	40
	47	1.22	45	24	16				14.3	13.5	12.6	78	66	54
	50	1.36	13	7	5				9.83	9.58	9.16	25	24	21
40	52	1.30	31	14	9	4.31E-3	4.20E-3	4.02E-3	11.4	11.1	10.7	40	37	33
	54	1.25	36	19	14				13.3	13.0	12.4	63	59	51
	58	1.32	18	11	8				11.4	11.2	10.2	40	38	28
45	60	1.28	38	14	10	4.64E-3	4.55E-3	4.13E-3	12.8	12.5	11.4	56	53	39
	62	1.23	72	37	20				15.1	14.8	13.5	93	86	65

5.3.3 L-Glutamic Acid Polymorphic Form Identification

5.3.3.1 Cooling Rate Effect on Polymorphism

The polymorphic form obtained from crystallization is determined by the polymorphic transformation process that mainly occurs at the nucleation stage. The powder x-ray diffraction analysis (PXRD) results of final products crystallized from different concentration solutions with cooling rates are shown in Figures 5.20 to 5.22. The pure α-form and β-form LGA PXRD patterns are also presented in each figure according to the PXRD ICDD cards, 00-041-1715 and 00-032-1701, respectively. Those peaks at 2θ=18.2°, 23.7°,26.6° and 33.2° are characteristic of α-form LGA, and the peaks at 2θ=20.5°, 21.9°,29.9° and 37.9° are characteristic of β-form LGA. Noting that the PXRD profiles displayed in this work have been re-scaled for better visual clarity and by comparing the characteristic peaks, each polymorphic form can be readily distinguished. The results show that, pure β-form was produced when 0.1°C/min cooling rate was used for all the four solution concentrations. Increasing the cooling rate to 0.25°C/min, the LGA crystals produced were found to be α-form and β-form mixed. With a cooling rate of 0.5°C/min, pure α-form was isolated with solution concentrations of 30g/L, 35g/L and 40g/L, but both α-form and β-form crystals were observed with 45g/ L concentration.
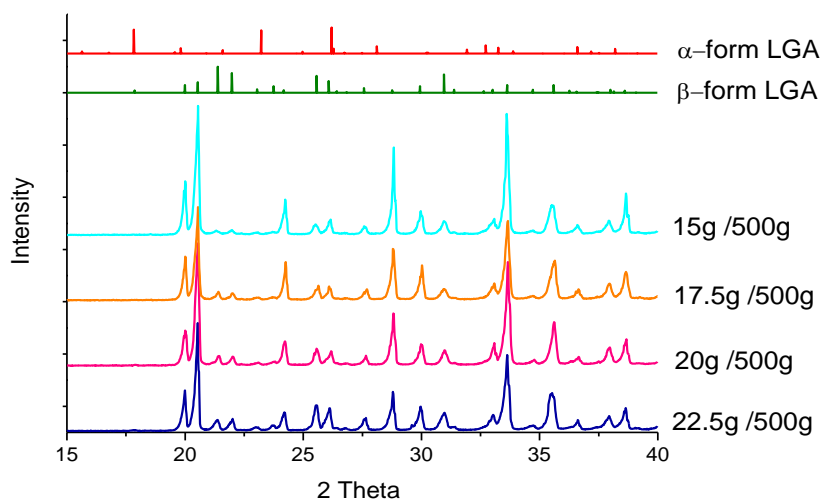
Figure 5.20: Powder X-ray diffraction profiles of LGA final slurry cooling at 0.1°C/min
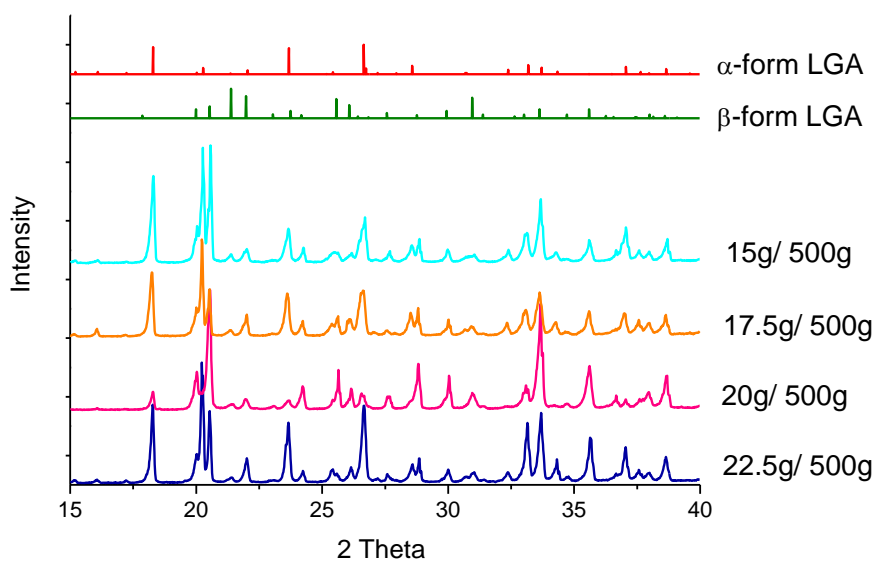
Figure 5.21: Powder X-ray diffraction profiles of LGA final slurry cooling at 0.25°C/min
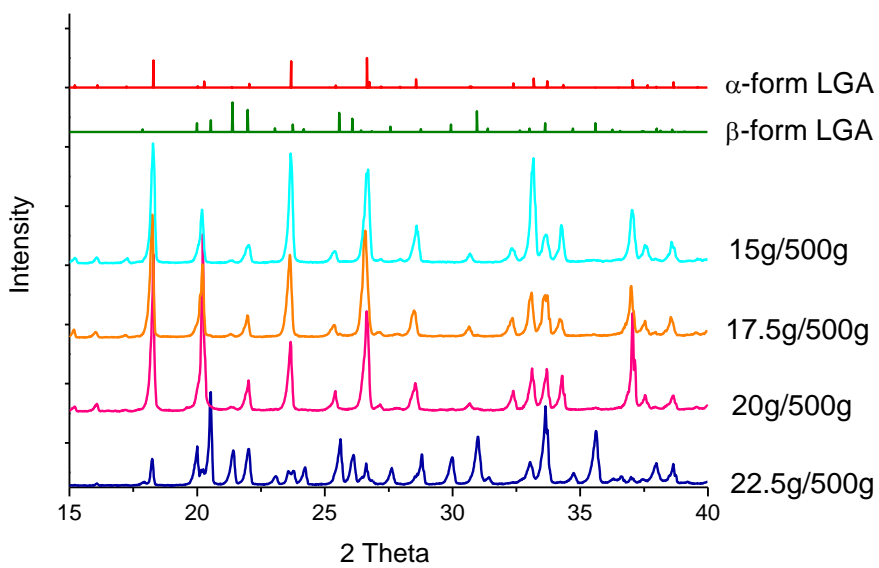
Figure 5.22: Powder X-ray diffraction profiles of LGA final slurry cooling with 0.5°C/min

Table 5.7: Polymorphism of l-glutamic acid crystals with various cooling rates at 10°C

Concentration g/ L	Cooling rate of 0.5°C/min	Cooling rate of 0.25°C/min	Cooling rate of 0.1°C/min
45	α+β	α+β	β
40	α	α+β	β
35	α	α+β	β
30	α	α+β	β

Table 5.7 summaries the polymorphic form generated from different concentration solutions at various cooling rates at final bottom temperature of 10°C. In summary, the cooling rate does influence the polymorphic formation of LGA: the slow cooling rate results in the pure stable β-form, while the fast cooling rate leads to the crystallization of the metastable α-form; both the α-form and the β-form are present at the medium cooling rate. These results contradict the finding of Ni et al. (Ni et al., 2004) but agree with the other works of the cooling rate effect on LGA polymorphism (Kitamura, 1989, Mougin et al., 2002, Liang et al., 2003). Otwald's step rule states that the least metastable form with the highest solubility should come out first due to the low energy barrier during the crystallization process and then transform to the stable form. Therefore, the metastable α-form of LGA should appear first and is followed by the transformation of α-form to the stable β-form. However, the sufficient long transformation time is requested. The reason that only the metastable α-form was produced at fast cooling rate of 0.5°C/min can be explained as there is no time for the metastable α-form to transform to the stable β-form. In order to examine whether or not the ultrasound irradiation can modify the formation of LGA polymorphic form, the moderate cooling rate of 0.25°C/min was chosen and the crystallization processes were treated with different level of ultrasonic power. The PXRD analysis of the crystal produced is shown in Figures 5.23 to 5.26.
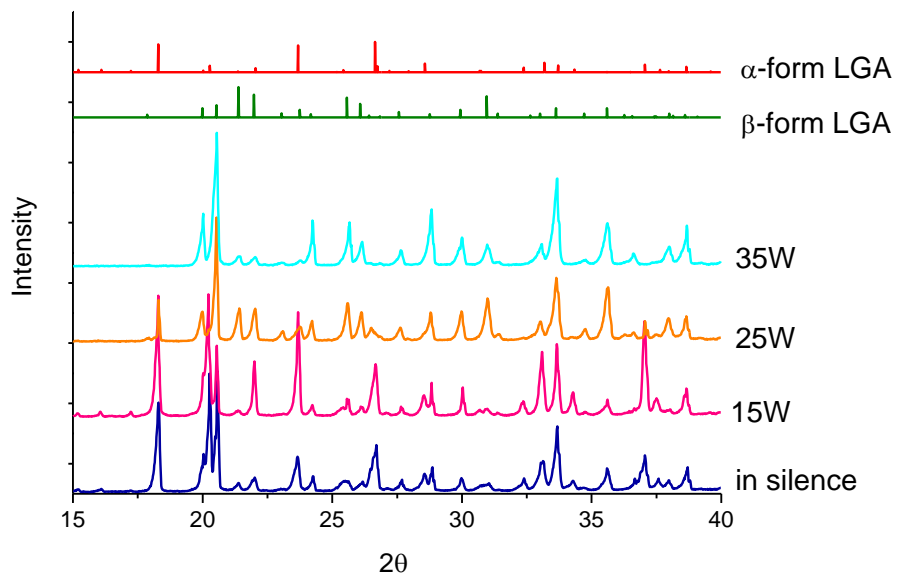
Figure 5.23: Ultrasound irradiation effect on LGA polymorphisms generated from a concentration of 30g/L, cooling rate of 0.25°C/min
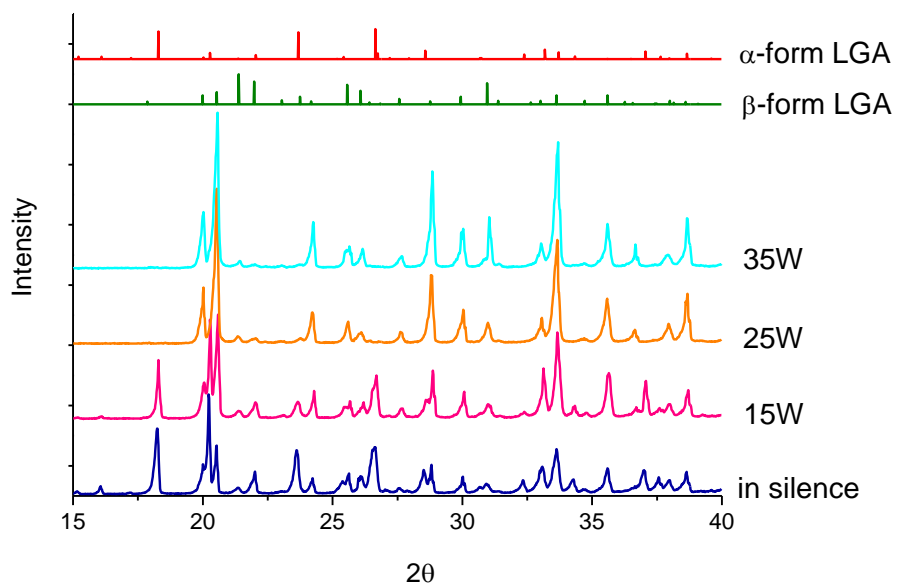
Figure 5.24: Ultrasound irradiation effect on LGA polymorphisms generated from a concentration of 35g/ L, cooling rate of 0.25°C/min
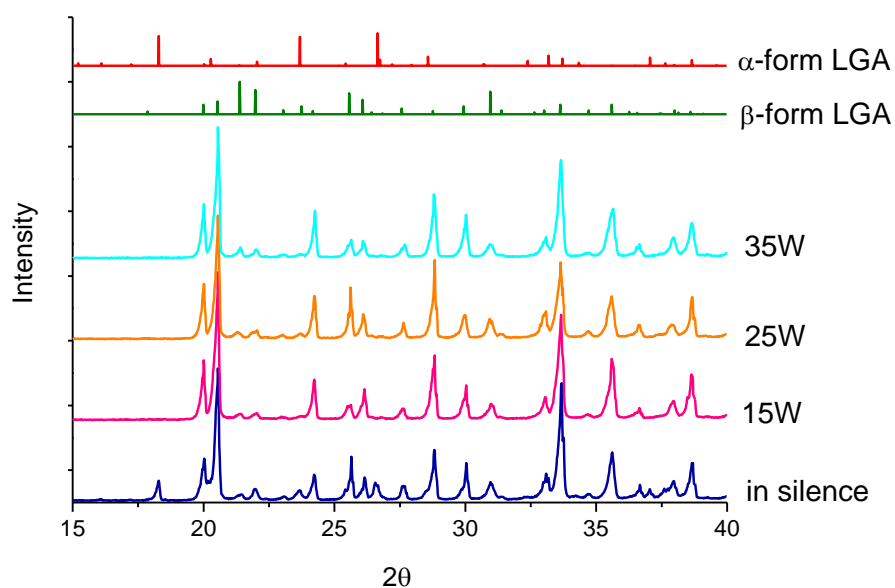
Figure 5.25: Ultrasound irradiation effect on LGA polymorphisms generated from a concentration of 40g/ L, cooling rate of 0.25°C/min
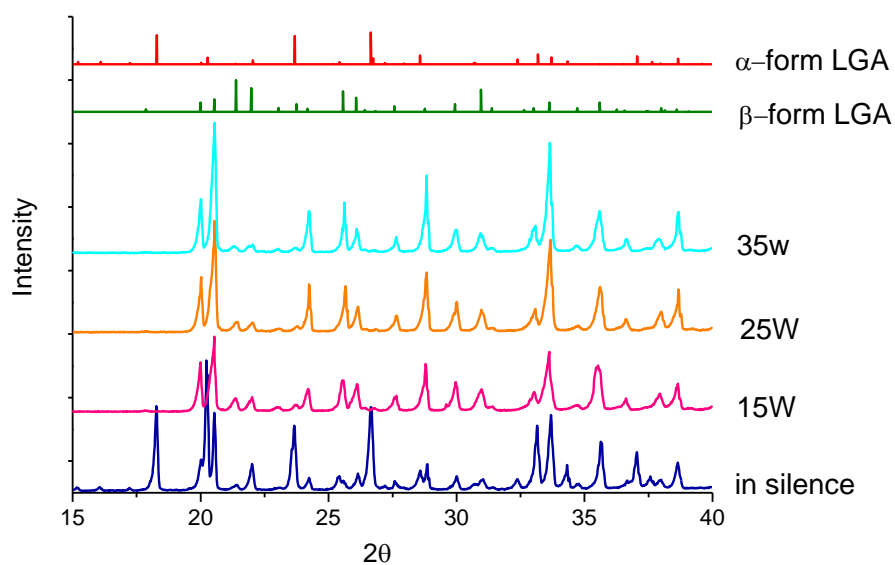
Figure 5.26: Ultrasound irradiation effect on LGA polymorphisms generated from a concentration of 45g/ L, cooling rate of 0.25°C/min

As can be seen from Figure 5.23, the specific peaks of α-form at 2θ=18.6° and 23.7° are disappeared when 35W ultrasound was applied, which indicates that the metastable α-form has completely transformed to the stable β-form. However, with

lower ultrasound treatment, 15W and 25W, the final slurry LGA polymorphisms with the moderate cooling rate are still the same as in the silent condition, found to be α-form and β-form mixed. The full transformation of the metastable α-form to the stable β-form was observed in presence of 25W and 35W ultrasound for concentration of35g/L , as shown in Figure 5.24. For the higher concentration solutions, 40g/L and 45g/L, the stable β-form was obtained exclusively for all the sonication conditions. Considering the PXRD analysis, the polymorphs of LGA with different ultrasound irradiation are summarized in Table 5.8. Clearly, power ultrasound irradiation favours the precipitation of the β-form suggesting the fact that ultrasound has an impact on LGA polymorphism. It can be also found that pure stable β-form can be easily obtained by applying high power of ultrasound. Moreover, for relatively high concentration solutions, the ultrasound power required to generate the stable polymorph is lower, only 15w in the current work for 40g/L and above. It is possibly attributed to the concentration effect on polymorph generation. According to the study of LGA carried out by Ni et al., the solution concentration played a significant role in crystal morphology: metastable α-form crystals were preferred at low to medium concentration, while stable β-form crystals were preferred at high concentration (Ni and Liao, 2008).

Table 5.8: Ultrasound effect on formation of LGA polymorphs

Ultrasound power	30g/L	35g/L	40g/L	45g/L
0 (in silence)	α+β	α+β	α+β	α+β
15W	α+β	α+β	β	β
25W	α+β	β	β	β
35W	β	β	β	β

5.3.3. 2 Crystallization Temperature Effect on Polymorphism

Besides the solution concentration and cooling rate, the crystallization temperature is another factor that determines the crystal polymorphism. At the same supersaturation of 1.3 without application of power ultrasound, the PXRD profile of LGA crystallized from different temperatures from 50°C to 20°C is shown in Figure 5.27. The only nucleated polymorph at 25°C and 20°C was the metastable α-form, implying that no α- to β-transformation occurred during the crystallization as the LGA polymorphic transformation was irreversible. The characteristic β peaks at 2θ=21.9° and 29.9° manifest the transformation of α- to β-form at crystallization temperatures of 40°C and 30°C but obviously, the transformation was not complete because the specific α-form peaks were still observed. At the higher crystallization temperature of 50°C, the isolation polymorphic form was found to be the stable β-form. These experimental results suggest that crystallization temperature has a remarkable effect on LGA polymorph formation: low crystallization temperature favours the precipitation of the metastable α-form while the stable β-form is favoured over the high crystallization temperature ranges. This reveals the findings reported by Kitamura who pointed out that full dissolution of α-form and transformation took place well above 45°C but below the crystallization temperature of 25°C, the transformation rate was very slow that only the preformed α-form persisted (Kitamura, 1989).
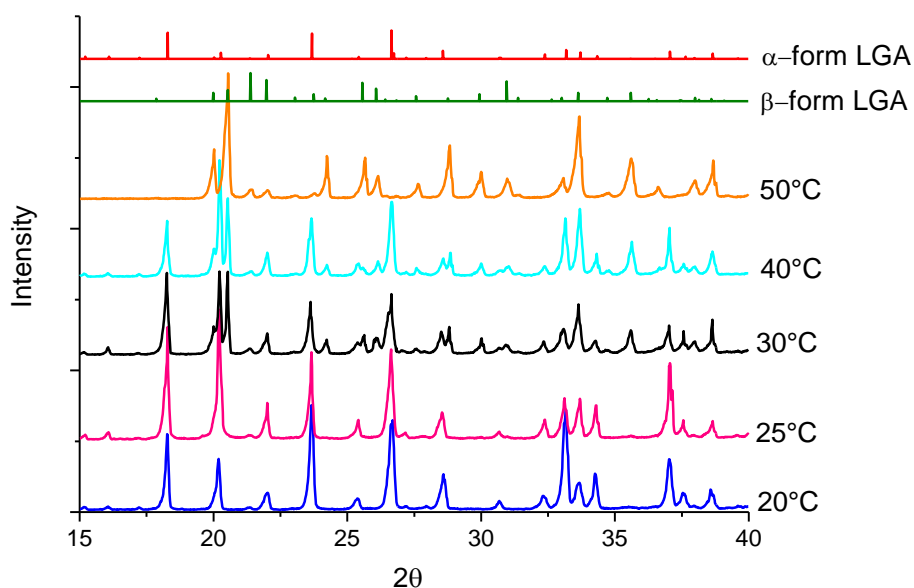
Figure 5.27: Power x-ray diffraction patterns of LGA crystallized from different temperatures

The PXRD pattern, presented in Figures 5.28 to 5.31, illustrated the potential effect of ultrasound on LGA polymorphism under different crystallization temperature conditions. Conforming to the pure α- and β-LGA PXRD profile, no β-form was observed in the absence of ultrasound and α-form LGA was the only polymorphic form isolated at 20°C (Figure 5.28). Experiments performed yielded pure metastable α-form with the application of 15W power ultrasound. If the ultrasound power was boosted up to 25W and 35W, the appearance of the specific β-form peaks indicated the transformation of α-form to β-form. Similar results were found at 25°C crystallization temperature, see Figure 5.29: polymorphic transformation occurred with 15W and 25W ultrasound irradiation and the particles produced were the admixture of both forms. When the ultrasound power is high enough (35W), the process was allowed to produce pure stable β-form which could not be observed at such a low temperature in the absence of ultrasound. Therefore, presumably, it is also possible to produce pure β-form with the help of power ultrasound irradiation at the higher temperature regions of 30°C and 40°C. Figures 5.30 and 5.31 indicate the conjecture, 25W ultrasound irradiation resulted in the full transformation of α-form LGA and hence the production of pure β-form at 30°C, while 15W ultrasound was

sufficient at 40°C crystallization temperature.
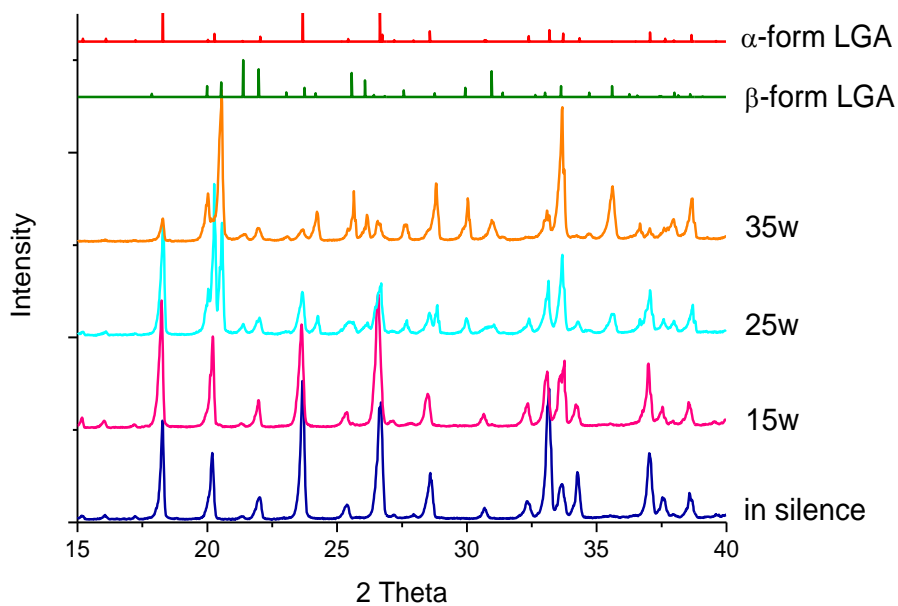
Figure 5.28: Power x-ray diffraction profile of LGA crystallized at 20°C using different ultrasound powers
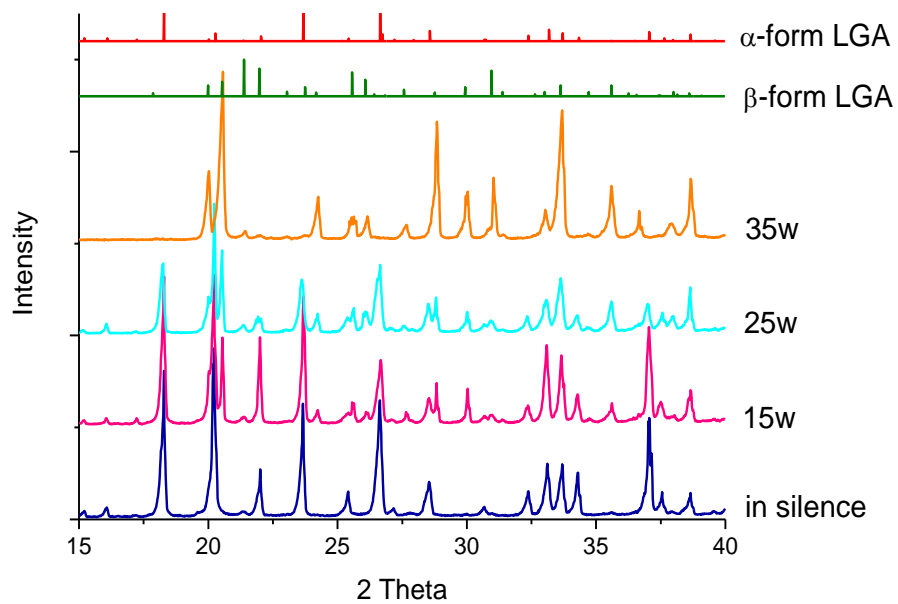
Figure 5.29: Power x-ray diffraction profile of LGA crystallized at 25°C using different ultrasound powers
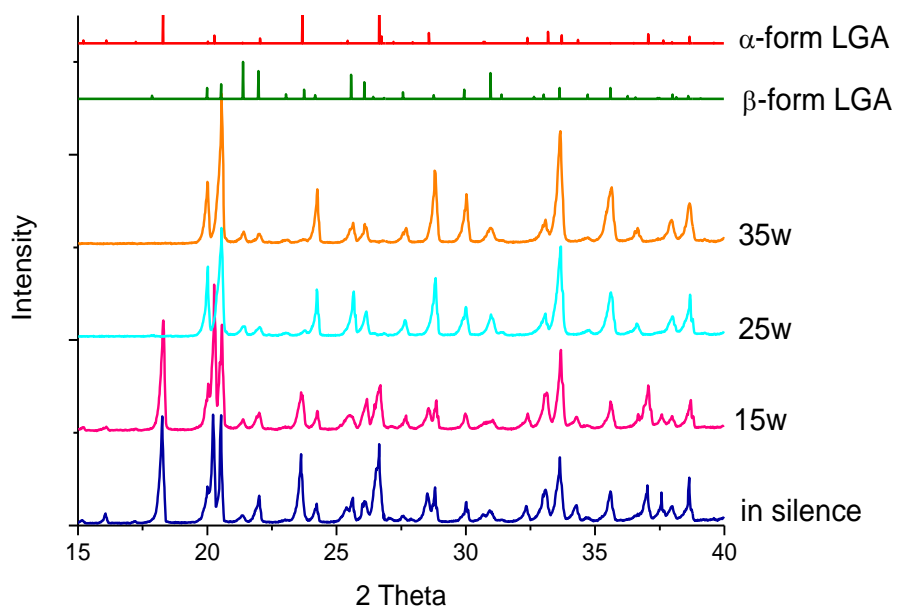
Figure 5.30: Power x-ray diffraction profile of LGA crystallized at 30°C using different ultrasound powers
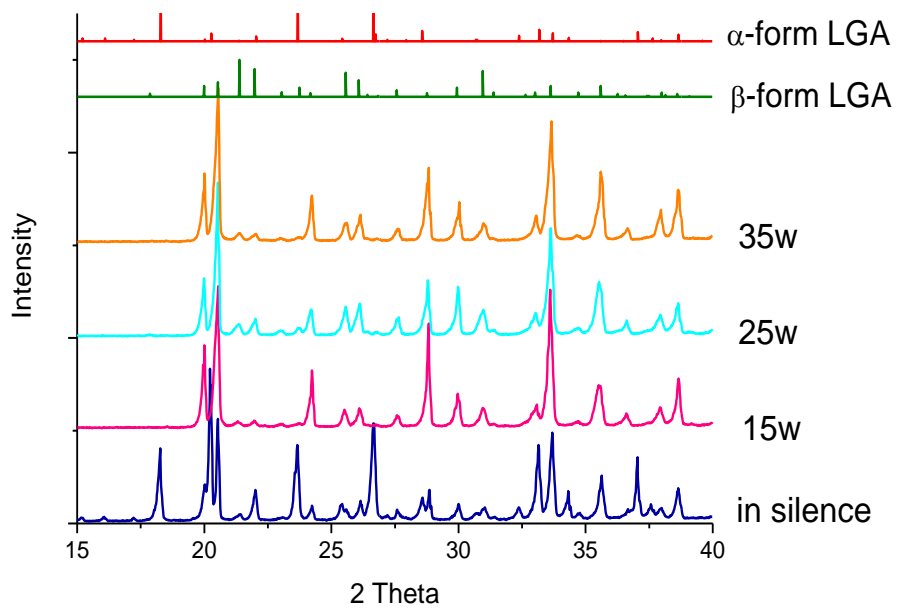
Figure 5.31: Power x-ray diffraction profile of LGA crystallized at 40°C using different ultrasound powers

Table 5.9: Polymorphs identification of LGA slurry crystallized from different temperatures

Temperature	In silence	With 15w US	With 25w US	With 35w US
50°C	β	-	-	-
40°C	α+β	β	β	β
30°C	α+β	α+β	β	β
25°C	α	α+β	α+β	β
20°C	α	α	α+β	α+β

The summary of the effect of ultrasound power on LGA crystallizing at different temperatures is displayed in Table 5.9. It is not difficult to conclude that ultrasound has a distinct effect on determination of LGA polymorphism. Sufficient ultrasound power allowed the arising of α- to β-form transformation, even at the low crystallization temperature extent where the transformation rate is very slow.

In conclusion, ultrasound-assisted LGA crystallization is preferred to produce the stable β-form, either in the context of using fast cooling rate or low crystallization temperature, where the crystallization is α-form favoured. Moreover, it is easier to obtained pure β-form LGA by applying high ultrasound power. Interestingly, the pure α-form was reported to be produced at high supersaturation levels of up to 4.2 with irradiation of power ultrasound which prevents the LGA polymorphic transformation (Hatakka et al., 2010). The transformation of LGA polymorphs has been proven to be the solution-mediated dissolution of the metastable α-form and the nucleation and growth of the stable β-form (Kitamura, 1989) and here are several possible mechanism interpretations with respect to the promotion effect caused by applied ultrasound.

In this context, Cao et al. (Cao et al., 2002) investigated the influence of ultrasound on polymers and proposed that the selective polymorphic form produced by the application of ultrasound was due to its selective acceleration of the growth on one of the polymorphic forms while repressing the growth of the other one. However, this mechanism seems not to be the case with LGA crystallization. Studies (Kitamura and

Funahara, 1994, Cashell et al., 2003, Ferrari and Davey, 2004) speculated that the stable β-form was nucleated and grown on the surface of α-form. Since the α-form acted as the heteronuclei for the β-form, any attribution process that abrades the α-form surface or advances the surface nucleation of the β-form will effectively improve the transformation process. Thanks to the strong turbulent motion caused by acoustic cavitation, ultrasound provided a well mixed and agitated crystallization environment which is typically propitious to the secondary nucleation of the stable β-form and subsequently speeds up the transformation rate. The postulation that power ultrasound expedites the diffusion and mass transfer is another possible explanation in term of its enhanced action (Guo et al., 2006a). Furthermore, the stable β-form has smaller solubility at all temperature ranges and higher associated free energy barrier than the metastable α-form. Without ultrasound irradiation, the α-form is therefore expected to nucleate and grow more fully in solutions. Ultrasound, as an external factor in crystallization, provides additional energy for the stable β-form to overcome its energy barrier, that is, it results in a greater nucleation rate of β-form. Therefore, ultrasound with precise power has the potential to modify and manipulate the synthesis of LGA polymorphs during the crystallization process.

5.4 Conclusion

This chapter has investigated the nucleation behaviour of ultrasound assisted LGA cooling crystallization. It was found that the metastable zone width was narrowed and nucleation can occur at a relative low supersaturation level where ultrasound was applied. The induction time was significantly reduced by ultrasound irradiation; the corresponding smaller calculated critical nucleus radius and interfacial tension imply the lower energy barrier for ultrasound involved nucleation. Both the apparent nucleation order and the nucleation constant were increased by application of power ultrasound, and hence resulted in the acceleration of the nucleation rate. Additionally, the promotion effect of power ultrasound increased with increasing ultrasound power. For the LGA polymorphism section, the stable β-form was tend to be generated with a fast cooling rate and a high crystallization temperature range, while the slow cooling

rate and low crystallization temperature was propitious to the isolation of the metastable α-form. Power ultrasound was indicated to favour the precipitation of the stable β-form LGA by enhancing the transformation rate from the metastable α-form. The preference for β-form catalysis was increased with the increase of ultrasound power. As a final remark, LGA polymorphs can be designed by ingenious combined controlling of the crystallization temperature, cooling rate and precise application of ultrasonic irradiation power.

Chapter 6

Nucleation Kinetics Development of Power Ultrasound Assisted L-Glutamic Acid Crystallization

Summary: The possible mechanism of ultrasound involving l-glutamic acid crystallization is addressed in this chapter by correlating the power ultrasound trigger nuclei number and collapse pressure in the solution.

6.1 Introduction

Power ultrasound, frequencies ranging from 20 kHz to 2 MHz, have been widely utilized and developed in chemical processing to promote or modify the chemical reaction. Ultrasound used as an extend factor plays an important role by controlling crystal structure, morphology, size distribution and rate of crystallization; this is so called sonocrystallization and has serious importance to the pharmaceutical industry. Sonocrystallization investigation has been carried out widely variety of material systems such as paroxetine (Craig, 1999), atopic acid (Anderson. H. W, 1995), amino acid (McCausland.L. J, 2001, Linda J. McCausland, 2004), large molecular system like proteins and high water soluble compound sugars (Ruecroft et al., 2005). Adequate research evidence has proved that ultrasound results in some promotion of crystallization processes, especially the nucleation stage (Qian and Botsaris, 1997, Guo et al., 2006b, Lyczko et al., 2002, Kelly et al., 1993); and ultrasonic effects also exhibit shifting particle size distribution (Enomoto et al., 1992, Shekunov and York, 2000, Price, 1997), efficiently avoiding aggregation of particles (Nývlt, 1995), modifying crystal morphology (Veltmans W H M, 1999) and polymorphs synthesis (Louhi-Kultanen et al., 2006, Ueno et al., 2003, Higaki Kaoru, 2001, Cao et al., 2002). The basic experimental work presented in Chapter 5 has indicated that power ultrasound with various application powers efficiently improved the nucleation rate and allowed nucleation to occur at a low supersaturation level for LGA crystallization. The reason why ultrasound exhibits as an auxiliary factor is not yet explained and it is necessary to discover the internal relevance of ultrasound and nucleation for sonocrystallization process development.

The cavitation bubbles created by the passage of ultrasound through the solution during the alternate compression and rarefaction cycles are believed to be the original causation of the sonochemistry effects, rather than the ultrasound wave itself. Some the possible theories are raised to explain the ultrasound effects. The hot-spot theory points out that bubble collapse leads to the extremely high local temperature and pressure, proved up to 5000°C and 2000 atms, and the violently and rapid energy

release providing the energy for the nucleation process and hence improve the crystallization process. To correlate the cavitation bubble pressure with the nucleation rate, Virone etc (Virone et al., 2006) calculated the induction time and compared it with the value obtained from experiment in a designed sonicator, but the results did not match. The localized turbulence induced by the shock wave and microstream is regarded as the decisive factor which greatly increases the collision between solid molecules and accelerates the boundary mass transfer. Corresponding studies found that the diffusion coefficient and the interfacial area were increased in presence of ultrasound and hence improved the mass transfer of solute (Guo et al., 2006b, Thompson, 2001). According to the surface chemical theory, the attraction between the nucleus surface and gas molecules will make the gas molecules assemble around the nucleus and present as a cloud which is able to reduce the solid-liquid interfacial tension. It is proposed (Qiu.Tai Q, 1993) that acoustic cavitation bubble collapse can produce this gas cloud and hence decrease the interfacial tension for nucleus formation. A hypothesis based on the evaporation described that evaporation of solvent into cavitation bubbles results in the increase of local solute concentration and the supersaturation therefore the promotion of crystallization (Wohlgemuth et al., 2009). And the segregation hypothesis from Grossier's work (Grossier et al., 2007) suggested that the large pressure gradient developed by cavitation bubble collapse can segregate large molecules or nano-particles and enhance the crystallization process in a metastable equilibrium state.

Even these research works have given great impetus to the development and understanding of the sonocrystallization mechanism, cavitation phenomenon associated with random bubble growth and collapse, as well as the uncertain calculation makes the sonocrystallization still not yet well explained and only a few researchers have established the relationship between crystallization and ultrasound in terms of physical-based parameters. This chapter provides cavitation bubble collapse pressure profiles and correlates the collapse pressure with the primary nucleation rate. In addition, based on the assumption of cavitation bubble collapse changing the local solution pressure and induced nuclei for crystal growth, the number of nuclei in the

solution from experimental results and cavitation involved parameters are calculated and compared, in order to explain the possible mechanism for ultrasound assisted LGA crystallization.

6.2 Collapsing Bubble Pressure Estimation of the Probe Ultrasonic System

Transient cavitation bubble propagation due to the pressure variation go through a life cycle of growth during a negative pressure cycle and collapse during a positive pressure cycle through which large amounts of energy are released into the surrounding area. This work assumes that the local pressure change caused by implosion of micro-bubbles is a contributing driving force in the nucleation process besides the solution supersaturation. According to the motion and continuity of cavitation bubbles, their dynamics, under an ultrasound pressure field, can be described by the Rayleigh-Plesset equation (Timothy J.Mason, 2002):

$$R\ddot{R} + (\frac{3}{2})\dot{R}^2 = \frac{1}{\rho}\left[(P_0 + \frac{2\gamma}{R_e} - P_v)\left(\frac{R_e}{R}\right)^{3K} - \frac{2\gamma}{R} - 4\eta\frac{\dot{R}}{R} - P_0 + P_A\sin(2\pi f_a t) \right] \qquad (6.1)$$

where $\dot{R} = \dfrac{dR}{dt}$ is the cavity bubble wall velocity, $\ddot{R} = \dfrac{d^2R}{dt^2}$ is the acceleration of the cavity wall, R is the cavitation bubble radius, R_e is the equilibrium bubble radius under ambient pressure, P_0 is the ambient pressure, P_v is the vapour pressure of the liquid, γ is the liquid surface tension, K is the polytropic index of the gas, η is the liquid viscosity, P_A is the amplitude of the ultrasound driving pressure relating to the ultrasonic system power and f is the frequency of acoustic sound.

A number of models have used the Rayleigh-Plesset equation to estimate the bubble size and cavitation pressure under acoustic field (Hilgenfeldt et al., 1998, Matula, 1999, Virone et al., 2006) however, the Rayleigh-Plesset equation is a second order non-linear differential equation involving a number of uncertain parameter estimations which make the calculation relatively complicated. Based on the

Rayleigh-Plesset equation, Gogate and Pandit developed the correlation using the easily measurable global parameters for common sonochemistry application (Gogate and Pandit, 2000):

$$P_{collapse} = 114(R_0)^{-1.88}(I)^{-0.17}(f)^{0.11}$$ (6.2)

This correlation can be used in all kind of the sonochemical application procedure design where the rigorous numerical solution of the Raylei-Plesset equation is not feasible. The parameters in Equation 6.2 used the initial cavity size R_0 in mm, the intensity I and frequency f of the irradiation ultrasound in W/cm^2 and kHz, respectively. Notably, there are corresponding ranges of usage for each parameter during collapse pressure calculation: 0.05mm<R_0<0.5mm, 10W/cm^2<I<300W/cm^2 and 10kHz<f<120kHz. Since the initial cavitation bubbles in this case are smaller than 0.05mm, this correlation is not propitious for pressure estimation.

Another simplified correlation given by Noltingk, Neppiras and Flynn (Timothy J.Mason, 2002) will be used in the present work instead for adiabatic bubble collapse maximum pressure determination. The equation relates the pressure in the bubble at its collapsing maximum size P, which equals to the vapour pressure of water at collapsing temperature, the transient cavitation bubble collapse pressure in the liquid $P_{collapse}$ and the polytropic index of gas mixture K can be expressed by:

$$P_{collapse} = P\left\{\frac{P_m(K-1)}{P}\right\}^{\frac{K}{K-1}}$$ (6.3)

For adiabatic collapse of bubbles containing air, K equals to 4/3. And with

$$P_m = P_h + P_a$$ (6.4)

where P_h is the hydrostatic pressure in the liquid and P_a is the acoustic field pressure defined by:

$$P_a = P_A \sin 2\pi f t$$ (6.5)

The applied power ultrasound amplitude P_A can be calculated from

$$P_A = \sqrt{2I\rho_L C_L}$$ (6.6)

where ρ_L is the density of solvent, C_L is the velocity of sound in water and with the

ultrasonic intensity I in W/cm^2:

$$I = \frac{P_{output}}{A_n}$$ (6.7)

here P_{output} is the output power of the ultrasonic probe and A_n is the surface area of ultrasound probe tip.

Assuming symmetric bubble collapse was halted abruptly by the compressed contents of the bubble resulting in the propagation of shock wave that expanded as a ring and travelled away from the collapsed centre. The shock wave was initially generated of collapse pressure amplitude but could only spread for a certain distance, which stopped when the pressure was reduced to ambient pressure. This predicted pressure upon collapse of the bubble will lead to the acceleration of nucleation rate in the solution and its calculation will be explained in detail later.

6.3 Nucleation Rate Expression under Bubble Collapse Pressure

The chemical potential of the solute in the solution is treated as the driving force of the nucleation, and it is pressure-dependent based on thermodynamic theory. Therefore, the solution pressure should be considered as a factor which affects bulk solution nucleation. $\Delta\mu$, which is the difference between the chemical potential of the solute in the solution and the chemical potential of the solid phase, defines the possibility of nucleation.

The nucleation rate for sonicated crystallization is believed to be heterogeneous primary nucleation (Kordylla et al., 2009) in which foreign bubbles reduce the free-surface enthalpy and consequently act as nucleation sites. The nucleation rate can be calculated as:

$$J = A' \exp\left(\frac{-16\pi v_c^2 \gamma_{eff}^3}{3k_B T \Delta\mu^2}\right)$$ (6.8)

where k_B is the Boltzmann constant, T is temperature, the factor v_c is the molecular

volume of the crystal and can be obtained from the solute molar mass M and the solid phase density ρ_c:

$$v_c = \frac{M}{\rho_C \cdot N_A}$$ (6.9)

In heterogeneous nucleation, the effective interfacial tension γ_{eff} is defined as

$$\gamma_{eff} = \psi^{1/3}(\theta)\gamma$$ (6.10)

with the pre-factor ψ determined from the wetting angle θ of the nuclei onto the foreign bubble surface.

$$\psi(\theta) = \frac{(2+\cos\theta)(1-\cos\theta)^2}{4}$$ (6.11)

For crystal formation under the diffusion controlled growth conditions, the factor A' in Equation 6.9 is proposed to be:

$$A' = (k_B T / v_c^2 \gamma_{eff})^{\frac{1}{2}} \cdot C_0 \cdot C \cdot D_{ab} \cdot lnS$$ (6.12)

where C is the concentration of bulk solution, S is the supersaturation, D_{ab} is the diffusion coefficient and C_0 represents the nucleation sites on the foreign surface and for heterogeneous nucleation, it is of value of approximately 10^{17} that is estimated from foreign surface area A_{for}, the molecular diameter d_m, and the adsorption properties He_{ad}:

$$C_0 = A_{for} \cdot He_{ad} \cdot C \cdot d_m \cdot N_A$$ (6.13)

Regarding the chemical potential term $\Delta\mu$, as mentioned before, it determines the possibility of nucleation and can be treated as the sum of supersaturation contribution $\Delta\mu(S)$ and pressure effect $\Delta\mu(P)$:

$$\Delta\mu = \Delta\mu(S) + \Delta\mu(P)$$ (6.14)

Based on the thermodynamics, if the partial molecular volumes v_s in the solution and the volume of the solute in the solid phase v_c are assumed to be pressure independent, the chemical potential with pressure change is expressed as (Kashchiev and van Rosmalen, 1995):

$$\Delta\mu(P) = \Delta\mu(P_0) - (v_c - v_s)(P - P_0) \tag{6.15}$$

The factor P_0 is the initial pressure and normally considered to be ambient pressure of 1 bar. The term $\Delta\mu(P_0)$ is given by

$$\Delta\mu(P_0) = k_B TIn[a / a_e(P_0)] \tag{6.16}$$

Here a and $a_e(P_0)$ are the activity of the solute and equilibrium activity between the solution and the solid phase under pressure P_0, respectively. It is worth noting that the value of activity is very difficult to calculate or measure, it can be approximated by solution concentration for dilute solutions and the term $\Delta\mu(P_0)$ is then pressure independent. Thus, whether the pressure change increases or reduces the chemical potential depends on the sign of the difference between the partial molecular volume and the solute volume in solid phase, the chemical potential increase with the increase of pressure when $v_c - v_s < 0$, and pressure increase results in the decrease of the chemical potential when $v_c - v_s > 0$. Based on the above equations, we can evaluate the nucleation rate under sonicated conditions associated to the bubble collapse pressure profile that described in Chapter 6.2.

6.4 Calculation of Nuclei Number in the Solution

To investigate the nucleation rate in the sonicated condition, induction time measurement was carried out due to the difficulties of direct measurement of the nucleation rate. The general method to determine the nucleation rate is from the inversely proportional relationship of induction time and the nucleation rate. Consider the fact that any induction time detecting device used in the experiment has its measurement limit for accurate crystal onset point determination, the induction time recorded from the experiment is actually a timescale including the real nucleation induction time and a period time of crystal growth. Taking the crystal growth effect into account, the induction time is described by the corresponding expression (Kashchiev, 2000):

$$t_{ind} = \left(\frac{a_d V}{b_f N_m} \right)^{1/\upsilon d} \left(\frac{1}{G} \right) \tag{6.17}$$

where a_d is the detected limit for the induction time measurement device (for turbidity used in this work, the detectable diameter of suspended crystal is about 10^{-6}m), V is the experimental solution volume, b_f is the shape factor of crystals (for spherical particles $b_f = 4\pi/3$, for disk particles $b_f = \pi H$ and for square particles $b_f = \pi H$ with H refers to the constant thickness of crystal), N_m is the total nuclei number in the solution, υ is the growth index of crystals (for parabolic growth $\upsilon=1/2$ and for linear growth $\upsilon=1$), d refers to the dimension of the growth based on the crystal shape (for 1D growth of needle like crystal $d=1$, for 2D growth of disk or square like crystal $d=2$ and for 3D growth of cubic or spherical like crystal $d=3$), G is the growth rate of crystals. The total nuclei number in the solution is hence calculated from corresponding experimental measured induction time.

Assume that the nuclei in the solution are induced by ultrasound irradiation, this nuclei number should also be a function of ultrasonic system parameters like frequency, power and insonation interval. According to the work of Virone et al. (Virone et al., 2006), the nucleus number in the solution is of the form:

$$N_m = B \cdot N_b \tag{6.18}$$

with total number of cavitation bubbles B

$$B = b' V_{cavitation} \cdot t_{insonation} \tag{6.19}$$

where b' is the bubble formation rate in the reactor, $V_{cavitation}$ is the cavitation volume in the reactor and with the nuclei number generated by each cavitation bubble N_b:

$$N_b = \bar{J} \cdot V_{effective} \cdot t_{shockwave} \tag{6.20}$$

$\bar{J}$ is the average nucleation rate over the lifetime $t_{shockwave}$ of shock wave produced during bubble collapse within the effective volume of shock wave $V_{effective}$.

To accomplish identification of the ultrasonic nucleation mechanism, the predicted nuclei number from ultrasound parameters will be compared with the nuclei number achieved from experimental induction time calculation, as shown in Figure 6.1.
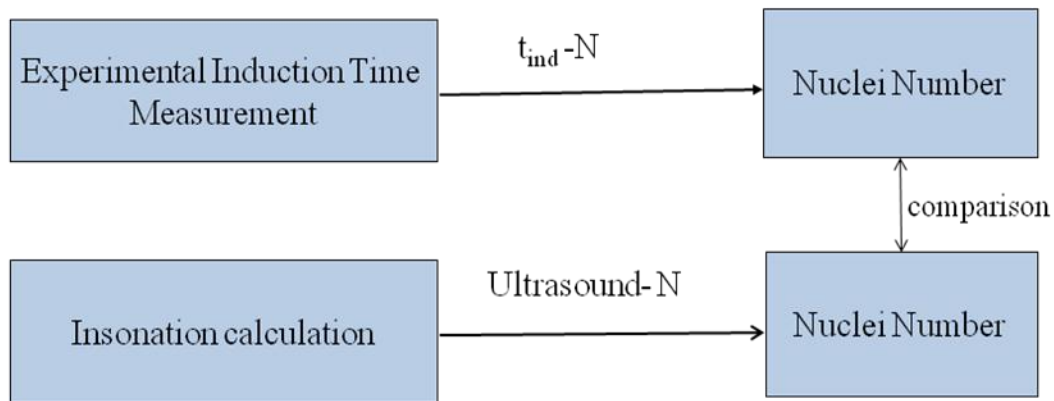
Figure 6.1: The framework of ultrasonic nucleation identification

6.5 Procedure and Experimental Set-up

All the experiments utilized a 100 mL automated double-jacketed reactor from HEL of WinIso software and the temperature of the solution was controlled by a FP50-HD Julabo via oil inlet jacket. The four blade glass stirrer was operated at a 150 r.p.m stirrer speed, together with Pt100 thermometers connected to the WinIso software. The fibre optic turbidity probe and amplifier from University of Leeds workshop were used for crystallization onset point determination. The P100/2-20 ultrasonic processor system with fixed 20 kHz frequency and adjustable ultrasonic power consisted of a step-detectable probe and ultrasonic generator. The immersion ultrasound probe during the experiment was positioned on a different side from turbidity probe in order to avoid the influence of bubble propagation on the turbidity measurement. The induction time experimental crystallizer and apparatus set-up are shown in Figure 6.2.
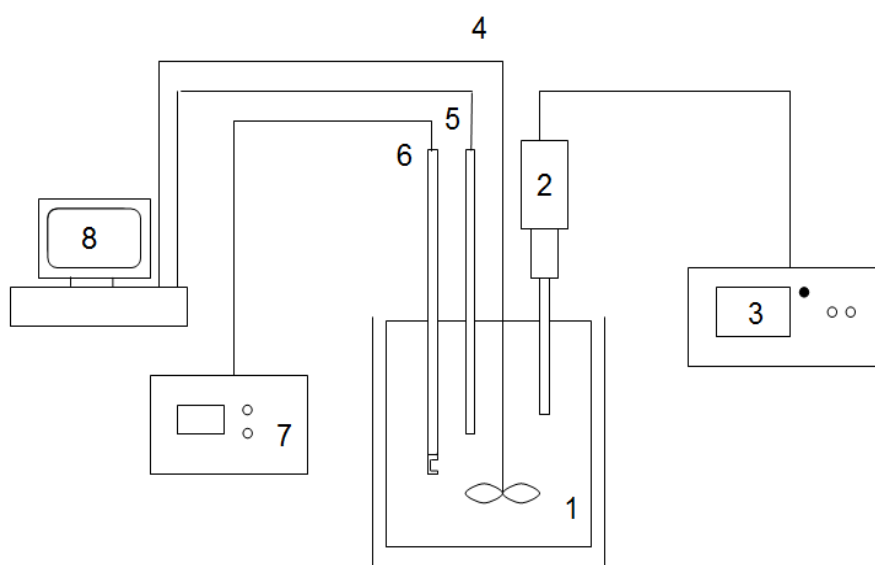
Figure 6.2: Experimental apparatus set-up. 1. double-jacket reactor; 2. ultrasound probe; 3.ultrasound generator system; 4. Stirrer; 5. Thermometer; 6. Turbidity probe; 7.turbidity amplifier; 8. computer

In this work, a concentration of 30g/L LGA in distill water was used for induction time measurement. Prepared solutions were heated up to 70℃ and kept for 1h to ensure LGA was dissolved properly. A crash cooled operation allowed temperature decreased to different selected bottom temperatures of 50℃ to 53℃ within the metastable zone corresponding to the concentration of solution based on the former determined data in Chapter 5. Bottom temperatures were kept constant and induction time was counted from the moment that the bottom temperature reached to detectable crystals occurring indicated by turbidity change. Power ultrasound was applied when the bottom temperature was reached. Two parts of induction time experiments were carried out for 1) different power (5w, 10w, 15w, 25w, 35w) with constant sonicated times of 180s; and 2) different insonation intervals (30s, 60s, 120s, 180s, 240s) with constant ultrasound power of 15w.   Each induction time measurement was repeated three times and the average value was taken as induction time in calculated.

6.6 Results and Discussion

6.6.1 Estimation of Maximum Collapse Pressure and Nucleation Rate

The first part of the results was the calculated maximum pressure upon the collapsed bubble from Noltingk, Neppiras and Flynn, Equation (6.3). Assuming the liquid contains only a small amount of gas or the gas has insufficient time for mass diffusion into the cavitation bubble, the gas pressure P in the bubble is equal to the vapour pressure of water P_v, the calculated parameters of concentration of 30g/L operated at 53℃ are listed in Table 6.1. Figure 6.3 shows the maximum pressure for different output power of ultrasound at varied experimental temperature ranges. The water vapour pressure is smaller at lower temperature and therefore results in the higher pressure during collapse. The higher output power of ultrasound, as is expected, generates higher collapse cavitation bubble pressure, ranging from 4970 atm to 2.44×10^5 atm for different temperature ranges.

Table 6.1 Calculation parameters and experimental conditions

Parameter	Value	Unit	Parameter	Value	Unit
T	326	K	C_0	10^{17}	#/m^3
P_h	1	atm	k_B	1.38×10^{-23}	J/K
P_v	0.143	atm	P_0	1	atm
K	4/3	-	v_c	1.56×10^{-28}	m^3
A_n	0.636	cm^2	v_s	1.68×10^{-28}	m^3
ρ	1000	kg/m^3	γ	1.80×10^{-3}	J/m^2
D_{ab}	10^{-9}	m^2/s	C	30	g/L
M	147.13×10^{-3}	kg/mol	S	1.02	-
N_A	6.02×10^{23}	#/mol	ρ_c	1560	kg/m^3
G	147.13×10^{-3}	m/s	a_d	0.05	-
b_f	0.01	-	V	7.0×10^{-5}	m^3
d	3	-	v	1	-
b'	1.95×10^{12}	#/m^{3}s			
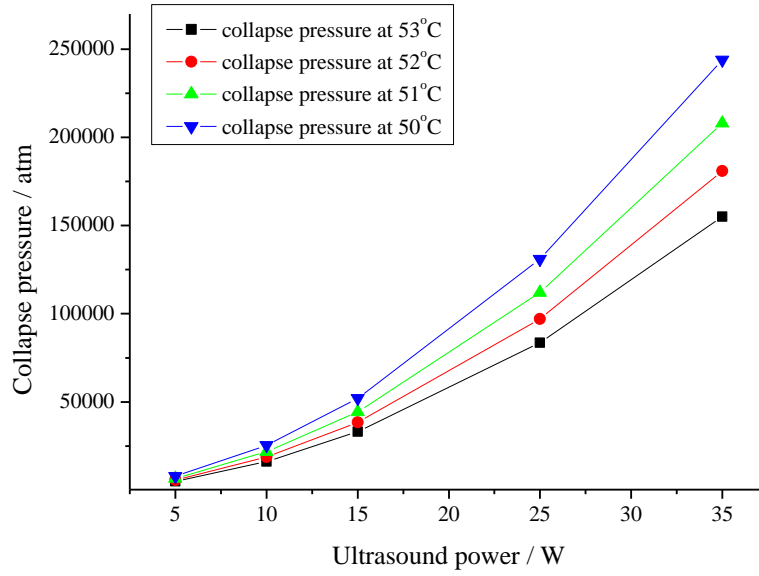
Figure 6.3: Maximum collapse pressure at different temperatures as a function of applied ultrasound power

The partial molecular volume v_s of l-glutamic acid was taken as 1.68×10^{-28} m^3 for S=1.02 according to the volumetric study of amino acid in aqueous medium (Muhammad J and Mohammad I, 2011) and the l-glutamic crystal volume v_c was calculated as 1.56×10^{-28} m^3 from Equation (6.9). A value of v_c-v_s=-1.2$\times 10^{-29}$ m^3 was thus calculated. Considering a heterogeneous nucleation mechanism, foreign bubbles reduced the interfacial tension, the wetting angle was set to 45° (Kordylla et al., 2009) which resulted in the pre-factor of ψ=0.058 and the interfacial tension of γ$_{eff}$ =0.0007 J/m^2 from Equation (6.11) and (6.10). In the present work, the activity term $a/a_e(P_0)$ in Equation (6.16) was approximated by the solution supersaturation ratio S for the reason that the activity can be replaced by solution concentration in sufficient dilute solution. Other parameters used to determine the nucleation rate are also listed in Table 6.1. The predicted primary nucleation rate for different supersaturation solutions under high collapse pressure from 1 atm to 100000 atm were calculated using Equation (6.8), as shown in Figure 6.4. At low pressure regions, from ambient pressure to about 10 atm, nucleation rate is not affected by pressure change,

because the supersaturation is still the dominant term during the nucleation process compared with the neglig ible pressure effect. Under pressure regions of 10 to 1000 atm, both supersaturation and pressure factors determine the nucleation rate, and for the four supersaturation solutions investigated in this work, increase of the local solution pressure accelerated the nucleation rate and the pressure effect on nucleation rate appeared more evident for relatively low supersaturation solution. However, when pressure is high enough, above 2000 atm, pressure change no longer improves the nucleation process. Similar calculation result has been reported by Virone et al. that above a specific pressure, the number of molecules in the critical nucleus, which can be determined by $n* = 2B/[\ln S - c(P - P_0 - 1)]^3$, was so small that the nucleation rate calculation that take pressure into account became invalid (Kashchiev and van Rosmalen, 1995, Virone et al., 2006). A plot of the nucleation rate at collapsing moment as a function of acoustical power is showed in Figure 6.5. The nucleation rates under different powers of ultrasonic irradiation were found to be the same, implying that the corresponding collapsed pressure had been too high that the values of the term $\exp(\dfrac{-16\pi v_c^{\,2}\gamma_{eff}^{\,3}}{3k_B T\Delta\mu^2})$ in Equation (6.8) were the same and the nucleation rate depended on the supersaturation dependent kinetic parameter *A'*. Although the nucleation rates at the collapsing moment appeared no difference, the total ultrasonic induced nuclei depend on the effective shock wave volume as well as the average nucleation rate within the action area. The following part of the results is the estimation of the shock wave action volume and the total nuclei number calculation.
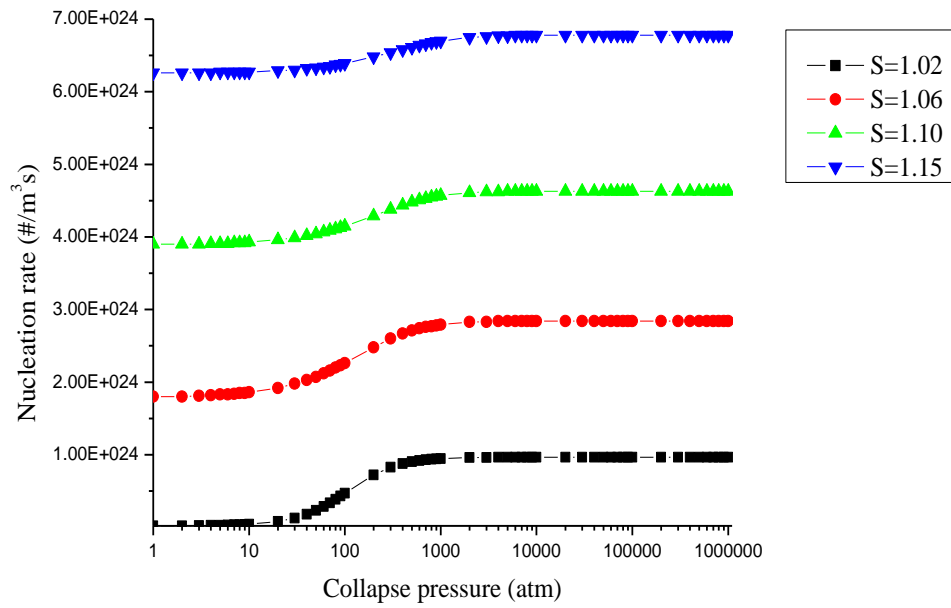
Figure 6.4: Developed nucleation rate over a range of collapse pressure for different supersaturation solutions
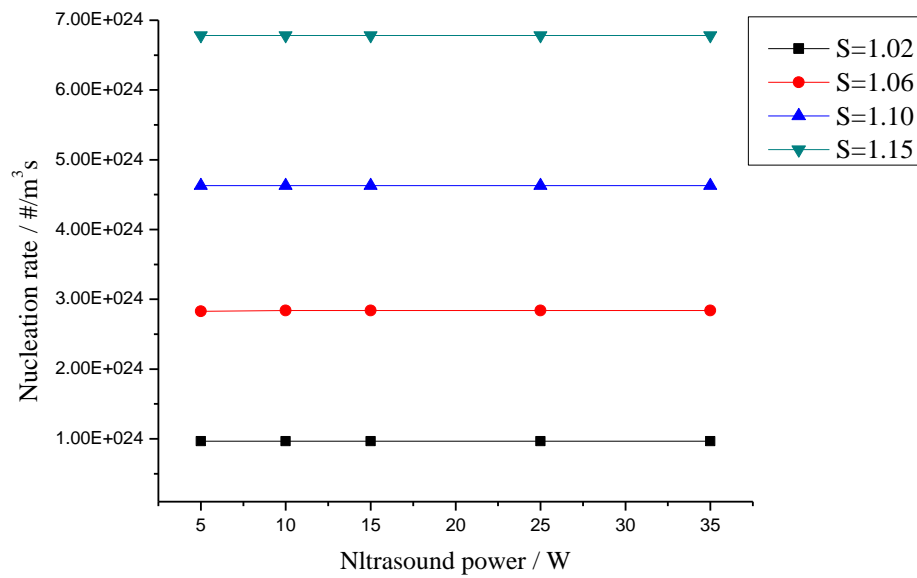
Figure 6.5: The calculated nucleation rate at collapsing moment with different acoustical power applied for different supersaturation solution

6.6.2 Ultrasound induced Nuclei Number Estimated from Acoustic Parameters

The travelling distance and time scale of the shock wave corresponding to pressure amplitude were estimated and fitted with second-order polynomial according to the previous investigation results proposed in (Virone et al., 2006, Pecha R and Gompf B, 2000), as shown in Figure 6.6. For collapse occurring at 35W output ultrasound power, the shock wave expanded to a distance of 248μm for lifetime of 68.5ns from the initial pressure 1.55×10^5 atm to the final ambient pressure 1 atm were obtained accordingly.
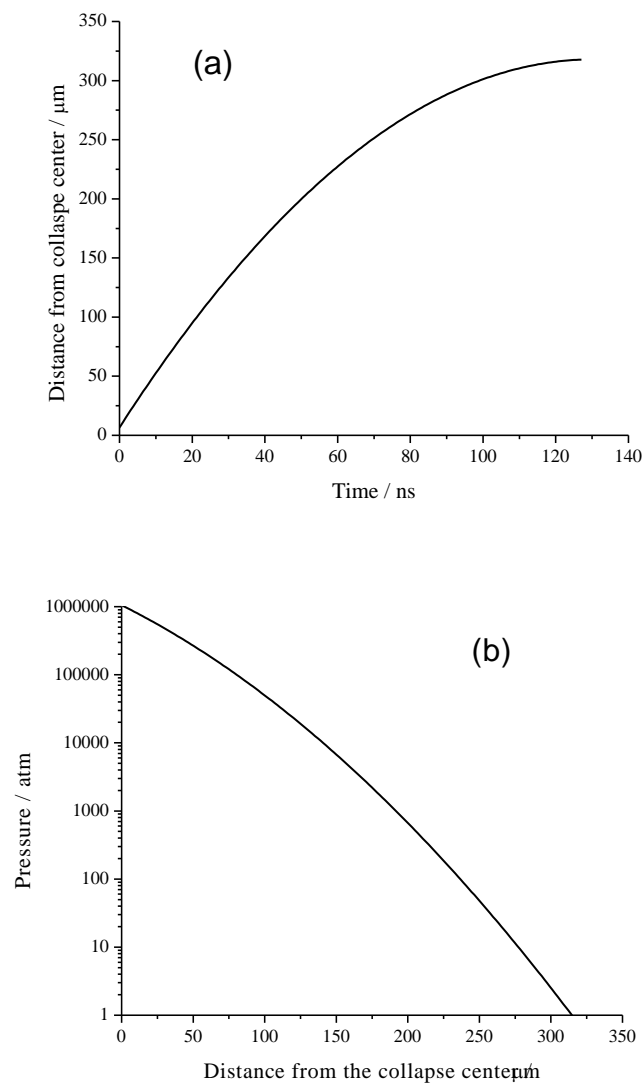
Figure 6.6: (a) travelling distance from the collapse centre (b) shock wave pressure amplitude change with distance

As is discussed in Chapter 3, the shock wave pressure decreases with the distance from the bubble interface and hence invokes gradients of the nucleation rate. The average nucleation rate $\overline{J}$ under the changed shock wave pressure amplitude was needed to characterize the overall nucleation rate in presence of ultrasound. The average nucleation rate is therefore determined from the nucleation rate profile over a grange of pressure, as seen in Figure 6.4, and calculated to be $2.92 \times 10^{25}\,\mathrm{m^{-3}s^{-1}}$. Thus, the nuclei number N_b that generated from a single cavitation bubble collapse with the value of 1.28×10^8 was evaluated from Equation 6.20. However, there is no precise method to calculate the collapsed bubble number and it depends on the ultrasound power, frequency and reaction vessel type. Until now, only few experimental studies have been devoted to estimate the cavitation bubble number. The bubble formation rate b' was set to be $1.95 \times 10^{12}\,\mathrm{m^{-3}s^{-1}}$ in the present study based on the work of Burdin et al. who characterized the acoustic cavitation bubble cloud by using phase Doppler technique (Tsochatzidis et al., 2001, Burdin et al., 1999). The cavitation volume $V_{cavitation}$ of $7 \times 10^{-5}\,\mathrm{m^3}$ was taken based on the solution volume, thus leading to the total cavitation bubble number B of 2.46×10^{10} in a 180s insonation interval with ultrasonic power of 35W, according to Equation 6.19. The total nuclei number N_m induced by ultrasound in the reactor was equal to the total bubble number multiplied by the nuclei number for each bubble collapse, a result of 3.14×10^{18} was found. Figure 6.7 reveals the total nuclei number calculated from acoustical parameters for varied ultrasound power with 180s insonation intervals. Similar calculation was taken for different insonation interval with constant 15W ultrasonic irradiation power, as shown in Figure 6.8.
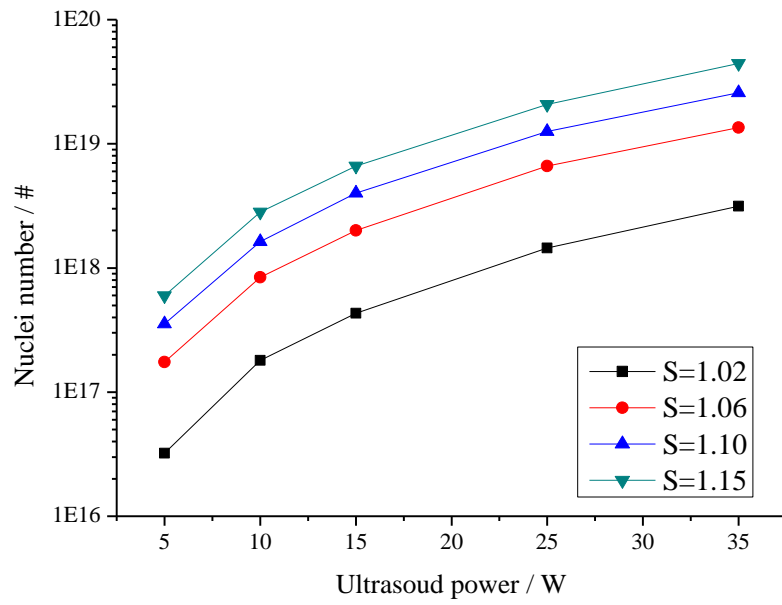
Figure 6.7: The total ultrasound induced nuclei number calculated from acoustical parameters for different ultrasound powers with 180s insonation interval
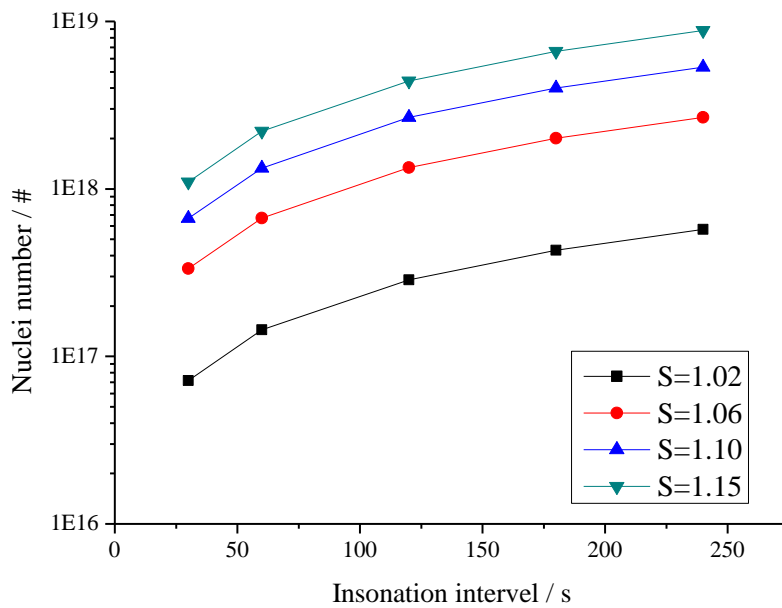
Figure 6.8: The total ultrasound induced nuclei number calculated from acoustical parameters for different insonation intervals with 15W ultrasonic irradiation power

As expected, the higher ultrasound power with faster average nucleation rate and greater effective volume could induce more nuclei within the same insonation interval, as seen in Figure 6.7. For the high supersaturation (S=1.15), the nuclei number was 4.43×10^{19} with 35W ultrasonic irradiation, which had been increased to 70 times as compared with the 5.99×10^{17} nuclei number with 5W ultrasonic irradiation. For the low supersaturation (S=1.02), the nuclei number with 35W ultrasonic power had been raised approximate 100 times as against the one with 5W ultrasound. The results in Figure 6.8 indicated that the induced nuclei number increased with the extension of insonation interval. This result corroborated the argument that power ultrasound had a promotion effect on nucleation, which is more obvious at low supersaturations and proportional to the ultrasonic power within the current experimental regions. Based on the above results, it is conceivable that the reduced induction time should be result from the increase of ultrasonic power and insonation interval.

6.6.3 Ultrasound Induced Nuclei Number Calculated from Induction Time Measurement

Experimental induction time was measured for different acoustical power and different insonation intervals. Figure 6.9 and 6.10 depict the measured induction time for different ultrasound powers and insonation intervals respectively, the crystal appeared faster when higher ultrasound power or longer insonation interval was applied which was consistent with the results predicted from ultrasound parameters. By drawing a line requesting a 60 min induction time, the critical conducted ultrasound power for four supersaturated solutions can be found, around 17W for S=1.15 but almost 31W for S=1.02. Likewise, for an induction time of 80 min, the critical insonation interval for S=1.15 is 48s while over 180s is needed for S=1.02.
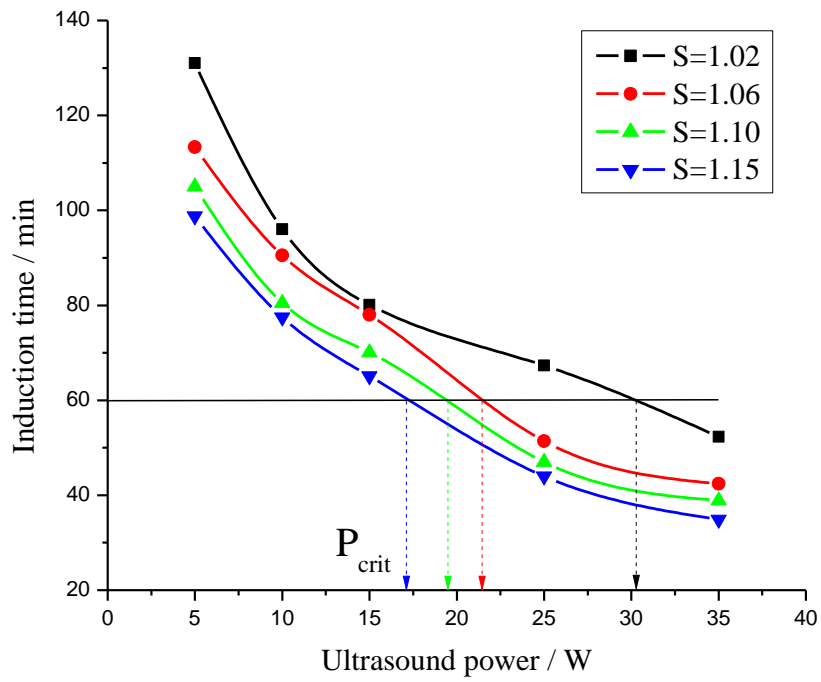
Figure 6.9: Measured induction time for different ultrasound powers with 180s insonation interval
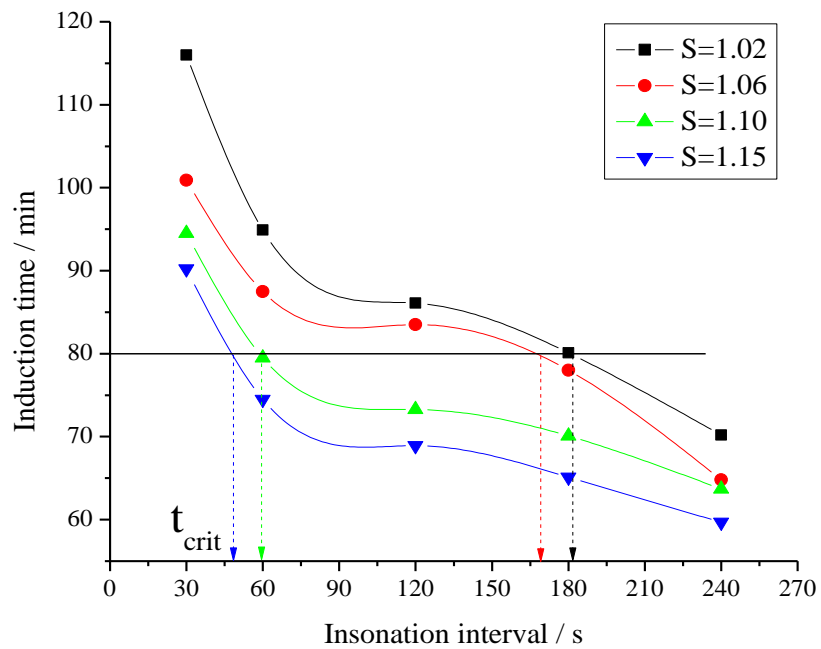
Figure 6.10: Measured induction time for different insonation intervals with 15W ultrasound power

From Equation 6.17, the total nuclei number in the solution can be calculated using measured induction time and will be compared with that number obtained from

ultrasound parameters calculation. Relative experimental conditions and calculation parameters are listed in Table 6.1 and the comparison of ultrasound parameters calculated nuclei number and experimental nuclei number were presented in Figure 6.11 for changed ultrasound power conditions. Unfortunately, it seems that the nuclei number obtained from different calculation paths are not in accordance, the nuclei number predicted from ultrasound parameters is much bigger than that calculated from the experimental induction time. But they both show the same tendency that with the increase of ultrasound power, the total nuclei number induced by ultrasonic irradiation increased.
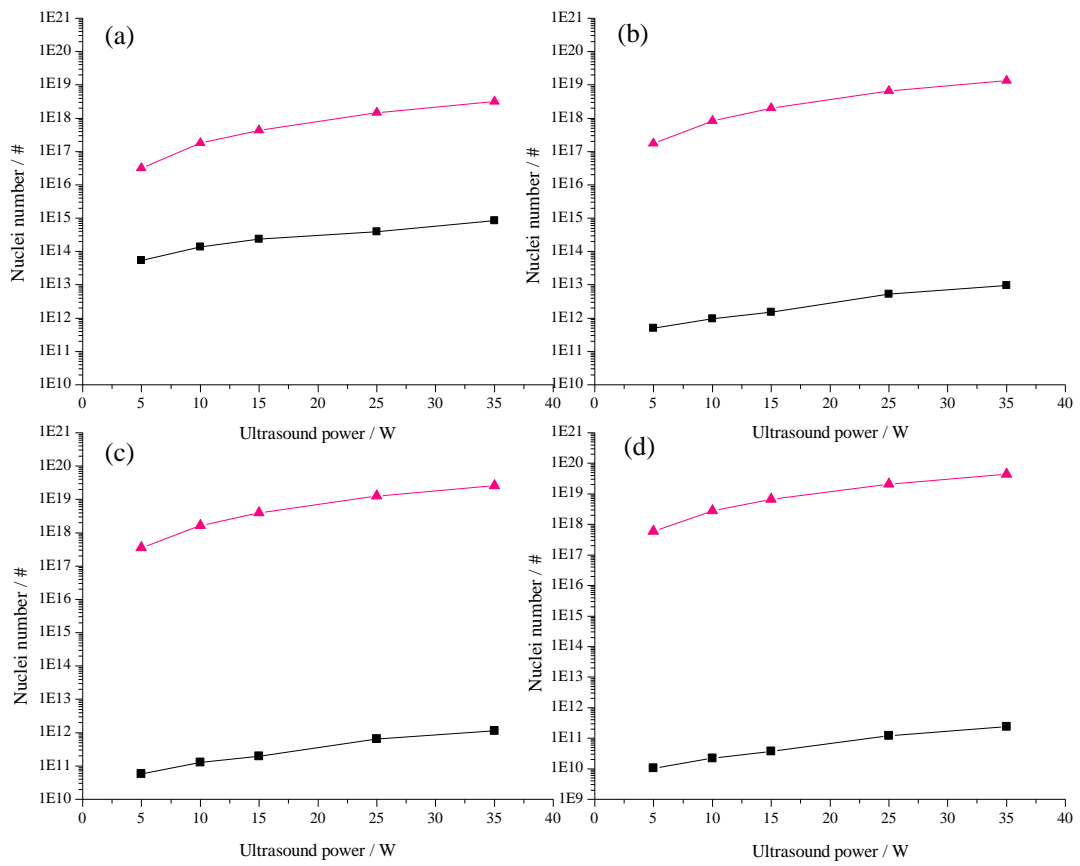
Figure 6.11: The comparison of calculated nuclei number from ultrasound parameters (▲) and experimental induction time (■) for different ultrasound powers with 180s insonation interval (a) S=1.02 (b) S=1.06 (c) S=1.10 (d) S=1.15

.
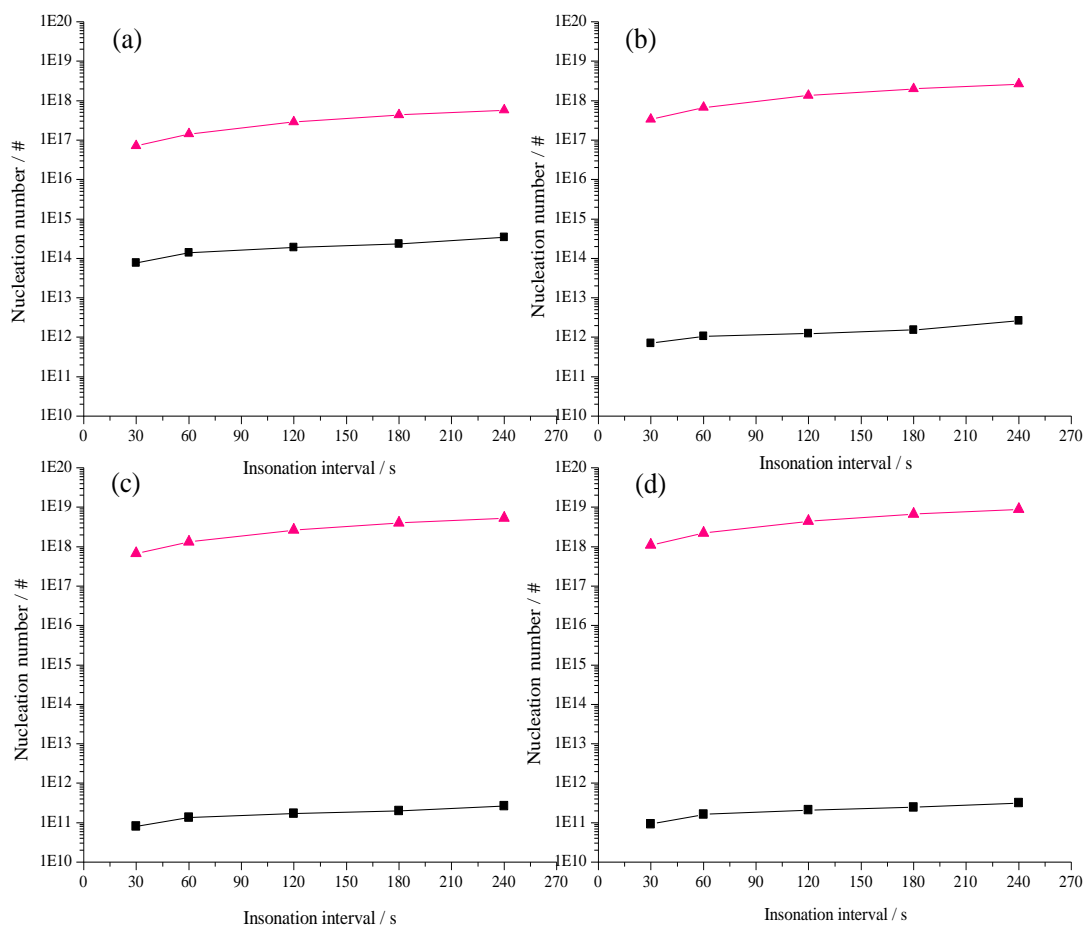
Figure 6.12: The comparison of calculated nuclei number from ultrasound parameters (▲) and experimental induction time (■) for different insonation intervals with 15W of ultrasound power irradiation (a) S=1.02 (b) S=1.06 (c) S=1.10 (d) S=1.

.

The same results were obtained for different insonation intervals with constant 15W ultrasonic irradiation, see Figure 6.12. It is worth noting that the measured induction times were explicitly reduced when supersaturation of the solution was elevated for both of the study sections, but the corresponding calculated nuclei numbers were found to be smaller for higher supersaturation with the same ultrasound power. This is because the induction time measurement error due to the detection instrument, especially when the supersaturation was high and the growth rate was fast. It can only be concluded from the results of the calculation that the ultrasound effects are

proportional to the cavitation issues as the higher power and longer insonation interval reflects on larger amounts of the nuclei number. The possible reasons that are conducive with the unmatched nuclei number are: 1) the turbidity measurement instrument used in the experiments was not sensitive enough and has no response to small crystals when they crystallize from the solution, and hence a delayed induction time measurement; 2) the inaccurate estimated pressure profile. The pressure upon the cavitation bubble was estimated based on the assumption that there is negligible gas in the collapsing bubble and the pressure in the bubble at the moment of collapse is equal to the vapour pressure. However, if the dissolved gas in the liquid does enter the bubble, the collapsed pressure will be smaller than was predicted. Obviously, the nucleation rate under the collapse pressure will be smaller, which results in a smaller amount of nuclei; 3) uncertain calculation was involved. The calculation in the current study was based on the single symmetrical bubble collapsing model; but the probe system in practice is a multi-bubble system with symmetrical and asymmetrical bubble collapse, which makes bubble collapse more complicated and difficult to characterize; 4) the shock wave may cause localized damage such as the fragmentation of nearby bubbles, and hence impact on the total estimated cavitation bubble number and the effective volume of each collapsing bubble.

6.7 Conclusion

The collapsing pressures upon the cavitation bubbles were calculated for different applied ultrasound powers, and based on the pressure profile, a developed approach considering the local pressure change was implemented to calculate the ultrasound induced nucleation rate during l-glutamic acid crystallization process. Experimental induction time measurement was carried out to determine the exact number of formed nuclei by ultrasonic irradiation. This number was then compared with the theoretically estimated nuclei number from ultrasound apparatus parameters in order to correlate the cavitation number and the nucleation events. The number values did not match possibly due to the difficulty in accurately describing the complicated cavitation

bubble system. However, the obtained results have proved that the nuclei number induced by ultrasound increased with increasing the ultrasound power and insonation interval. In addition, the effect of ultrasound on nucleation appeared to be proportional to the cavitation issue. At present, the approach only provides a potential evaluation method for ultrasonic nucleation mechanism investigation but it is also an important step forward in understanding of sonocrystallization. A more comprehensive model and further development are still needed.

Chapter 7

Studies of Power Ultrasound Effects on the Crystal Growth Kinetics of L-Glutamic Acid

Summary: Power ultrasound affected seeding growth studies of α-form L-glutamic acid at high supersaturation levels and low supersaturation levels are delivered in this chapter. The particle size distribution under various ultrasound power influences is also provided along with the strategy of particle size distribution optimization.

7.1 Introduction

As another stage of crystallization after the initial nucleation of crystal, growth of the particle is of importance in industrial crystallization performance. The growth rate of the dominant face determines the crystal habit, the particle size distribution and hence the quality of the final pharmaceutical products. There are different methods to obtain the crystal growth rate, through either single crystal growth measurement using image technique or bulk solution overall growth rate evaluation with on-line/off-line particle sizing equipment. However, the particle sizing instruments available do not always perform satisfactorily due to the high dependence of their measurement principles on particle shape. Although the effects of power ultrasound during the nucleation process are evident, its influence on crystal growth seems not so dramatic and there is very limited literature on ultrasound assisted growth studies.

Early in 1974, ultrasound had been reported to successfully accelerate sugar crystal growth compared with mechanical agitation (Kortnev and Martynovskaya, 1974) and crystal growth rate was ultrasound intensity and frequency dependent (Le Bras, 1967). Ultrasound influence on crystal growth rate was also proved to be supersaturation driving force dependent. For relatively slow growth rate at low supersaturation, i.e. 10^{-10} m/s, growth rate was double when ultrasound was used and for the fast growth rate of 10^{-7} m/s at high supersaturation, ultrasound appeared to have no effect on crystal growth rate (Arakelyan, 1987) . According to the work of Boels et al. (Boels et al., 2010a), the volumetric growth rate of calcite under ultrasound irradiation was enhanced by 46% and their later study (Boels et al., 2010b) presented that the effect of inhibitor NTMP mitigated in presence of ultrasound. The mass growth rate of potash alum was also found to be faster in comparison with silent conditions as ultrasound increased the rate of desupersaturation and hence the growth rate (Amara et al., 2004). However, a retardation effect, up to 62-76%, was observed on calcium carbonate growth under an ultrasonic field but the mechanism, the nature, the morphology and the crystal size were not influenced by ultrasound application (Dalas, 2001). Therefore, it can be concluded that the effects of ultrasound on crystal growth

are very diverse and it is difficult to analyze its impact on growth separately from nucleation.

The purpose of this chapter is to investigate the LGA crystal growth under the irradiation of power ultrasound and elucidate the possible growth mechanism in presence of ultrasound. Concerning the utilization of the ultrasound instrument which may probably affect the on-line measurement, crystal size and size distribution in this work is evaluated from off-line Morphologi G3. Seeding growth measurement at different ranges of supersaturation is carried out for cooling-based batch crystallization to avoid the nucleation effect. Finally, the effect of ultrasound on particle size distribution is also presented as well as the ultrasound assistance particle size control strategies.

7.2 Methodology and Instrumentation

7.2.1 In-situ Solution Concentration Measurement

Solution supersaturation is the thermal dynamic driving force for crystal growth and the ability to measure the concentration of solution during the growth process is fundamental, due to its direct determination of supersaturation which is the excess of solution concentration over corresponding solubility.

In the growth experiments, solution concentration was measured using Attenuated Total Reflectance-Fourier Transform InfraRed spectroscopy (ATR-FTIR) based on the principle of different arrangements of chemical protons, neutrons and electrons having different absorption of specific region wavelengths of light. The calibration spectrum data was collected for L-glutamic acid concentration from 3 to 60g/L and the temperature ranged from 10 to 80°C. The spectra of solution during experiments were captured every 30 seconds and recorded in a text file. Then, through the in-house designed software and PLS model based MATLAB programs, the spectra data will automatically process to the solution concentration value. It is worth noting that both the calibration profile and programming were collected and developed by former PhD researcher Chaoyang Ma from the Institute of Particle Science and Engineering,

University of Leeds. In his work, the transflectance NIR calibration data was obtained using solutions and slurries of varied solution concentration, particle size, solid concentration and temperature to predict the multiple properties of both phase based on the genetic algorithm and support vector machine (GA-SVM) approach (Ma, 2010).

7.2.2 L-Glutamic Acid Seed Tests

In order to determine the suitable ultrasound power and serviceable LGA seeds, seed tests were carried out first before growth measurement. Sieved seeds (150-212μm sieved size for β-form seeds and 106-150μm for α-form seeds) of 3g were put into 1L prepared saturated aqueous solution with a concentration of 35g/L at 45°C and treated with ultrasound irradiation for 30 mins. Considering different shapes and the friability of two LGA polymorphic crystals, 15w and 5w ultrasound power was utilised for needle-like β-form seed tests while 25w, 15w and 5w ultrasound power was set for prismatic α-form seed tests. The final size distribution was analyzed using Morphologi G3 and compared with the initial seeds in order to determine the appropriate irradiation power in growth measurement.

7.2.3 Seeded Growth at High Supersaturation Level

To evaluate the growth of LGA at high supersaturation levels (1.9>S>1.4), 34g/L LGA solution was prepared with 1000mL distilled water and kept at 80°C for 2 hours to ensure the complete dissolution of the LGA solids. The solution was first rapidly cooled to 40°C and then slowly cooled using a cooling rate of 0.5°C/min in order to achieve the relatively high supersaturation level during the growth. 5% mass weight α-form seeds of 106-150μm were added to the saturated solution at 40°C to study the growth. Crystals were allowed to grow for 60 mins and samples were filtered every 5 mins and rinsed with methanol immediately to avoid solution retention. Finally, the particle size distribution was measured after 12 hours drying at 60°C. Growth was

observed under silent conditions and with 5W ultrasonic sonication to investigate whether or nor the employed ultrasonic irradiation was able to affect the growth of LGA. In ultrasound assisted experiments, power ultrasound was added at the same time as the seeds and throughout the entire growth period. Four experimental runs are carried out for kinetic parameters determination under different experimental conditions.

7.2.4 Seeded Growth at Low Supersaturation Level

The same experimental procedures described above were taken for growth investigation at low levels of supersaturation (1.15<S<1.4). However, after crash cooling, the temperature was isothermally maintained at 40°C and hence the supersaturation was getting smaller during growth. LGA seeds were added once a temperature of 40°C was reached, together with ultrasound irradiation. Four experimental runs are carried out for kinetic parameters determination under different experimental conditions.

7.2.5 Effect of Ultrasound on Particle Shape and Size Distribution

The particle morphology and size distribution of final produced crystals from seeded growth experiments at different supersaturation levels in Section7.2.3 and 7.2.4 are examined by Morphologi G3 and optical microscopy.

In order to investigate the ultrasound effect on LGA morphology and particle size distribution, a working solution was prepared by addition of 45g l-glutamic acid to 1L distilled water and was heated to 80°C for 2 hours for complete dissolution of chemicals. The working solution was cooled at a cooling rate of 0.5°C/min to 5°C. Variant ultrasound power (5W, 15W and 25W) was added at different stages of crystallization: 1) first stage: constant ultrasonic irradiation was initiated at the beginning of the experiment and stopped after 1 mins of spontaneous nucleation, conventional growth was allowed for 80 mins; 2) first+second stage: constant

ultrasonic irradiation was applied at the beginning of the experiment and eliminated after 15 mins of nucleation, conventional growth was allowed for 65 mins. Final crystals were filtered, washed with methanol and dried at 60°C for 12 hours then examined using Morphology 3 and microscopy to verify the ultrasound effect on crystal shape and particle size distribution after growth.

The experimental set-up consisted of a double walled glass reactor, a propeller with a stirring velocity of 200 r.p.m., a thermometer, ATR-FTIR, FBRM and 20 kHz ultrasound (Figure 7.1). Reactor temperature was controlled by the circulating oil and the experiment was conducted using WinISO software. The solution concentration was obtained from ATR-FTIR spectrum. The FBRM was used to monitor the solid phase during crystal growth.
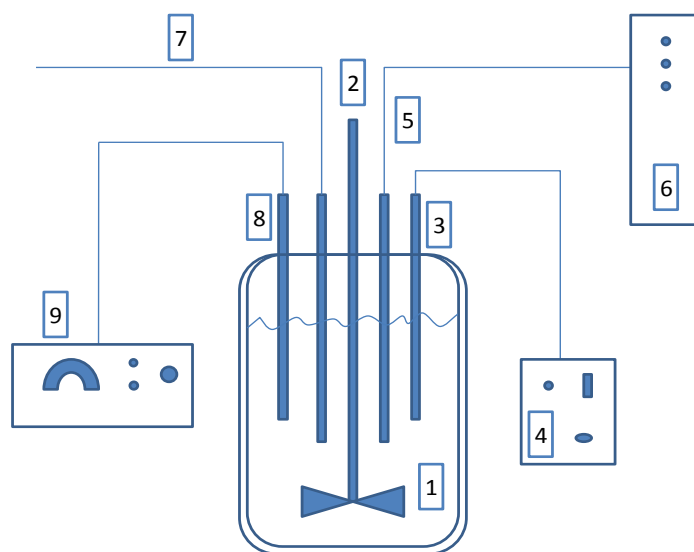
Figure 7.1: Experimental set-up consisting of (1) 1L double-jacketed reactor (2) stirrer (3) FBRM probe (4) Lasentec FBRM generator (5) ATR-FTIR probe (6) ATR-FTIR (7) thermometer (8) ultrasound horn (9) ultrasonic transducer

7.3 Results and Discussion

7.3.1 L-Glutamic Acid Seeds Test

The effect of ultrasound irradiation on β-form form seeds is shown in Figure 7.2 and suggests that with ultrasound irradiation, the particle size of the seeds was significantly reduced, even with only 5W of ultrasound. The large size peak at around 200μm disappeared and the number fraction of small particles (<10μm) markedly increased due to the breakage of the seeds. This can also be observed from the microscopic pictures that the initial needle-like seeds were fragmented to short plate particles after 30mins of 5W ultrasound treatment and even smaller powder like crystals were found under 15W ultrasound irradiation. Therefore, it is impossible to use LGA β-form seeds for growth investigation because of the fragility of the seeds. In addition, the small broken fragments are usually associated with the secondary nucleation which enhances the difficulty of ultrasound affecting growth investigation.
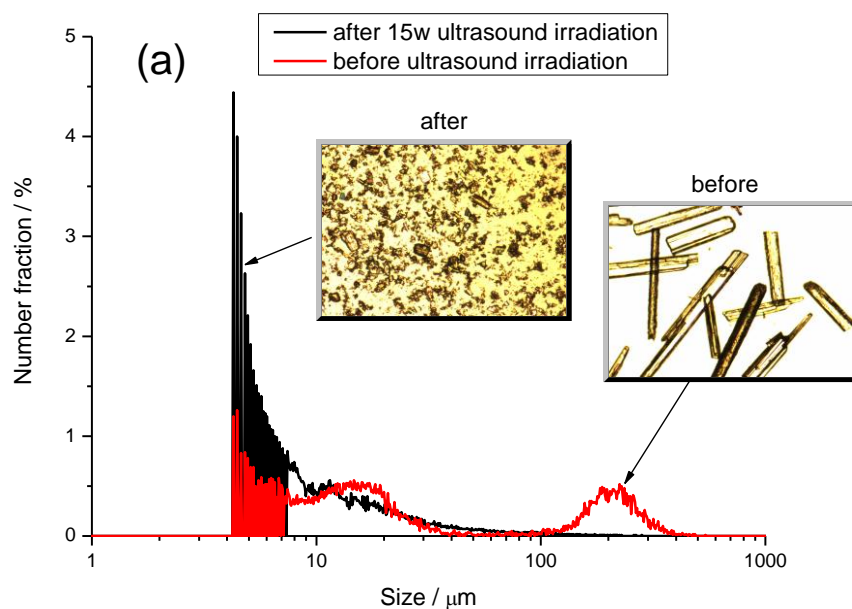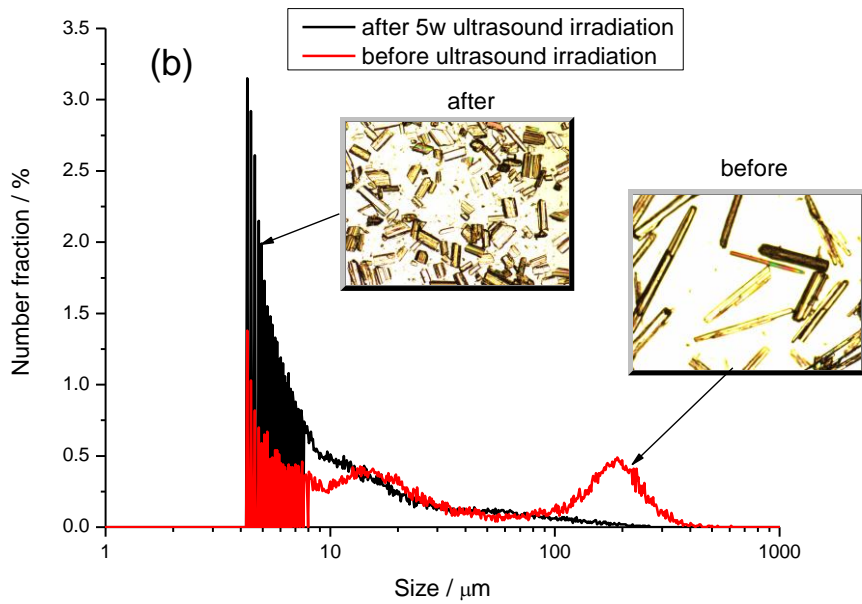
Figure 7.2: Effect of ultrasound on initial β-form seeds. (a) with 15W ultrasound power (b) with 5W ultrasound power

Figure 7.3 shows how the different ultrasound powers affect on α-form seeds at 25W, 15W and 5W respectively. The evolution of crystal size distribution shows clearly that 25W and 15W power of ultrasound can lead to breakage of the α-form seeds to some extent. This is also confirmed by the microscopic images: with 25W ultrasound, the α-form seeds were totally mashed and no initial size crystal was observed after the irradiation; with 15W of ultrasound, the large amount of small fragment crystals together with some unbroken α-form seeds revealed that a part of the initial seeds was broken in the ultrasonic field. If only 5W of ultrasound power was used, the particle size distributions showed only tiny differences in distribution peak and the number fraction and hence proved that 5W ultrasound irradiation has no effect on LGA the α-form seeds. In contrast, prismatic α-form is more suitable for LGA growth in ultrasound field than the needle-like β-form. Thus, 5W of ultrasound power and sieving size of 106~150μm α-form seeds will be utilized in the following seeding growth measurement.

(a)

(b)

132
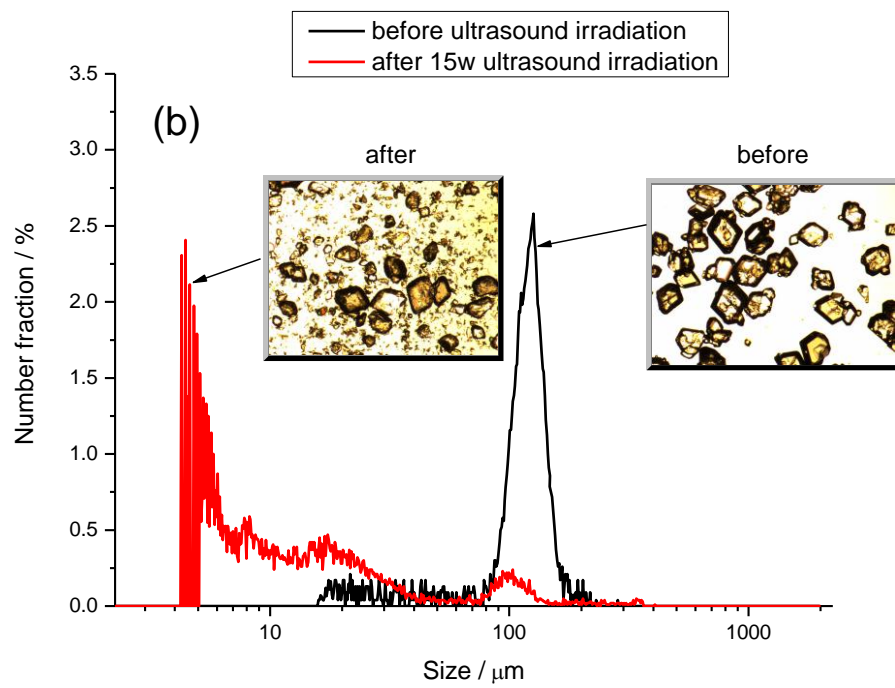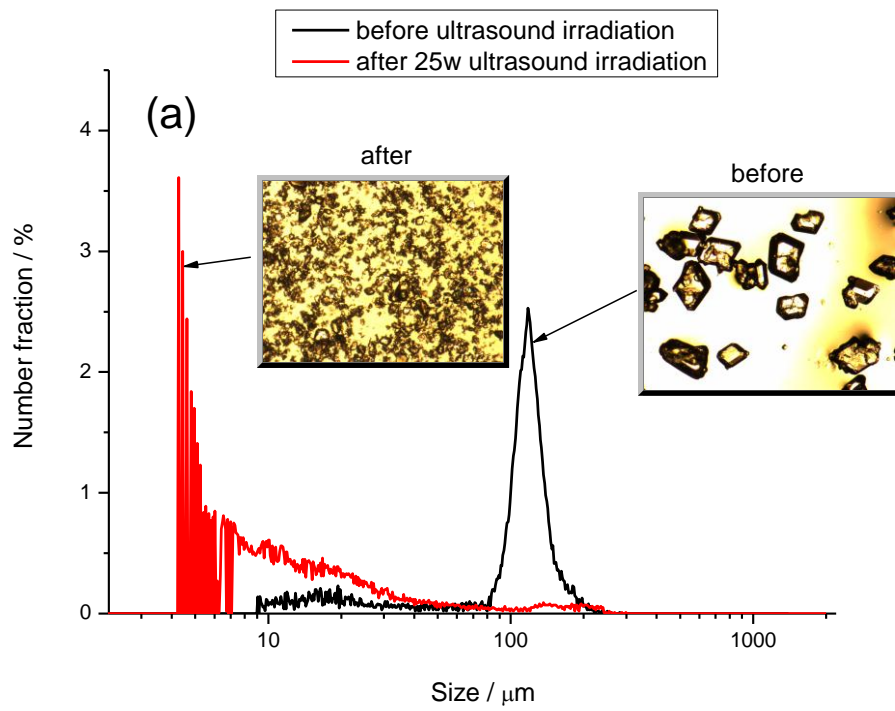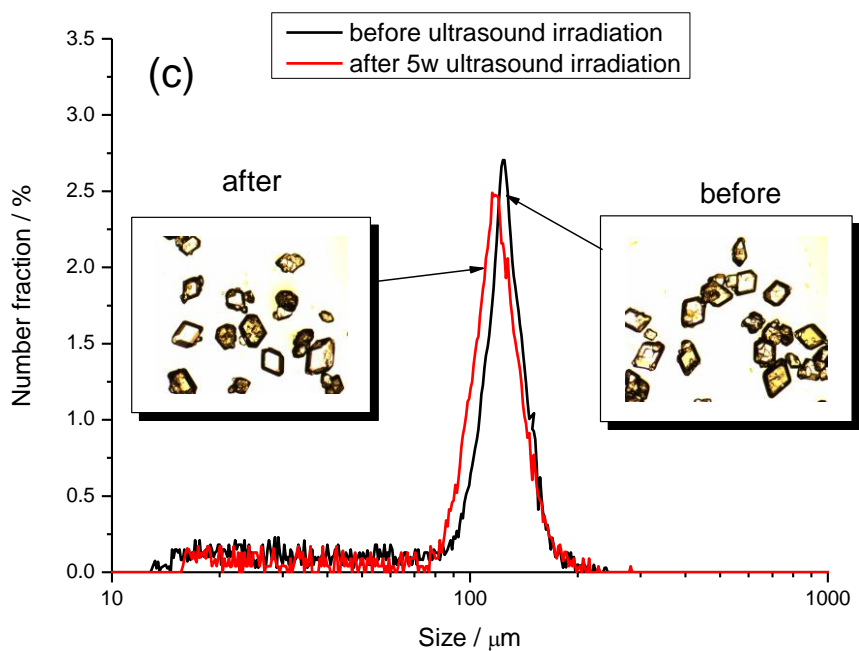
Figure 7.3: Effect of ultrasound power on LGA α-form seeds (a) 25W (b) 15W (c) 5W

7.3.2 LGA Seeded Growth at High Supersaturation Level

In order to avoid the ultrasound-induced secondary nucleation during growth, 5% of mass weight α-form seeds were added to provide sufficient surface for growth. The Lasentec Focused Beam Reflectance Measurement was applied to observe the number counts of crystals passing through the probe window during growth measurement and making sure there is growth only, rather than the nucleation and growth occurring in parallel.
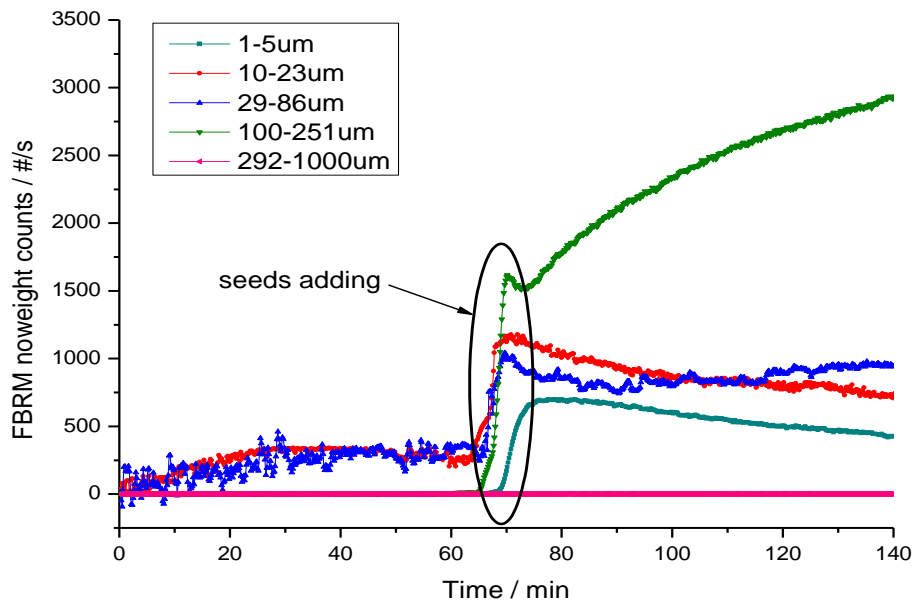
1Figure 7.4: FBRM noweight counts for different size range crystals from 1μm to1000μm

Different size ranges of crystals passing through the probe window were counted and presented in Figure 7.4. The unweight counts for the size ranging from 1 to 292μm suddenly increasing due to the adding of seeds to the solution. Because the seed sizes added were from 106μm to 150μm with no seeds growing over 292μm, identical number counts for 292~1000μm size range were found, see the pink curve. Contrarily, the reducing number of 1~5μm and 10~23μm size range of crystal indicated that no new nuclei were generated after seeding. In other words, seeds were constantly growing and resulted in an increased number of the counts above 29μm. Similar monitoring results were also found in other experiments which indicated that there was no nucleation employed through the growth measurement.
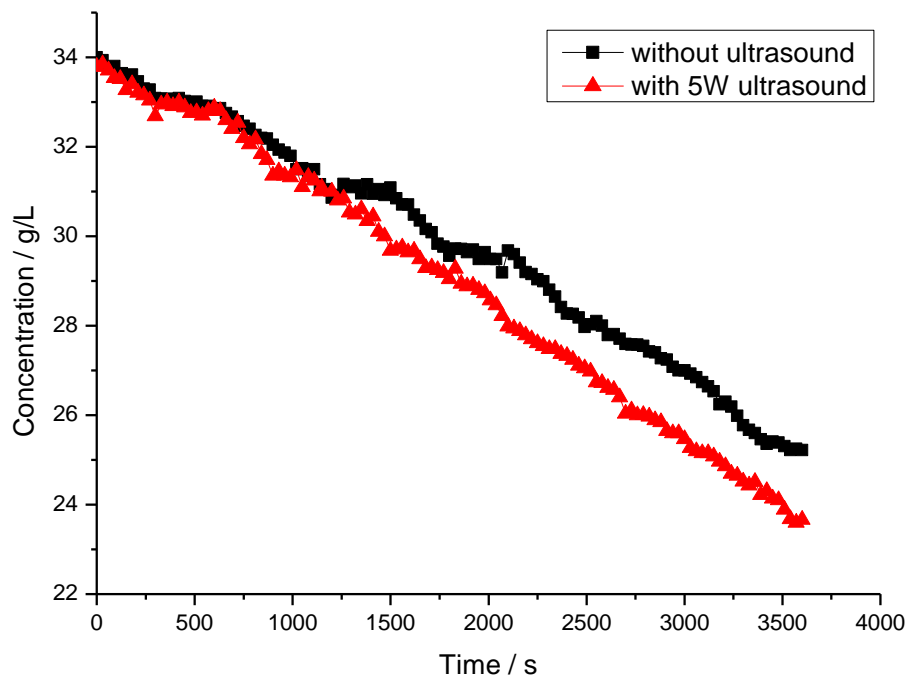
Figure 7.5: Evolution of solution concentration during the growth for silent condition and with 5W of ultrasound irradiation

The evolution of solution concentration of two growing systems is shown in Figure 7.5. With the application of 5W of ultrasound, the concentration was reduced more rapidly than that without ultrasound. Therefore, at the same supersaturation level, power ultrasound should have a stimulative effect on the growth rate of crystals. The off-line particle size distribution results without application of ultrasound are presented in Figure 7.6. The periodic parallel translation of PSD corresponded to the growth of crystals and the decrease of peak height resulted from either the partial dispersion of agglomerated seeds, or the measuring error from sampling and the instrument. Figure 7.7 depicts the measured crystal size and the supersaturation evolution during growth with 5W of ultrasound sonication.
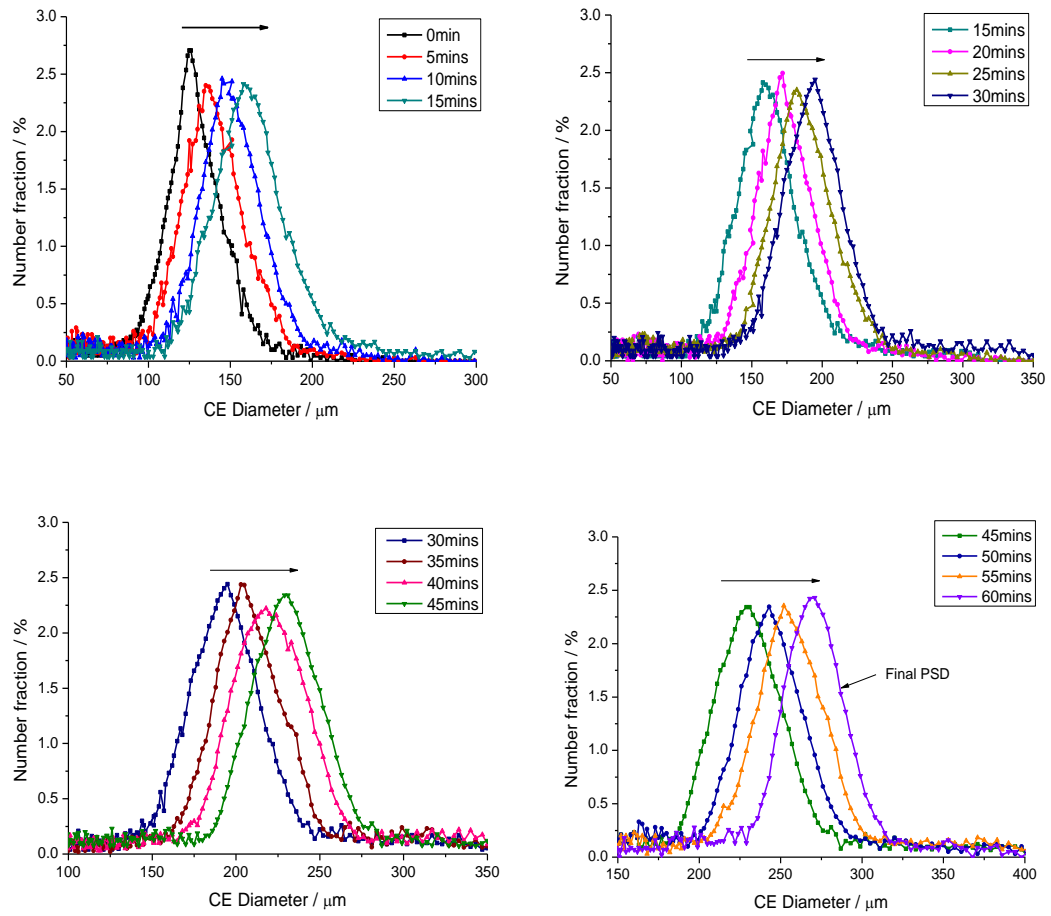
Figure 7.6: Evolution of PSD during seeding growth in silent conditions, cooling rate of 0.5°C/min
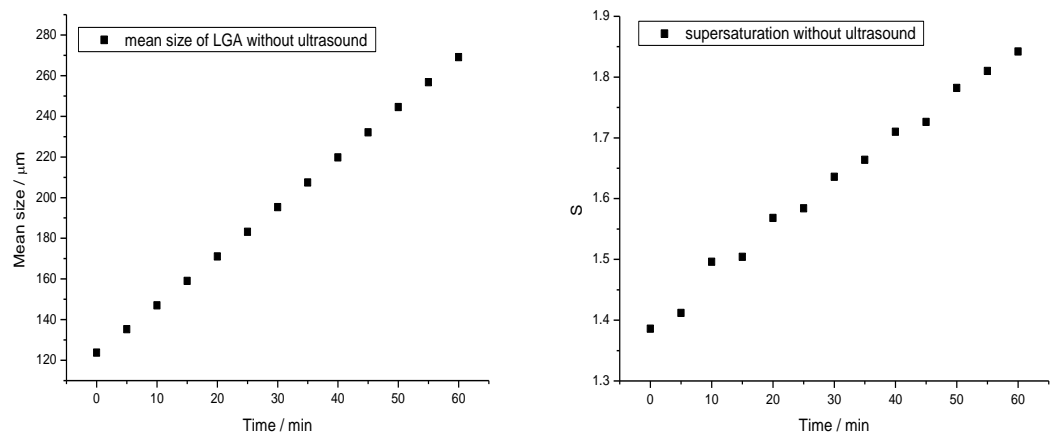
Figure 7.7: Profile of LGA mean size versus time (left) and supersaturation versus time (right) in 5w ultrasound presence growth

The growth rate of the crystals is expressed by the following phenomenological formula (Mullin, 1993):

$$G = k_g S^{n'} \tag{7.1}$$

where G is the growth rate, m/s, S is the relative supersaturation of the solution, k_g is the growth constant and n' is the growth order.

Between two near sample taking instants, it can be assumed that the equation is linear, and crystals are growing with the same shape and identical number without nucleation. The growth of the crystals can be calculated from the size difference between initial particle size L_1 and final particle size L_2 after constant growth interval t as:

$$G = \frac{dL}{dt} = \frac{L_2 - L_1}{t} \tag{7.2}$$

The corresponding supersaturation is evaluated from the measured value of two measured instants:

$$S = \frac{S_1 + S_2}{2} \tag{7.3}$$

Therefore, the growth rate plot as a function of supersaturation ratio in silent conditions and in 5W ultrasound field is shown in Figure 7.8. The growth rates at supersaturation ratio range from 1.4 to 2.0 with applied 5W ultrasound are a little superior compared with those in absence of ultrasound which conform to the estimation of concentration evolution.

The growth constant and growth order can be deduced from the logarithmic curves of G and S from Equation (7.1) with the slope equal to the growth order and the intercept equal to the logarithmic growth constant (Figure 7.9). Therefore, $n'=0.23646$ and 0.23366, $k_g=3.6457\times10^{-8}$ and 3.604×10^{-8} in the absence and presence of ultrasound, respectively. Since these values with and without ultrasound are very close to each other, it can be concluded that ultrasound did not change the kinetics and the mechanism of growth and ultrasound had a small elevated effect on LGA growth at high supersaturation levels.
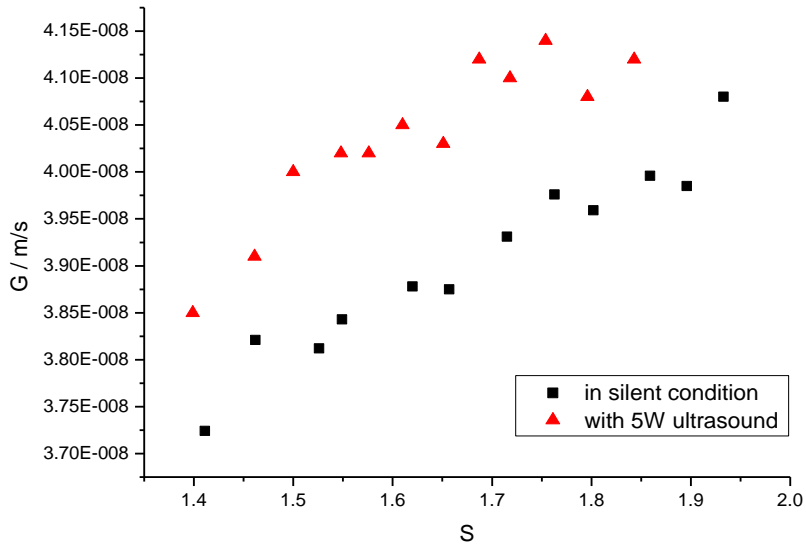
Figure 7.8: Growth rate defined as the time derivative of the integrated mean size of LGA seeds
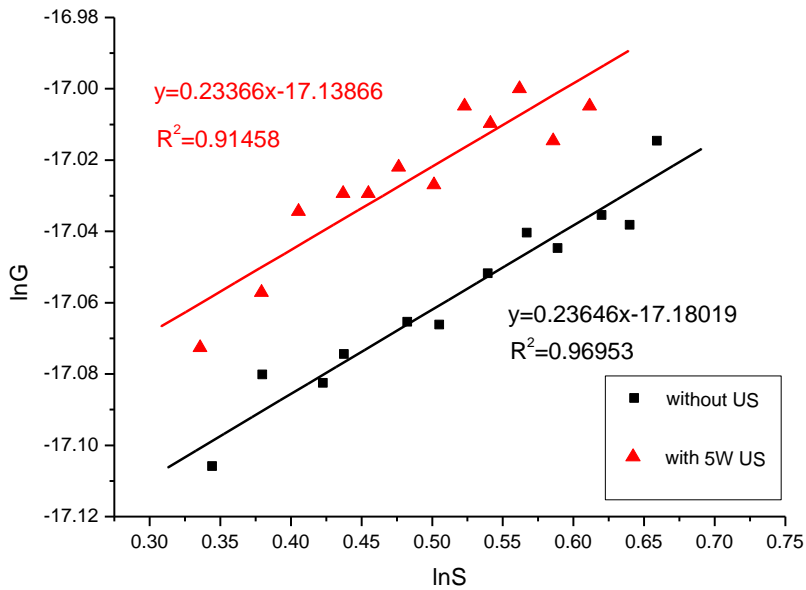
Figure 7.9: Kinetics of LGA seeding growth in presence of 5W ultrasound and in absence of ultrasound, at a cooling rate of 0.5 °C/min

7.3.3 LGA Seeded Growth at Low Supersaturation Level

It was discussed previously that ultrasound effect on crystal growth is supersaturation-dependent, experiments presented in this section were carried out at

relatively low supersaturation regions where temperature was kept constant and no cooling rate was applied. Without application of cooling, solution supersaturation decreased during the growth from, initially, 1.4 to about 1.15, see Figure 7.10. With the same initial seeds, the particle size exhibited faster gain after 20 mins of growth where 5W ultrasound was applied. Nevertheless, the supersaturation evolution did not show clear variation for both experimental systems, possibly because of the slow growth rate.
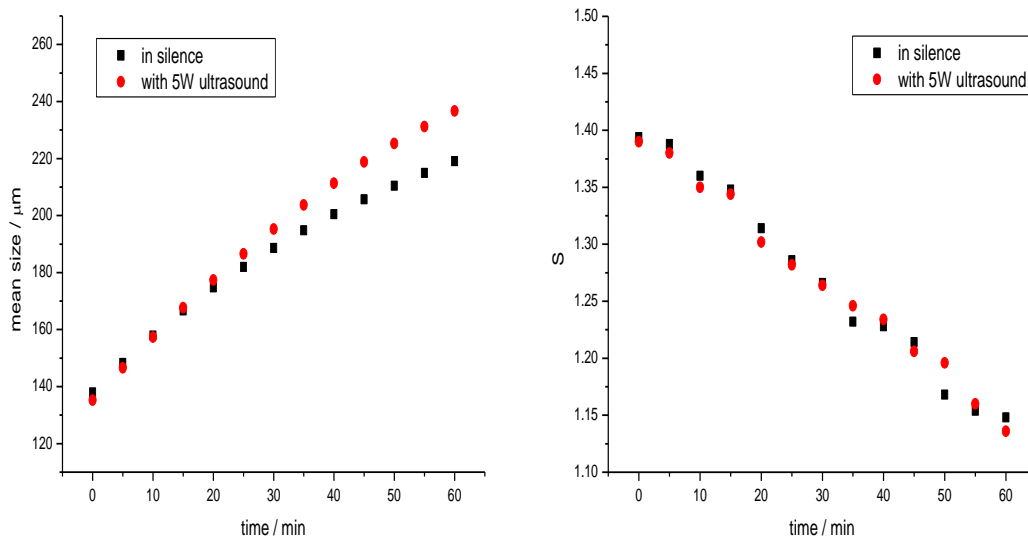
Figure 7.10: Evolution of LGA PSD (left) and solution supersaturation (right) in absence of ultrasound and in presence of 5W ultrasound during growth, at constant temperature 40°C

Table 7.1 lists the recorded particle size, solution concentration and the calculated growth rate. It can be seen that the growth rates in presence of ultrasound were explicitly greater than that in absence of ultrasound in all the supersaturation ranges under investigation. This result differs from the growth at high supersaturation levels, which indicated the postulate that ultrasound effect on crystal growth is supersaturation dependent. The logarithmic plots of the growth rate, G, as a function of supersaturation S, are presented in Figure 7.11. From the slope of linear regression line, the apparent growth order without ultrasonic irradiation was found to be 4.70532. On the other hand, a decreased apparent growth order was obtained, n'=3.9237, when 5W ultrasound was applied. The interception resulted in the k_g= 7.10×10^{-9} and

1.09×10^{-8} in the absence and presence of ultrasound, respectively. It can be concluded that the increase of k_g is the main reason for the improvement of growth rate in the ultrasound field. The growth rate constant is a function of the active growth sites on the seeds surface, the increase of growth constant in the presence of ultrasound revealed that ultrasound irradiation effectively increased the growth sites on the seeds for the incorporation of solute units. It also points to the surface reaction-control both in the absence and presence of an applied ultrasound field.

Table 7.1: Evolution of solution concentration, supersaturation, PSD and calculated growth rate in absence and in presence of ultrasound during growth from 34g/L solution at 40°C

Time t, (s)	Equilibrium concentratio n C*, (g/L)	Concentration C, (g/L)		Supersaturation S, (-)		Mean size L, ($\times10^{-6}$m)		Growth rate dL/dt, (m/s)	
		silent	5w US	silent	5w US	silent	5w US	silent	5w US
0	24.369	33.970	33.873	1.394	1.390	137.96	135.25	1.39E-8	1.81E-8
300	24.369	33.824	33.629	1.388	1.380	148.31	146.56	1.48E-8	1.99E-8
600	24.369	33.142	32.898	1.360	1.350	157.88	157.30	1.60E-8	2.14E-8
900	24.369	32.849	31.728	1.348	1.344	166.67	167.68	1.73E-8	2.50E-8
1200	24.369	32.021	31.241	1.314	1.302	174.80	177.40	1.88E-8	2.55E-8
1500	24.369	31.339	30.802	1.286	1.282	181.97	186.58	2.08E-8	2.80E-8
1800	24.369	30.851	30.364	1.266	1.264	188.60	195.28	2.21E-8	2.90E-8
2100	24.369	30.023	30.071	1.232	1.246	194.84	203.68	2.39E-8	3.06E-8
2400	24.369	29.925	29.389	1.228	1.234	200.48	211.33	2.71E-8	3.24E-8
2700	24.369	29.584	29.145	1.214	1.206	205.67	218.83	2.93E-8	3.46E-8
3000	24.369	29.463	28.268	1.168	1.196	210.47	225.25	3.19E-8	3.58E-8
3300	24.369	28.122	28.268	1.154	1.160	214.91	231.22	3.45E-8	3.77E-8
3600	24.369	27.976	27.683	1.148	1.136	219.08	236.65		
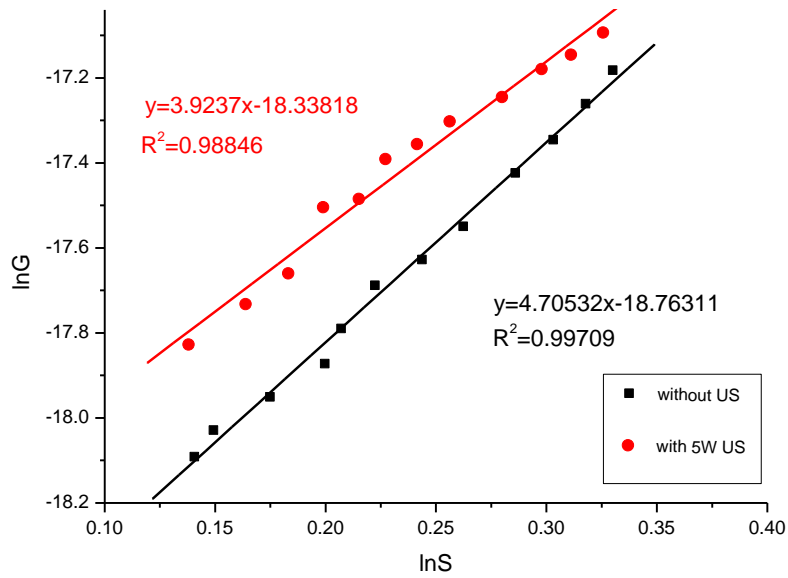
Figure 7.11: Kinetics of seeded growth LGA with 5W ultrasound and without ultrasound, at constant temperature 40°C
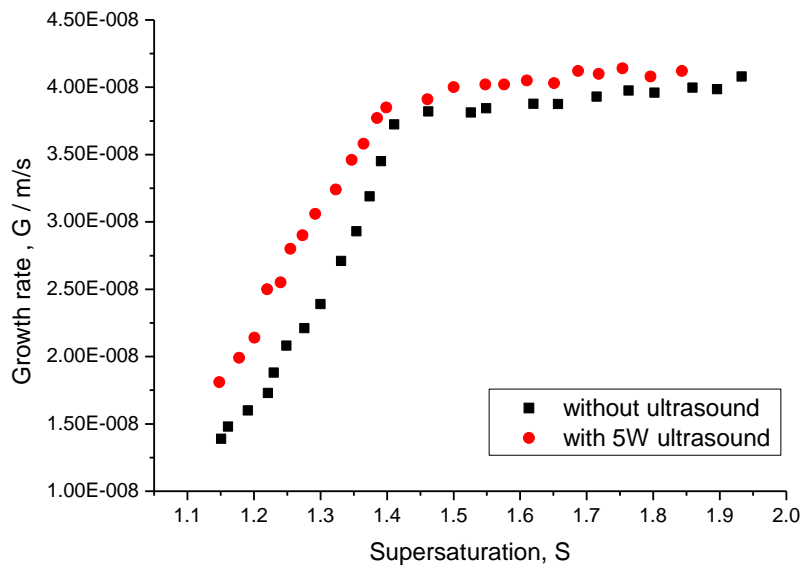
Figure 7.12: Growth rate of α-LGA under silent conditions and 5W ultrasonic irradiation conditions versus supersaturation

To clarify the ultrasound effect on α-form LGA growth, the growth rate versus solution supersaturation ratio plot for both low and high level ranges in the absence and presence of ultrasound is demonstrated in Figure 7.12. The evaluated growth parameters from four experimental runs for varied supersaturation levels provide

consistent results, as shown in Table 7.2, indicating the reliable experimental results.

Table 7.2 Growth kinetics parameters from four experimental runs

High S	Without ultrasound		With 5W ultrasound	
Experimental Run	k_g	n'	k_g	n'
Run 1	3.4711×10^{-8}	0.23124	3.4753×10^{-8}	0.23913
Run 2	3.6457×10^{-8}	0.23646	3.6040×10^{-8}	0.23366
Run 3	3.6025×10^{-8}	0.24021	3.6146×10^{-8}	0.23160
Run 4	3.5432×10^{-8}	0.23357	3.5913×10^{-8}	0.23521
Low S	Without ultrasound		With 5W ultrasound	
Experimental Run	k_g	n'	k_g	n'
Run 5	8.0365×10^{-9}	4.6238	1.2581×10^{-8}	3.7621
Run 6	7.6131×10^{-9}	4.7522	1.1893×10^{-8}	3.8116
Run 7	7.1019×10^{-9}	4.7053	1.0862×10^{-8}	3.9237
Run 8	8.1204×10^{-9}	4.5930	1.1142×10^{-8}	3.8216

It can be seen explicitly from the results that ultrasound did exhibit a positive effect on growth. In the presence of ultrasound with power of 5W, the growth rates were superior over all the supersaturation ranges than where no ultrasound was applied. However, the ultrasonic improvement was especially outstanding at the low supersaturation level, which is in agreement with the previous theoretical study (Arakelyan, 1987). Note that the higher limit of the low supersaturation in this work is about 1.4, and above 1.4, the α-form LGA growth rates were likely to be the same and ultrasound contribution became restricted compared with the low supersaturation regions.
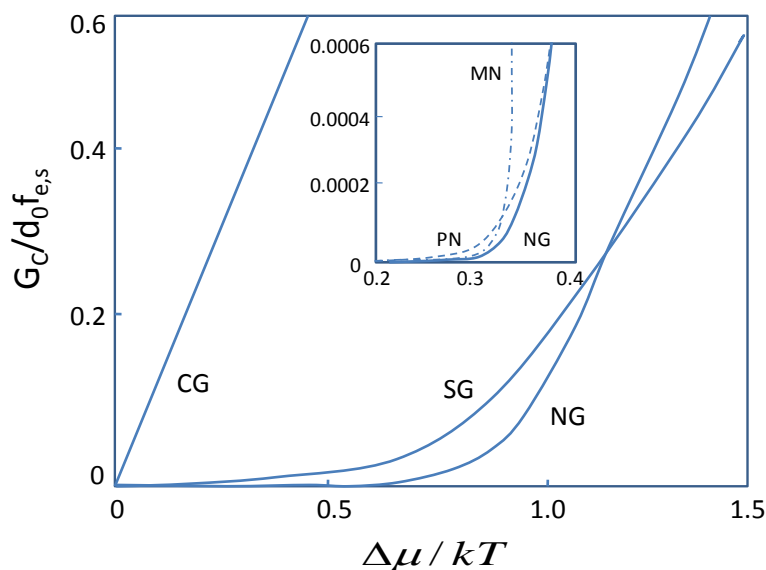
Figure 7.13: Supersaturation dependence of the growth rate: curve of CG for continuous growth; curve SG for spiral growth; curve NG for nucleation-mediated growth; curves PN and MN for polynuclear and mononuclear growth, respectively (Kashchiev, 2000)

This result is contrary to the ultrasound retardation effect reported by Dalas (Dalas, 2001) who considered ultrasound influenced the dehydration and surface diffusion steps of the growth units and hence the growth rate. However, the ultrasound effect on the dehydration process was not observed in the experiments. In this case, the parabolic growth rate curve reflected a nucleation-mediated 2-D growth mechanism according to the dependence of growth rate on supersaturation given by Kaschiev (Figure 7.13), and it is more likely that seeding growth of α-form LGA experienced the polynuclear growth rather than the mononuclear growth which also coincided with the growth kinetic results. It was well introduced in Chapter 2 that the growth process comprises two steps in series: 1) the mass transfer or the diffusion of growth units through the bulk fluid boundary layer from the supersaturated solution, and 2) the surface reaction process including the adsorption of the growth units on the growing surface, the diffusion of the growth units along the surface and the incorporation of the growth units to the growth sites. As these two steps are consecutive, the slower step will be rate determining. Therefore, the crystal growth can be either diffusion-controlled or surface integration-controlled distinguished by the

corresponding rate determining step. In the 2-D growth mechanism, the supersaturation is normally high and growth is surface-integration controlled. To explain the influence of ultrasound irradiation on growth rate, the possible hypothesis is at low supersaturation, the application of ultrasound efficiently expedites the surface nucleation and provides more active growth sites for crystal growth, this had been indicated by the calculated greater growth constant where ultrasound was utilised. For crystal growth in highly supersaturated solution, as the supersaturation is high enough for seed surface nucleation and already the existing sufficient growth sites, the ultrasonic reinforced effect becomes finite compared with that without ultrasound. Whereas, ultrasound did not affect or change the mechanism of growth for different supersaturation levels, this is consistent with the observation results of their apparent growth orders.

7.3.4 Effect of Ultrasound Irradiation on Crystal Characteristics

7.3.4.1 Crystal Morphology and Particle Size Distribution after Seeded Growth

The crystals recovered from α-form LGA seeded growth at different supersaturation levels were examined using microscopy. The shape of α-form crystals was retained in their original prismatic shape after growth and had not been modified by applying 5W of ultrasound, as seen in Figure 7.14. Figure 7.15 exemplifies the final particle size distribution of crystals produced after seeded growth with and without ultrasound. As can be seen, the particle mean sizes of grown LGA crystal with treatment of 5W ultrasound are 236.6μm and 269.1μm at low supersaturation levels and high supersaturation levels, respectively; which is larger than the size of those grown without ultrasound, about 219.1μm and 265.6μm due to the faster growth rate enhanced by ultrasound irradiation. However, the narrowed particle size distributions were not found when low power ultrasound was applied.
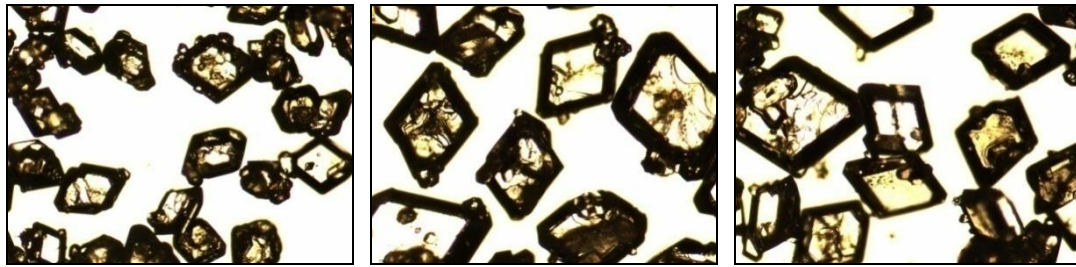
Initial seeds   Grown crystals in silence   Grown crystals with ultrasound

Figure 7.14: Microscopic images of α-form LGA crystals obtained from seeded growth at low supersaturation levels
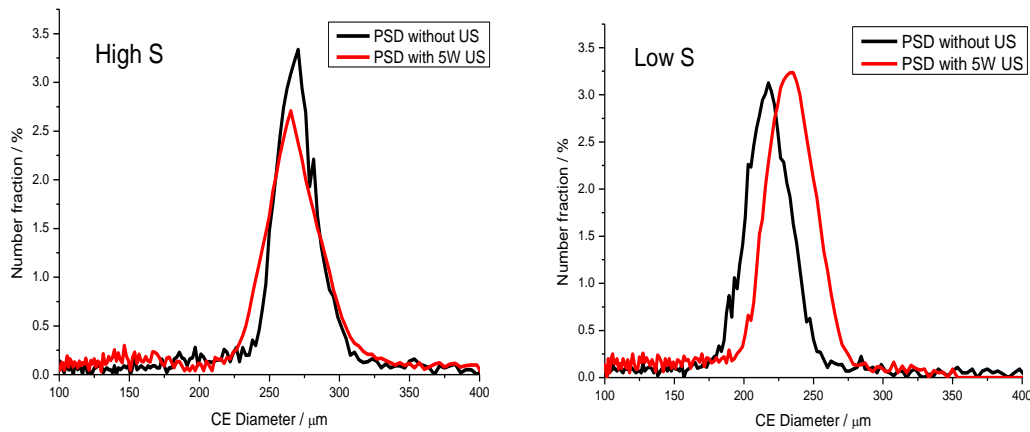
Figure 7.15: Particle size distribution of α-form LGA crystals after growth, with 106~150μm initial seeds: grown at high supersaturation (left) and low supersaturation (right)

7.3.4.2 Crystal Morphology and Particle Size Distribution in Spontaneous Crystallization

Figure 7.16 illustrates the variation of final particle size distribution in the absence of, and short bursts of 5W, 15W and 25W ultrasound at the first crystallization stage. It can be clearly seen that the mean size of the final LGA crystal was about 120μm without ultrasonic irradiation with the maximum crystal size over 500μm due to the agglomeration of the particles. When ultrasound was added, the final crystal sizes were reduced, with a mean size of 107μm where 5w ultrasound was applied and only 50μm where 25w ultrasound power was utilized. In the mean time, the number fraction of large size crystals was decreased, indicating that ultrasound commendably

prevented particles from agglomeration. On the other hand, raising the ultrasound power resulted in a narrower size distribution; this can be ascribed to the ultrasound initialising smaller and more uniform nuclei at the nucleation stage for crystal growth in succession. This can also be observed from microscopic pictures of grown LGA crystals in Figure 7.17, more regular and even crystals were obtained with the application of ultrasound, and increasing the ultrasound power did not modify the morphology of the crystals. The shape of the crystal depends on the growth rate on each crystal surface, and the unchanged LGA morphology implied that the ultrasound effect is kinetic rather than equilibrium nature which is consistent with the ultrasound assisted spontaneous precipitation investigation of vaterite presented by Dalas (Dalas, 2001).
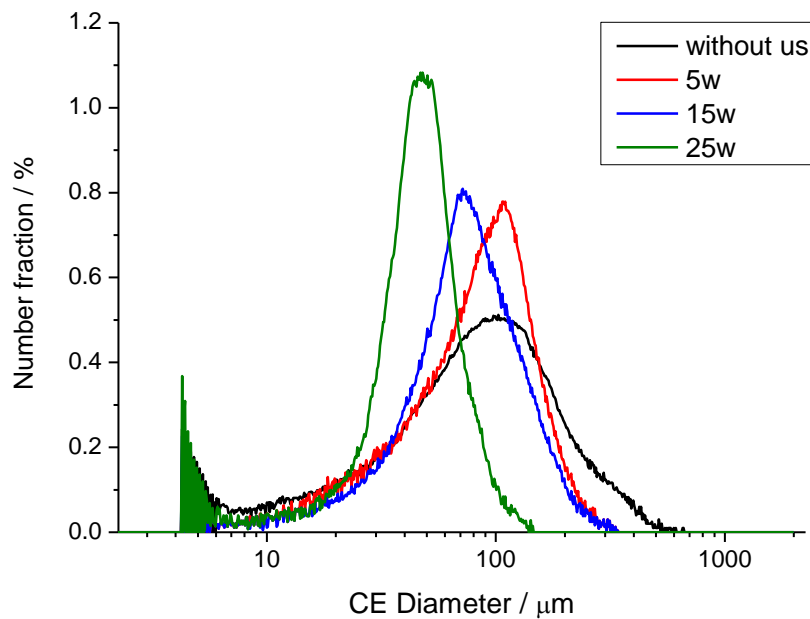
Figure 7.16: Comparison of LGA final PSD with ultrasonic irradiation at first stage

(a) Grown crystals without ultrasound   (b) Grown crystals with 5w ultrasound

(c) Grown crystals with 15w ultrasound   (d) Grown crystals with 25w ultrasound
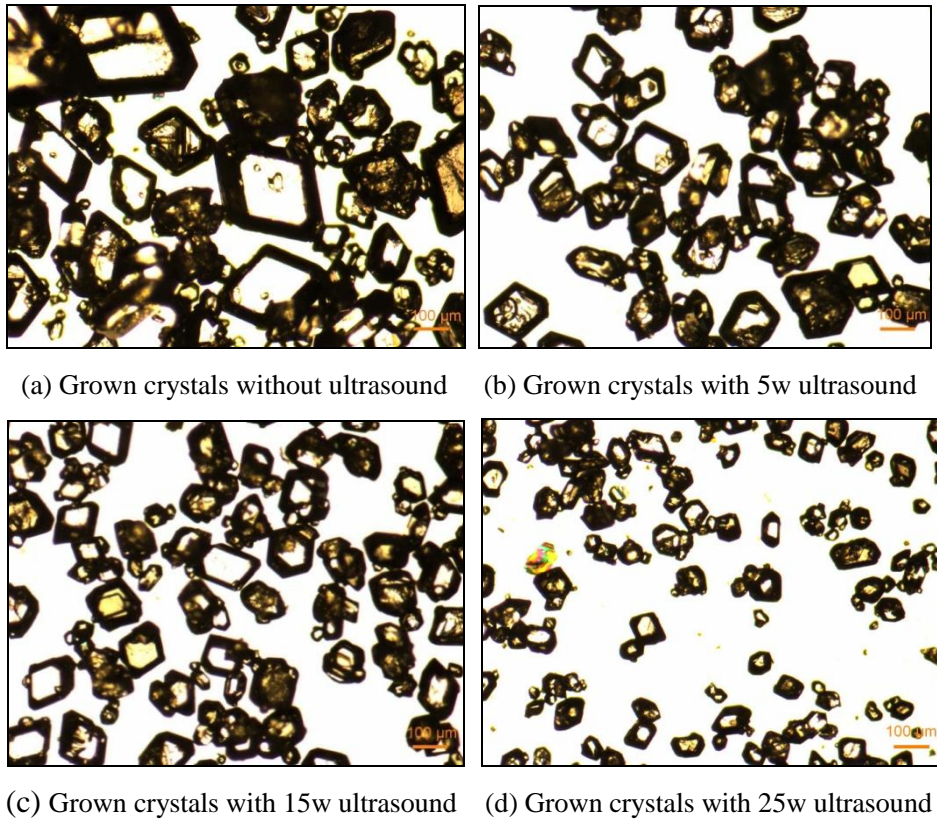
Figure 7.17: Microscopic images of grown LGA crystals with ultrasound application at first stage

The final particle size distribution of different powers of ultrasound application at the first and second stage is presented in Figure 7.18. Compared with the large particle size and widespread size distribution of crystals produced in silent conditions, the mean size was reduced to 60μm and notably narrower particle size distribution was detected where 5w ultrasound was applied, the amount of smaller crystals ($< 40\mu m$) was increased due to the ultrasound induced secondary nucleation. At higher ultrasound powers of 15w and 25w, the mean size of LGA crystal was only 10.4μm and 8.4μm, respectively. On top of that, the amount of small crystals under 10μm was increased dramatically with increasing the ultrasound power and almost no large crystals were observed. This was confirmed by photomicrographs of final crystals shown in Figure 7.19. 5W ultrasound irradiation resulted in a less sharp crystal edge and more spherical crystals in shape with hundreds of microns in size as well as some fine particles, possibly due to the abrasion of the crystal surface, see Figure 7.19(a). The large amount of small and undefined crystals produced under 15W and 25W

147

ultrasound irradiation, as shown in Figure 7.17(c) and (d), suggest that higher ultrasound power and intensity can facilitate prolific nucleation to the solution.

Therefore, the particle size and crystal morphology of LGA can be potentially improved and controlled through the judicious application of precise ultrasound power at different crystallization stages with various insonation intervals. With a short burst of ultrasound to the nucleation stage, the crystallization is allowed to produce uniform, relatively large and well-shaped crystals. With a longer time and continuous bursts throughout the nucleation and growth stages, the isolated crystals were very small.
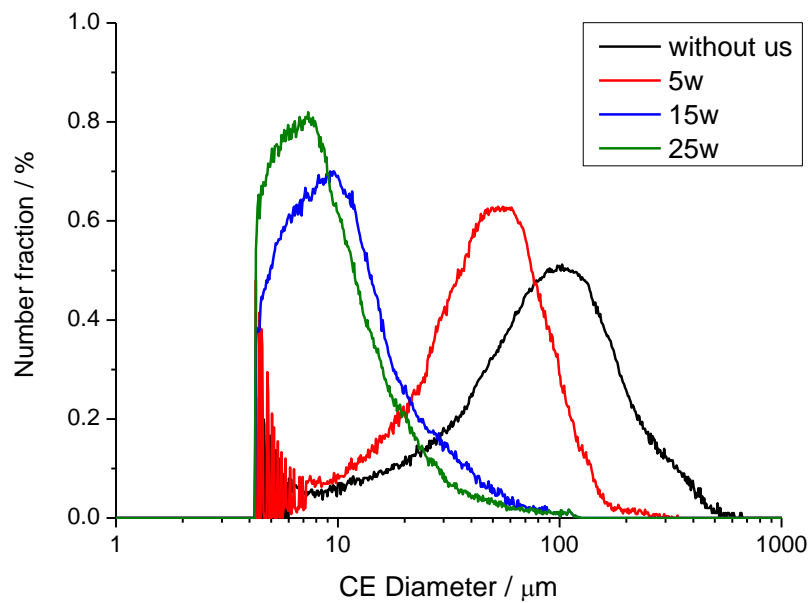
Figure 7.18: Comparison of LGA final PSD with ultrasonic irradiation at first and second stage
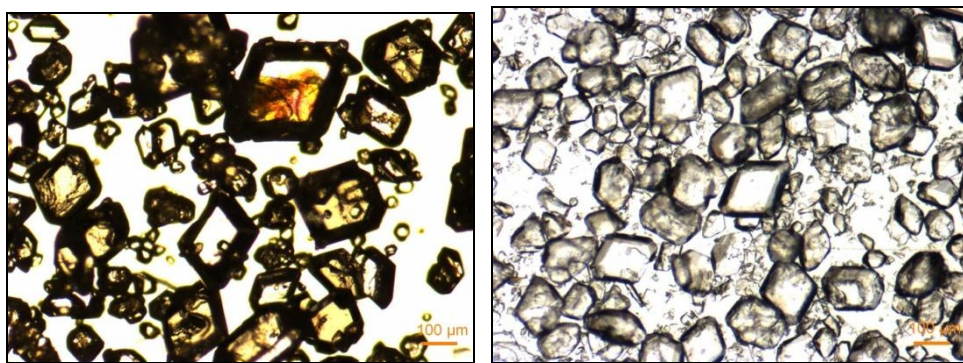
(a) Grown crystals without ultrasound   (b) Grown crystals with 5w ultrasound
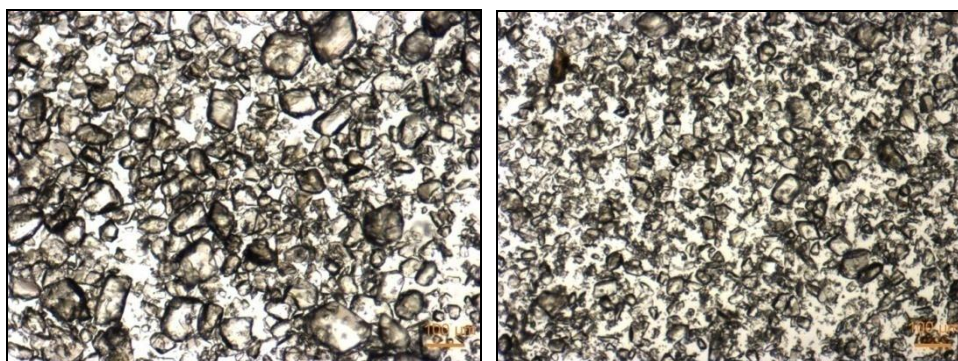
(c) Grown crystals with 15w ultrasound	(d) Grown crystals with 25w ultrasound

Figure 7.19: Microscopic images of grown LGA crystals with ultrasound application at first and second stage

7.4 Conclusion

The effect of 5W ultrasound irradiation on LGA growth was studied based on the seeded experiment. The results showed that the effect of ultrasound on α-LGA growth rate was supersaturation dependent: appeared explicitly accelerated with 5w ultrasound power at low supersaturation ratio (< 1.4 in this case study) where the growth constant was increased by ultrasound and had almost no effect at high supersaturation ratio. The possible mechanism is given as 2-D nucleation growth: ultrasound irradiation enhances the surface nucleation and provides more active growth sites for full growth at low supersaturation, no evident improvement in surface nucleation when supersaturation is adequately high. However, the observed effect of ultrasound on α-LGA cannot spread to wider ultrasound power ranges because the increase of ultrasound power led to the secondary nucleation and the breakage of seeds, that is, no growth behaviour could be observed.

This chapter also investigated the ability of using ultrasound to manipulate the particle size and crystal morphology during spontaneous crystallization. It was found that uniform, relatively large and even crystals with narrowed particle size distribution can be obtained by applying a short burst of ultrasound to the nucleation stage. Longer insonation throughout the nucleation and growth stage can result in small crystals through prolific nucleation, and less sharp edged and more spherical crystals can be isolated with low ultrasonic power sonication.

Chapter 8

Population Balance Modelling and Simulation of Alpha L-Glutamic Acid Seeded Growth

Summary: Population balance modelling is proposed in this chapter to simulate the α-LGA seeding growth process. The predicted concentration profile, growth rate and crystal size distribution with and without irradiation of ultrasound are compared with the former experimental data obtained in Chapter 7.

8.1 Introduction

The specific crystal habit and desirable particle size distribution are the challenging tasks in industrial crystallization and, in order to achieve the desirable particle size distribution at an industrial level, controlling supersaturation via cooling profile determination and optimizing the operating conditions like agitation, seeding and acidification are the routine control variables in the crystallization process. Ultrasound is another interesting approach to precipitation processes to control the crystal shape and tailor the size distribution in the past few decades. No matter which route is adopted in crystallization process control, laboratory work is essential, but numerical modelling development of crystallization is also very important for efficient process control and scale-up investigation. The population balance approach, together with the crystallization kinetics model describing the particle characteristics, provides the potential for presenting the progress of particle density distribution

The landmark population balance concept was raised by Randolph and Larson and applied to the simulation of the crystallization process in 1971(Randolph and Larson, 1971). Later on, different crystallization models were developed based on the formal population balance equation. For more accurate description of crystal size, a bi-dimensional population balance model was presented by Puel et al.(Puel et al., 2003a, Puel et al., 2003b) to simulate the evolution of two characteristic size dimensions (the length and the width) of needle-like crystals while Oullion et al. (Oullion et al., 2007b, Oullion et al., 2007a) employed the model on plate-like crystal seeded crystallization process. A multi-dimensional population balance was utilized to investigate the growth of rod-like l-glutamic acid crystals and potassium dihydrogen phosphate (Ma et al., 2007). Studies looking at the l-glutamic acid precipitation with the help of population balance modelling are numerous. Scholl et al. (Scholl et al., 2007) combined population balance modelling and process analytical technologies to identify the α-LGA seeded growth mechanism. They also proposed the effect of agglomeration on l-glutamic acid seeded batch crystallization. In their population balance model, the nucleation, growth and agglomeration kinetics were accounted for

particle size distribution prediction. The morphological population balance modelling was given by Ma and Wang (Ma and Wang, 2012) for l-glutamic acid facet growth kinetics model identification and experimental validation.

Although comprehensive numerical simulation models have been developed for the crystallization process, there are very few reports on ultrasound involved crystallization system simulation and modelling due to the complication of condition assumption and parameter evaluation. Amount those, Kordylla et al. (Kordylla et al., 2009) proposed a crystallization model based on one-dimensional population balance considering a kinetic expression for ultrasound induced nucleation mechanism to predict the concentration, nucleation rate and particle size distribution. They assumed a heterogeneous nucleation mechanism together with secondary nucleation and used physical properties instead of model parameters during modelling and hence, evaluated the optimized ultrasound application for the desired product specifications. Yasui et al. (Yasui et al., 2011) extended and developed this model to nanoparticle sonochemical synthesis of $BaTiO_3$ numerical simulation. Their study suggested that aggregation only took place between primary particles and other aggregates but the nanoparticle aggregates were disintegrated by acoustic cavitation. A theoretical model correlating the nuclei number that generated by ultrasound and the solution temperature and pressure was addressed by Saclier (Saclier et al., 2010). The model based on Hicking's mechanism illustrated that the increase of supersaturation level during crystallization resulted from the extremely high pressure at the final stage of acoustic cavitation bubbles through which the equilibrium freezing temperature was increased. Recently, Ubbenjans (Ubbenjans et al., 2012) presented a model for the ultrasonic wave propagation in the total growth system of melt, and simulated the melt flow and the temperature distribution during crystallization. The study pointed out that ultrasound irradiation effectively helped the reduction of the harmful diffusion boundary layer.

The simulation work in this chapter focuses on the seeded growth of l-glutamic acid (LGA) in presence of ultrasound treatment and a one-dimensional population balance model is used to simulate the concentration profile and growth rate, as well as the

crystal size distribution. The ultrasound effect is addressed in the kinetic parameter of growth rather than the individual physical-based parameters in the simulation model according to the empirical kinetic expression aimed at providing reliable evidential data for α-form LGA ultrasonic assistance growth mechanism analysis. The simulation was delivered by applying the commercial software package gPROMS.

8.2 The gPROMS Process Modelling System

gPROMS is a general process modelling system package developed by Process System Enterprises Limited. It is an equation-oriented modelling tool that provides a general purpose modelling environment for process and equipment design and development as well as the optimization of operating processes. The main platform of gPROMS is the gPROMS ModelBuilder with the fundamental entity MODEL, which depicts the physical and chemical properties of plant; TASK, which represents the employed control action, governed relationship and operation procedures on the plant; and PROCESS, which generally comprises a TASK driving a MODEL. Therefore, gPROMS can handle a complex realistic modelling process.

Traditional simulation systems are either discrete or continuous and since gPROMS combines discrete and continuous processes, it is particularly suitable for particulate process modelling and simulation. Other advantages of gPROMS are its capability for steady-state and dynamic simulation, ability to apply high-level declarative modelling, carrying out optimization activities, parameter estimation and data reconciliation. Another novel feature of gPROMS is that it enables description and handling of model discontinuities of a very general nature and defines different equation forms under different conditions (Pantelides and Oh, 1996). In this case, a population balance approach is adopted to describe the dynamic change of crystal number density and size during the batch growth. However, population balance models normally consist of the partial differential equations (population balance equations, etc.), the ordinary differential equations (mass balance equations, etc.), the integral equations

(solid suspension calculation from particle size distribution, etc.) and the algebraic equations (solid-liquid equilibrium, etc.) which results in the difficulty of solving such integral-partial differential algebraic equations (IPDAEs). In gPROMS, the IPDAE system can be reduced to ordinary differential and algebraic equations (DAEs) by discretizing the distribution domain between the minimum and maximum crystal size and a number of different methods have been performed on gPROMS MODELS for discretization schemes and finite difference methods (Pantelides and Oh, 1996, Lee et al., 1999). Thus, population balance mathematical models can be easily solved by its advanced solution algorithms, the additional details of the finite difference method to solve population balance equation was reported in (Lee et al., 1999). Table 8.1 provides the available numerical model in gPROMS accompanied by the approximation order for partial derivatives and integrals corresponding to each finite difference method. As there is no numerical method suitable for solving all the problems, it is important to select the correct method for efficient and accurate solution procedure.

Table 8.1 Numerical method for distributed system in gPROMS (Ltd., 2004)

Numerical method	Keyword	Order(s)	Partial derivatives	Integrals
Centered finite difference method	CFDM	2,4,6	YES	YES
Backward finite difference method	BFDM	1,2	YES	YES
Forward finite difference method	FFDM	1,2	YES	YES
Orthogonal collocation on finite elements method	OCFEM	2,3,4	YES	YES
Gaussian quadratures		5		YES

As a high-fidelity and relatively new mathematic commercial modelling programmer, gPROMS has been used in laboratory scale batch crystallization and continuous crystallization processes for particle size and size distribution prediction. In the early 1990s, this general purpose software package was developed (Barton and Pantelides, 1994) and latterly utilized in a continuous mixed suspension mixed product removal

crystallization unit (CMSMPR) modelling potassium sulphate cooling crystallization process (Pantelides and Oh, 1996). The use of gPROMS in practical industrial batch plant operation simulation represented its capacity in process modelling, from pure continuous to batch (Winkel et al., 1995). Asteasuain et al. resolved dynamic simulation and the start-up optimization problem based on the interface gOPT of gPROMS simulator (Asteasuain et al., 2001) and they also presented a gPROMS implemented comprehensive steady-state model for high-pressure polymerization of ethylene in a tubular reactor (Asteasuain and Brandolin, 2008). To date, gPROMS has been employed to simulate and predict the crystal size properties in different solubility models (Widenski et al., 2010) and study the parameter estimation as well as the optimization of secondary nucleation for batch crystallization processes (Kalbasenka et al., 2011).

In this research work, gPROMS was adopted for LGA seeded growth kinetics simulation based on the population balance model.

8.3 The Population Balance Model of Seeded Growth

8.3.1 Population Balance Equation

The population balance approach offers the population of crystals to describe the dynamic variations of particle size and distribution during the crystallization process. Based on Randolph and Larson's theory (Randolph and Larson, 1971), the formal manner of the population balance of the crystal population density distribution $n(L)$ as a function of time t for a well-mixed constant volume batch crystallizer can be written as:

$$\frac{\partial n(L,t)}{\partial t} + \frac{\partial Gn(L,t)}{\partial L} = B - D \tag{8.1}$$

where G is the crystal growth rate, B is the birth function resulting from the nucleation and breakage, D is the death function corresponding to the agglomeration and

dissolution. It is worth noting that L in the equation is the characteristic size of the crystals. The growth in this work is assumed to be size-independent and no nucleation occurs which can be carefully designed and controlled during the growth experiment. As the agglomeration and breakage are also assumed to be negligible and not taken account of in the model, the growth only population balance equation becomes:

$$\frac{\partial n(L,t)}{\partial t} + G\frac{\partial n(L,t)}{\partial L} = 0 \tag{8.2}$$

However, in order to avoid the numerical calculation problem in gPROMS caused by the potentially large magnitude of crystal number density $n(L)$, Equation (8.2) is deduced to the logarithmic form:

$$\frac{\partial \ln n(L,t)}{\partial t} + G\frac{\partial \ln n(L,t)}{\partial L} = 0 \tag{8.3}$$

8.3.2 The Mass Balance and Growth Rate Parameters

The total mass balance of the crystal in the solution is expressed as follows:

$$\frac{dC}{dt} = 3k_v\rho_c G\int_0^{L\max} n(L,t)L^2 dL \tag{8.4}$$

where k_v is the crystal shape factor, ρ_c is the crystal density, C is the solution concentration. The model initial and boundary conditions are given as:

$$C(0) = C_{initial} \tag{8.5}$$

$$n(0,t) = 0 \tag{8.6}$$

$$n(L,0) = n_0(L) \tag{8.7}$$

with C_0 being the initial concentration of growth experiment solution while $n_0(L)$ refers to the seed size distribution. As stated before, there is no nucleation occurs but the growth only, the growth rate G is defined by the empirical equation

$$G = k_g S^{n'} \tag{8.8}$$

here k_g and n' are the crystal growth constant and growth order, respectively. S is the supersaturation ratio (solution concentration C/equilibrium concentration C*). The value of growth parameters k_g and n' are estimated from the former experimental data in Chapter 7. The predicted results will be compared with those data obtained from experiments for validation. The numerical method Backward Finite Difference Method is employed for population balance equation solution in gPROMS.

8.4 Results and Discussion

8.4.1 Seeded Growth Simulation at High Supersaturation

The various parameters used for seeding growth simulation in the absence of ultrasound irradiation are listed in Table 8.2. With first order backward finite difference discretization method and 1200 granularities for the particle size distribution domain, a typical gPROMS simulation output of reactor crystal density in natural logarithmic terms along with size and time is shown in Figure 8.1.

Table 8.2 Parameter values to describe the seeding growth process at high S in silent condition

Parameter	Value	Unit	Parameter	Value	Unit
C_{intial}	0.034	kg/L	T_{int}	40	°C
ρ_c	1560	kg/m^3	ρ_l	1000	kg/m^3
b	0.5	°C/min	k_v	0.5236	-
k_g	3.6457×10^{-8}	-	n'	0.2365	-
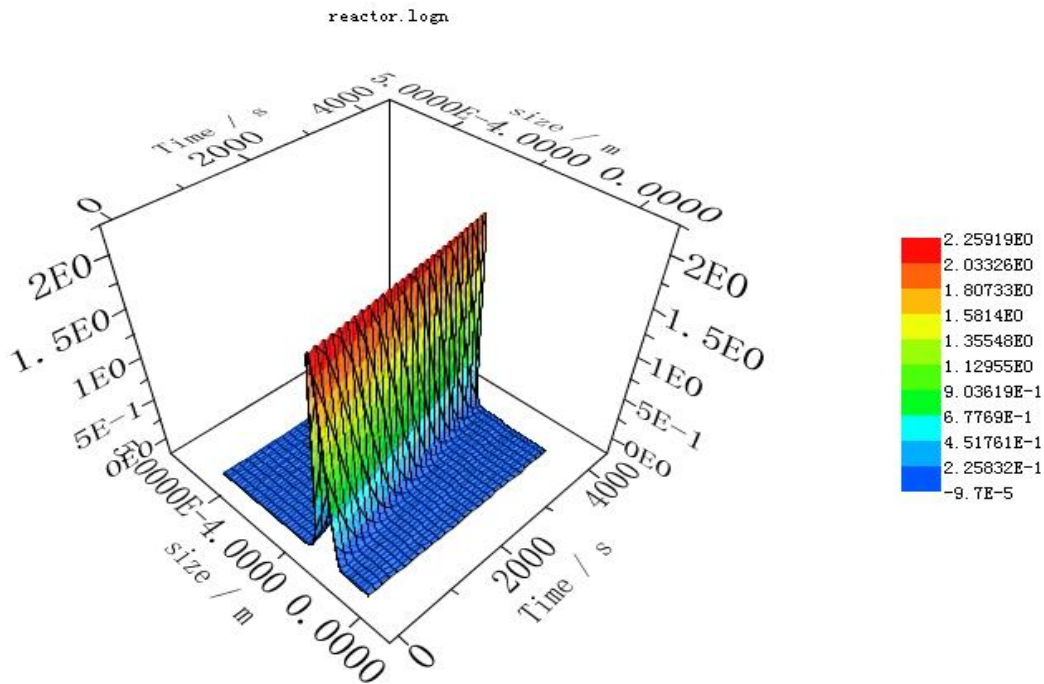
Figure 8.1: Variation of crystal population density n(L) with size (L) and time (t) for l-glutamic acid seeding growth in absence of ultrasound at high supersaturation ratio

It can be observed from Figure 8.1 that the peaks of crystal density shifted from initial small seed size to final larger size, reflecting the growth of LGA seeds. As the process did not experience nucleation and growth was assumed to be size independent, the population density curve was kept in the same distribution shape and height. Figure 8.2 shows the comparison of final particle size distribution of experimental data and simulated prediction results for growth in silent conditions and in 5W of ultrasound field. The measured and estimated PSD for both of the systems shows good agreement. It is worth noting that the final PSD of LGA crystals is broader than that grown in silent conditions which contrasted with the investigation of ultrasound effect on final crystal size of crystallization in Chapter 7; within the narrow range of about 240~320μm for ultrasound absence and 220~335μm for 5W ultrasound presence. This is because the simulation was only carried out for the growth process where the ultrasound effect on PSD mainly acting on the nucleation step was not taken into account. In addition, due to fact that the sampling and measuring error existed even

for the same batch of seeds, the initial particle size distribution for two system experiment and simulation study were dissimilar.
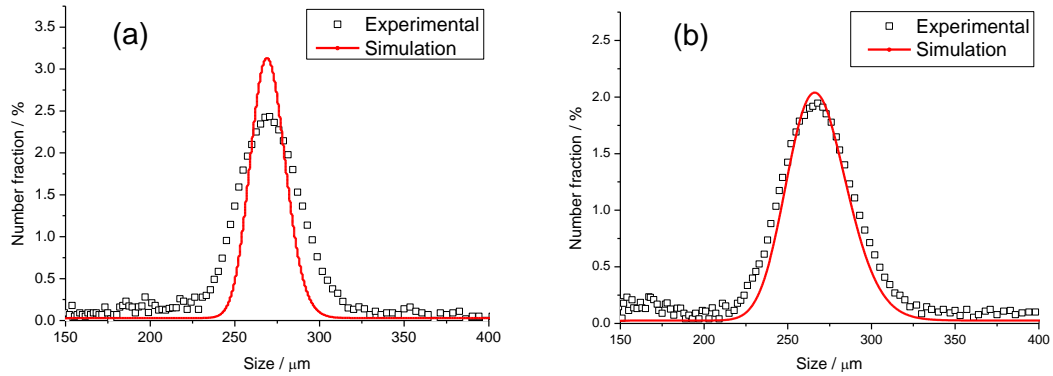
Figure 8.2: Final particle size distributions experimental and simulation comparison in (a) silent conditions (Expmean=265.60μm, Simumean=265.80μm) and (b) ultrasound field (Expmean=269.08μm, Simumean=269.90μm) at high supersaturation ratio. Symbols: experimental data; lines: simulation results
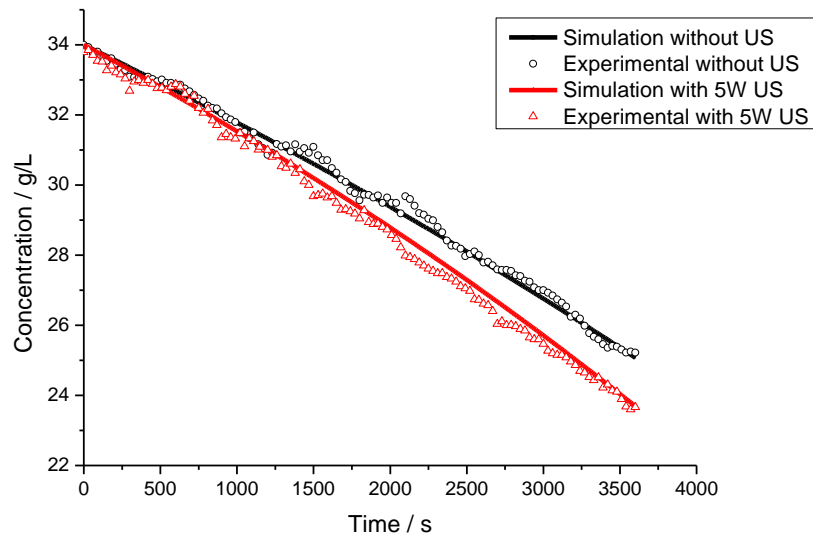
Figure 8.3: Comparison of the measured and model predicted solution concentration from seeding moment without ultrasound and with 5W of ultrasound at high supersaturation ratio. Symbols: experimental data; lines: simulation results

Figure 8.3 provides the solution concentration profile for experimental and simulation results of ultrasound absent and present systems from the α-LGA seeding moment. As can be seen, the solution concentration decrease with increasing time due to the persistent growth of crystals and the deviation between the presence and absence of ultrasound increased with increasing time because of the corresponding slightly faster growth rate where ultrasound was applied. The comparison of experimental and simulation results has shown satisfactory agreement for both growth condition studies.

The experimental and simulation growth rates of α-LGA in absence and in presence of ultrasound field are presented in Figure 8.4. With the experimental kinetics of growth obtained from the work in Chapter 7, the 5W ultrasound assisted growth rates over all the supersaturation range were found to be slightly faster than those achieved in absence of ultrasound. Considering the experimental work here involving bulk crystallization with a large amount of crystals and the off-line particle sizing procedures, the experimental results and the simulation predictions can still be considered satisfactory agreement, although there was a deviation.
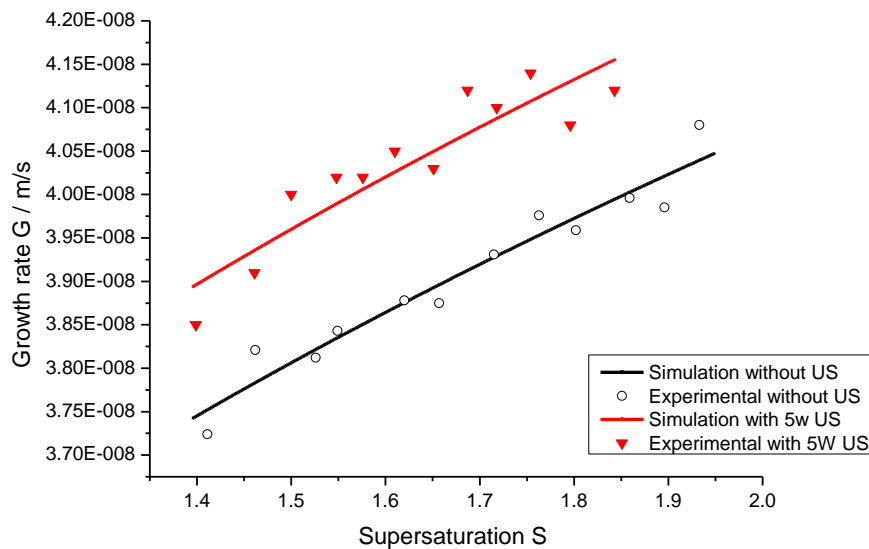
Figure 8.4: Comparison between the measured and predicted growth kinetics of α-LGA as a function of supersaturation at high supersaturation ratio. Symbols: experimental data; lines: simulation results

8.4.2 Seeded Growth Simulation at Low Supersaturation

To allow for the validation of growth kinetics and the effect of ultrasound on growth at a low supersaturation range, the same simulation work was implemented. The parameter values and process conditions adhibited in growth modelling are shown in Table 8.3.

Table 8.3: The simulation parameters for seeded growth at low S

Parameter	Value	Unit	Parameter	Value	Unit
C_{intial}	0.034	kg/L	T_{int}	40	°C
ρ_c	1560	kg/m^3	ρ_s	1000	kg/m^3
b	0.5	°C/min	k_v	0.5236	-
k_g(without US)	7.101×10^{-9}	-	n'(without US)	4.7053	-
k_g(with US)	1.0862×10^{-8}	-	n' (with US)	3.9237	-
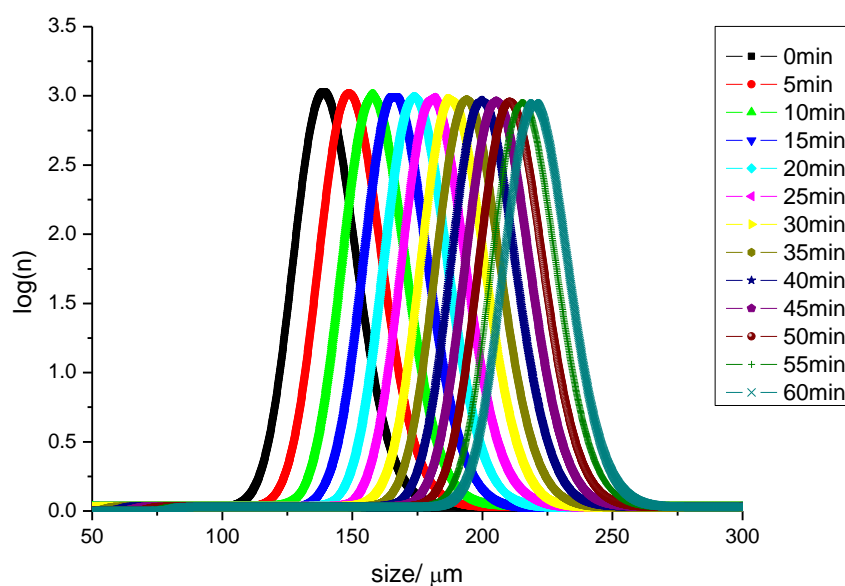
Figure 8.5: Variation of LGA particle size distribution during the growth at low supersaturation

Figure 8.5 represents the predicted LGA particle size distribution during 60mins growth period. The growth results in the increase of crystal size and after 30mins growing time, the crystal growth rate decreased owing to the dropping of supersaturation, in other words, the decrease of growth driving force. The comparison of experimental and simulation of final particle size distribution for growth in silence and in ultrasound is shown in Figure 8.6. It can be observed that the particle size distribution computed results of different conditions agreeing reasonable well with the experimental results. The shifted particle size and reduced number fraction can be attributed to the unavoidable agglomeration, or breakage of crystals during growth which are not accounted for in the simulation model. When comparing the supersaturation along with the growth of experimental work and simulation results, it can be found that the experimental supersaturation curves are slightly oscillatory (see Figure 8.7). However, they still nicely follow the model prediction trend.
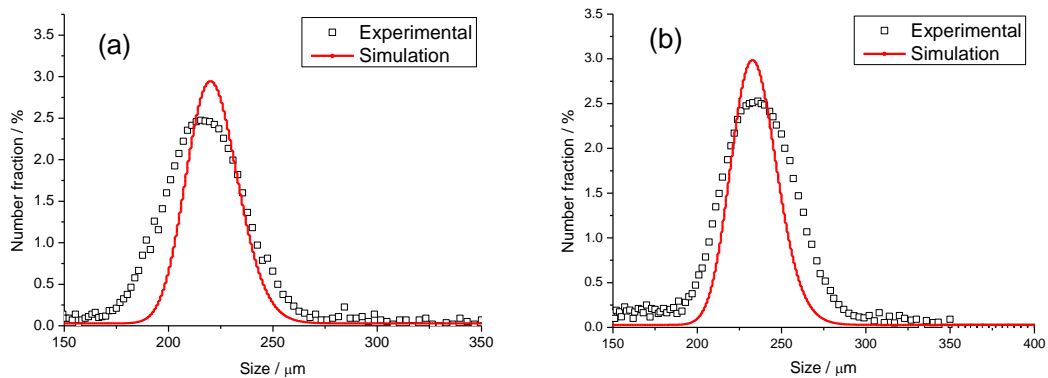
Figure 8.6: Final particle size distributions experimental and simulation comparison in (a) silent conditions (Expmean=219.08μm, Simumean=222.00μm) and (b) ultrasound field (Expmean=236.65μm, Simumean=232.70μm) obtained at low supersaturation ratio. Symbols: experimental data; lines: simulation results
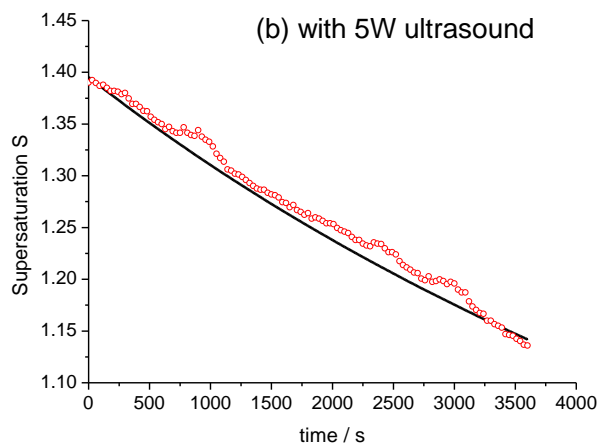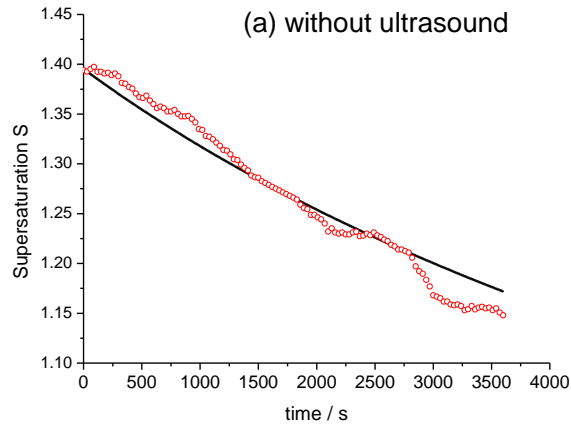
Figure 8.7: Comparison of supersaturation during the growth for the experimental and simulation in (a) silent conditions and (b) ultrasound field obtained at low supersaturation ratio. Symbols: experimental data; lines: simulation results

8.5 Conclusion

A population balance model for α-LGA seeded growth simulation is demonstrated in this chapter. The predicted results are compared with those obtained from experiments based on the on-line process analytical technology ATR-FTIR spectroscopy to monitor the solution concentration and off-line particle sizing using Morphologi G3 to measure the particle size distribution. The estimated results of the concentration profile, final particle size distribution and growth rate for different growth conditions, without ultrasound and with 5W ultrasound irradiation, were found to satisfactorily agree with the experimental results. The modelling, as an additional evidence of

163

validation means, has been proved that the growth kinetics of α-LGA obtained from former experimental works are reliable and dependable.

Chapter 9

Conclusions and Future Work

Summary: This chapter outlines the overview of the main conclusions drawn from the study presented in this thesis and suggestions for the direction of future work.

9.1 Conclusions

Ultrasonic technology has been successfully employed and developed over the past few decades in the chemical and pharmaceutical industries. Reliable evidence from previous research work proved that power ultrasound can induce nucleation in a controlled and reproducible way and replace seeding technology in crystallization. Furthermore, judicious application of ultrasound can assist in the generation of designed polymorphs and the manipulation of particle size.

However, ultrasound effects on the nucleation, growth, polymorphism and the crystal characteristics seemingly depend on the particular material system and considerable operating conditions. The precise crystallization kinetics and mechanism for ultrasound action on crystallization are still not fully understood and remain to be established. This research work not only carefully reviews the up-to-date knowledge concerning sonocrystallization, but also systematically investigates the application of ultrasound in l-glutamic acid crystallization, and a developed approach was utilized to deconstruct the challenge of kinetics and mechanism study. The main conclusions of the important findings arising from this project are summarized as follows:

1. To investigate the LGA nucleation kinetics in the applied ultrasound field, the metastable zone width and the induction time were examined. It was observed that the metastable zone width is narrowed and the induction time is significantly reduced when ultrasound is present, especially at low supersaturations. The classical Nývlt's analysis revealed that the apparent nucleation order and the nucleation constant are both increased by ultrasonic irradiation, and hence result in the acceleration of the LGA nucleation rate. The calculated results of the interfacial tension and the critical nucleus radius suggested that ultrasound reduces the nucleation energy barrier and makes nucleation occur quite readily. It was also found that the ultrasound effect on LGA nucleation is increased with increasing ultrasonic energy input.

2. Driven by the need for better understanding of the nucleation mechanism in presence of ultrasound, a developed approach was formulated to correlate the cavitation number and nucleation event. It was found that the estimated maximum pressure upon the collapsing bubble is of the magnitude of 10^5 atm which sufficiently contributes an additional driving force except the supersaturation to the crystallization system. The reconstructed nucleation rate considering the pressure factor was implemented for total ultrasound induced nuclei number prediction. The results obtained revealed that the nuclei induced by ultrasonic irradiation increases with the increase of the ultrasound power and insonation interval, indicating the suggestion that the ultrasound effect on crystallization is proportional to the cavitation issue. However, the prediction nuclei number did not match the one calculated from the experimentally measured induction time, possible reasons are the uncertain cavitation system characterization and detective instrument limit. Although the correlation is not successful, it still provides a potential method for sonocrystallization mechanism investigation.

3. Since the presence of ultrasound irradiation usually involves the primary and secondary nucleation, previous researchers barely studied the ultrasound effect on crystal growth itself. The investigation on LGA seeded crystal growth in a low ultrasound field (5W) was set to attain a deep insight into ultrasound effects on crystal growth. Results proved that ultrasound effects on crystal growth rate are supersaturation dependent. Ultrasound accelerates the LGA growth rate at relatively low supersaturations, but it has no effect on growth at high levels of supersaturation. The calculated growth kinetics suggested that ultrasound irradiation leads to the improvement of growth sites on the seeded crystals because the ultrasound does not impact the growth rate order but increases the growth rate constant. Additionally, the growth mechanism in the ultrasound field is believed to be the 2-D nucleation mechanism and surface nucleation-controlled. Ultrasound enhances the crystal surface nucleation and this is the reason it only promotes the crystal growth at low supersaturations.

4. A population balance model considering the growth only was employed to describe the behaviour of crystal population during the growth and identify the experimental growth measurement. The estimated concentration profile, final size distribution and growth rate were found to satisfactorily agree with the experimental results, implying the reliable and substantial growth rate measurement in previous work.

5. The effect of operating conditions on LGA polymorphism behaviour was studied. The pure metastable α-form LGA can be isolated by using fast cooling rate in low crystallization temperature regions, 0.5°C/min and under 25°C in this work. Using a slow cooling rate of 0.1°C/min and crystallizing in high temperature regions, above 50°C, the crystals produced were found to be pure β-form. When applying a moderate cooling rate and crystallization temperature, both of the polymorphic forms were obtained. Interestingly, ultrasonic irradiation was found to selectively favour the appearance of the stable β-form, even at the low crystallization temperature regions and with a fast cooling rate where the transformation rate of the α-form to β-form is very slow. The results proved the important link between LGA polymorphism and ultrasound, which is the improving effect of ultrasonic irradiation on the polymorphic transformation rate. Furthermore, the transformation rate was believed to be increased with the increase of ultrasound power.

6. The extensive observation of ultrasound influence on the characterization of final crystals was also carried out. The results demonstrated that a short burst of ultrasound at an early stage of nucleation results in more even and well-shaped crystals. A long time application of ultrasound throughout the nucleation and growth stages, on the other hand, can give much finer crystals due to the prolific nucleation induced by ultrasound. The higher the ultrasound power, the narrower the particle size distribution and the smaller the mean size. It was observed that ultrasound irradiation does not change the morphology of LGA crystals.

9.2 Suggestions of Future Work

Although some interesting and promising results were found in this work, there are more challenges that need to be addressed. The current limits needing to be overcome and some suggestions for the direction of future work are discussed and given as follows:

1. In this work, the approach employed to correlate the acoustic cavitation and nucleation event contains a series of bubble collapse calculations which are based on the single bubble model. However, the probe system used in this work produces a multi-bubble system, which involves both symmetric and asymmetric bubble collapses. This makes collapsing bubbles more difficult to characterize and results in some uncertain calculation parameters. The shock wave estimation in this work also ignored the unavoidable local damage on nearby bubbles. Thus, it is necessary to consider a more comprehensive multi-bubble model and the damage issue to first obtain an accurate calculation and eventually illustrate the mechanism.

2. It is demonstrated in this work that ultrasound irradiation favoured the precipitation of the stable β-form, and the ultrasonic power also affects the polymorphic transformation rate from α-form. The powder x-ray diffraction data only is used to identify the polymorphism of the final produced LGA crystals but overlook the transformation behaviour and fraction. The semi-quantitative analysis of the x-ray diffraction allows the weight fraction identification of each polymorphic form by comparing the integrated intensities of the diffraction peaks from each of the known phases. The contradictory effect of ultrasound irradiation on LGA polymorphs formation reported was that pure α-form can be produced with sonication at high level of supersaturation (Hatakka et al., 2010). It can be conceived that initial supersaturation plays an important role in the application of ultrasound in control of LGA polymorphism and it will be of great importance to

study this factor.

3. In this work, the LGA growth kinetics was determined based on the growth from bulk solution in a batch crystallizer which may cause problems of inaccurate particle sizing and unexpected nucleation. To effectively identify the growth mechanism in an ultrasound field, it will be more appropriate to study the kinetics by observing single crystal growth. It is worth attempting to design a growth cell with sonicator where the single crystal is mounted and the growth is measured in flowing saturated solution.

4. The population balance model used in this work is just an additional means of validation for the experimental growth kinetics determination. Therefore, the simulation model assumes the growth only, the growth is size independent and the breakage and aggregation can be ignored. However, these factors need to be deliberately and carefully considered in practical experiment design. In future work, it will be necessary to add these items to the population balance model in order to thoroughly investigate the effect of ultrasound on crystallization and final product particle size.

5. It is well known that ultrasound related variables, such as the ultrasound power, sonication duration and the horn tip size, have significant effect on the sonocrystallization process and crystal characteristics. In this work, a probe with fixed tip size was used in all the experiments to examine the ultrasound effect. It will be of interest to study the ultrasonic irradiation effect by changing the size of the horn.

References

AMARA, N., RATSIMBA, B., WILHELM, A. & DELMAS, H. (2004) Growth rate of potash alum crystals: comparison of silent and ultrasonic conditions. *Ultrasonics Sonochemistry,* 11**,** 17-21.

ANDERSON. H. W, C. J. B., STAUNTON. H. F (1995) Crystallization of Adipic Acid. *United State Patent,* 5,471,001.

APFEL, R. E. (1997) Sonic effferverscence. A tutorial on acoustic cavitation. *J. Acoust.Soc.Am.,* 101**,** 1227-1237.

ARAKELYAN, V. (1987) Effect of ultrasound on crystal growth from melt and solution. *Acta Physica Hungarica,* 61**,** 185-187.

ASTEASUAIN, M. & BRANDOLIN, A. (2008) Modeling and optimization of a high-pressure ethylene polymerization reactor using gPROMS. *Computers & Chemical Engineering,* 32**,** 396-408.

ASTEASUAIN, M., TONELLI, S. M., BRANDOLIN, A. & BANDONI, J. A. (2001) Dynamic simulation and optimisation of tubular polymerisation reactors in gPROMS. *Computers & Chemical Engineering,* 25**,** 509-515.

BARRETT, P. & GLENNON, B. (1999) In-line FBRM Monitoring of Particle Size in Dilute Agitated Suspensions. *Particle & Particle Systems Characterization,* 16**,** 207-211.

BARTON, P. I. & PANTELIDES, C. C. (1994) Modeling of Combined Discrete/ Continuous Processes. *AIChE Journal,* 40**,** 966-979.

BIRD, R. B., STEWART, W. E. & LIGHTFOOT, E. N. (1960) *Transport phenomena*, John Wiley and Sons.

BOELS, L., WAGTERVELD, R. M., MAYER, M. J. & WITKAMP, G. J. (2010a) Seeded calcite sonocrystallization. *Journal of Crystal Growth,* 312**,** 961-966.

BOELS, L., WAGTERVELD, R. M. & WITKAMP, G. J. (2010b) Ultrasonic reactivation of phosphonate poisoned calcite during crystal growth. *Ultrasonics Sonochemistry,* 18**,** 1225-1231.

BURDIN, F., TSOCHATZIDIS, N. A., GUIRAUD, P., WILHELM, A. M. & DELMAS, H. (1999) Characterisation of the acoustic cavitation cloud by two laser techniques. *Ultrasonics Sonochemistry,* 6**,** 43-51.

BURTON, W. K., CABRERA, N. & FRANK, F. C. (1951) The Growth of Crystals and the Equilibrium Structure of their Surfaces. *Philosophical Transactions of the Royal Society of London. Series A, Mathematical and Physical Sciences,* 243**,** 299-358.

CAO, Y., XIANG, M. & LI, H. (2002) The effects of ultrasonic irradiation on the crystalline structures of nucleated polypropylene. *Journal of Applied Polymer Science,* 84**,** 1956-1961.

CASHELL, C., CORCORAN, D. & HODNETT, B. K. (2003) Secondary nucleation of the β-polymorph of l-glutamic acid on the surface of α-form crystals. *Chemical Communications***,** 374-375.

CHOW-MCGARVA, R. C.-Y. (2004) A study on the sonocrystallization of ice. *Department of Food Science.* Leeds, University of Leeds.

CHOW, R., BLINDT, R., CHIVERS, R. & POVEY, M. (2003) The sonocrystallization of ice in sucrose solutions: primary and secondary nucleation. *Ultrasonics,* 41**,** 595-604.

CRAIG, S. J., D.A (1999) *World paten,* WO 00/32598.

DALAS, E. (2001) The effect of ultrasonic field on calcium carbonate scale formation. *Journal of Crystal Growth,* 222**,** 287-292.

DALAS, E. & KOUTSOUKOS, P. G. (1989) The effect of magnetic fields on calcium carbonate scale formation. *Journal of Crystal Growth,* 96**,** 802-806.

DALVI, S. V. & DAVE, R. N. (2010) Analysis of nucleation kinetics of poorly water-soluble drugs in presence of ultrasound and hydroxypropyl methyl cellulose during antisolvent precipitation. *International Journal of Pharmaceutics,* 387**,** 172-179.

DAVEY, R. J. & GARSIDE, J. (2000) *From Moleculars to Crystallizers:An Introduction to Crystallization,* New York, Oxford University Press Inc.

DAVIS, T. D., MORRIS, K. R., HUANG, H., PECK, G. E., STOWELL, J. G., EISENHAUER, B. J., HILDEN, J. L., GIBSON, D. & BYRN, S. R. (2003) In Situ Monitoring of Wet Granulation Using Online X-Ray Powder Diffraction. *Pharmaceutical Research,* 20**,** 1851-1857.

DENNEHY, R. D. (2003) Particle Engineering Using Power Ultrasound1. *Organic Process Research & Development,* 7**,** 1002-1006.

DEVARAKONDA, S., EVANS, J. M. B. & MYERSON, A. S. (2003) Impact of Ultrasonic Energy on the Crystallization of Dextrose Monohydrate. *Crystal Growth & Design,* 3**,** 741-746.

DHARMAYAT, S., CALDERON DE ANDA, J., HAMMOND, R. B., LAI, X., ROBERTS, K. J. & WANG, X. Z. (2006) Polymorphic transformation of l-glutamic acid monitored using combined on-line video microscopy and X-ray diffraction. *Journal of Crystal Growth,* 294**,** 35-40.

DODDS, J., ESPITALIER, F., LOUISNARD, O., GROSSIER, R., DAVID, R., HASSOUN, M., BAILLON, F., GATUMEL, C. & LYCZKO, N. (2007) The Effect of Ultrasound on Crystallisation-Precipitation Processes: Some Examples and a New Segregation Model. *Particle & Particle Systems Characterization,* 24**,** 18-28.

DUNUWILA, D. D. & BERGLUND, K. A. (1997) ATR FTIR spectroscopy for in situ measurement of supersaturation. *Journal of Crystal Growth,* 179**,** 185-193.

DUNUWILA, D. D., CARROLL II, L. B. & BERGLUND, K. A. (1994) An investigation of the applicability of attenuated total reflection infrared spectroscopy for measurement of solubility and supersaturation of aqueous citric acid solutions. *Journal of Crystal Growth,* 137**,** 561-568.

ENOMOTO, N., SUNG, T., NAKAGAWA, Z. & LEE, S. (1992) Effect of ultrasonic waves on crystallization from a supersaturated solution of alum. *Journal of Materials Science,* 27**,** 5239-5243.

FERRARI, E. S. & DAVEY, R. J. (2004) Solution-Mediated Transformation of α to

β-Glutamic Acid: Rate Enhancement Due to Secondary Nucleation. *Crystal Growth & Design,* 4**,** 1061-1068.

FLYNN, H. G. (1964) Physics of acoustic cavitation in liquids. IN MANSON, W. P. (Ed.) *Physical Acoustics.* New York, Academic Press.

FRANCK, F. C. (1949) The influence of dislocations on crystal growth. *Discussions of the Faraday Society,* 5**,** 48-54.

FRAWLEY, J. J. & CHILDS, W. J. (1968) Dynamic nucleation of supercooled metals *Trans.Metall.Soc.A.I.M.E.,* 242**,** 256.

GARTI, N. & ZOUR, H. (1997) The effect of surfactants on the crystallization and polymorphic transformation of glutamic acid. *Journal of Crystal Growth,* 172**,** 486-498.

GIROLAMI, M. W. & ROUSSEAU, R. W. (1986) Initial breeding in seeded batch crystallizers. *Industrial & Engineering Chemistry Process Design and Development,* 25**,** 66-70.

GIULIETTI, M., SECKLER, M. M., DERENZO, S., RÉ, M. I. & CEKINSKI, E. (2001) Industrial crystallization and precipitation from solutions: State of the technique. *Brazilian Journal of Chemical Engineering,* 18**,** 423-440.

GOGATE, P. R. & PANDIT, A. B. (2000) Engineering Design Method for Cavitational Reactors: I. Sonochemical Reactors. *AIChE Journal,* 46**,** 372-379.

GRACIN, S. & ÅKE, C. R. (2004) Polymorphism and Crystallization of p-Aminobenzoic Acid. *Crystal Growth and Design,* 4**,** 1013-1023.

GRACIN, S., UUSI-PENTTILÄ, M. & RASMUSON, Å. C. (2005) Influence of Ultrasound on the Nucleation of Polymorphs of p-Aminobenzoic Acid. *Crystal Growth & Design,* 5**,** 1787-1794.

GROSSIER, R., LOUISNARD, O. & VARGAS, Y. (2007) Mixture segregation by an inertial cavitation bubble. *Ultrasonics Sonochemistry,* 14**,** 431-437.

GUO, Z., JONES, A. G. & LI, N. (2006a) The effect of ultrasound on the homogeneous nucleation of during reactive crystallization. *Chemical Engineering Science,* 61**,** 1617-1626.

GUO, Z., JONES, A. G. & LI, N. (2006b) Interpretation of the ultrasonic effect on induction time during BaSO4 homogeneous nucleation by a cluster coagulation model. *Journal of Colloid and Interface Science,* 297**,** 190-198.

GUO, Z., ZHANG, M., LI, H., WANG, J. & KOUGOULOS, E. (2005) Effect of ultrasound on anti-solvent crystallization process. *Journal of Crystal Growth,* 273**,** 555-563.

HAGENSON, L. C. & DORAISWAMY, L. K. (1998) Comparision of the effects of ultrasound and mechanical agitation on a reacting solid-liquid system. *Chemical Engineering Science,* 58**,** 131-148.

HAMMOND, R. B., LAI, X., ROBERTS, K. J., THOMAS, A. & WHITE, G. (2004) Application of In-Process X-ray Powder Diffraction for the Identification of Polymorphic Forms during Batch Crystallization Reactions. *Crystal Growth & Design,* 4**,** 943-948.

HAMMOND, R. B., PENCHEVA, K. & ROBERTS, K. J. (2005) Simulation of Energetic Stability of Facetted l-Glutamic Acid Nanocrystalline Clusters in

Relation to Their Polymorphic Phase Stability as a Function of Crystal Size. *The Journal of Physical Chemistry B,* 109**,** 19550-19552.

HAMMOND, R. B., PENCHEVA, K. & ROBERTS, K. J. (2007) Molecular Modeling of Crystalâ^'Crystal Interactions between the Î±- and Î²-Polymorphic Forms of l-Glutamic Acid Using Grid-Based Methods. *Crystal Growth & Design,* 7**,** 875-884.

HARTMAN, P. & PERDOCK, W. G. (1955) On the relations between structure and morphology of crystals. *Acta Crystallographica,* 8**,** 49-52.

HATAKKA, H., ALATALO, H., LOUHI-KULTANEN, M., LASSILA, I. & HÄGGSTRÖM, E. (2010) Closed-loop control of reactive crystallization Part II: polymorphism control of l-glutamic acid by sonocrystallization and seeding. *Chemical Engineering and Technology,* 33**,** 751-756.

HIGAKI KAORU, U. S., KOYANO TETSUO, SATO KIYOTAKA (2001) Effects of ultrasonic irradiation on crystallization behavior of tripalmitoylglycero and Cocoa butter. *Journal of the American Oil Chemists' Society,* 78**,** 513-518.

HILGENFELDT, S., BRENNER, M. P., GROSSMANN, S. & LOHSE, D. (1998) Analysis of Rayleigh Plesset dynamics for sonoluminescing bubbles. *Journal of Fluid Mechanics,* 1998**,** 171 - 204.

HOLZFUSS, J., RÜGGEBERG, M. & BILLO, A. (1998) Shock Wave Emissions of a Sonoluminescing Bubble. *Physical Review Letters,* 81**,** 5434-5437.

HOTTOT, A., NAKAGAWA, K. & ANDRIEU, J. (2008) Effect of ultrasound-controlled nucleation on structural and morphological properties of freeze-dried mannitol solutions. *Chemical Engineering Research and Design,* 86**,** 193-200.

HUNT, J. D. & JACKSON, K. A. (1966) Nucleation of solid in an undercooled liquid by cavitation. *Journal of Applied Physics,* 37**,** 254.

ICHITSUBO, T., MATSUBARA, E., KAI, S. & HIRAO, M. (2004) Ultrasound-induced crystallization around the glass transition temperature for Pd40Ni40P20 metallic glass. *Acta Materialia,* 52**,** 423-429.

JASCO (2008) FTIR Seminar. http://www.jasco.hu/konyvtar/FT-IR-Grundl.-Seminar.pdf.

KALBASENKA, A., HUESMAN, A. & KRAMER, H. (2011) Modeling batch crystallization processes: Assumption verification and improvement of the parameter estimation quality through empirical experiment design. *Chemical Engineering Science,* 66**,** 4867-4877.

KASHCHIEV, D. (2000) *Nucleation: basic theory with applications,* Oxford, Butterworth-Heinemann.

KASHCHIEV, D. & VAN ROSMALEN, G. M. (1995) Effect of Pressure on Nucleation in Bulk Solutions and Solutions in Pores and Droplets. *Journal of Colloid and Interface Science,* 169**,** 214-219.

KELLY, D. R., HARRISON, S. J., JONES, S., MASOOD, M. A. & MORGAN, J. J. G. (1993) Rapid crystallisation using ultrasonic irradiation - sonocrystallisation. *Tetrahedron Letters,* 34**,** 2689-2690.

KHAN, S. (2008) Application of On-line ATR-FTIR Spectroscopy for Monitoring,

Controlling and Scaling-up the Batch Crystallization of L-Glutamic Acid. *Institude of Particle Science and Engineering.* Leeds, University of Leeds.

KHOROSHEV, G. A. (1963) Collapse of vapor-air cavitation bubbles. *Soviet Phys.-Acoust.,* 9**,** 275-279.

KIM, S., WEI, C. & KIANG, S. (2003) Crystallization Process Development of an active pharmaceutical ingredient and particle engineering via the use of ultrasonics and temperature cycling *Organic Process Research & Development,* 7**,** 997-1001.

KIM, Y. H., LEE, K., KOO, K. K., SHUL, Y. G. & HAAM, S. (2002) Comparison study of mixing effect on batch cooling crystallization of 3-nitro-1,2,4-triazol-5-one(NTO) using mechanical stirrer and ultrasound irradiation. *Crystal Research and Technology,* 37**,** 928-944.

KITAMURA, M. (1989) Polymorphism in the crystallization of L-glutamic acid. *Journal of Crystal Growth,* 96**,** 541-546.

KITAMURA, M. (2003) Control of Polymorphism in Crystallization of Amino Acid. *Dev.Chem.Eng.Mineral Process.,* 11**,** 579-602.

KITAMURA, M. (2009) Strategy for control of crystallization of polymorphs. *CrysEngComm,* 11**,** 949-964.

KITAMURA, M. & FUNAHARA, H. (1994) Effect of l- and d-phenylalanine on crystallization and transformation of l-glutamic acid polymorphs. *Journal of chemical engineering Japan,* 27**,** 124-126.

KITAMURA, M. & ISHIZU, T. (2000) Growth kinetics and morphological change of polymorphs of L-glutamic acid. *Journal of Crystal Growth,* 209**,** 138-145.

KITAMURA, M. & NAKAMURA, T. (2001) Inclusion of amino acids and the effect on growth kinetics of l-glutamic acid. *Powder Technology,* 121**,** 39-45.

KORDYLLA, A., KOCH, S., TUMAKAKA, F. & SCHEMBECKER, G. (2008) Towards an optimized crystallization with ultrasound:effect of solvent properties and ultrasonic process parameters. *Journal of Crystal Growth,* 310**,** 4177-4184.

KORDYLLA, A., KRAWCZYK, T., TUMAKAKA, F. & SCHEMBECKER, G. (2009) Modeling ultrasound-induced nucleation during cooling crystallization. *Chemical Engineering Science,* 64**,** 1635-1642.

KORTNEV, A. V. & MARTYNOVSKAYA, N. V. (1974) Effect of ultrasound on the latent period of crystallization from supersaturated solutions. *Inst.Stali.Splavov.,* 77**,** 98-100.

KOSSEL, W. (1934) Zur Energetik von Oberflächenvorgängen. *Annalen der Physik,* 413**,** 457-480.

KOUGOULOS, E., JONES, A. G., JENNINGS, K. H. & WOOD-KACZMAR, M. W. (2005) Use of focused beam reflectance measurement (FBRM) and process video imaging (PVI) in a modified mixed suspension mixed product removal (MSMPR) cooling crystallizer. *Journal of Crystal Growth,* 273**,** 529-534.

KOUGOULOS, E., MARZIANO, I. & MILLER, P. R. (2010) Lactose particle engineering: Influence of ultrasound and anti-solvent on crystal habit and particle size. *Journal of Crystal Growth,* 312**,** 3509-3520.

KUROTANI, M. & HIRASAWA, I. (2008) Polymorph control of sulfamerazine by ultrasonic irradiation. *Journal of Crystal Growth,* 310**,** 4576-4580.

KUROTANI, M. & HIRASAWA, I. (2010) Effect of ultrasonic irradiation on the selective polymorph control in sulfamerazine. *Chemical Engineering Research and Design,* 88**,** 1272-1278.

KUROTANI, M., MIYASAKA, E., EBIHARA, S. & HIRASAWA, I. (2009) Effect of ultrasonic irradiation on the behavior of primary nucleation of amino acids in supersaturated solutions. *Journal of Crystal Growth,* 311**,** 2714-2721.

LAUTERBORN, W., KURZ, T., METTIN, R. & OHL, C. D. (1999) Experimental and Theoretical Bubble Dynamics. *Advances in Chemical Physics.* John Wiley & Sons, Inc.

LE BRAS, A. (1967) Action des ultrasons sur les processus physicochimiques. *Rev.Chim.Miner,* 4**,** 283-315.

LEE, G., MEYER, X. M., BISCANS, B., LE LANN, J. M. & YOON, E. S. (1999) Adaptive finite difference method for the simulation of batch crystallization. *Computers & Chemical Engineering,* 23, Supplement**,** S363-S366.

LEIGHTON, T. G. (1997) *The acoustic bubble,* San Diego, Academic Press.

LEPOINT-MULLIE, F., DE PAUW, D., LEPOINT, T., SUPIOT, P. & AVNI, R. (1996) Nature of the 'extreme conditions' in single sonoluminescing bubbles. *The Journal of Physical Chemistry,* 100**,** 12138-12141.

LEWINER, F., FEVOTTE, G., KLEIN, J. P. & PUEL, F. (2001a) Improving batch cooling seeded crystallization of an organic weed-killer using on-line ATR FTIR measurement of supersaturation. *Journal of Crystal Growth,* 226**,** 348-362.

LEWINER, F., KLEIN, J. P., PUEL, F. & FEVOTTE, G. (2001b) On-line ATR FTIR measurement of supersaturation during solution crystallization processes. Calibration and applications on three solute/solvent systems. *Chemical Engineering Science,* 56**,** 2069-2084.

LI-YUN, C., CHUAN-BO, Z. & JIAN-FENG, H. (2005) Influence of temperature, [Ca2+], Ca/P ratio and ultrasonic power on the crystallinity and morphology of hydroxyapatite nanoparticles prepared with a novel ultrasonic precipitation method. *Materials Letters,* 59**,** 1902-1906.

LI, H., LI, H. R., GUO, Z. & LIU, Y. (2006) The application of power ultrasound to reaction crystallization. *Ultrasonics Sonochemistry,* 13**,** 359-363.

LI, H., WANG, J., BAO, Y., GUO, Z. & ZHANG, M. (2003) Rapid sonocrystallization in the salting-out process. *Journal of Crystal Growth,* 247**,** 192-198.

LIANG, J. (2002) Process Scale Dependence of L-glutamic Acid Batch Crystallised from Aqueous Solution in relation to Reactor Internals, Reactant Mixing and Process Conditions. *Department of Mechanical and Chemical Engineering.* Edinburgh, Heriot-Watt University.

LIANG, K., WHITE, G., WILKINSON, D., FORD, L. J., ROBERTS, K. J. & WOOD, W. M. L. (2003) An Examination into the Effect of Stirrer Material and Agitation Rate on the Nucleation of l-Glutamic Acid Batch Crystallized from Supersaturated Aqueous Solutions. *Crystal Growth & Design,* 4**,** 1039-1044.

LINDA J. MCCAUSLAND, P. W. C. (2004) Power ultrasound-A means to promote and control crystallization in biotechonology. *Biotechnology and Genetic Engineering Reviews,* 21**,** 3-10.

LINDENBERG, C., KRATTLI, M., CORNEL, J. & MAZZOTTI, M. (2008) Design and Optimization of a Combined Cooling/Antisolvent Crystallization Process. *Crystal Growth & Design,* 9**,** 1124-1136.

LOUHI-KULTANEN, M., KARJALAINEN, M., RANTANEN, J., HUHTANEN, M. & KALLAS, J. (2006) Crystallization of glycine with ultrasound. *International Journal of Pharmaceutics,* 320**,** 23-29.

LUQUE DE CASTRO, M. D. & PRIEGO-CAPOTE, F. (2007) Ultrasound-assisted crystallization (sonocrystallization). *Ultrasonics Sonochemistry,* 14**,** 717-724.

LYCZKO, N., ESPITALIER, F., LOUISNARD, O. & SCHWARTZENTRUBER, J. (2002) Effect of ultrasound on the induction time and the metastable zone widths of potassium sulphate. *Chemical Engineering Journal,* 86**,** 233-241.

MA, C. (2010) Particle Distribution Shape Control in Crystallization Processes. *Institute of Particle Science and Engineering.* Leeds, University of Leeds.

MA, C. Y. & WANG, X. Z. (2012) Model identification of crystal facet growth kinetics in morphological population balance modeling of l-glutamic acid crystallization and experimental validation. *Chemical Engineering Science,* 70**,** 22-30.

MA, C. Y., WANG, X. Z. & ROBERTS, K. J. (2007) Multi-dimensional population balance modeling of the growth of rod-like L-glutamic acid crystals using growth rates estimated from in-process imaging. *Advanced Powder Technology,* 18**,** 707-723.

MACKELLAR, A. J., BUCKTON, G., NEWTON, J. M., CHOWDHRY, B. Z. & ORR, C. A. (1994) The controlled crystallisation of a model powder: 1. The effects of altering the stirring rate and the supersaturation profile, and the incorporation of a surfactant (poloxamer 188). *International Journal of Pharmaceutics,* 112**,** 65-78.

MANSON, T. J. (1991) *Practical sonochemistry: User's guide to applications in chemistry and chemical engineering,* Chichester, Ellis Horwood Limited.

MARGULIS, M. A. (1996) *Sonochemistry and Cavitation,* London, Gordon & Breach.

MASON, T. J. (1999) *Sonochemistry*, Oxford University Press.

MATULA, T. J. (1999) Inertial cavitation and single-bubble sonoluminescence. *Philosophical Transactions of the Royal Society of London. Series A: Mathematical, Physical and Engineering Sciences,* 357**,** 225-249.

MCCAUSLAND.L. J, C. P. W., MARTIN.P.D (2001) Use of power of sonocrystallization for improved properties. *Chemical Engineering Progress,* 97**,** 56-61.

MIERS, H. A. & ISAAC, F. (1906) Refractive indices of crystallizing solutions. *Journal of the Chemical Society* 89**,** 413-454.

MIERS, H. A. & ISAAC, F. (1907) The spontaneous crystallization of binary mixtures. *Proceddings of the Royal Society,* A79**,** 322-351.

MIYASAKA, E., EBIHARA, S. & HIRASAWA, I. (2006a) Investigation of primary nucleation phenomena of acetylsalicylic acid crystals induced by ultrasonic irradiation: ultrasonic energy needed to activate primary nucleation. *Journal of Crystal Growth,* 295**,** 97-101.

MIYASAKA, E., KATO, Y., HAGISAWA, M. & HIRASAWA, I. (2006b) Effect of ultrasonic irradiation on the number of acetylsalicylic acid crystals produced under the supersaturated condition and the ability of controlling the final crystal size via primary nucleation. *Journal of Crystal Growth,* 289**,** 324-330.

MONNIER, O., FEVOTTE, G., HOFF, C. & KLEIN, J. P. (1997) Model identification of batch cooling crystallizations through calorimetry and image analysis. *Chemical Engineering Science,* 52**,** 1125-1139.

MOUGIN, P., WILKINSON, D. & ROBERTS, K. J. (2002) In Situ Measurement of Particle Size during the Crystallization of l-Glutamic Acid under Two Polymorphic Forms: Influence of Crystal Habit on Ultrasonic Attenuation Measurements. *Crystal Growth & Design,* 2**,** 227-234.

MUHAMMAD J & MOHAMMAD I (2011) Volumetric Studies of Some Amino Acids in Aqueous Medium at Different Temperatures. *Journal of the Chemical Society of Parkistan,* 33.

MULLIN, J. W. (1993) *Crystallization*, Edition Butter Worth-Heinemann Ltd.

MULLIN, J. W. & JANČIĆ, S. J. (1979) Interpretation of metastable zone widths. *Trans Institution of Chemical Engineering,* 57**,** 188-193.

NANEV, C. N. & PENKOVA, A. (2001) Nucleation of lysozyme crystals under external electric and ultrasonic fields. *Journal of Crystal Growth,* 232**,** 285-293.

NARDUCCI, O. & JONES, A. G. (2012) Seeding in Situ the Cooling Crystallization of Adipic Acid using Ultrasound. *Crystal Growth & Design*.

NARDUCCI, O., JONES, A. G. & KOUGOULOS, E. (2011) Continuous crystallization of adipic acid with ultrasound. *Chemical Engineering Science,* 66**,** 1069-1076.

NAUMAN, E. B. (1972) Theory of particulate processes, analysis and techniques of continuous crystallization, A. D. Randoph and M. A. Larson, Academic Press, New York (1971), 251 pages. . *AIChE Journal,* 18**,** 670-670.

NEPPIRAS, E. A. (1980) Acoustic cavitation. *Phys.Rep.,* 61**,** 159-284.

NI, X.-W., VALENTINE, A., LIAO, A., SERMAGE, S. B. C., THOMSON, G. B. & ROBERTS, K. J. (2004) On the Crystal Polymorphic Forms of l-Glutamic Acid Following Temperature Programmed Crystallization in a Batch Oscillatory Baffled Crystallizer. *Crystal Growth & Design,* 4**,** 1129-1135.

NI, X. & LIAO, A. (2008) Effects of Cooling Rate and Solution Concentration on Solution Crystallization of l-Glutamic Acid in an Oscillatory Baffled Crystallizer. *Crystal Growth & Design,* 8**,** 2875-2881.

NISHIDA, I. (2004) Precipitation of calcium carbonate by ultrasonic irradiation. *Ultrasonics Sonochemistry,* 11**,** 423-428.

NOLTINGK, B. E. & NEPPIRAS, E. A. (1951) Cavitation produced by ultrasonics: theoretical conditions for the onset of cavitation. *Proc Phys Soc,* 64**,**

1032-1038.

NUNES, R. C. R., PEREIRA, R. A., FONSECA, J. L. C. & PEREIRA, M. R. (2001) X-ray studies on compositions of polyurethane and silica. *Polymer Testing,* 20**,** 707-712.

NÝVLT, J. (1968) Kinetics of nucleation in solutions. *Journal of Crystal Growth,* 3/4**,** 377-383.

NÝVLT, J., ŽÁČEK, S (1995) Effect of Ultrasonics on Agglomeration. *Crystal Research and Technology,* 30**,** 1055-1063.

OHL, C. D., KURZ, T., GEISLER, R., LINDAU, O. & LAUTERBORN, W. (1999) Bubble dynamics, shock waves and sonoluminescence. *Philosophical Transactions of the Royal Society of London. Series A,* 357**,** 269-294.

OULLION, M., PUEL, F., F茅 VOTTE, G., RIGHINI, S. & CARVIN, P. (2007a) Industrial batch crystallization of a plate-like organic product. In situ monitoring and 2D-CSD modelling. Part 2: Kinetic modelling and identification. *Chemical Engineering Science,* 62**,** 833-845.

OULLION, M., PUEL, F., F茅 VOTTE, G., RIGHINI, S. & CARVIN, P. (2007b) Industrial batch crystallization of a plate-like organic product. In situ monitoring and 2D-CSD modelling: Part 1: Experimental study. *Chemical Engineering Science,* 62**,** 820-832.

PANTELIDES, C. C. & OH, M. (1996) Process modelling tools and their application to particulate processes. *Powder Technology,* 87**,** 13-20.

PECHA R & GOMPF B (2000) Microimplosions:Cavitation collaspe and shock wave emission on a nanosecond scale. *Physical Reviw Letter,* 84**,** 1328-1330.

PERKINS, J. P. (2000) World Patent WO 00/35579 B1.

PRICE, C. (1997) Ultrasound—the key to better crystals for the pharmaceutical industry. *Pharmaceutical Technology   Europe,* 9**,** 78.

PRICE, G. J., MAHON, M. F., SHANNON, J. & COOPER, C. (2011) Composition of Calcium Carbonate Polymorphs Precipitated Using Ultrasound. *Crystal Growth & Design,* 11**,** 39-44.

PUEL, F., FEVOTTE, G. & KLEIN, J. P. (2003a) Simulation and analysis of industrial crystallization processes through multidimensional population balance equations. Part 1: a resolution algorithm based on the method of classes. *Chemical Engineering Science,* 58**,** 3715-3727.

PUEL, F., FEVOTTE, G. & KLEIN, J. P. (2003b) Simulation and analysis of industrial crystallization processes through multidimensional population balance equations. Part 2: a study of semi-batch crystallization. *Chemical Engineering Science,* 58**,** 3729-3740.

QIAN, R.-Y. & BOTSARIS, G. D. (1997) A new mechanism for nuclei formation in suspension crystallizers: the role of interparticle forces. *Chemical Engineering Science,* 52**,** 3429-3440.

QIU.TAI Q, Y. H. L., SHU G.CHEN (1993) Acoustic Field Effect on Sucrose Solution Nucleation. *Acoustic Technology,* 1**,** 15-20.

RANDOLPH, A. D. & LARSON, M. A. (1971) Theory of Particulate Process:Analysis and Techniques of Continuous crystallization. *Academic*

Press,. New York.

RANDOLPHA, A. D. & LARSON, M. A. (1971) Theory of Particulate Process:Analysis and Techniques of Continuous crystallization. *Academic Press,*. New York.

REVALOR, E., HAMMADI, Z., ASTIER, J.-P., GROSSIER, R., GARCIA, E., HOFF, C., FURUTA, K., OKUSTU, T., MORIN, R. & VEESLER, S. (2011) Usual and unusual crystallization from solution. *Journal of Crystal Growth,* 312**,** 939-946.

ROELANDS, C. P. M., TER HORST, J. H., KRAMER, H. J. M. & JANSENS, P. J. (2007) Precipitation mechanism of stable and metastable polymorphs of L-glutamic acid. *AIChE Journal,* 53**,** 354-362.

RUECROFT, G., HIPKISS, D., LY, T., MAXTED, N. & CAINS, P. W. (2005) Sonocrystallization: The use of ultrasound for improved industrial crystallization. *Organic Process Research & Development,* 9**,** 923-932.

SACLIER, M., PECZALSKI, R. & ANDRIEU, J. (2010) A theoretical model for ice primary nucleation induced by acoustic cavitation. *Ultrasonics Sonochemistry,* 17**,** 98-105.

SAKATA, Y. (1961) Studies on the Polymorphism of L-glutamic Acid: Part 2. Measurement of solubilies. *Agricultural and Biological Chemistry,* 25**,** 835-837.

SCHOLL, J., BONALUMI, D., VICUM, L., MAZZOTTI, M. & MÃ¼LLER, M. (2006) In Situ Monitoring and Modeling of the Solvent-Mediated Polymorphic Transformation of l-Glutamic Acid. *Crystal Growth & Design,* 6**,** 881-891.

SCHOLL, J., LINDENBERG, C., VICUM, L. & BROZIO, J. (2007) Precipitation of α L-glutamic acid: determination of growth kinetics. *Faraday Discussions,* 136**,** 247-264.

SHEKUNOV, B. Y. & YORK, P. (2000) Crystallization processes in pharmaceutical technology and drug delivery design. *Journal of Crystal Growth,* 211**,** 122-136.

SPARKS, R. G. & DOBBS, C. L. (1993) The Use of Laser Backscatter Instrumentation for the on-line measurement of the particle size distribution of emulsions. *Particle & Particle Systems Characterization,* 10**,** 279-289.

STRICKLAND-CONSTABLE, R. F. (1972) *AIChE Symposium Series,* 68**,** 1.

SUSLICK, S. K. (1989) The effects of ultrasound. *Scientific American,* 260**,** 80-86.

SWALLOWE, G. M., FIELD, J. E., REES, C. S. & DUCKWORTH, A. (1989) A photographic study of the effect of ultrasound on solidification. *Acta Metallurgica,* 37**,** 961-967.

TADAYYON, A. & ROHANI, S. (1998) Determination of Particle Size Distribution by Par-Tec® 100: Modeling and Experimental Results. *Particle & Particle Systems Characterization,* 15**,** 127-135.

TANG, Z. X. & SHI, L. E. (2008) Preparation of nano-MgO using ultrasonic method and its characteristics. *Ecl. Quím.,* 33**,** 15-20.

THOMPSON, R. W. (2001) Nucleation, growth and seeding in zeolite synthesis. IN

EDITION, S. R. (Ed.) *Verified syntheses of Zeolitic materials.* Amsterdam, Elsevier Science B.V.

TIMOTHY J.MASON & PETERS, D. (2002) *Practical Sonochemistry: Power Ultrasound Uses and Applications* Chichester, Horwood Publishing Limited.

TIMOTHY J.MASON, J. P. L. (2002) *Applied Sonochemistry: Uses of Power Ultrasound in Chemistry and Processing,* Weinheim, Wiley-VCH Verlag GmbH.

TSOCHATZIDIS, N. A., GUIRAUD, P., WILHELM, A. M. & DELMAS, H. (2001) Determination of velocity, size and concentration of ultrasonic cavitation bubbles by the phase-Doppler technique. *Chemical Engineering Science,* 56, 1831-1840.

UBBENJANS, B., FRANK-ROTSCH, C., VIRBULIS, J., NACKE, B. & RUDOLPH, P. (2012) Numerical analysis of the influence of ultrasonic vibration on crystallization processes. *Cryst.Res.Technol.,* 47, 279.

UENO, S., RISTIC, R. I., HIGAKI, K. & SATO, K. (2003) In Situ Studies of Ultrasound-Stimulated Fat Crystallization Using Synchrotron Radiation. *The Journal of Physical Chemistry B,* 107, 4927-4935.

VAXELAIRE, P. (1995) U.S.Patent 5,384,508.

VELTMANS W H M, A. E. D. M. V. D. H. (1999) Sonocrystalisation of hydrazinium nitroformate to improve product characteristics. *14th International Symosium on Industrial Crystallization.* University of Cambridge, Institution of Chemical Engineers.

VIRONE, C., KRAMER, H. J. M., VAN ROSMALEN, G. M., STOOP, A. H. & BAKKER, T. W. (2006) Primary nucleation induced by ultrasonic cavitation. *Journal of Crystal Growth,* 294, 9-15.

VOLMER, M. (1939) *Kinetic der Phasenbildung,* Steinkopff, Leipzig.

VWR-WEBSITE.

WANG, Z., COMYN, T. P., GHADIRI, M. & KALE, G. M. (2011) Maltose and pectin assisted sol-gel production of Ce0.8Gd0.2O1.9 solid electrolyte nanopowders for solid oxide fuel cells. *Journal of Materials Chemistry,* 21, 16494-16499.

WIDENSKI, D., ABBAS, A., ROMAGNOLI, J. & RITA MARIA DE BRITO ALVES, C. A. O. D. N. A. E. C. B. (2009) A Theoretical Nucleation Study of the Combined Effect of Seeding and Temperature Profile in Cooling Crystallization. *Computer Aided Chemical Engineering.* Elsevier.

WIDENSKI, D. J., ABBAS, A. & ROMAGNOLI, J. A. (2010) Comparison of different solubility equations for modeling in cooling crystallization. *Chemical Engineering and Processing: Process Intensification,* 49, 1284-1297.

WINKEL, M. L., ZULLO, L. C., VERHEIJEN, P. J. T. & PANTELIDES, C. C. (1995) Modelling and simulation of the operation of an industrial batch plant using gPROMS. *Computers & Chemical Engineering,* 19, Supplement 1, 571-576.

WOHLGEMUTH, K., KORDYLLA, A., RUETHER, F. & SCHEMBECKER, G. (2009) Experimental study of the effect of bubbles on nucleation during batch cooling crystallization. *Chemical Engineering Science,* 64, 4155-4163.

WOHLGEMUTH, K., RUETHER, F. & SCHEMBECKER, G. (2010) Sonocrystallization and crystallization with gassing of adipic acid. *Chemical Engineering Science,* 65**,** 1016-1027.

WU, H., REEVES-MCLAREN, N., JONES, S., RISTIC, R. I., FAIRCLOUGH, J. P. A. & WEST, A. R. (2009) Phase Transformations of Glutamic Acid and Its Decomposition Products. *Crystal Growth & Design,* 10**,** 988-994.

YASUI, K., TUZIUTI, T. & KATO, K. (2011) Numerical simulations of sonochemical production of BaTiO3 nanoparticles. *Ultrasonics Sonochemistry,* 18**,** 1211-1217.

YOREO, J. J. D. & G, P. (2003) Principles of crystal nucleation and growth. *Review in Menealogy and Geochemistry* 54**,** 57-93.